

# **THERMAL PROPERTIES OF STRONGLY CORRELATED BOSONIC AND FERMIONIC SUPERFLUIDS**

*By*

**ABHISHEK JOSHI**  
**PHYS08201005001**

**Harish-Chandra Research Institute, Allahabad**

*A thesis submitted to the  
Board of Studies in Physical Sciences  
In partial fulfillment of requirements  
for the Degree of*  
**DOCTOR OF PHILOSOPHY**  
*of*

**HOMI BHABHA NATIONAL INSTITUTE**



**July, 2019**

# Homi Bhabha National Institute<sup>1</sup>

## Recommendations of the Viva Voce Committee

As members of the Viva Voce Committee, we certify that we have read the dissertation prepared by Abhishek Joshi entitled "Thermal Properties of strongly correlated bosonic and fermionic superfluids" and recommend that it may be accepted as fulfilling the thesis requirement for the award of Degree of Doctor of Philosophy.

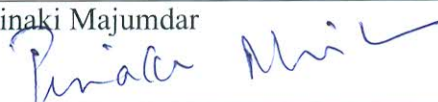
Chairman – Prof. Sumathi Rao

Date: 07-08-2020



Guide / Convener – Prof. Pinaki Majumdar

Date: 07-08-2020



Examiner – Prof. Subhasis Sinha

Date: 07-08-2020



Member 1- Prof. Prasenjit Sen

Date: 07-08-2020



Member 2- Prof. Ujjwal Sen

Date: 07-08-2020



Member 3- Prof. S. Naik

(Superannuated in Feb 2020)

Date: -

Final approval and acceptance of this thesis is contingent upon the candidate's submission of the final copies of the thesis to HBNI.

I/We hereby certify that I/we have read this thesis prepared under my/our direction and recommend that it may be accepted as fulfilling the thesis requirement.

Date: 07.08.2020

Place: Prayagraj



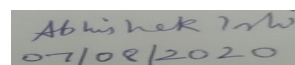
Prof. Pinaki Majumdar  
Guide

<sup>1</sup> This page is to be included only for final submission after successful completion of viva voce.

## STATEMENT BY AUTHOR

This dissertation has been submitted in partial fulfillment of requirements for an advanced degree at Homi Bhabha National Institute (HBNI) and is deposited in the Library to be made available to borrowers under rules of the HBNI.

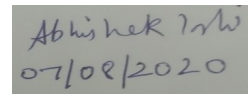
Brief quotations from this dissertation are allowable without special permission, provided that accurate acknowledgement of source is made. Requests for permission for extended quotation from or reproduction of this manuscript in whole or in part may be granted by the Competent Authority of HBNI when in his or her judgment the proposed use of the material is in the interests of scholarship. In all other instances, however, permission must be obtained from the author.

A rectangular box containing a handwritten signature 'Abhishek Joshi' and the date '07/08/2020' in black ink.

Abhishek Joshi

## DECLARATION

I, hereby declare that the investigation presented in the thesis has been carried out by me. The work is original and has not been submitted earlier as a whole or in part for a degree / diploma at this or any other Institution / University.

A rectangular box containing a handwritten signature 'Abhishek Joshi' and the date '07/08/2020' in blue ink.

Abhishek Joshi



## **List of Publications arising from the thesis**

### **Journal**

1. “The impact of speckle disorder on a superfluid fermi system”, Abhishek Joshi, and Pinaki Majumdar Phys. Rev. B. 100, 045149,.
2. “Thermal transition of the modulated superfluid for spin-orbit coupled correlated bosons in optical lattice”, Arijit Dutta, Abhishek Joshi, Krishnendu Sengupta, and Pinaki Majumdar , Phys. Rev. B, 99, 195126
3. “A classical fluctuation theory of the superfluid, Mott, and normal phases of correlated bosons” , Abhishek Joshi, Pinaki Majumdar , The European Physical Journal B 93, 1.

### **Preprint**

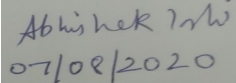
4. “Thermal decoherence in strongly correlated Bose liquid”, Abhishek Joshi, and Pinaki Majumdar arXiv:1712.04433.

### **Conferences**

1. School and Workshop on Physics of Cold Atoms, Hri Allahabad (2014). Presented poster titled “The impact of speckle disorder on fermi superfluids ”.
2. International Workshop on Bose Einstein Condensation and Related Phenomena. Presented poster titled “Superfluid to Mott transition: classical fluctuation approach”.

### **Others**

1. Teaching Assistant for the course “Condensed Matter Physics-1” during August-December, 2014.



Abhishek Joshi

## **DEDICATION**

*Dedicated to my parents N.C. Joshi and Promila Joshi,  
my brother Nitesh*

## ACKNOWLEDGEMENTS

I would like to express my gratitude to my advisor, Prof. Pinaki Majumdar, for his support, patience, and encouragement during my graduate studies. This thesis would not have been possible without his technical and editorial guidance. I would like to sincerely thank him for finding the time for listening to the little problems and roadblocks that unavoidably crop up during the course of graduate studies. His innumerable lessons are not restricted to Physics but goes beyond.

I express my sincere gratitude to all my teachers at HRI. I am indebted to Prof. Ashoke Sen, Prof. Sumathi Rao, Prof. Raj Gandhi, Prof. Biswarup Mukhopadhyay, Prof. Anirban Basu, Prof. G. V. Pai, Prof. Prasenjit Sen, Prof. Aditi Sen De, Prof. Ujjwal Sen, Prof. A. Dutta, Prof. Sriram, Prof Tirthankar, Prof. S. Naik and Prof. Ravindran for the excellent teaching and discussions. I am grateful to the people in the administrative and technical section of HRI. In particular, I would like to mention Rajiv, Chandan, Ravi, Mr. Sanjay Verma, and Mr. Amit Khulve for their constant supports.

I am grateful to Prof. Sengupta and my colleague Arijit Dutta for the collaboration. It gives me immense pleasure to mention the joy, I got from the numerous captivating discussions during the completion of collaborative work. The discussion sessions with my colleagues Krashna Mohan Tripathi, Uttam Singh, Samrat Kadge, Sauri Bhattacharya, Aditya Banerjee, Udit Khanna, Dibya, Priyanka Mohan, Roji Pius, Utkarsh Mishra and my seniors Rajarshi Tiwari, Sabyasachi, Saurabh Pradhan, Nyayabanta, Trilochan, Manjari and Yogeshwar have been very enlightening and motivated me to learn more.

Next I would like to thanks all my friends at HRI with whom I spent the most beautiful time in HRI. I would like to sincerely thanks KMT, Manish, Uttam, Tushar, Samrat, Ram Lal, Bhuvanesh ji, Sadhuji, Pradeepji(pantry), Sidharth, Rajesh, Lalit, Anurag and Harsh for their constant support both financially and mentally during last years of my graduate studies. I am forever grateful to my parents and to my brother, Nitesh, for supporting me throughout my academic career.

# Contents

<b>Summary</b>	<b>1</b>
<b>List of Figures</b>	<b>3</b>
<b>1 Experimental motivation</b>	<b>25</b>
1.1 Introduction . . . . .	25
1.2 Ultracold atomic systems . . . . .	26
1.2.1 Atom-light interaction . . . . .	26
1.2.2 Trapping of atoms . . . . .	27
1.2.3 Cooling of atoms . . . . .	27
1.2.4 Optical lattice . . . . .	28
1.2.5 Feshbach resonance . . . . .	30
1.3 The Bose Hubbard model . . . . .	32
1.3.1 General introduction . . . . .	34
1.3.2 Static properties . . . . .	37
1.3.3 Dynamical properties . . . . .	40
1.3.4 Experiments on dynamics . . . . .	43
1.3.5 Open issues . . . . .	50
1.4 Spin-orbit (SO) coupling . . . . .	51
1.4.1 Engineering SO coupling in Ultracold atoms(Continuum) . . . . .	52
1.4.2 SOC in optical lattices . . . . .	54
1.4.3 Open Issue in SOC: . . . . .	56
1.5 Disorder in an optical lattice . . . . .	56
<b>2 Theoretical tools</b>	<b>61</b>

2.1	Introduction . . . . .	61
2.2	Bose Hubbard model . . . . .	61
2.2.1	Theory approaches . . . . .	61
2.2.2	Unresolved issues . . . . .	65
2.2.3	Path integral formulation . . . . .	66
2.2.4	Static path approximation (SPA) . . . . .	68
2.2.5	Perturbed SPA . . . . .	69
2.2.6	Static measurables . . . . .	72
2.2.7	Estimation of $T_c$ . . . . .	73
2.2.8	Excitation spectra . . . . .	75
2.3	Spin-orbit coupled bosons . . . . .	78
2.3.1	Theory approaches . . . . .	78
2.3.2	Lattice model . . . . .	84
2.3.3	Computational method . . . . .	88
2.3.4	Measurables . . . . .	89
2.4	Disordered Fermi superfluids . . . . .	90
2.4.1	Microscopic model . . . . .	90
2.4.2	Speckle disorder . . . . .	90
2.4.3	Monte Carlo strategy . . . . .	91
2.4.4	Measurables . . . . .	93
<b>3</b>	<b>A classical fluctuation approach to correlated bosons</b>	<b>95</b>
3.1	Introduction . . . . .	95
3.2	Model and method . . . . .	97
3.3	Results on the ground state . . . . .	100
3.4	Finite temperature behaviour . . . . .	102
3.4.1	Phase diagram . . . . .	102
3.4.2	Superfluid phase . . . . .	103
3.4.3	Mott insulator . . . . .	108
3.4.4	Normal Bose liquid . . . . .	111

---

3.5	Discussion . . . . .	113
3.5.1	The thermal transition . . . . .	113
3.5.2	Size dependence . . . . .	115
3.5.3	Computational cost . . . . .	116
3.5.4	Three dimensions . . . . .	116
3.5.5	Future applications . . . . .	117
3.6	Conclusions . . . . .	117
<b>4</b>	<b>Finite temperature spectra of the Bose Hubbard model</b>	<b>119</b>
4.1	Introduction . . . . .	119
4.2	Model and method . . . . .	122
4.3	Spectrum at zero temperature . . . . .	124
4.3.1	Superfluid ground state . . . . .	124
4.3.2	Mott ground state . . . . .	128
4.4	Spectra at finite temperature . . . . .	128
4.4.1	Low temperature superfluid . . . . .	128
4.4.2	Superfluid to Bose liquid transition . . . . .	133
4.4.3	Low temperature Mott phase . . . . .	135
4.4.4	High temperature Bose liquid . . . . .	138
4.4.5	Finite temperature phase diagram . . . . .	140
4.5	Discussion . . . . .	141
4.5.1	Analysing the $T = 0$ results . . . . .	141
4.5.2	A model for finite $T$ spectra . . . . .	144
4.6	Conclusions . . . . .	150
<b>5</b>	<b>Spin-orbit coupled correlated bosons in an optical lattice</b>	<b>151</b>
5.1	Introduction . . . . .	151
5.2	Model and method . . . . .	153
5.2.1	Model . . . . .	154
5.2.2	Effective Hamiltonian . . . . .	155

---

5.2.3	Methods . . . . .	157
5.2.4	Indicators . . . . .	159
5.3	Variational ground state . . . . .	160
5.4	Finite temperature results . . . . .	164
5.5	Understanding of thermal scales . . . . .	166
5.6	Discussion . . . . .	170
5.7	Conclusion . . . . .	172
<b>6</b>	<b>Impact of speckle disorder on Fermi superfluids</b>	<b>173</b>
6.1	Introduction . . . . .	173
6.2	Model and method . . . . .	176
6.3	Ground state . . . . .	178
6.3.1	Spatial behaviour . . . . .	178
6.3.2	Phase diagram . . . . .	180
6.3.3	Density of states . . . . .	181
6.4	Thermal fluctuations . . . . .	182
6.4.1	Phase diagram . . . . .	182
6.4.2	Speckle variation . . . . .	185
6.4.3	Disorder variation . . . . .	185
6.5	Discussion . . . . .	186
6.5.1	Ground state properties . . . . .	186
6.5.2	Phase coupling scales . . . . .	191
6.5.3	Cold atom experiments . . . . .	193
6.6	Conclusion . . . . .	194
<b>7</b>	<b>Summary of the thesis</b>	<b>195</b>
<b>A</b>	<b>Appendix A</b>	<b>199</b>
A.1	Approximate SPA functional at $T = 0$ . . . . .	199
A.2	Approximate PSPA functional at $T = 0$ . . . . .	200
A.3	Internal energy . . . . .	202

A.3.1	Approximation I: SPA . . . . .	202
A.3.2	Approximation II: PSPA . . . . .	203
A.4	Momentum distribution . . . . .	204
<b>B</b>	<b>Appendix B</b>	<b>209</b>
B.1	Random phase approximation (RPA) . . . . .	209
<b>C</b>	<b>Appendix C</b>	<b>211</b>
C.1	Effective action in the spin orbit problem . . . . .	211
<b>D</b>	<b>Appendix D</b>	<b>213</b>
D.1	Derivation of an effective XY model . . . . .	213
	<b>Bibliography</b>	<b>217</b>



# List of Figures

1.1	Velocity distribution of a gas of rubidium atoms as it is cooled. From left to right - just before appearance of the condensate, appearance of the condensate, after further evaporative cooling [10] . . . . .	26
1.2	Optical lattice potentials formed by superimposing two or three orthogonal standing waves. (a) In a 2D optical lattice, the atoms are confined to an array of tightly confining 1D potential tubes. (b) In 3D, the optical lattice can be approximated by a simple cubic array of tightly confining harmonic oscillator potentials at each lattice site [2] . . . . .	29
1.3	Image of Gaussian beam used in ultracold atoms. The radial profile of laser beams used in cold atom experiments. Beams is propagating along the $z$ direction, where $r$ is the radial distance from the $z$ -axis, $w(z)$ is the beam width in the radial direction, $w_0$ is the minimum beam width called beam waist, $z_R$ is the Rayleigh length, and $\lambda$ is the wavelength of the laser. [1] . . . . .	30
1.4	Basic two-channel model for a Feshbach resonance. The phenomenon occurs when two atoms colliding at energy $E$ in the entrance channel resonantly couple to a molecular bound state with energy $E_c$ supported by the closed channel potential. In the ultracold domain, collisions take place near zero energy, $E \rightarrow 0$ . Resonant coupling is then conveniently realized by tuning $E_c$ near 0 if the magnetic moments of the closed and open channels differ. [12] . . . . .	31
1.5	Variation of the $s$ -wave scattering length $a$ across a Feshbach resonance for a varying magnetic field $B$ [13] . . . . .	31

1.6	Interpretation of the Bose Hubbard model parameters for atoms in an optical lattice. $t$ is the hopping amplitude between neighbouring minima. $U$ is the Hubbard interaction energy between the two atoms localized at the same minimum. . . .	33
1.7	(a) At low laser intensity the atoms can move freely between valleys - a superfluid state, (b) when the laser intensity is hiked up atoms get trapped in individual minima, since tunneling costs a large repulsive energy, and the system is Mott insulating [22]. . . . .	34
1.8	Ground state phase diagram in the $zt/U, \mu/U$ plane obtained using MFT. The Mott lobes correspond to integer particle numbers while the surrounding regions are superfluid. . . . .	36
1.9	Momentum distribution patterns after atoms are released from a 3D optical lattice for potentials with depth: (a) 0, (b) $3E_r$ , (c) $7E_r$ , (d) $10E_r$ , (e) $13E_r$ , (f) $14E_r$ , (g) $16E_r$ , and (h) $20E_r$ . The expansion time was 15ms. [26] . . . . .	37
1.10	Momentum distributions and cross sections at $U/t = 4, 8, 20$ in 2D. Each row shows a single momentum distribution normalized by the total atom number; the lines in the top right panel indicate trajectories along which four cross sections were taken. The left panel shows the average of these four sections (black solid line); the red dashed lines denote the fit to the bimodal distribution. [27] . . . .	38
1.11	Single site imaging of the atom number fluctuations across the SF-Mott transition. Even number of particle is associated with empty sites. The particle density is maintained such that Mott insulator has one particle. Top row: As one tunes the optical depth from $6E_r$ to $16E_r$ double occupancies are suppressed and Mott insulator at $16E_r$ has one particle per site. Middle row: Results for top row. Solid circle represents atom present and open circle indicate absence of atom. Bottom row: Time of flight imaging results indicating loss of coherence as one hikes up the optical depth. [30] . . . . .	39

- 1.12 Energy density as a function of the order parameter. The ordered phase (superfluid) has minima for non zero value of order parameter. Two types of low energy excitation exist - Goldstone (phase) and Higgs (amplitude) modes. The Goldstone mode has its origin in phase twist and the Higgs mode is associated with change in magnitude of the order parameter. As  $J/U$  decreases beyond critical coupling the minimum of the energy density is at zero. In the disordered phase two gapped mode exist namely particle and hole excitation. [41] . . . . . 44
- 1.13 Softening of the Higgs mode. (a) The fitted gap values  $h\nu_0/U$  (circles) show a characteristic softening close to the critical point. Horizontal and vertical error bars denote the experimental uncertainty of the lattice depths and the fit error for the centre frequency of the error function, respectively. Vertical dashed lines denote the widths of the fitted error function and characterize the sharpness of the spectral onset. The blue shading highlights the superfluid phase (b) Temperature response to lattice modulation (circles and connecting blue line) and fit with an error function (solid black line) for the three different points labeled in a. As the coupling  $j(t/U)$  approaches the critical value  $j_c$ , the change in the gap values to lower frequencies is clearly visible (from panel 1 to panel 3). Vertical dashed lines mark the frequency  $U/h$  corresponding to the on-site interaction. Each data point results from an average of the temperatures over 50 experimental runs. [41] 45
- 1.14 The low-frequency response in the superfluid regime shows a scaling compatible with the prediction  $(1 - j/j_c)^{-2}\nu^3$ . Shown is the temperature response rescaled with  $(1 - j/j_c)^{-2}$  for  $V_0=10E_r$  (grey),  $9.5E_r$  (black),  $9E_r$  (green),  $8.5E_r$  (blue) and  $8E_r$  (red) as a function of the modulation frequency. The black line is a fit of the form  $a\nu^b$  with a fitted exponent  $b=2.9$ . The inset shows the same data points without rescaling, for comparison. [41] . . . . . 46

1.15	Experimental set up for Bragg spectroscopy. Ultracold atoms are loaded into the optical lattice, and energy and momentum is transferred to the sample by shining light using two laser beams incidenting at an angle. The angle of incidence could be changed by changing the angle between two laser beams and could be used to scan the Brillouin zone.[56]	48
1.16	Energy absorption (a) and quasi-momentum density (b),(c) spectra for a square pulse. Energy absorption (a) and quasi-momentum density (b),(c) spectra for a square pulse at high intensity $V = 0.1E_r$ (insets: weak intensity $V = 0.005E_r$ ) in the intermediate interaction $s = 9$ regime and for Bragg momentum $ \vec{p}_B  = \frac{\pi}{a}$ . The resonance frequencies predicted from the maxima of the high intensity energy absorption spectra (plotted as gray squares in (d)) contain a systematic uncertainty quantified by the FWHM of the pulse after 10ms $\sim 3.26/J$ indicated by the error bars and shaded region in (d). The comparison with the true quasiparticle energies (dashed white lines in (a-c), black circles in (d)) reveals significant discrepancies. For comparison in (d): The blue dotted line is the Bogoliubov result, the green dashed lines are the results from for the amplitude and sound modes $\omega(\vec{k}) = \psi_0 \sqrt{2U n \epsilon_k}$ with $\psi_0$ determined by GW). [58]	49
1.17	a) Laser beams of frequency $\omega_1, \omega_2$ induce Raman transition between internal states $ a\rangle$ and $ b\rangle$ . (b)Change in momentum of gas $\vec{k} = \vec{k}_1 - \vec{k}_2$ due to Raman transition.	53
1.18	Spin-resolved time-of-flight image of the momentum distribution for three values of temperature $T$ and condensate fraction $f$ . At $T = 63nK$ , the population imbalance of the condensate shows that it is in a magnetized phase.[81]	54
1.19	Finite temperature phase diagram of spin-orbit coupled bosons[81]	55

1.20	The experimental set up to introduce speckle disorder in an optical lattice [?]. The atoms are trapped using optical dipole trap (gray lines). The lasers are superimposed to create 3D optical lattice(red). The speckle field is imposed on the atoms (green). The optical speckle field is produced by passing a 532 nm laser beam through a holographic diffuser and focusing it onto the atoms. The two dimensional representation of lattice is shown where two hyperfine states of atom are represented using different color. . . . .	57
2.1	Left panel: Comparison of phase diagram of the square lattice Bose-Hubbard model in the space of interaction and temperature for $n = 1$ using various approaches. Right panel: ground- state phase diagram in the space of $t/U$ and $\mu/U$ , showing the first two Mott lobes surrounded by superfluid under various approaches. . . . .	65
2.2	The coupling $C_{ij}$ between the boson field $b_i$ and the auxiliary field $\psi_j$ . The reference site $i$ is taken to be the origin $(0, 0)$ . The plot highlights the rapid decay of $C_{ij}$ with separation $R_{ij}$ , justifying a ‘cluster treatment’ (see text) of the energy cost. . . . .	68
2.3	Left Panel: Plot of the $\mathbf{q} = 0$ structure factor at various lattice sizes as a function of temperature. Right panel: plot of $\alpha_L$ as a function of system size defined below. . . . .	74
2.4	Top: The band structure for $\gamma = 0.3$ . The dispersion has a four fold symmetry. The minima occur at finite wavevectors, as is evident from the projection of the lower band onto the x-y plane. Bottom: The noninteracting density of states for three different values of $\gamma$ . $\gamma = 0$ has the usual tight binding form in 2D, while for finite $\gamma$ one observes a dip at zero along with a linearly rising behavior which is reminiscent of the Dirac cone present in the band structure at the $\Gamma$ point. All energies are in units of $t$ . . . . .	79

2.5	Classical magnetic phases for the classical spin model determined by Monte Carlo annealing on a $36 \times 36$ site square lattice.[157] . . . . .	81
2.6	Classical magnetic states in the Mott insulating limit of the spin-orbit coupled Bose-Hubbard model. (a) Spiral-1 state; coplanar spin-orientation rotating along (11). (b)Spiral-2 state; coplanar spin-orientation rotating along (10). (c) Vortex crystal; $2 \times 2$ unit cell with $\pi/2$ rotation along each bond. (d) Skyrmion crystal; the $3 \times 3$ unit cell is highlighted with a gray box. The central spin points in the positive $z$ direction, while the remaining spins tumble outward toward $-z$ direction.[157] . . . . .	82
2.7	Mott lobes in the $t/U, \mu/U$ plane for different values of spin orbit coupling and interspecies interaction strength. With increasing spin orbit coupling the Mott-superfluid phase boundary is shift to larger values of $t/U$ . [157] . . . . .	83
2.8	The speckle correlation function $(\langle V(\vec{x})V(\vec{x} + \vec{r}) \rangle - \langle V(\vec{x}) \rangle^2 / \langle V(\vec{x})^2 \rangle)$ for $V = 1$ , plotted as a function of $r/\sigma$ , by actually sampling our disorder configurations. The function should be universal, and die off for $r/\sigma \gg 1$ , but sampling on a $24 \times 24$ lattice leads to the non universal features at large $\sigma$ . . . . .	90
3.1	The ground state of the 2D Bose Hubbard model for varying $\mu/t$ and $U/t$ . The region within the lobe is a Mott insulator with $n = 1$ . The inner lobe, with a smaller $(t/U)_c$ is SPA result (and same as mean field theory). The outer lobe, with larger $(t/U)_c$ , is the PSPA result and is indistinguishable from QMC. . . .	99
3.2	Energy functions in SPA and PSPA. The open circles show the SPA and PSPA energy functions, plotted for an uniform order parameter, $\Phi$ , for the values of $U/t$ indicated. The SPA and PSPA minima match with each other in panels (a) and (b), in panel (c) the difference is noticeable, while in (d) the SPA minimum is at finite $\Phi$ while the PSPA minimum has shifted to zero. The firm lines are even order Landau fits to the energy functions to $\mathcal{O}(\Phi^6)$ . . . . .	101

- 3.3 Landau parameters for (a) SPA and (b) PSPA. In SPA  $a_4 > 0$  for all  $U/t$ ,  $a_6$  is negligible, and the second order transition is driven by sign change in  $a_2$ . For PSPA  $a_2, a_6 > 0$  at all  $U/t$ . There is always a minimum at  $\Phi = 0$ , and the transition is driven by a decreasing  $a_4$ . . . . . 102
- 3.4 Superfluid  $T_c$  from different methods for the 2D Bose Hubbard model at filling  $n = 1$ . We use  $U_c(0)$ , the  $T = 0$  critical interaction, and  $T_c^{max}$ , the maximum superfluid  $T_c$ , to characterise each scheme. (i) Mean field theory (MFT) yields  $U_c(0) = 24t$  and  $T_c^{max} = 6t$ , (ii) for our simplest method, the SPA,  $U_c(0) = 24t$  and  $T_c^{max} \sim 2.5t$ , (iii) for the PSPA,  $U_c(0) \sim 17t$  and  $T_c^{max} \sim 2.5t$ . For full quantum Monte Carlo (iv)  $U_c(0) \sim 17t$  and  $T_c^{max} \sim 2t$ . . . . . 103
- 3.5 MC snapshot of spatial correlations in the superfluid. Top:  $U = 6t$ , bottom:  $U = 15t$ . The maps indicate the correlation  $C_i$  of the hybridisation at a site with its four neighbours.  $C_i = \sum_{\delta} |\Phi_i| |\Phi_{i+\delta}| \cos(\theta_i - \theta_{i+\delta})$ . The patterns are quasi homogeneous at low  $T$ , with a larger value for  $U = 6t$ . The  $U = 6t$  pattern fragments slower with temperature. Even for  $T > T_c$  small spontaneous clusters with large correlation are present. System size  $32 \times 32$ . . . . . 104
- 3.6 (a)-(b): Distribution of the magnitude of the local hybridisation in the superfluid regime. The lowest temperature in the data set is  $T = 0.2t$  at which amplitude fluctuations are already visible. The distributions appear gaussian in the weaker  $U$  systems. (c)-(d): Mean and standard deviation of  $|\Phi|$ . In the superfluid ( $U/t \lesssim 16$ ) the mean falls only weakly between  $T = 0$  and  $T_c$ , and somewhat faster for  $T \gtrsim T_c$ . The fluctuation ‘width’ is fitted to a form  $\Phi_{wid} = BT^\beta$  at low  $T$ . We find  $\beta \approx 0.5$  at both  $U = 6t$  and  $15t$ . . . . . 105
- 3.7 The correlation length  $\xi(T)/L$  inferred from  $\mathbf{q}$  dependence of  $S(\mathbf{q})$ , at  $U = 6t, 15t$ .  $\xi$  ‘diverges’ as  $T \rightarrow 0$  and is larger at  $U = 6t$  than at  $15t$  at all temperature. This is consistent with the spatial patterns in Fig.6. . . . . 105

- 3.8 The momentum distribution,  $n(\mathbf{k})/N = \langle \langle a_{\mathbf{k}}^\dagger a_{\mathbf{k}} \rangle \rangle / N$ , for varying interaction strength and temperature in the superfluid phase. The intensity scale is linear and varies across the panel to simultaneously capture the condensate peak in the superfluid state and show the particle distribution in high temperature normal phase. . . . . 106
- 3.9 Momentum distribution in the superfluid. (a) Low  $T$  data from QMC [163], (b) data at same parameter points from PSPA. (c)-(d) Scan of  $n_{\mathbf{k}}$  for  $\mathbf{k}$  from  $(0, 0) \rightarrow (0, \pi)$ , at  $U = 6t$  and  $15t$  We have shown these results on a log scale to highlight behaviour over the large  $k$  window. . . . . 107
- 3.10 Energy and specific heat in the superfluid. (a) Compares the  $T$  dependence of the kinetic energy at  $U = 10t$  between QMC and PSPA. The match is excellent. SPA energies are significantly higher. (b) Shows the internal energy  $E(T)$  at three  $U$  values, the change in slope suggestive of a thermal transition. (c) The  $C_v$  showing the broad peak at low  $U$  associated with the thermal transition, and a two peak at feature at  $U = 15t$  - one at  $T \sim t$  associated with the thermal transition, another at  $T \sim 4t$  associated with amplitude fluctuations. . . . . 107
- 3.11 Spatial map of  $C_i = \sum_{\delta} |\Phi_i| |\Phi_{i+\delta}| \cos(\theta_i - \theta_{i+\delta})$  in the Mott insulator. Top row  $U = 20t$ , bottom  $U = 30t$ .  $C_i$  vanishes as  $T \rightarrow 0$  since the  $\Phi_i \rightarrow 0$ . Thermal fluctuations generate finite  $\Phi_i$  when  $T \neq 0$  and these can correlate over a small neighbourhood. The tendency is stronger at  $U$  near  $U_c$  rather than in the deep Mott phase at  $U = 30t$ . System size  $32 \times 32$ . . . . . 108
- 3.12 (a)-(b) Distribution of  $|\Phi|$  in the Mott insulator. The lowest temperature is  $T = 0.2t$  at which amplitude fluctuations are already visible. (c) Mean and (d) standard deviation of  $|\Phi|$ . In the Mott phase the mean is zero at  $T = 0$  but rises quickly attaining a value  $\sim 0.5$  that of the weak  $U$  superfluid at  $T \sim 3t$ . Both the mean value and width increase as  $\sqrt{T}$ . . . . . 109



- 3.13 Momentum distribution  $n(k_x, k_y)/N$  in the Mott regime. Top row:  $U = 20t$ , bottom:  $U = 30t$ . In the mean field Mott state  $n(k_x, k_y) = 1$  at all  $T$ . Here, quantum fluctuations generate a correction of  $\mathcal{O}(t_k/U)$  at  $T = 0$  and finite  $T$  brings in additional corrections. At a given  $T$  the correction weakens with increasing  $U/t$  . . . . . 110
- 3.14  $n(k_x, 0)/N$  for varying  $U$  and  $T$  in the Mott regime. (a) Low  $T$  QMC data [163] on a  $24 \times 24$  lattice, *i.e.*,  $N = 576$ . In a mean field state occupancy would have been  $\mathbf{k}$  independent and  $\sim 0.002$ . The QMC number at  $U = 16.7t$ , just into the Mott state is 10 times larger at  $\mathbf{k} = (0, 0)$ . (b) Our result for the parameters comparable to QMC. The  $\mathbf{k}$  dependence is much weaker than QMC and the  $\mathbf{k} \rightarrow 0$  values much smaller. (c)-(d) Show  $T$  dependence of our results at  $U = 20t$  and  $30t$  respectively for system size  $32 \times 32$  lattice, *i.e.*,  $N = 1024$ . 111
- 3.15 Behaviour in the normal Bose liquid. Top row: spatial map of  $C_i = \sum_{\delta} |\Phi_i| |\Phi_{i+\delta}| \cos(\theta_i - \theta_{i+\delta})$  from MC snapshots. The spatial correlation weakens as one moves from  $U = 6t$  to higher values. Bottom row: the thermally averaged momentum distribution  $n(k_x, k_y)$ . At  $U = 6t$  the distribution is still reasonably peaked, with the  $\mathbf{k} = (0, 0)$  value being  $\sim 8$  times the mean value (0.001). Increasing  $U$  reduces the peak and flattens out the distribution but there is no dramatic difference between  $U = 15t$  and  $U = 20t$  which evolved, respectively, from a superfluid and a Mott insulator. . . . . 112
- 3.16 Indicators for the normal Bose ‘liquid’ at  $T = 3t$ . (a) Mean amplitude  $\Phi_{av}$ , (b) fluctuation width  $\Phi_{wid}$ , (c) correlation length  $\xi(U)$ , and (d) momentum distribution  $n(k_x, 0)$ . Note that although  $U = 6t$  and  $U = 30t$  are a ‘strong superfluid’ and a ‘deep Mott insulator’ at  $T = 0$ , their  $\Phi_{av}$  and  $\Phi_{wid}$  are within a factor of 2 at  $T = 3t$ . The correlation length, on this  $L = 32$  system is  $\gtrsim 2$  lattice spacing at  $U = 6t$  and  $\lesssim 1$  at  $U = 30t$ .  $n(\mathbf{k} = (0, 0))$  differs only by a factor of 2 between the extreme  $U$  values. . . . . 113

- 3.17 Left: the coupling function  $a_{ij}$  that enters the effective XY model. It depends only on the band structure of the non interacting system. Right: Comparison of  $T_c$  obtained from the effective XY model with  $T_c$  from the SPA based Monte Carlo. For  $U \gtrsim 0.5U_c$ , the match is reasonable. At smaller  $U$  the mean amplitude suppression with increasing temperature is a significant effect. . . . . 115
- 3.18 Size dependence of the  $\mathbf{q} = (0,0)$  structure factor at  $U = 4t, 15t$ . At both these  $U$  values the function, and the superfluid onset temperature is almost size independent for  $L \gtrsim 24$ . . . . . 116
- 4.1 Spectral function and density of states in the superfluid ground state. From left to right along each row,  $U = 2t, 10t, 15t$ . First row: A map of  $|A(\mathbf{k}, \omega)|$ , where  $A(\mathbf{k}, \omega)$  is the spectral function, for the diagonal scan  $\mathbf{k} : (0,0) \rightarrow (\pi, \pi)$ . Second row: the lineshape of  $|A(\mathbf{k}, \omega)|$ , highlighting the variation in the residue, and the resolution limited lineshape. Third row: the density of states  $N(\omega)$ . Note the growing negative energy weight as  $U/t$  increases. . . . . 125
- 4.2 Key features of the  $T = 0$  spectrum. (a) Superfluid velocity, (b) difference in energies at  $\mathbf{k} = (0,0)$  and  $(\pi, \pi)$  for the gapless positive mode and the gapped positive mode, (c) dependence of the residue at  $\mathbf{k} = (0,0)$  on  $U/t$ , (d) same at  $\mathbf{k} = (\pi, \pi)$  . . . . . 126
- 4.3 Spectral function and density of states in the Mott ground state. From left to right along each row,  $U = 25t, 30t$ . First row:  $|A(\mathbf{k}, \omega)|$  second row: the lineshape of  $|A(\mathbf{k}, \omega)|$ , and third row: density of states  $N(\omega)$ . . . . . 127

- 4.4 Spectral function and density of states in the superfluid phase at finite temperature. Upper rows:  $|A(\mathbf{k}, \omega)|$  with increasing temperature for  $U = 2t$  (first row),  $U = 10t$  (second row) and  $U = 15t$  (third row). Bottom row: density of states  $N(\omega)$ . Notice the merger of the Goldstone mode with the weakly dispersive upper branch as  $T$  is increased, and the loss in weight of the negative frequency branch for  $U = 2t$  and  $10t$ . . . . . 129
- 4.5 Parametrisation of the finite  $T$  spectral data in the superfluid regime. First column: mean dispersion, second column: residue, third column: broadening for the gapless band at positive energy, fourth column: broadening for amplitude band at positive energy. From first row to last row,  $U$  varies from  $2t, 10t, 15t$ . . . 130
- 4.6 Map of the  $\mathbf{k}$  dependence of  $\omega_{\mathbf{k}}$  and  $\gamma_{\mathbf{k}}$  for the positive phase band and amplitude band at  $U = 10t$  at  $T = 0.3T_c$  in the first quadrant of Brillouin zone. (a) dispersion  $\omega_{k_x, k_y}$  for the positive gapless band (GM) (b) dispersion  $\omega_{k_x, k_y}$  for the positive amplitude band (HM), (c) broadening  $\Gamma_{k_x, k_y}$  for the positive gapless band (GM), (d) broadening  $\Gamma_{k_x, k_y}$  for the positive amplitude band (HM) . . . . 131
- 4.7 Temperature dependence of  $\Gamma_{\mathbf{k}}$  for few  $\mathbf{k}$  values. (a)-(b) Positive gapless band, and (d)-(e) positive gapped band.  $U = 4t$  and  $U = 10t$  and  $0 < T < 0.7T_c$ . Symbols are the exact data points and dotted line is the fit using power law form  $\Gamma_{\mathbf{k}} \sim AT^\alpha$ . (c) Exponent  $\alpha$  as a function of  $\mathbf{k}$  for  $U = 4t$  and  $10t$  for the positive gapless band. Similarly (f) shows the exponent for the positive gapped band. . . 133
- 4.8 Evolution of spectral map for  $U = 10t$  from  $0.6T_c$  to  $1.2T_c$ . Notice the merging of gapless and gapped band as temperature rises. . . . . 134
- 4.9 Spectral map for  $U = 4t, 10t, 15t, 22t$  close to  $T_c$ . There is continuous evolution of spectral map as one goes from below  $T_c$  to above  $T_c$ . No sharp features are seen in the spectral map as one goes above the transition temperature. . . . . 134

- 4.10 Spectra in the finite temperature Mott state.  $|A(\mathbf{k}, \omega)|$  with increasing temperature. First row:  $U = 25t$ , second row:  $U = 30t$ . . . . . 135
- 4.11 Density of states  $N(\omega)$  (a)  $U = 25t$  and (b)  $U = 30t$ . The increase in gap and suppression of van-Hove like peak with temperature is visible . . . . . 136
- 4.12 Parametrisation of the spectral data. First column: mean dispersion, second column: residue, third column: broadening for the particle band, fourth column: broadening for hole band. Top row:  $U = 25t$ , Bottom row:  $U = 30t$ . . . . . 136
- 4.13 Temperature dependence of  $\Gamma_k$  for few  $k$  values for the positive gapped band shown in (a) for  $U = 25t$  and (b) for  $U = 30t$  between 0 to  $0.5E_g$ . Symbols are the exact data points and dotted line is the fit using power law form  $\Gamma_k \sim AT^\alpha$ . (c) shows the plot of exponent  $\alpha$  as a function of  $k$  for  $U = 25t$  and  $30t$  for the positive gapped band. . . . . 137
- 4.14 The effect of increasing interaction in the  $T > T_c$  normal Bose liquid. First row:  $|A(\mathbf{k}, \omega)|$  second row: lineshapes, third row:  $N(\omega)$  Fourth row:  $P(|\Phi|)$ . From left to right  $U = 2t, 10t, 22t, 25t$ . The opening of gap with increasing interaction strength is visible. The temperature is  $T = 3t$ . . . . . 138
- 4.15 (a) Dispersion, (b) residue and (c) damping for the  $U$  variation at  $T = 3t$ . . . . 139
- 4.16  $U$  dependence of the positive mode damping for few  $k$  values at  $T = 3t$ . . . . . 139

- 4.17 Left Panel: Map of the single particle gap in the spectrum between  $0.8U_c$  to  $1.2U_c$  for temperature between 0 to  $3t$ . The temperature rise leads to opening of gap even below  $U_c$ . With increase in temperature single particle gap begins to increase. Right Panel: ‘Phase diagram’ of the 2D-BHM in terms of its spectral properties. Shows the superfluid to normal transition temperature,  $T_c$ , the temperature  $T_g$  above which the spectrum shows a gap. Below the shaded area the spectrum is four mode and four mode fit works well. Above the shaded area, spectrum has two bands one on the positive side of the frequency axis and another on the negative side of the frequency axis. Within the shaded area transition from four mode to two mode occur due to merging of gapped and gapless band with rising temperature. . . . . 140
- 4.18 Spectral results obtained by approximating the atomic Green’s function to order  $|\Phi|^2$ . Top row: Spectral map in the superfluid phase. Along the row  $U = 12t, 15t, 18t$ . Bottom row: Comparison between exact RPA in the groundstate with the approximate calculation. Dotted line is the exact result and open circles are result from approximate calculation. (a) superfluid velocity obtained from slope of dispersion of gapless band (b) amplitude mode gap at  $\vec{k} = (0, 0)$  (c) residue of gapless and gapped band at  $\vec{k} = (\pi/12, \pi/12)$ . . . . . 143
- 4.19 Comparison between spectra obtained from exact RPA calculation and approximate calculation at three  $U$  values and for three  $\vec{k}$  as a function of temperature. Top row  $U = 10t$ , Middle row  $U = 22t$  and Third row  $U = 30t$ . For each of these comparison is shown at three temperature values  $T = 0.5t, 1.0t, 2.0t$ . The match between two calculation is good at large  $\vec{k} = (\pi/2, \pi/2)$  and  $(\pi, \pi)$  but at  $(\pi/12, \pi/12)$  match is bad except deep in the Mott phase. Last row shows the comparison of lineshapes obtained from two calculation in the normal state  $T = 3.0t$ .  $U$  values are  $10t, 22t, 30t$  as one moves along the row. Solid lines are approximate calculation and open circles are exact results. . . . . 145

- 4.20 Temperature dependence of amplitude ‘width’ and damping scales. a)  $\Phi_{wid}$  b) width of atomic Green’s function around one of the  $T = 0$  pole. c) width of positive band obtained from exact RPA calculation at  $\vec{k} = (\pi/2, \pi/2)$ . The results are shown for  $U = 10t, 22t, 30t$ . Open circles are exact results and firm lines are  $T^{1/2}$  fit, indicating the tempearture behaviour is same for all these quantities. . . . . 147
- 4.21  $U$  dependence of amplitude ‘width’ and damping scales. a)  $\Phi_{wid}$  b) width of positive gapless band. c) width of gapped positive band obtained from exact RPA calculation at  $\vec{k} = (\pi/2, \pi/2)$ . The results are shown for  $T/t = 0.5t, 1.5t, 2.5t$ . The curves are non-monotonic as a function of interaction strength with point of maxima shifting to lower  $U$  values as temperature rises. . . . . 147
- 5.1 Left panels (a1-a4): The variational families chosen for minimization. The ratio  $|\phi_{k_0}^+|/|\phi_{k_0}^-|$  has been plotted in color and  $(Re[\phi_{k_0}^-], Im[\phi_{k_0}^-])$  has been plotted using arrows. Right panels (b1-b4): the magnetic textures corresponding to the left panels. The  $(\mathbf{m}_x, \mathbf{m}_y)$  components have been plotted using arrows, while the  $\mathbf{m}_z$  component has been plotted in color. (a1, b1) represent a typical single mode configuration, (a2, b2) a two mode, (a3, b3) a four mode, and (a4, b4) a vortex configuration. The single mode and the two mode configurations arise in the ground state but the four mode and the vortex configurations do not. . . . . 153
- 5.2 Variational ground state phase diagram. The variation of superfluid order parameter is shown in color. Left panel a1-a3 shows the results for  $\lambda=0.5$ , at  $\gamma = 0, 0.3\pi$  and  $0.5\pi$  respectively. The superfluid phase in these cases is a plane wave state with homogeneous FM order. The right panel b1-b3 shows the same plot for  $\lambda=1.5$ . In this case, the superfluid phase has a two mode superposition which leads to a stripe like magnetic texture - FIG.5.6. The dashed lines demarcate the superfluid and Mott phase boundaries as calculated from the effective Landau functional described in section 5.5. . . . . 154

- 5.3 Classification of the ground state superfluid phases for  $U/t = 10$ . For  $\lambda < 1$  and  $\gamma = 0$  we get a homogeneous superfluid in which  $\langle b_{i\alpha}^\dagger \rangle$  remains constant throughout the system. The phase-twisted superfluid has homogeneous amplitude of  $\langle b_{i\alpha}^\dagger \rangle$ , but its phase modulates from site to site. The Z-FM is a homogeneous phase in which there is condensation in only one of the spin state. The stripe phase supports spatial modulation in both the amplitude and the phase of  $\langle b_{i\alpha}^\dagger \rangle$ , and is characterized by stripe-like patterns in the magnetic texture, FIG. 5.6. For  $\gamma > 0.4$  the stripe phase shows a  $(\pi, \pi)$  order, which is the Z-AFM phase mentioned in Ref. [157]. . . . . 155
- 5.4 Top: The band structure for  $\gamma = 0.3$ . The dispersion has a four fold symmetry. The minima occur at finite wavevectors, as is evident from the projection of the lower band onto the x-y plane. Bottom: The noninteracting density of states for three different values of  $\gamma$ .  $\gamma = 0$  has the usual tight binding form in 2D, while for finite  $\gamma$  one observes a dip at zero along with a linearly rising behavior which is reminiscent of the Dirac cone present in the band structure at the  $\Gamma$  point. All energies are in units of  $t$ . . . . . 156
- 5.5 Left panels (a1-a4): The variational families chosen for minimization. The ratio  $|\phi_{k_0}^+|/|\phi_{k_0}^-|$  has been plotted in color and  $(\text{Re} [\phi_{k_0}^-], \text{Im} [\phi_{k_0}^-])$  has been plotted using arrows. Right panels (b1-b4): the magnetic textures corresponding to the left panels. The  $(\mathbf{m}_x, \mathbf{m}_y)$  components have been plotted using arrows, while the  $\mathbf{m}_z$  component has been plotted in color. (a1, b1) represent a typical single mode configuration, (a2, b2) a two mode, (a3, b3) a four mode, and (a4, b4) a vortex configuration. The single mode and the two mode configurations arise in the ground state but the four mode and the vortex configurations do not. . . . . 157

- 5.6 Real space snapshot of magnetic texture in the ground state at  $\gamma=0.3$  for (a)  $\lambda = 0.5$  and (b)  $\lambda = 1.5$ . The  $m_z$  component has been shown in color while the  $m_x - m_y$  components have been denoted via vectors. The  $\lambda=0.5$  state is a phase-twisted superfluid with no magnetic component out of the plane, whereas all the in-plane vectors get aligned at  $-\frac{\pi}{4}$  to the x axis. The  $\lambda=1.5$  state shows a stripe-like magnetic pattern whose pitch is controlled by the spin-orbit coupling. 161
- 5.7 The ground state momentum distribution as a function of spin-orbit  $\gamma$  has been plotted columnwise for  $\gamma = 0, 0.3$  and  $0.5$ . The top row shows the plots for  $\lambda = 0.5$  with  $U$  fixed at  $10$ . With increasing  $\gamma$  the condensation wave-vector moves from  $(0,0)$  to  $(k_0, k_0)$ , accompanied by slight depletion of the peak. The bottom row represents  $\lambda = 1.5$  with  $u = 4t$ . In this case, as  $\gamma$  is tuned from zero, the condensate splits from a single peak feature at  $(0,0)$  to two peaks at  $(-k_0, -k_0)$  and  $(k_0, k_0)$  with equal no. of particles at both points. The total condensate fraction, which has contributions from both the peaks, gets slightly depleted with increasing  $\gamma$  . . . . . 162
- 5.8 The thermal phase transition scales for (a)  $\lambda = 0.5$  and (b)  $\lambda = 1.5$ . The  $T_c(U)$  result for different  $\gamma$  are shown in color. The low temperature phase is a superfluid with condensation at a wavevector governed by  $\gamma$ . Beyond  $T_c(U, \gamma)$  the system is a normal Bose liquid. For a fixed  $U$ ,  $T_c$  decreases with increase in  $\gamma$  due to renormalization of the bandwidth. . . . . 163



- 5.9 The thermal evolution of the momentum distribution function ( $n_{\mathbf{k}}$ ) has been plotted in the left panel for  $\lambda = 0.5$  at  $U = 14t$ , and in the right panel for  $\lambda = 1.5$  for  $U = 10t$ . The first two rows show evolution of the normalized  $n_{\mathbf{k}}$  for  $\gamma = 0$  and  $0.5$  respectively. The columns show thermal broadening of the  $n_{\mathbf{k}}$  peaks as the system is heated up from a low temperature (a1, a4) to the critical temperature  $T_c$  (a2, a5), and finally to a high temperature (a3, a6) where the superfluidity has been lost. The right panel shows the same sequence for  $\lambda = 1.5$ . The last row shows the  $n_{\mathbf{k}}$  projection along the two diagonals of the square BZ for  $\gamma = 0.5$ . For finite  $\gamma$  the low temperature distribution is sharply peaked at  $(k_0, k_0)$  and  $(-k_0, -k_0)$  (b4). As the temperature reaches close to  $T_c$  small weights appear at the symmetry related points  $(k_0, -k_0)$  and  $(-k_0, k_0)$  in the BZ due to thermal fluctuations (b5). In the high temperature state one can observe significant thermal broadening of the features at relevant  $k$ -points (b6). 165
- 5.10 Spatial snapshots of  $\mathbf{m}_i$  for  $\lambda = 1.5$  at  $U = 10$  illustrating the temperature variation of the magnetic textures across the thermal transition. The spin density wave survives to intermediate temperatures and vanishes for  $T \gg T_c$ . The planar components get disordered at a lower temperature scale as compared to the z-component. All energies are in units of  $t$ . . . . . 166
- 5.11 Thermal evolution of the structure factor peak has been plotted for a  $16 \times 16$  lattice at  $\lambda = 0.5$  in the first column (a1-a3), and for  $\lambda = 1.5$  in the second column (b1-b3). All energies are in units of  $t$ . . . . . 167
- 5.12 Schematic level scheme of two-species bosons in the atomic limit. . . . . 168
- 5.13 Comparison of ordering temperatures as obtained from the SPA based monte-carlo scheme ( $T_c$ ) with that obtained from the second order Landau functional ( $T^*$ ), at  $\lambda = 1.5$  for (a)  $\gamma = 0$ , (b)  $\gamma = 0.3$  and (c)  $\gamma = 0.5$ . . . . . 169

- 6.1 The speckle correlation function  $\langle V(\vec{x})V(\vec{x} + \vec{r}) \rangle - \langle V(\vec{x}) \rangle^2$  for  $V = 1$ , plotted as a function of  $r/\sigma$ , by actually sampling our disorder configurations. The function should be universal, and die off for  $r/\sigma \gg 1$ , but sampling on a  $24 \times 24$  lattice leads to the non universal features at large  $\sigma$ . . . . . 177
- 6.2 Maps for spatial patterns in the ground state. The top row shows the disorder potential  $V_i$  for fixed  $V$  and four speckle sizes  $\sigma$ . Patterns for different  $V$  can be generated by simply scaling these up. Notice the more random  $V_i$  landscape at small  $\sigma$  and the progressively smoother variation at larger  $\sigma$ . The lower set of panels shows the amplitude  $|\Delta_i|$  for varying  $V$  and  $\sigma$ . From the top row down  $V = 0.5t, 1.5t, 2.5t$ . The small  $V$  large  $\sigma$  pattern has the strongest order while the large  $V$  small  $\sigma$  panel has the weakest order. Spatially,  $|\Delta_i|$  anti-correlates with the extremes in  $V_i$ . . . . . 179
- 6.3 Order in the ground state: (a). The superfluid order parameter, *i.e.*, the pairing field structure factor  $S(\mathbf{q} = (0, 0))$ , extrapolated down to  $T = 0$ , as a function of disorder strength  $V$  at various speckle size  $\sigma$ . The critical disorder for SF to insulator transition increases with  $\sigma$ . (b) The ground state phase diagram at  $U = 4t$  and  $n = 0.9$  that emerges from the data in panel (a). The dotted line is a fit  $V_c(\sigma) - V_c(0) \propto \sigma^{2.4}$ . . . . . 180
- 6.4 Density of states in the ground state. Panels (a)-(c) show the DOS at three strengths of disorder  $V$  and for four  $\sigma$  at each  $V$ . Increase in  $\sigma$  sharpens the coherence peak but also suppresses the gap. Panels (d)-(f) show the same data as in (a)-(c) now highlighting the variation with  $V$  at fixed  $\sigma$ . Here increasing  $V$  suppresses both the coherence peak and the gap. . . . . 181

- 6.5 Variation of the superfluid  $T_c$  with disorder and speckle correlation length. (a) Disorder dependence for various  $\sigma$ . At  $V = 0$  we have the ‘clean’  $T_c$ . The rate of fall with  $V$  decreases with increasing  $\sigma$ . (b) Firm lines:  $T_c$  for varying  $\sigma$  and three values of  $V$ . Dotted lines:  $T_g$  - low  $T$  gap to high  $T$  pseudogap crossover temperature. . . . . 182
- 6.6 Speckle size and temperature dependence of  $\Delta_0.\Delta_i$  at strong disorder.  $\Delta_0$  is the pairing field at a reference (corner) site. The overlap is based on a single MC configuration at  $V = 2t$  and the  $\sigma, T$  indicated. Increasing  $\sigma$  augments intersite correlation, with the largest  $\sigma$  lowest  $T$  panel (top right) having the strongest correlation. Bottom row: Density of states at  $V = 2t$ , showing  $\sigma$  and  $T$  dependence. At low  $\sigma$  the low  $T$  state shows no coherence peak, and a broad gap that smears out with increasing  $T$ . At  $\sigma = 4$  there is a reasonable coherence feature, and a smaller gap at low  $T$ . The gap fills more quickly with rising  $T$  than at  $\sigma = 1$ . The behaviour in panels (b)-(c) interpolate between (a) and (d). . . . 183
- 6.7 Disorder and temperature dependence of  $\Delta_0.\Delta_i$  at moderate speckle size,  $\sigma = 2$ . At fixed temperature along the row the correlation decreases with increase in  $V$ . The correlation is strongest at  $V = 0.5t$  and  $T = 0.01t$  and decreases with increasing  $V$  or  $T$ . Bottom row: DOS at  $\sigma = 2$ , showing  $V$  and  $T$  dependence. The suppression in coherence peak is seen with increasing temperature and disorder strength. The gap in the density of states reduces with increasing temperature. This effect is more pronounced at small disorder strength. . . . . 184
- 6.8 Maps for the effective potential  $V_{eff}$  for varying speckle size and disorder strength. The disorder is  $V = 0.5t, 1.5t, 2.5t$  from top to bottom, while the speckle size is  $\sigma = 1, 2, 3, 4$  from left to right. The bottom left panel - large  $V$  and small  $\sigma$  - has the most fluctuating pattern while the top right panel - small  $V$  and large  $\sigma$  - has the smoothest profile. . . . . 186

- 6.9 (a)-(c) shows  $P(V_{eff})$  at  $V = 0.5t, 1.5t, 2.5$ , respectively, comparing  $\sigma = 1$  with  $\sigma = 4$ . Inset of Panel (c) shows the variance  $\delta V_{eff}$  with respect to  $V$  at  $\sigma = 1, 4$ . At a given  $V$  the variance is slightly larger at  $\sigma = 4$  compared to  $\sigma = 1$ . (d) The normalised  $C(\vec{r})$  as a function of disorder for two speckle sizes. The behaviour suggests that the spatial correlation in  $V_{eff}$  is dictated by just  $\sigma$  and is unaffected  $V$ . . . . . 187
- 6.10 The distribution of  $|\Delta_i|$  in the ground state comparing the  $\sigma$  dependence at  $V = 0.5t, 1.5t, 2.5t$ . At larger  $V$  the effect of  $\sigma$  is to create a distribution with large weight at low amplitude. . . . . 188
- 6.11 DOS and IPR in the background of the bare disorder,  $V_i$ . The DOS naturally broadens with  $V$  but is not very sensitive to  $\sigma$ . The IPR however is sensitive to  $\sigma$  and shows weaker localisation (smaller IPR) at larger  $\sigma$ . . . . . 189
- 6.12 DOS and IPR in the presence of the effective disorder  $V_i^{eff} = V_i + \phi_i$ . We have ignored the pairing effects in this calculation. The  $V_i^{eff}$  problem has larger bandwidth, due to the larger effective disorder, and greater localisation compared to the bare disorder. The IPR is much larger than in the  $V_i$  problem, and much larger at  $\sigma = 1$  compared to  $\sigma = 4$ . . . . . 190
- 6.13 (a) The comparison of  $T_c$  scales in the clean limit, between full QMC, our MC result (SPA) and the XY model in the text. We operate near the peak  $T_c$ , the BCS-BEC crossover regime. The SPA well approximates the QMC answer. The XY model also succeeds in capturing the non-monotonic dependence of  $T_c$  on  $U/t$ . (b) Sum of nearest neighbour XY couplings versus sum of all couplings including nearest neighbour. For small to moderate  $U$  the model has significant long range couplings and it is only at very large  $U$  that it can be truncated to nearest neighbour. . . . . 191

6.14	Comaparison of $T_c$ scales obtained from exact MC with the XY model for two speckle sizes. Fig a) shows the comparison for speckle size 1 and Fig b) shows the comparison for speckle size 4. The difference in the results of the two calculation increases with decrease of disorder. . . . .	192
6.15	Distribution of nearest neighbour bonds, averaged over the system and disorder configurations (a) $\sigma = 1$ and (b) $\sigma = 4$ . With increase in disorder strength distribution becomes broad and peak of the distribution shifts to small values of $J_{nn}$ . At the same disorder the peak is $P(J_{nn})$ is at a larger $J_{nn}$ at larger $\sigma$ . This is the origin of the larger $T_c$ . . . . .	193

## Summary of the thesis

- Chapter 1 consists of a brief review of ultracold atoms and the optical lattice. We quickly summarise the way various lattice models are simulated. We then move to discuss experimental techniques used to probe static quantities like the momentum distribution of bosons, single site imaging to probe number fluctuations, and dynamical properties probed by lattice modulation spectroscopy and Bragg spectroscopy.

- Chapter 2 reviews the theoretical tools available to study superfluid bosons and fermions and then moves to a discussion of the method that we employ. We describe the complementary auxiliary field approaches used for the Bose and Fermi problems. For bosons we start with a standard path integral formulation [139, 150?] and then decouple the kinetic term using a Hubbard-Stratonovich transformation. If the corresponding auxiliary field is treated as classical we arrive at what is called a ‘static path approximation’ (SPA) for the partition function. When leading order quantum corrections are retained one obtains the ‘perturbed static path approximation’ (PSPA). We have used both the SPA and PSPA as part of a Monte Carlo strategy in studying the BHM. Spectral features are obtained via a real space implementation of the random phase approximation (RPA). For fermions we decouple the interaction term into density and pairing channels and treat the corresponding auxiliary fields as static. These are then sampled in the quenched disorder background of the speckle potential.

- Chapter 3 presents thermodynamic results for the 2D Bose Hubbard model at density  $n = 1$  using the method presented in Chapter 2. We solve the model using both the SPA and PSPA

variants of the method. We obtain  $T_c$  scales that dramatically improve on mean field theory and are within about 20% of quantum Monte Carlo estimates. The SPA ground state, however, is mean field, with an overestimate of the critical interaction,  $U_c$ , for the superfluid to Mott transition. The PSPA strikingly improves the  $U_c$  and the overall thermal phase diagram.

- Chapter 4 focuses on the single particle spectral function of the Bose Hubbard model at integer filling. We use the SPA to generate the equilibrium backgrounds and a real space implementation of the random phase approximation (RPA) for the Green's functions. This leads to the well known RPA answers in the ground state but captures the progressive damping of the modes with increasing temperature. Deep in the superfluid regime a four mode structure characterises the momentum resolved spectral function  $A(\mathbf{k}, \omega)$ . The dispersion and weight of these features changes with interaction but are almost temperature independent while the damping varies roughly as  $T^\alpha f_{\mathbf{k}}$ , where  $T$  is the temperature, and  $\alpha \sim 0.5$ . The normal state and the Mott phase, on the other hand, are described by a two mode structure at each  $\mathbf{k}$ , gapped at strong interaction and ungapped in the weakly correlated normal state. Near critical coupling the superfluid undergoes a thermal transition to a 'Bose liquid' that is gapped, with progressive widening of the gap with increasing temperature. We suggest an approximate analytic argument for the observed dispersion and temperature dependent linewidth of the modes.

- **Chapter 5** investigates the thermal physics of a Bose-Hubbard model with Rashba spin-orbit coupling starting from a strong coupling mean-field ground state. The essential role of the spin-orbit coupling ( $\gamma$ ) is to promote condensation of the bosons at a finite wavevector  $\mathbf{k}_0$ . We find that the bosons display either homogeneous or phase-twisted or orbital ordered superfluid phases, depending on  $\gamma$  and the inter-species interaction strength ( $\lambda$ ). We show that an increase of  $\gamma$  leads to suppression of the critical interaction  $U_c$  for the superfluid to Mott insulator transition in the ground state, and a reduction of the  $T_c$  for superfluid to Bose-liquid transition at a fixed interaction strength. We capture the thermal broadening in the momentum distribution function, and the real space profiles of the thermally disordered magnetic textures, including their homogenization for  $T \gtrsim T_c$ . We provide a Landau theory based description of the ground state phase boundaries and thermal transition scales, and discuss experiments which can test our theory.

- Chapter 6 studies the impact of correlated disorder on an intermediate coupling Fermi superfluid. Optical lattice experiments which probe the effect of disorder on superfluidity often use a speckle pattern for generating the disorder. Such speckle disorder is spatially correlated. While fermionic superfluidity in the presence of uncorrelated disorder is well studied, the impact of correlated disorder, particularly on thermal properties of the superfluid, is poorly understood. We provide a detailed study of the impact of speckle disorder, for varying speckle size and disorder magnitude, on the ground state and thermal properties of a Fermi superfluid. We work in the coupling regime of BCS-BEC crossover in a two dimensional lattice. For a fixed disorder strength, an increase in speckle size leads to smoothening of the self-consistent background potential, increase in the critical disorder needed for a superfluid-insulator transition, and an increase in superfluid  $T_c$ . Along with these hints at decrease in effective disorder, speckle correlations also suppress the superfluid gap and the gap formation temperature - effects normally associated with increasing disorder. We correlate these effects with the effective potential and the single particle localisation effects in the ground state.



# Summary

In the thesis we studied models of superfluidity that do not have a straightforward condensed matter realisation. In the Bose case we focus on the Bose Hubbard model (BHM) at filling  $n = 1$ , where increasing interaction drives a superfluid to Mott insulator transition. The thesis devises a new approach to this much studied problem, first establishing thermodynamic results which can be compared to quantum Monte Carlo (QMC) and then moving on to spectral features which are hard to access with other methods. We study the problems above using a thermal field theory that uses a classical auxiliary field to mimic on site particle number fluctuations while treating local interactions exactly. This generalises the original ‘mean’ field theory of the Bose Hubbard model to a full lattice field theory. It allows us to use a computationally cheap and physically transparent approach to the thermal physics, obtaining results comparable to full quantum Monte Carlo (QMC). Spectral features are obtained via a real space implementation of the random phase approximation (RPA) on the equilibrium configurations. This leads to the well known RPA answers in the ground state but captures the progressive damping of the modes with increasing temperature. Deep in the superfluid regime a four mode structure characterises the momentum resolved spectral function  $A(\mathbf{k}, \omega)$ . The normal state and the Mott phase, on the other hand, are described by a two mode structure at each  $\mathbf{k}$ , gapped at strong interaction and ungapped in the weakly correlated normal state. An extension of this approach allows us to study spin-orbit coupling in bosons with internal degrees of freedom. In the spin-orbit problem we study the thermal scales and the fate of the spatial textures and momentum distribution at finite temperature.

In the Fermi case we studied an intermediate coupling superfluid in the presence of spatially correlated ‘speckle’ disorder. Optical lattice experiments which probe the effect of disorder on superfluidity often use a speckle pattern for generating the disorder. Such speckle disorder is spatially correlated. We provide a detailed study of the impact of speckle disorder, for varying speckle size and disorder magnitude, on the ground state and thermal properties of a Fermi superfluid.

# Experimental motivation

## 1.1 Introduction

Understanding the dynamics of quantum many body systems is one of the outstanding problems in physics. While the governing Schrodinger equation is well known, a solution of it for more than a few particles poses a major challenge. Theorists have invested decades of effort in devising methods for solving many particle problems to, gain insight into collective behaviour. An experimental breakthrough in atomic physics [1] occurred in the 1990's, yielding 'solutions' to many idealised many body problems.

Atoms cooled to ultralow temperature, and trapped in a region of space by magnetic or optical means, display many of the quantum effects that one knows of in the solid state. Using atoms as degrees of freedom, and modulated optical fields to mimic the 'solid state background', one can engineer many-body Hamiltonians and use them as analog simulators of solid state phenomena. The great advantage in these systems is (i) the control that can be exercised on the model parameters, and (ii) the freedom from extrinsic effects like phonons and disorder.

Ultracold atomic physics is now not just limited to simulating models of relevance to solid state experiments, they have begun to probe questions which are beyond the conventional solid state. For example bosons, which have limited realisation in condensed matter (showing up only in  $\text{He}^4$ , Josephson junction arrays, *etc.*) have cold atom realisations in 'integer spin' atomic species. One can study strong correlation effects in these Bose systems, as well as the impact of

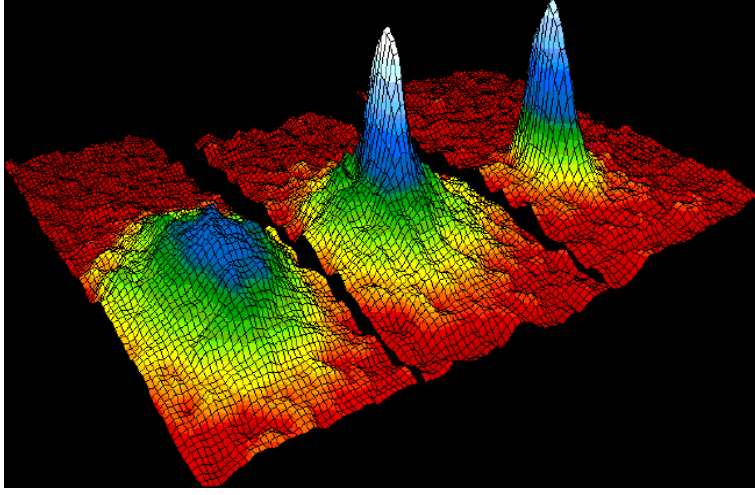


Figure 1.1: Velocity distribution of a gas of rubidium atoms as it is cooled. From left to right - just before appearance of the condensate, appearance of the condensate, after further evaporative cooling [10]

disorder, spin-orbit coupling, *etc.*

In this thesis we study correlated systems motivated by their realisation in optical lattices. The major part of the thesis is dedicated to the study of strongly correlated bosons: the canonical superfluid-Mott transition in ‘single species’ bosons, and the effect of spin-orbit coupling in multi-species bosons. We also study a Fermi superfluid, exploring the role of ‘speckle disorder’ which is ubiquitous in optical systems but harder to realise in the solid state.

This chapter briefly describes the experimental possibilities in cold atom systems, while Chapter 2 describes our theoretical tools. The four chapters thereafter describe results on specific problems.

## 1.2 Ultracold atomic systems

### 1.2.1 Atom-light interaction

To make atoms useful for experiments one needs to control them by using optical means or a magnetic field. The coupling of an atom to a laser field is described by

$$H_{int} = -\hat{\vec{d}} \cdot \vec{E}(\vec{r}, t) \quad (1.1)$$

where,  $\vec{E}(t) = E_0(\vec{r})\vec{e}\cos(\omega t)$ , is the electric field due to a laser,  $\vec{e}$  is the direction of polarization and  $\vec{d}$  is the dipole moment operator. The dipole moment operator is given by  $\hat{d} = \sum_i \vec{r}_i$  where  $\vec{r}_i$ , is the position of  $i^{th}$  electron of the atom relative to the nucleus. This leads to an atom feeling a spatially dependent effective potential given by [2, 3]

$$V(\vec{r}, \omega) = -\frac{1}{2}\alpha(\omega) \langle E^2(\vec{r}, t) \rangle \quad (1.2)$$

where  $\alpha(\omega)$  is the dynamical polarizability. Here  $\langle \dots \rangle_t$  denotes an average over one oscillation period of the electric field, with  $\langle E^2(\vec{r}, t) \rangle = E_0(\vec{r})^2/2$ .  $\alpha(\omega)$  has both real and imaginary parts. If  $Re[\alpha(\omega)] > 0$ , at the frequency of the laser field, then atoms are attracted to the maxima of the laser intensity, otherwise they are pulled towards the minima.

### 1.2.2 Trapping of atoms

To perform an experiment, atoms need to be trapped. The trapping of atoms in a spatial region is done using magnetic and optical traps, [4–8], using the principles described above.

In trapping of atoms using a magnetic field, a region with a local minimum in the magnitude of the magnetic field is created. The atoms which are low field seeking can be trapped at the minimum of the magnetic field, if they do not have enough kinetic energy to escape.

In case of optical traps, a focused laser beam is used. The forces due to laser intensity on atoms could be attractive or repulsive, depending on whether the laser frequency is tuned below or above the atomic transition frequency. Depending on the detuning, atoms can be trapped in the spatial minima or maxima of the laser intensity.

### 1.2.3 Cooling of atoms

At room temperature the thermal energy of atoms is too high and the de Broglie wavelength is much smaller than the mean interatomic separation. To enhance quantum effects, the atomic gases need to be cooled such that their de Broglie wavelength becomes larger than interatomic distances. The cooling is done in two steps: (i) Doppler cooling, and (ii) evaporative cooling [9].

In case of Doppler cooling, the laser frequency is tuned below the transition frequency, such

that static atoms do not absorb photons. The atom moving against the direction of the laser beam can absorb photons due to the Doppler shift. On absorbing the photon the atom goes into an excited state and then returns to the ground state by stimulated emission. During stimulated emission a photon is emitted in a random direction. So to cool the atoms, wavelength is long for the atoms to absorb at rest. But the atoms which are in motion against the laser beam find wavelengths to be shortened due to the Doppler effect and absorb photons. The atom undergoes spontaneous emission. The atom slows down due to recoil. The excited state has a finite life time given by natural linewidth. As the atoms slowed down, Doppler shift became less than natural linewidth and Doppler cooling came to a halt.

Below which evaporative cooling is used. In case of evaporative cooling the trapping potential is lowered and high energy atoms are allowed to escape, in the process reducing the average energy of the remaining atoms. These atoms collide and equilibrate to a lower temperature.

The first Bose-Einstein condensates were created by Eric Cornell, Carl Weiman and co-workers at JILA in June 1995 using rubidium atoms [10] and by Wolfgang Ketterle using sodium atoms [11] four months later. The Bose-Einstein condensate has a macroscopic occupation of the lowest single particle state below a critical temperature, Fig.1.1.

Using Doppler and sub Doppler cooling, temperatures could be lowered to microkelvin and could be further lowered to  $10 - 100nK$  using evaporative cooling.

#### 1.2.4 Optical lattice

In the presence of an optical lattice commensuration effects arise leading to interesting phases not seen in the continuum. Optical lattices in ultracold systems are created by interference of two counter propagating laser beams, Fig.1.2. The resulting potential felt by the atom is given by equation 1.2.

The radial profile of laser beams used in cold atom experiments is Gaussian in nature, Fig.1.3. For such beams, propagating along the  $z$  direction, the light intensity is given by [2]

$$I(r, z) = I_0 e^{-2r^2/w(z)^2} \quad (1.3)$$

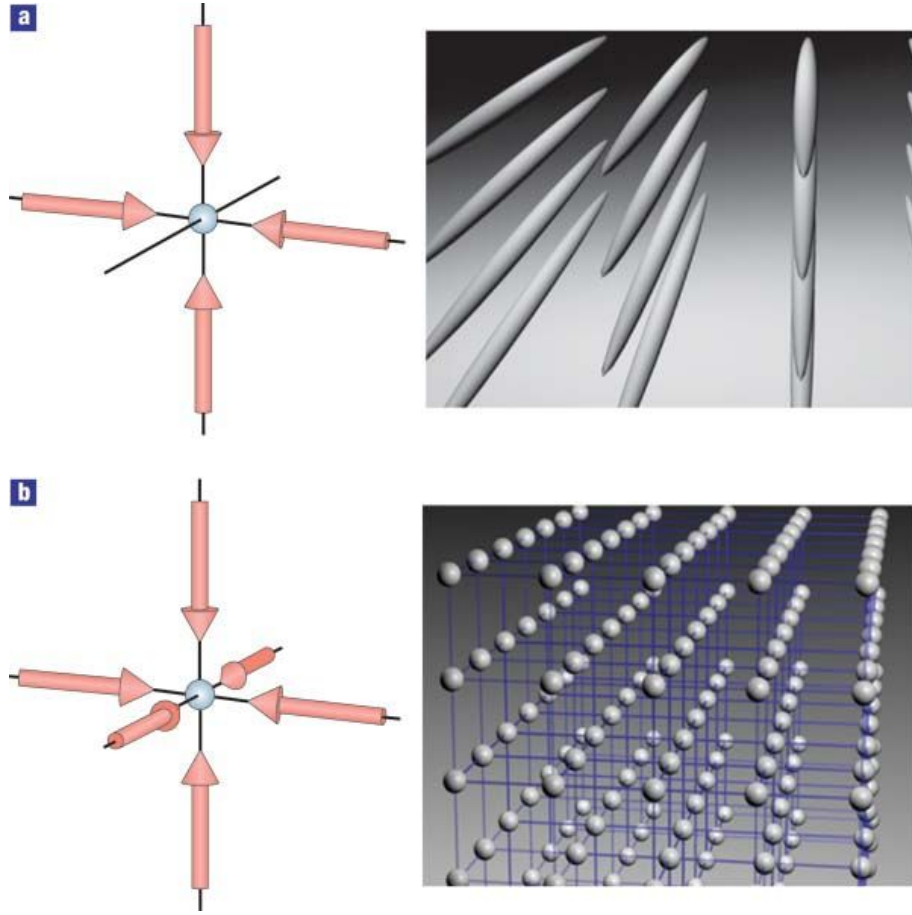


Figure 1.2: Optical lattice potentials formed by superimposing two or three orthogonal standing waves. (a) In a 2D optical lattice, the atoms are confined to an array of tightly confining 1D potential tubes. (b) In 3D, the optical lattice can be approximated by a simple cubic array of tightly confining harmonic oscillator potentials at each lattice site [2]

where  $r$  is the radial distance from the  $z$ -axis,  $w(z) = w_0 \sqrt{1 + (\frac{z}{z_R})^2}$  is the beam width in the radial direction,  $w_0$  is the minimum beam width called beam waist,  $z_R = \frac{\pi w_0^2}{\lambda}$  is the Rayleigh length, and  $\lambda$  is the wavelength of the laser.  $I_0$  depends on the power of the laser beam. For  $z \ll z_R$ , the resulting lattice potential can be approximated by [2]

$$V(\vec{r}) = -V_0 e^{-\frac{2(x^2+y^2)}{w_0^2}} \cos^2(k_L z) \approx -V_0 \cos^2(k_L z) \left(1 - \frac{2(x^2 + y^2)}{w_0^2}\right) \quad (1.4)$$

For most applications, deviations from periodicity may be ignored and one can assume depends only on the  $z$  coordinate:  $V(\vec{r}) = -V_0 \cos^2(k_L z)$ , where  $V_0$  is the trap depth which depends on the intensity of laser beam and the detuning parameter. This generates the simplest possible one dimensional lattice.

To create periodic potentials in higher dimensions, one requires orthogonal sets of counter

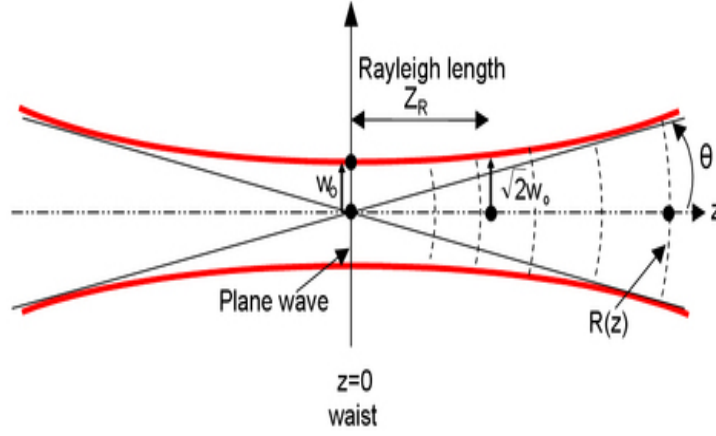


Figure 1.3: Image of Gaussian beam used in ultracold atoms. The radial profile of laser beams used in cold atom experiments. Beams is propagating along the  $z$  direction, where  $r$  is the radial distance from the  $z$ -axis,  $w(z)$  is the beam width in the radial direction,  $w_0$  is the minimum beam width called beam waist,  $z_R$  is the Rayleigh length, and  $\lambda$  is the wavelength of the laser. [1]

propagating laser beams. The optical potential so generated is given by sum of standing waves. The lattice constant  $a$ , is related to the laser wavelength  $\lambda$  by  $a = \lambda/2$ .

For deep optical lattices the potential is harmonic at a site. The depth of the harmonic potential is measured in terms of recoil energy ( $E_r$ ). So the lattice depth is measured in terms of this recoil energy. The recoil energy  $E_r$  is defined as,  $E_r = \hbar k^2/2m$ , where  $k$  is the momentum of the photon and  $m$  is the mass of atom

By changing the angle it is possible to produce lattices with different symmetries such as hexagonal, square or triangular.

### 1.2.5 Feshbach resonance

The interparticle interaction in an atomic gas can often be tuned using a Feshbach resonance. Fig.1.4 shows two molecular potential curves  $V_{bg}(R)$  and  $V_c(R)$ . For a collision process with a small energy  $E$ ,  $V_{bg}(R)$  represents the open channel connecting two free particle states during a scattering process and  $V_c(R)$  represents the closed channel supporting a bound molecular state of energy  $E$ .

A Feshbach resonance is said to occur when the energy difference between bound molecular states in the closed channel and scattering state in the open channel is tuned to zero [12]. This can be done either magnetically, known as magnetically tuned Feshbach resonance [14, 15], or by

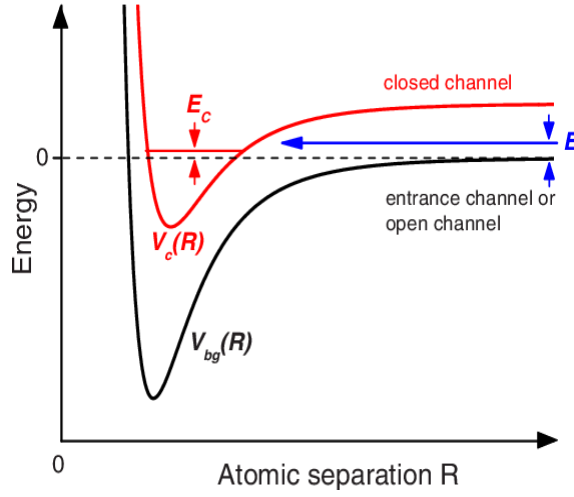


Figure 1.4: Basic two-channel model for a Feshbach resonance. The phenomenon occurs when two atoms colliding at energy  $E$  in the entrance channel resonantly couple to a molecular bound state with energy  $E_c$  supported by the closed channel potential. In the ultracold domain, collisions take place near zero energy,  $E \rightarrow 0$ . Resonant coupling is then conveniently realized by tuning  $E_c$  near 0 if the magnetic moments of the closed and open channels differ. [12]

using an optical method, known as optically tuned Feshbach resonance [16, 17]. The Feshbach resonance provides a way to vary the interaction strength by changing the scattering length of elastic collisions. When the Feshbach resonance is magnetically tuned, the s-wave scattering length is given by [18]  $a(B) = a_{bg}(1 - \frac{\Delta}{B-B_0})$ , see Fig. 1.5. Here  $B_0$  and  $\Delta$  denote the resonance position and width, respectively, and  $a_{bg}$  is the so-called background scattering length. A detailed review on Feshbach resonance can be found in [12].

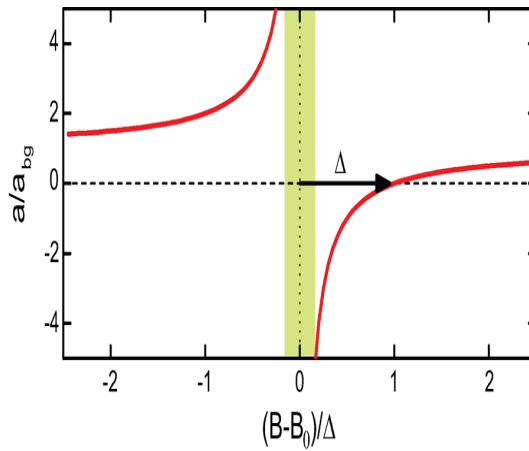


Figure 1.5: Variation of the s-wave scattering length  $a$  across a Feshbach resonance for a varying magnetic field  $B$  [13]



### 1.3 The Bose Hubbard model

The Bose Hubbard model (BHM) was first introduced by Fisher et al [19] to describe the ground state of dirty superconductors and He<sup>4</sup> adsorbed in a porous medium. It was Jaksch et.al [20] who pointed out that the BHM could be simulated with cold atoms.

The Hamiltonian of bosons moving in an optical lattice is given by,

$$H = \int d^3 \vec{r} \hat{\psi}^\dagger(\vec{r}) \hat{h}(\vec{r}) \hat{\psi}(\vec{r}) + \int d^3 \vec{r} d^3 \vec{r}' \hat{\psi}^\dagger(\vec{r}) \hat{\psi}(\vec{r}) V(\vec{r} - \vec{r}') \hat{\psi}^\dagger(\vec{r}') \hat{\psi}(\vec{r}') \quad (1.5)$$

$$\hat{h}(\vec{r}) = -\frac{\hbar^2}{2m} \nabla^2 + V_{ext}(\vec{r}) - \mu$$

with  $\hat{\psi}^\dagger(\vec{r})$  and  $\hat{\psi}(\vec{r})$ , being the bosonic creation and annihilation operator respectively.  $V_{ext}(\vec{r})$  is the external potential that the atom feels due to the presence of the optical lattice. At low temperature and in the dilute limit the two body interaction can be approximated by a contact interaction  $V(\vec{r} - \vec{r}') = g \delta(\vec{r} - \vec{r}')$  where  $g = 2\pi\hbar^2 a_s/m$ , with  $a_s$  being the s-wave scattering length. Since the external potential is periodic, the eigenfunction which diagonalize the quadratic part of the Hamiltonian has the form [21],

$$\Psi_{\vec{k}}^l(\vec{r}) = e^{i\vec{k} \cdot \vec{r}} \Phi_{\vec{k}}^l(\vec{r}) \quad (1.6)$$

where  $\Phi_{\vec{k}}^l(\vec{r})$  are the Bloch function with periodicity of optical potential,  $l$  is the band index and  $\vec{k}$  is the Bloch momentum. For deep optical lattice, one can use new set of wavefunctions known as Wannier functions. These are localized around each well and in terms of Bloch functions given by,

$$w_l(\vec{r} - \vec{r}_i) = \frac{1}{L^2} \sum_{\vec{k}} e^{i\vec{k} \cdot \vec{r}} \Phi_{\vec{k}}^l(\vec{r}) \quad (1.7)$$

Here  $L^2$  are the number of lattice site, and  $\vec{r}_i$  is the location of  $i^{th}$  lattice site.

The Wannier basis corresponding to the periodic potential can be used to expand the creation

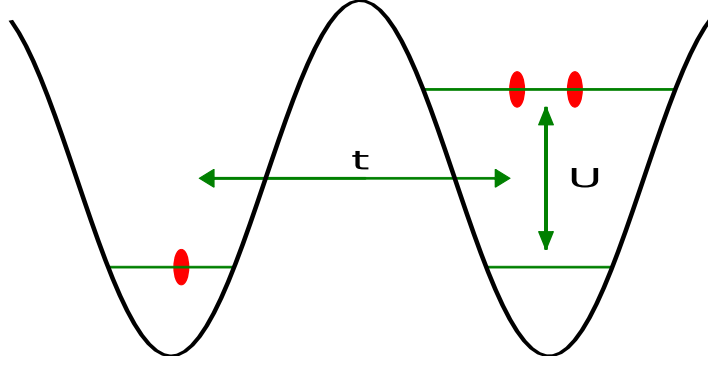


Figure 1.6: Interpretation of the Bose Hubbard model parameters for atoms in an optical lattice.  $t$  is the hopping amplitude between neighbouring minima.  $U$  is the Hubbard interaction energy between the two atoms localized at the same minimum.

and annihilation operators, e.g:

$$\hat{\psi}(\vec{r}) = \sum_{i,l} w_l(\vec{r} - \vec{r}_i) \hat{b}_{i,l} \quad (1.8)$$

Here  $w_l(\vec{r} - \vec{r}_i)$  is the Wannier function and  $\hat{b}_{i,l}^\dagger$  and  $\hat{b}_{i,l}$  are the creation and annihilation operator corresponding to the  $i^{th}$  lattice site and  $l^{th}$  Bloch band respectively.

Since at low temperature, for deep optical lattices, the bosonic atoms populate only the lowest Bloch band, we retain only terms involving the lowest band Wannier states. In this limit the low energy effective Hamiltonian, Fig.1.6, is given by

$$H_{eff} = - \sum_{ij} t_{ij} \hat{b}_i^\dagger \hat{b}_j + \frac{U}{2} \sum_i \hat{n}_i (\hat{n}_i - 1) - \mu \sum_i \hat{n}_i \quad (1.9)$$

This is the Bose Hubbard model.  $t_{ij}$  is the amplitude for a boson to tunnel from site  $\vec{r}_i$  to site  $\vec{r}_j$  and  $U$  is the cost to put more than one boson at a site. In terms of Wannier basis they are expressed as

$$\begin{aligned} t_{ij} &= \int d^3\vec{r} w_0(\vec{r} - \vec{r}_i) \left( -\frac{\hbar^2}{2m} \nabla^2 + V_{ext}(\vec{r}) \right) w_0(\vec{r} - \vec{r}_j) \\ U &= 2g \int d^3\vec{r} |w_0(\vec{r} - \vec{r}_i)|^4 \end{aligned} \quad (1.10)$$

Since the external potential is periodic,  $U$  is same at each lattice site. Under harmonic approximation for Wannier orbitals, when Wannier orbital are chosen to be that of eigenfunction of

harmonic oscillator at located at a site,

$$U = \sqrt{8\pi} \frac{E_r a_s}{a} \left( \frac{V_0}{E_r} \right)^{3/4}$$

$$t = V_0 \left( \frac{\pi^2}{4} - 1 \right) e^{-\pi^2/4 \sqrt{\frac{V_0}{E_r}}} \quad (1.11)$$

### 1.3.1 General introduction

The single species BHM has three phases (i) a normal phase at high temperature, (ii) a Mott insulating (MI) phase at zero temperature and commensurate filling for  $U \gg zt$ , where  $z$  is the coordination number of the lattice, and (iii) a superfluid (SF) phase occurring at low temperature. Fig.1.7 shows a cartoon where by tuning the interaction strength drives a superfluid (with local particle number fluctuations) to a Mott insulator (with a fixed particle number at each site). The superfluid has a phase rigidity and a gapless spectrum, whereas the Mott insulator is incompressible and has a gapped spectrum. The increase in temperature leads to thermal transition from the superfluid to the normal phase. To build some insight we quickly review the simply solvable limits of the BHM.

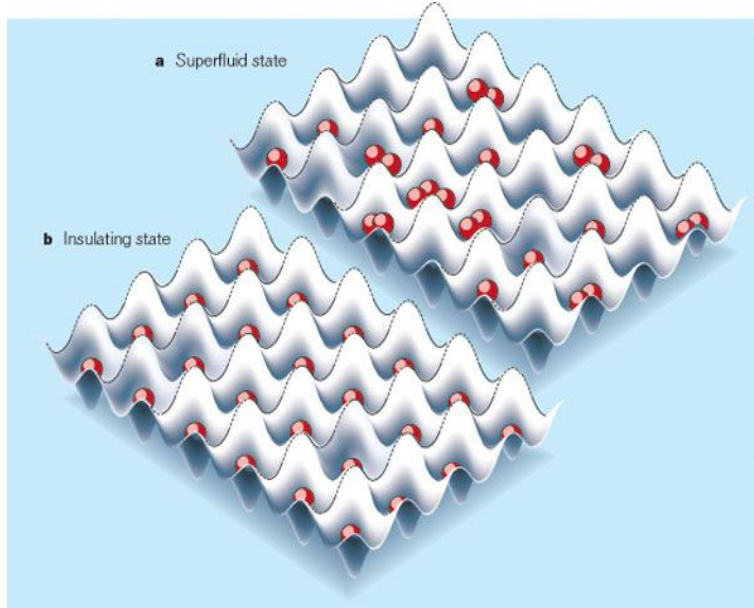


Figure 1.7: (a) At low laser intensity the atoms can move freely between valleys - a superfluid state, (b) when the laser intensity is hiked up atoms get trapped in individual minima, since tunneling costs a large repulsive energy, and the system is Mott insulating [22].

### 1.3.1.1 Non interacting limit

In the non-interacting limit the Bose-Hubbard model reduces to

$$\begin{aligned} H &= \sum_{\langle ij \rangle} t_{ij} \hat{b}_i^\dagger \hat{b}_j - \mu \sum_i \hat{n}_i \\ &= \sum_{\vec{k}} (\epsilon_{\vec{k}} - \mu) \hat{b}_{\vec{k}}^\dagger \hat{b}_{\vec{k}} \end{aligned} \quad (1.12)$$

where  $\epsilon_{\vec{k}} = -2t(\cos(k_x a) + \cos(k_y a))$ . The occupation number at wavevector  $\vec{k}$  at any temperature  $T$  is given by  $n_{\vec{k}} = \frac{1}{\exp(\beta(\epsilon_{\vec{k}} - \mu)) - 1}$ , where  $\beta = 1/T$ . At  $T = 0$ , this leads to macroscopic occupancy in the lowest eigenstate. The corresponding wavefunction is  $[\hat{b}_{\vec{k}=0}^\dagger]^N |0\rangle$ .

If the occupancy of the lowest eigenstate continues to be macroscopic for a temperature window  $T < T_c$  the system is said to form a Bose-Einstein condensate. In this window the chemical potential is pinned to the lowest eigenvalue. For  $T > T_c$  the chemical potential varies with  $T$  to keep the total particle number fixed. In free space a BEC can occur only in dimensions  $d > 2$ .

### 1.3.1.2 Atomic limit

In the atomic limit the BHM reduces to

$$H = \frac{U}{2} \sum_i \hat{n}_i(\hat{n}_i - 1) - \mu \sum_i \hat{n}_i \quad (1.13)$$

In this limit, for  $\mu$  between  $n - 1 < \mu/U < n$ , there are exactly  $n$  bosons at each site. This describes the Mott insulator phase, where at each site the particle number is fixed and the excitation spectrum is gapped. The particles are localized and the ground state at filling  $n = 1$  is  $\Pi_{i=1}^N \hat{b}_i^\dagger |0\rangle$ .

### 1.3.1.3 Mean field theory

When  $U$  and  $t$  are both finite mean field theory (MFT) provides an analytic handle on the BHM [19, 23]. In mean field theory, one writes  $\hat{b}_i^\dagger = \phi + \delta \hat{b}_i^\dagger$  where  $\delta \hat{b}_i^\dagger = \hat{b}_i^\dagger - \langle \hat{b}_i^\dagger \rangle$  in the kinetic term

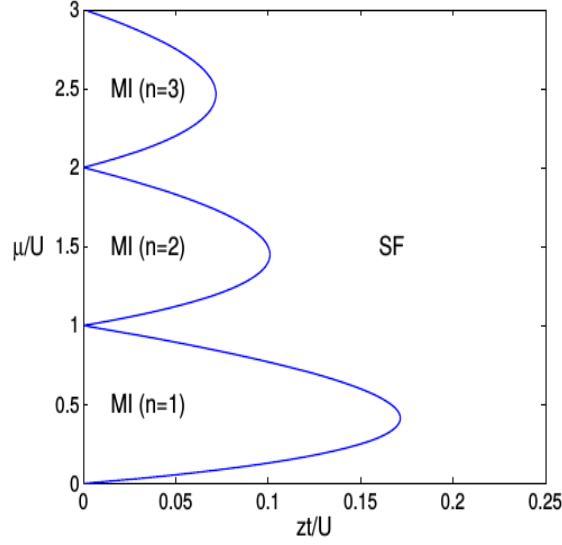


Figure 1.8: Ground state phase diagram in the  $zt/U, \mu/U$  plane obtained using MFT. The Mott lobes correspond to integer particle numbers while the surrounding regions are superfluid.

and neglects quadratics in fluctuations. In this approximation the BHM reduces to

$$H_{MF} = \sum_i \left\{ -zt\phi(\hat{b}_i^\dagger + \hat{b}_i) + \frac{U}{2}\hat{n}_i(\hat{n}_i - 1) - \mu \sum_i \hat{n}_i \right\} \quad (1.14)$$

with  $\phi = \langle \hat{b}^\dagger \rangle$ . The original BHM is now a sum of single site Hamiltonians. The occupation number basis can be used to express this Hamiltonian in matrix form. The local matrix size is infinite since the boson occupation number can be 0, 1, 2, ... When  $U$  is moderately large the matrix can be truncated to some finite size appropriate to the  $U$  value. The  $H_{MF}$  is then exactly diagonalized numerically and the  $\phi = \langle \hat{b}^\dagger \rangle$  computed self consistently.

If  $\phi \neq 0$  the local eigenstates are superpositions of particle number states and the system allows particle number fluctuations. This attribute, combined with a ‘phase coherent’  $\phi_i$  - related to  $U(1)$  symmetry breaking, characterises the superfluid. If  $\phi = 0$  the system is a Mott insulator, a trivial state with bosons localized at sites. The mean-field approach provides qualitatively correct prediction of the ground state phase diagram of the Bose-Hubbard model. Fig.1.8 shows the phase diagram in  $zt/U, \mu/U$  plane obtained using MFT.

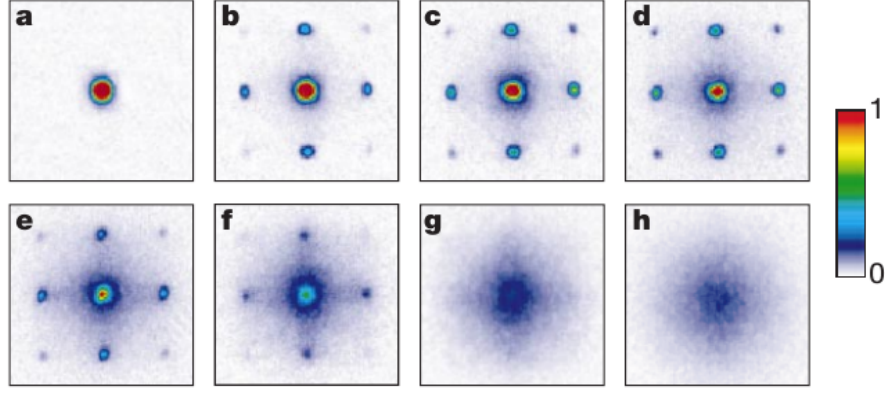


Figure 1.9: Momentum distribution patterns after atoms are released from a 3D optical lattice for potentials with depth: (a) 0, (b)  $3E_r$ , (c)  $7E_r$ , (d)  $10E_r$ , (e)  $13E_r$ , (f)  $14E_r$ , (g)  $16E_r$ , and (h)  $20E_r$ . The expansion time was 15ms. [26]

### 1.3.2 Static properties

The standard way of probing the static properties of quantum gases is through time of flight methods - which provides an estimate of the momentum distribution, or through in situ imaging - which reveals local particle number fluctuations.

#### 1.3.2.1 Time of flight imaging

The earlier experiments probing bosons in optical lattice used time of flight methods [24–27]. Using time of flight methods they measured the momentum distribution of bosons and compared with theory. The standard procedure in time of flight experiments is to switch off the confining and optical lattice potentials and allow the atomic gas to expand freely. The expansion is imaged. This provides information on the momentum distribution of the quantum gas before the lattice potential was switched off. The real space density can be measured using standard absorption imaging methods. Assuming that the expansion of gas is ballistic, the density distribution  $n(\vec{r}, t)^{exp}$  seen during expansion is related to momentum distribution  $n(\vec{k}, t)^{latt}$  in lattice by

$$n(\vec{r})^{exp} = (M/\hbar t)^3 |w(\vec{k})|^2 G(\vec{k})^{latt} \quad (1.15)$$

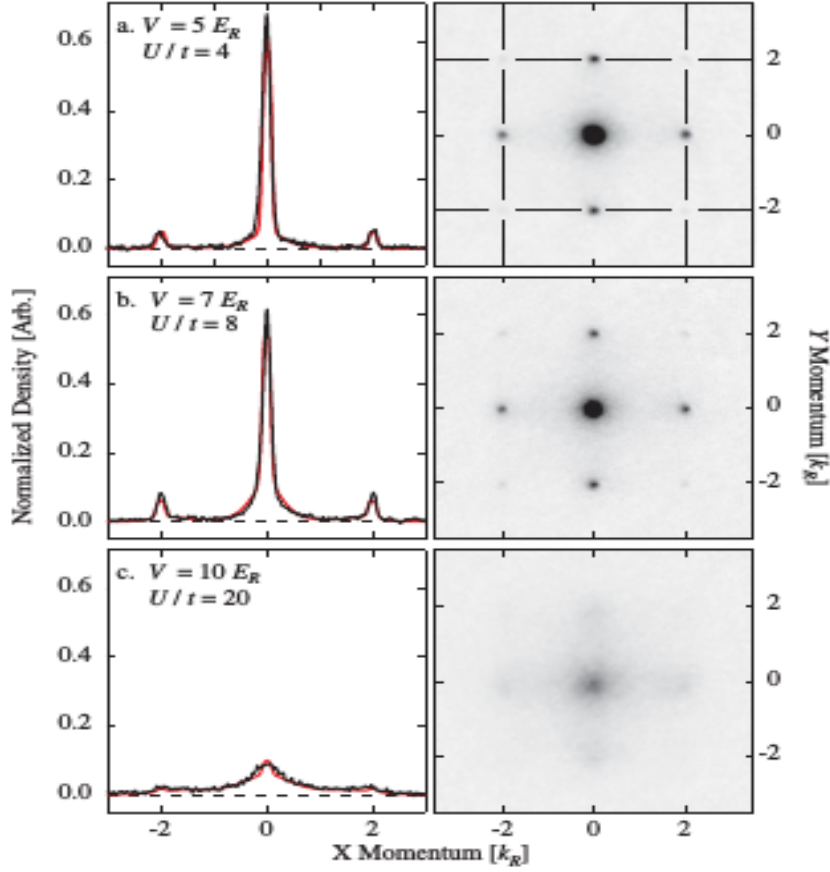


Figure 1.10: Momentum distributions and cross sections at  $U/t = 4, 8, 20$  in 2D. Each row shows a single momentum distribution normalized by the total atom number; the lines in the top right panel indicate trajectories along which four cross sections were taken. The left panel shows the average of these four sections (black solid line); the red dashed lines denote the fit to the bimodal distribution. [27]

$\vec{k}$  is related to  $\vec{r}$  by  $\vec{k} = M\vec{r}/\hbar t$  assuming ballistic expansion,  $w(\vec{k})$  is the Fourier transform of the Wannier function and

$$G(\vec{k})^{latt} = \frac{1}{V} \sum_{\vec{r}, \vec{r}'} e^{i\vec{k} \cdot (\vec{r} - \vec{r}')} \langle b_{\vec{r}}^\dagger b_{\vec{r}'} \rangle_{eq} \quad (1.16)$$

where  $eq$  stands for equilibrium, before lattice and trap potentials are switched off.

It should be noted that the observed density distribution after time of flight can deviate from the in-trap momentum distribution, if interaction effects during the expansion occur, or the expansion time is not so long that the initial size of the atom cloud can be neglected.

Fig.1.9 shows results on the momentum distribution obtained via time of flight experiments for 3D Bose Hubbard model [26]. The images are shown for different values of optical depth  $V_0$

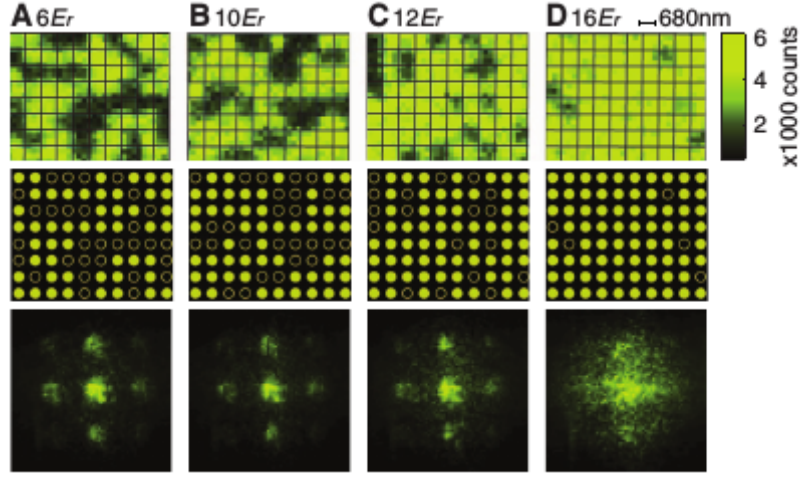


Figure 1.11: Single site imaging of the atom number fluctuations across the SF-Mott transition. Even number of particle is associated with empty sites. The particle density is maintained such that Mott insulator has one particle. Top row: As one tunes the optical depth from  $6E_r$  to  $16E_r$ , double occupancies are suppressed and Mott insulator at  $16E_r$  has one particle per site. Middle row: Results for top row. Solid circle represents atom present and open circle indicate absence of atom. Bottom row: Time of flight imaging results indicating loss of coherence as one hikes up the optical depth. [30]

ranging between 0 to  $20E_r$ . In the absence of the optical lattice ( $V_0 = 0$ ) a sharp peak at zero momentum is visible. The height of the peak diminishes with increase in the lattice depth, and subsidiary peaks at reciprocal lattice vectors show up. Beyond a critical lattice depth the sharp  $k = 0$  peak vanishes.

Fig.1.10 shows the results for condensate fraction for single-band 2D Bose-Hubbard model [27] with Rb atoms in an optical lattice as a function of lattice depth. The system crosses over from a superfluid to a Mott-insulating phase. By tracking the peak of the momentum distribution the experiment determines the critical interaction for superfluid to Mott transition to be  $U \approx 15.8t$ .

Similarly by measuring the width and peak of the condensate fraction, full  $T_c$  vs  $U/t$  was determined for the 3D BHM at unity filling. The experimental results were then compared with QMC and match was excellent [28].

### 1.3.2.2 In situ imaging

The real space density distribution can be observed via an ‘in situ’ imaging method [29, 30]. Using this method the on-site number statistics can be probed across the superfluid-Mott transition. In



‘in situ’ imaging, atoms are ejected in pairs, leaving the site occupied only if it’s occupation is odd [31]. Fig. 1.11, A to D, shows images as the depth of the lattice is increased. The ‘empty’ sites correspond to even numbers of bosons. As one increases the optical lattice depth the number of sites with even numbers of particles decrease. In the above experiment particle density is maintained such that the Mott insulator has one particle. In the Mott insulator phase at  $16E_r$ , particle number fluctuation is heavily suppressed - there are very few sites with even number, (0 or 2), of particles.

### 1.3.3 Dynamical properties

In the previous section, we described experiments measuring thermodynamic quantities such as the momentum distribution of bosons and the  $T_c$  of the condensate. Experiments have also begun probing the excitation spectrum. Before discussing experimental results, we briefly review the theoretically known results on the excitation spectrum.

#### 1.3.3.1 Weakly interacting limit

In the weakly interacting limit the BHM can be solved using the Bogoliubov approach [32–35].

$$H_{BHM} = - \sum_{ij} t_{ij} \hat{b}_i^\dagger \hat{b}_j + \frac{U}{2} \sum_i \hat{n}_i (\hat{n}_i - 1) - \mu \sum_i \hat{n}_i \quad (1.17)$$

There are  $N$  sites and wavevectors  $\vec{k}$  run over the first Brillouin zone.

$$\hat{b}_i^\dagger = \frac{1}{\sqrt{N}} \sum_{\vec{k}} \hat{b}_{\vec{k}}^\dagger e^{i\vec{k} \cdot \vec{r}_i} \quad (1.18)$$

In the momentum basis the Hamiltonian can be expressed as

$$H_{BHM} = \sum_{\vec{k}} (\epsilon_{\vec{k}} - \mu) \hat{b}_{\vec{k}}^\dagger \hat{b}_{\vec{k}} + \frac{U}{2N} \sum_{\vec{k}_1 \vec{k}_2 \vec{k}_3 \vec{k}_4} \hat{b}_{\vec{k}_1}^\dagger \hat{b}_{\vec{k}_2}^\dagger \hat{b}_{\vec{k}_3} \hat{b}_{\vec{k}_4} \delta(\vec{k}_1 + \vec{k}_2 - \vec{k}_3 - \vec{k}_4) \quad (1.19)$$

where  $\epsilon_{\vec{k}} = -2t(\cos(k_x a) + \cos(k_y a))$ .

If the total number of particles is  $N_b$ , at weak interaction most of the particles,  $N_0 = \langle \hat{b}_0^\dagger \hat{b}_0 \rangle$

would condense into lowest eigenstate. In the Bogoliubov approximation, quantum operators are replaced by classical average plus fluctuation  $\hat{b}_{\vec{k}} = \sqrt{N_0}\delta_{\vec{k},0} + a_{\vec{k}}$ , where  $a_{\vec{k}}$  describes quantum fluctuation around the condensate. We replace operators  $\hat{b}_{\vec{k}}$  by  $\sqrt{N_0}\delta_{\vec{k},0} + a_{\vec{k}}$  in the  $H_{BHM}$ .

The  $H_{BHM}$  has now terms independent, linear, quadratic, cubic and quartic in terms of  $a_{\vec{k}}$  and  $a_{\vec{k}}^\dagger$ .

To obtain the optimum number of atoms in the condensate, in presence of interaction, the energy is to be minimized with respect to  $N_0$ . At the minimum, the term of Hamiltonian that is linear in fluctuations should vanish. The term linear in fluctuations is given by

$$H^1 = (-\mu + U\frac{N_0}{N} - zt)\sqrt{N_0}(\hat{a}_0 + \hat{a}_0^\dagger) \quad (1.20)$$

For  $H^1$  to vanish  $\mu = Un_0 - zt$  where  $n_0 = N_0/N$  and  $z$  is the coordination number. In  $H_{BHM}$  we keep terms till quadratic order in  $a_{\vec{k}}$  and  $a_{\vec{k}}^\dagger$ . We drop off higher order terms of cubic and quartic orders. This leads to approximating  $H_{BHM}$  by  $H_{BG}$ , which contains terms till second order in fluctuations given by

$$H_{BG} = E_0 + \sum_{\vec{k}} (\epsilon_{\vec{k}} - \mu) \hat{a}_{\vec{k}}^\dagger \hat{a}_{\vec{k}} + \frac{U}{2} n_0 (\hat{a}_{\vec{k}}^\dagger \hat{a}_{-\vec{k}}^\dagger + \hat{a}_{\vec{k}} \hat{a}_{-\vec{k}} + 4\hat{a}_{\vec{k}}^\dagger \hat{a}_{\vec{k}}) \quad (1.21)$$

where  $E_0 = (-zt - \mu + \frac{1}{2}Un_0)N_0$  is the energy of the condensate.

The  $H_{BG}$  can be diagonalized using a Bogoliubov transformation:

$$\begin{aligned} \hat{\gamma}_{\vec{k}} &= u_{\vec{k}} \hat{a}_{\vec{k}} + v_{\vec{k}} \hat{a}_{-\vec{k}}^\dagger \\ \hat{\gamma}_{-\vec{k}}^\dagger &= v_{\vec{k}}^* \hat{a}_{\vec{k}} + u_{\vec{k}}^* \hat{a}_{-\vec{k}}^\dagger \end{aligned} \quad (1.22)$$

with  $|u_{\vec{k}}|^2 - |v_{\vec{k}}|^2 = 1$ . Using the above transformation and demanding that the Hamiltonian is quadratic and has no anomalous terms in  $\Gamma_{\vec{k}}$  operators:

$$H_{BG} = -\frac{1}{2}Un_0N_0 + \frac{1}{2} \sum_{\vec{k}} (\omega_{\vec{k}} - (\bar{\epsilon}_{\vec{k}} + Un_0)) + \sum_{\vec{k}} \omega_{\vec{k}} \hat{\gamma}_{\vec{k}}^\dagger \hat{\gamma}_{\vec{k}} \quad (1.23)$$

where

$$\begin{aligned}
\bar{\epsilon}_{\vec{k}} &= \epsilon_{\vec{k}} + zt \\
\omega_{\vec{k}} &= \sqrt{\bar{\epsilon}_{\vec{k}}^2 + 2Un_0\epsilon_{\vec{k}}} \\
|v_{\vec{k}}|^2 &= |u_{\vec{k}}|^2 - 1 = \frac{1}{2}\left(\frac{\epsilon_{\vec{k}} + Un_0}{\omega_{\vec{k}}} - 1\right)
\end{aligned} \tag{1.24}$$

The calculation predicts a dispersion linear in  $|\vec{k}|$  for small momentum and  $\sim |\vec{k}|^2$  for large momentum. The weakly interacting Bose gas has also been studied in the presence of trap [35].

### 1.3.3.2 Strong coupling limit

In the strong coupling limit, when  $U/t \gg 1$ , one can do perturbation theory in  $t/U$  to obtain the low energy dispersion in the Mott state [36].

$$\begin{aligned}
H_{BHM} &= H_0 + H_{kin} \\
H_0 &= \frac{U}{2} \sum_i \hat{n}_i(\hat{n}_i - 1) - \mu \sum_i \hat{n}_i \\
H_{kin} &= - \sum_{ij} t_{ij} \hat{b}_i^\dagger \hat{b}_j
\end{aligned} \tag{1.25}$$

To know the excitation spectrum we have to look at the poles of single particle Green's function.

This is given by

$$G_{ij}(\tau, 0) = - \frac{Tr[e^{-\beta H_{BHM}} T_\tau \hat{b}_i(\tau) \hat{b}_j^\dagger(0)]}{Tr[e^{-\beta H_{BHM}}]} \tag{1.26}$$

Within the RPA scheme [36]

$$[G^{-1}]_{ij}(\tau, 0) \approx [G_0^{-1}]_{ij}(\tau, 0)\delta_{ij} + \delta(\tau, 0)t_{ij} \tag{1.27}$$

We take Fourier transform with respect to imaginary time to get an equation diagonal in frequency:

$$[G^{-1}]_{ij}^{RPA}(i\omega_n) = [G_0^{-1}]_{ij}(i\omega_n)\delta_{ij} + t_{ij} \tag{1.28}$$

where the  $\omega_n$  are bosonic Matsubara frequencies.

If at  $T = 0$  there are  $n$  bosons at each site in the atomic problem then

$$\begin{aligned}
[G_0]_{ii}(i\omega_n) &= \frac{n+1}{i\omega_n + \mu - Un} - \frac{n}{i\omega_n + \mu - U(n-1)} \\
G^{RPA}(\vec{k}, i\omega_n) &= \frac{1 - z_{\vec{k}}}{i\omega_n - E_{\vec{k}}^-} + \frac{z_{\vec{k}}}{i\omega_n - E_{\vec{k}}^+} \\
E_{\vec{k}}^{\pm} &= \epsilon_{\vec{k}} + \epsilon_n^+ - \epsilon_n^- \pm \sqrt{\epsilon_{\vec{k}}^2 + 2\epsilon_{\vec{k}}U(2n+1) + U^2/2} \\
\epsilon_n^+ &= -\mu + Un \\
\epsilon_n^- &= \mu - U(n-1) \\
z_{\vec{k}} &= \frac{E_{\vec{k}}^+ + \mu + U}{\sqrt{\epsilon_{\vec{k}}^2 + 2\epsilon_{\vec{k}}U(2n+1) + U^2}}
\end{aligned} \tag{1.29}$$

The Mott phase has two modes, one at positive energy (particle mode) with dispersion  $E_{\vec{k}}^+$ , the other at negative energy (hole mode) with dispersion  $E_{\vec{k}}^-$ . The excitation spectrum is gapped.

### 1.3.3.3 Near the SF-Mott transition

Close to the superfluid-Mott transition boundary, the low energy physics is described by a Lorentz invariant theory [37]. This describes the dynamics of a complex order parameter  $\Psi = |\Psi|e^{i\theta}$ . The ordered phase (superfluid) is associated with non zero value of the order parameter while the Mott phase has zero order parameter. Within the ordered phase, the energy density in terms of  $|\Psi|$  and  $\theta$  has a ‘mexican hat’ shape, Fig.1.12, and the order parameter takes on a non- zero value in the minimum of this potential. Its phase,  $\theta$ , has a definite value, breaking the  $U(1)$  symmetry of the Hamiltonian. Expanding around the symmetry-broken ground state leads to two types of mode: a Nambu–Goldstone mode and a Higgs mode [38–40]. These modes are related to phase and amplitude variations of  $\Psi$ , respectively, Fig.1.12. The phase mode is gapless and amplitude mode has a finite excitation gap which begins to soften as one approaches the superfluid to Mott transition in the ground state.

### 1.3.4 Experiments on dynamics

From the simple theory we have discussed we know that the excitation spectrum is gapless in the superfluid and gapped in the Mott phase. While the weak coupling superfluid has only one gapless (Goldstone) mode - at positive energy - increasing the interparticle interaction leads

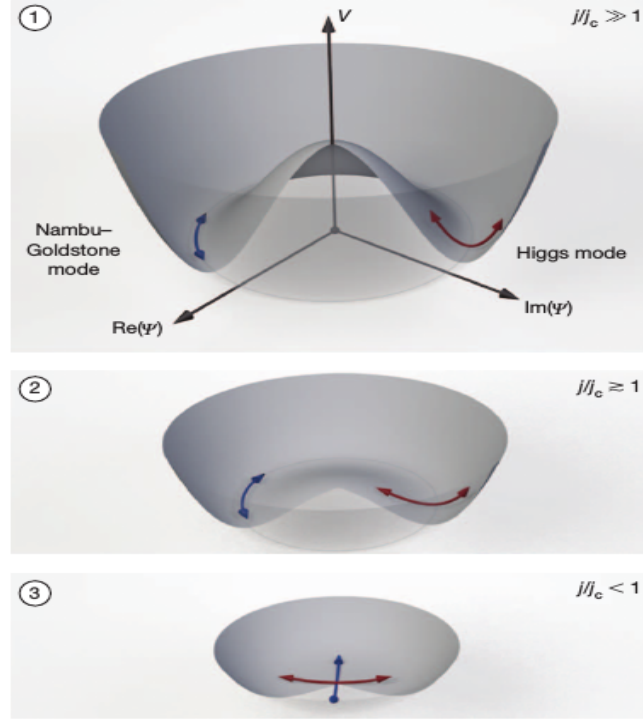


Figure 1.12: Energy density as a function of the order parameter. The ordered phase (superfluid) has minima for non zero value of order parameter. Two types of low energy excitation exist - Goldstone (phase) and Higgs (amplitude) modes. The Goldstone mode has its origin in phase twist and the Higgs mode is associated with change in magnitude of the order parameter. As  $J/U$  decreases beyond critical coupling the minimum of the energy density is at zero. In the disordered phase two gapped mode exist namely particle and hole excitation. [41]

to a more complex mode structure. The strong correlation superfluid has an amplitude mode (gapped) and a Goldstone mode (gapless) on *both sides* of the frequency axis. How the weight transfers from the weak coupling mode to the four mode structure is something we discuss in Chapter 4.

Experimentally the single particle spectrum of the BHM has never been measured although there are proposals for ARPES-like schemes [42, 43] or higher band Bragg spectroscopy [44] to measure the single particle spectra. Experimental techniques used to determine the dynamical properties of cold atoms in an optical lattice focus on the two particle spectrum. We next discuss these methods, called Bragg spectroscopy and lattice modulation spectroscopy.

### 1.3.4.1 Lattice modulation spectroscopy

To measure the excitation spectrum the optical lattice is modulated with a frequency  $\nu$  [41, 45, 46]. The periodic modulation of lattice height is given by  $V_x(t) = \delta V_0 \cos(\nu t)$ . The effect of lattice

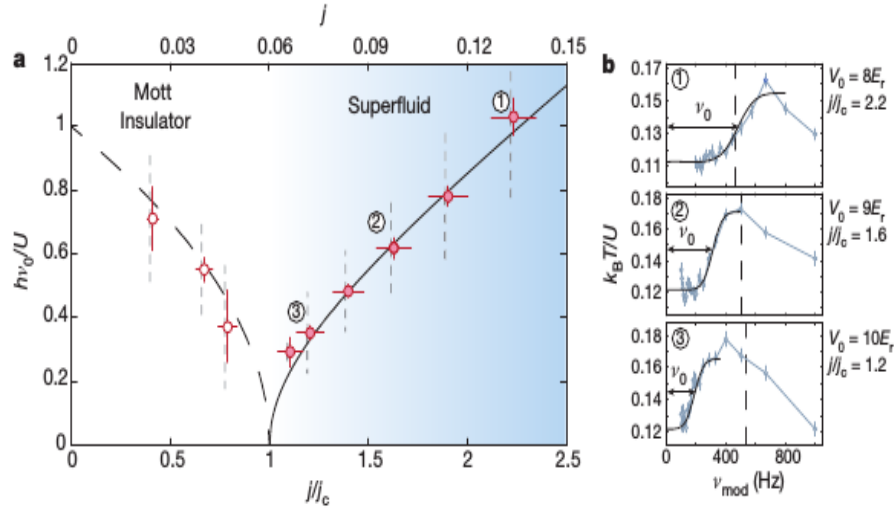


Figure 1.13: Softening of the Higgs mode. (a) The fitted gap values  $h\nu_0/U$  (circles) show a characteristic softening close to the critical point. Horizontal and vertical error bars denote the experimental uncertainty of the lattice depths and the fit error for the centre frequency of the error function, respectively. Vertical dashed lines denote the widths of the fitted error function and characterize the sharpness of the spectral onset. The blue shading highlights the superfluid phase (b) Temperature response to lattice modulation (circles and connecting blue line) and fit with an error function (solid black line) for the three different points labeled in a. As the coupling  $j(t/U)$  approaches the critical value  $j_c$ , the change in the gap values to lower frequencies is clearly visible (from panel 1 to panel 3). Vertical dashed lines mark the frequency  $U/h$  corresponding to the on-site interaction. Each data point results from an average of the temperatures over 50 experimental runs. [41]

modulation is to perturb the Bose Hubbard Hamiltonian via a periodic modulation  $\delta V_0 \cos(\nu t)$ . This affects the parameters  $(U, t)$  of the BHM making them time dependent. The dominant effect of periodic modulation is on the kinetic energy term, and the effect on the interaction energy is weaker.

The Bose Hubbard Hamiltonian to first order in  $\delta V$  is given by,

$$\hat{H}(t) = \hat{H}_{BHM} + \delta f(t) \hat{K} \quad (1.30)$$

where  $\hat{K}$  is the kinetic term,  $\delta f(t) = \delta f_0 \cos(\nu t)$ ,  $\delta f_0 = (\frac{1}{4} - \sqrt{\frac{V_0}{E_r}}) \frac{\delta V_0}{V_0}$ .

The periodic modulation changes the energy of the system. Within linear response theory, the rate of change of energy is given by [47]

$$\dot{E} = \frac{\nu}{2} S(\nu, T) |\delta f_0|^2 + P(\nu, T) \quad (1.31)$$

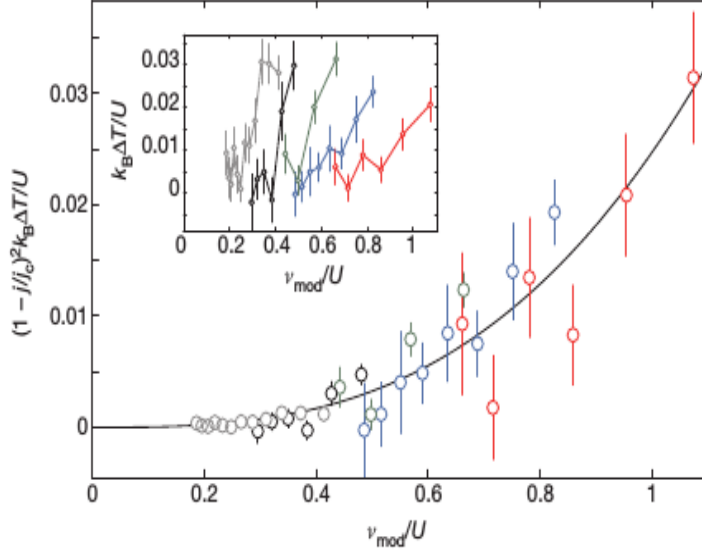


Figure 1.14: The low-frequency response in the superfluid regime shows a scaling compatible with the prediction  $(1 - j/j_c)^{-2} \nu^3$ . Shown is the temperature response rescaled with  $(1 - j/j_c)^{-2}$  for  $V_0=10E_r$  (grey),  $9.5E_r$  (black),  $9E_r$  (green),  $8.5E_r$  (blue) and  $8E_r$  (red) as a function of the modulation frequency. The black line is a fit of the form  $a\nu^b$  with a fitted exponent  $b=2.9$ . The inset shows the same data points without rescaling, for comparison. [41]

Here  $S(\nu)$  is the kinetic energy spectral function,  $P(\nu, T)$  is the heating power from other mechanisms. To leading order,  $P(\nu, T)$  can be approximated as frequency independent,  $P(T)$ . Under linear response, the determination of energy transfer then boils down to calculation of hopping correlator given by

$$S(\nu) = \sum_{n,m} (\exp(-\beta E_m) - (\exp - \beta E_n)) |\langle n | \hat{K} | m \rangle|^2 \delta(\nu + E_n - E_m) \quad (1.32)$$

where  $E_n$  are the many particle eigenstates and  $|n\rangle$  the eigenstates.

The computation of the kinetic energy correlator is related to a two particle Green's function. This suggests that within the validity of linear response theory, peak response will be seen for frequencies which are close to eigen energies of the unperturbed BHM Hamiltonian.

In the experiments the modulation is stopped after a certain time and system is left to thermalize. If the system is assumed to be quasistatic, then effect of periodic modulation can be understood in terms of temperature change. The final temperature shift can be deduced from the

following self-consistent equation:

$$T(\nu, t) - T(\nu, 0) = \int_0^t dt' \frac{\dot{E}(\nu, T(\nu, t'))}{C(T(\nu, t'))} \quad (1.33)$$

where  $C(T(\nu, t'))$  stands for the specific heat. In the experiment after the system has thermalized the lattice depth is adiabatically hiked up to reach the atomic limit ( $\frac{t}{U} \sim 0$ ) and the temperature of the system is measured based on single-atom-resolved detection technique [29, 30].

Fig.1.13b shows the plot of temperature response for a lattice modulation as a function of frequency  $\nu$  for various coupling strength. The temperature response is fitted to a function of the form

$$T = T_0 + \frac{\Delta T}{2} \left( \text{erf} \left( \frac{\nu_{mod} - \nu_0}{\sigma} \right) + 1 \right) \quad (1.34)$$

where  $T_0, \Delta T, \nu_0$  and  $\sigma$  are the fitting parameters,  $\nu_0$  characterises the mean frequency and  $\sigma$  is the broadening. The mean frequency  $\nu_0$  shifts to lower value as one approaches the critical coupling. This suggests that gap is decreasing as one approaches the critical point suggesting softening of Higgs mode.

Fig.1.13a shows the value of  $\nu_0$  for each coupling strength and  $\sigma$  is shown as vertical dashed line. The ratio  $\nu_0/\sigma$  remains constant as one approaches the critical coupling. This means that as  $\nu_0$  decreases  $\sigma$  also decreases. Similar gapped response is seen in the Mott insulating regime with the gap closing continuously when approaching the critical point

The softening of spectral response in the superfluid phase has been identified with the Higgs mode. The value of  $\nu_0$  matches quantitatively well with the Gutzwiller calculation including a trap except near critical coupling. The Gutzwiller calculation cannot be used to understand broadening scales.

Fig.1.14 shows that the low-frequency response in the superfluid regime shows a scaling  $(1 - j/j_c)^{-2} \nu^3$ . The low frequency part of the response is expected to be governed by a process coupling amplitude mode to a pair of phase mode with opposite momenta. Since the probe couples to  $|\Psi|^2$  the response is expected to scale as  $\nu^3$  at low frequencies [48]. The experiment above has confirmed the existence of a Higgs mode in the superfluid phase. The response is gapped in



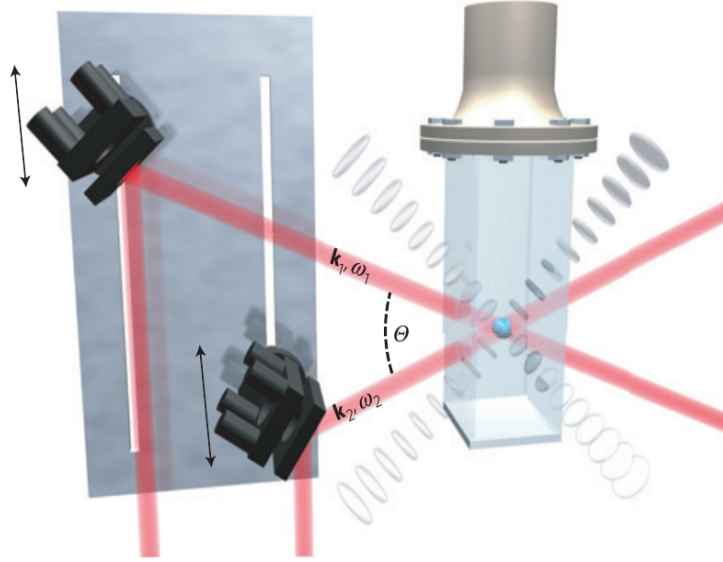


Figure 1.15: Experimental set up for Bragg spectroscopy. Ultracold atoms are loaded into the optical lattice, and energy and momentum is transferred to the sample by shining light using two laser beams incidenting at an angle. The angle of incidence could be changed by changing the angle between two laser beams and could be used to scan the Brillouin zone.[56]

the Mott phase consistent with RPA calculation [49].

### 1.3.4.2 Bragg Spectroscopy

In Bragg spectroscopy, two laser beams with wave vectors  $\vec{k}_1$  and  $\vec{k}_2$  with frequency  $\omega_1$  and  $\omega_2$  are focused on the sample, leading to an inelastic photon scattering process, illustrated in Fig.1.15. The potential the atoms feel due to the two photon process is given by  $V \cos(\vec{q} \cdot \vec{r} - \omega t) \hat{n}_i$  with  $\vec{q} = \vec{k}_1 - \vec{k}_2$  and  $\omega = \omega_1 - \omega_2$ . As the energy transfer can be tuned by changing the two laser frequencies and the momentum transfer can be tuned by changing the laser angle. Bragg spectroscopy provides access to the excitation spectrum over the full Brillouin zone.

The Hamiltonian describing the Bragg perturbation is given by

$$\hat{H}_{Bragg} = \frac{V}{2} (e^{-i\omega t} \hat{\rho}_{\vec{p}_b}^\dagger + e^{i\omega t} \hat{\rho}_{\vec{p}_b}) \quad (1.35)$$

where  $\hat{\rho}_{\vec{p}_b}^\dagger = \sum_{\vec{p}} b_{\vec{p}+\vec{p}_b}^\dagger b_{\vec{p}}$

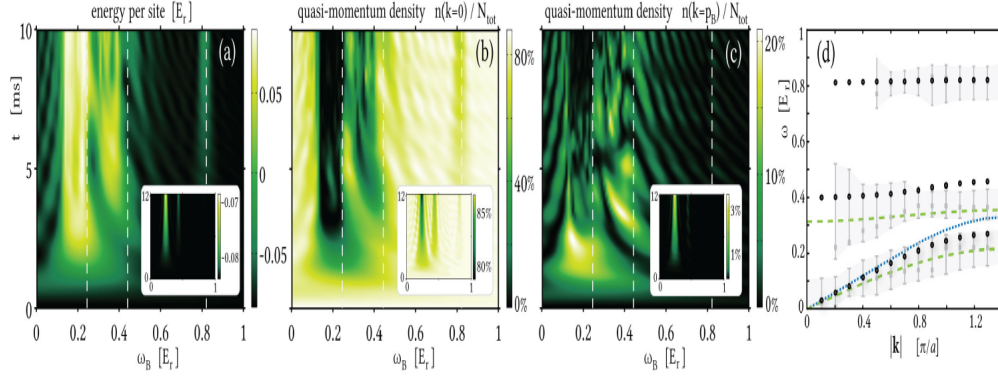


Figure 1.16: Energy absorption (a) and quasi-momentum density (b),(c) spectra for a square pulse. Energy absorption (a) and quasi-momentum density (b),(c) spectra for a square pulse at high intensity  $V = 0.1E_r$  (insets: weak intensity  $V = 0.005E_r$ ) in the intermediate interaction  $s = 9$  regime and for Bragg momentum  $|\vec{p}_B| = \frac{\pi}{a}$ . The resonance frequencies predicted from the maxima of the high intensity energy absorption spectra (plotted as gray squares in (d)) contain a systematic uncertainty quantified by the FWHM of the pulse after 10ms  $\sim 3.26/J$  indicated by the error bars and shaded region in (d). The comparison with the true quasiparticle energies (dashed white lines in (a-c), black circles in (d)) reveals significant discrepancies. For comparison in (d): The blue dotted line is the Bogoliubov result, the green dashed lines are the results from for the amplitude and sound modes  $\omega(\vec{k}) = \psi_0 \sqrt{2U n \epsilon_k}$  with  $\psi_0$  determined by GW). [58]

Under linear response the energy absorption rate is given by [50, 51]

$$\dot{E} = \frac{V^2}{2} \int d\omega' \omega' [S(\vec{p}_B, \omega') - S(-\vec{p}_B, -\omega')] \frac{\sin((\omega - \omega')t)}{\omega - \omega'} \quad (1.36)$$

Here  $S(\vec{p}_B, \omega)$  is the dynamic structure factor,

$$S(\vec{q}, \omega) = \sum_{n,m} e^{-\beta E_n} |\langle n | \delta \rho_{-\vec{q}} | m \rangle|^2 \delta(\omega - \omega_{nm}) \quad (1.37)$$

where  $\delta \rho_{-\vec{q}} = \sum_i (\hat{n}_i - \langle n_i \rangle) e^{-i\vec{q} \cdot \vec{r}_i}$  and  $\omega_{nm} = E_m - E_n$ . The sum runs over all eigenstates of the system  $|n\rangle, |m\rangle$ .

The system shows a response whenever the Bragg frequency matches the energy difference  $E_n - E_m$ , between the two eigenstates of the BHM Hamiltonian. The peak height depends on the transition probability  $|\langle n | \delta \rho_{-\vec{q}} | m \rangle|^2$ .

Early experiments using Bragg spectroscopy were performed on weakly interacting condensates [52, 53], then extended to strong interactions without a lattice [54]. They have been used in

optical lattices [55–57] and have confirmed the existence of the amplitude mode in the 3D BHM [58].

Fig. 1.16 shows the result of Bragg spectroscopy for the 3D Bose Hubbard model [58]. The response of the system in the limit of very small  $V$  is shown in the inset of Fig. 1.16a–1.16c whereas in the main figure response is shown for  $V = 0.1E_r$ . The response of the system is sharply peaked for small  $V$ , while there is a drastic non-trivial broadening for large  $V$ . From the energy absorption spectra, resonance frequencies are predicted by looking at the maximum of energy absorption spectra as a function of frequency and momenta shown in Fig. 1.16d. The error bars and shaded quantifies the systematic uncertainty in the extracted energies.

At intermediate interactions shown in Fig. 1.16d, neither Bogoliubov theory (dotted blue line), nor the theory presented by Huber [59] for strong interactions (dashed green lines) apply. Here, the dispersion relation obtained by the dynamic GW method or RPA [49] (black circles in Fig. 1.16d) remains valid.

### 1.3.5 Open issues

There exists an excellent match between theoretical and experimental quantities, when it is about thermodynamic quantities. While QMC provides high accuracy numerical results for the thermodynamic features, one would want methods that (i) shed light on the key physical effects, and (ii) allow access to dynamical properties. Mean field theory [19, 23], although quantitatively not very accurate, highlights the crucial effect of particle number fluctuation in the superfluid ground state. More sophisticated methods, *e.g.* strong coupling expansion [60, 61], variational calculations [62], the projection operator technique [63], cluster Gutzwiller [64] and variational cluster schemes [65–68] improve on the mean field ground state and yield results that agree well with QMC for the zero temperature transition.

There is less insight into the finite temperature situation. Mean field theory has a finite temperature generalisation but leads to a large overestimate of  $T_c$  scales. Slave particle methods [69, 70], dynamical mean field theory [71–73] have been used to study the thermal physics. Among the many methods, only the results of BDMFT compare reasonably well with QMC

in terms of thermal properties. The single particle excitation spectra has been computed using approximate methods RPA [49], slave boson method [59, 69] at zero temperature. There are only few results available at finite temperature using BDMFT [74] in 3D and QMC in 1D [75]. The results of BDMFT and QMC match with RPA at low temperature. The weights and nature of the bands could not be resolved because of errors in analytical continuation issue.

For two particle quantities results are available using RPA Green's function over Mott phase [76] and slave particle methods [59] in the vicinity of Sf-Mott phase boundary at zero temperature. Only few results are available for two particle quantities at finite temperature using QMC in 2D [39]. The detailed finite temperature study of two particle excitation spectra is lacking. On the other hand detailed experimental results are available for two particle excitation spectra using Bragg spectroscopy [58].

In terms of computing dynamical quantities at finite temperature, both BDMFT and QMC result becomes unreliable at very low frequency when the spectral weight is relatively small due to large errors in analytical continuation from Matsubara to real frequencies. The experiments are further complicated by the presence of trap and finite temperature. In order to make detailed comparison with experiments a method is required which not only provides quantitatively accurate thermal results but is also free from analytical continuation issue when it comes to computation of real time quantities.

In Chapter 2 we present an alternate method, with emphasis on *spatial fluctuations*, which we believe are important in lower dimensions, and include temporal (quantum) fluctuations only approximately. In Chapter 3 we describe in detail our thermal results and in Chapter 4 we provide results on single particle excitation spectra and leave computation of two particle quantities for future work.

Though in experiments there is an overall trap we have not done calculation in presence of trap. Our methods are general enough to include the effects of trap under LDA approximation.

## 1.4 Spin-orbit (SO) coupling

Spin-orbit coupling (SOC) involves a coupling between the spin of a particle and its translational motion. In solids it arises from the motion of electrons in the electric field produced by the

nuclei. In ultracold systems spin-orbit coupling is artificially generated. There are three types of spin orbit coupling predominantly discussed in literature.

*Rashba SOC:* The Rashba spin orbit coupling leads to momentum dependent splitting of bands. In solid state system it is associated with asymmetry of crystal potential. The model Hamiltonian describing Rashba spin orbit coupling is given by

$$H_R = \alpha(\sigma \times \vec{p}) \cdot \hat{z} \quad (1.38)$$

Here  $\alpha$  denotes strength of spin orbit coupling,  $\vec{p}$  denotes momentum and  $\sigma$  stands for Pauli matrix.

*Dresselhaus SOC:* The Dresselhaus spin orbit coupling is given by

$$H_D = \beta(-\sigma_x p_y - \sigma_y p_x) \quad (1.39)$$

where  $\beta$  denotes strength of spin orbit coupling,  $\sigma_x$  and  $\sigma_y$  are Pauli matrices and  $p_x$  and  $p_y$  are momentum along x and y direction.

*Abelian SOC:* Abelian SOC is generated by equal mixture of Rashba and Dresselhaus.

$$H_A = \Gamma(-\sigma_y p_x) \quad (1.40)$$

Here  $\Gamma$  denotes strength of spin orbit coupling.

This section provide a brief review on spin-orbit effects in ultracold atoms.

### 1.4.1 Engineering SO coupling in Ultracold atoms(Continuum)

**Abelian SOC:** One uses atoms with two internal states and couples them through Raman transition. So that change in the internal state is accompanied by a momentum boost  $|k|$  [77–80]. Atoms with two internal states,  $|a\rangle$ ,  $|b\rangle$ , are considered, separated by an energy  $\omega_0$ . One also needs an ‘excited state’  $|e\rangle$ . The gas is exposed to two laser beams with wave vectors  $\vec{k}_1$  and  $\vec{k}_2$  and frequency  $\omega_1$  and  $\omega_2$ . The two beams are taken with different polarization  $\pi$  or  $\sigma^\pm$ , such that one of the beams only couples  $|a\rangle$  to  $|e\rangle$  and other beam couples  $|b\rangle$  to  $|e\rangle$ .

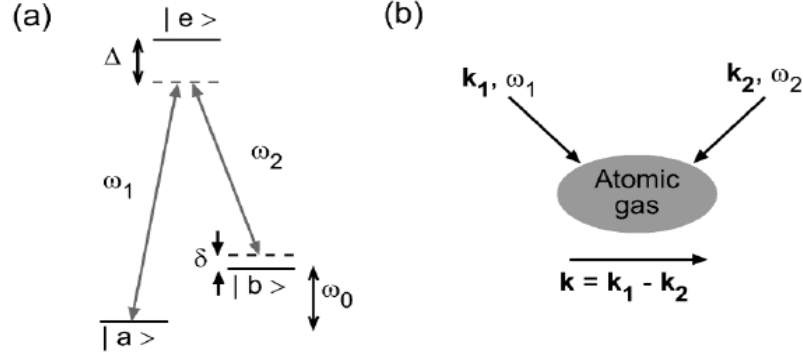


Figure 1.17: a) Laser beams of frequency  $\omega_1, \omega_2$  induce Raman transition between internal states  $|a\rangle$  and  $|b\rangle$ . (b) Change in momentum of gas  $\vec{k} = \vec{k}_1 - \vec{k}_2$  due to Raman transition.

An atom in state  $|a\rangle$  absorbs a photon and goes to  $|e\rangle$ . The atom in excited state  $|e\rangle$  de-excites due to stimulated emission to state  $|b\rangle$ . The overall process creates a coupling between two internal states given by

$$V(\vec{r}, t) = \frac{\Omega}{2} e^{-i\vec{k}\cdot\vec{r} - \omega t} |a\rangle \langle b| + h.c. \quad (1.41)$$

A biased Zeeman field along the  $\vec{y}$  direction is applied, splitting the two states by Zeeman energy  $\omega_z$  and thus detuning from the Raman resonance  $\delta = (\omega_1 - \omega_2) - \omega_z$ . If one assumes that laser beams are focused on the sample along x-directions with wave vectors  $\pm k_r \hat{x}$  the effective Hamiltonian is:

$$H_{so} = \frac{(k_y^2 + k_z^2)}{2m} + \frac{(k_x - k_r \sigma_z)^2}{2m} - \frac{\delta}{2} \sigma_z + \frac{\Omega}{2} \sigma_x \quad (1.42)$$

The above Hamiltonian describing Abelian spin-orbit coupling has been realized experimentally [77] and has been explored to obtain the finite temperature phase diagram with  $\delta = 0$  [81].

The Hamiltonian has two degenerate single particle minima for  $\Omega < 4E_r$  and these two degenerate minima have opposite magnetization. The nature of the Bose condensate is determined by interactions.

It has been found experimentally for  $\Omega < 0.2E_r$ , bosons condense into superposition of these two states leading to stripe order with spatial translational symmetry broken. For  $0.2E_r < \Omega < 4E_r$ , bosons condense into either of the minimum thus restoring the translational symmetry. But

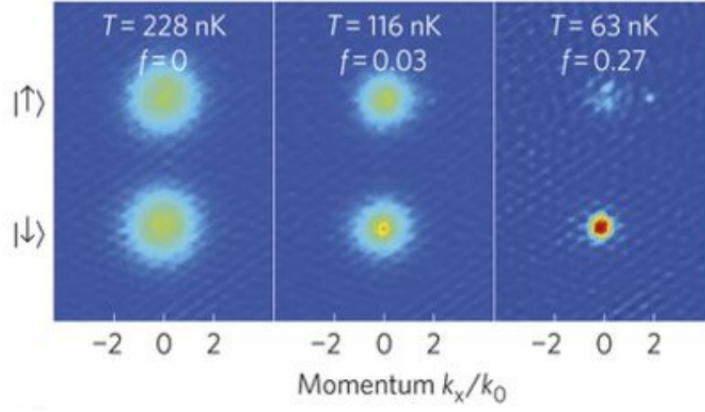


Figure 1.18: Spin-resolved time-of-flight image of the momentum distribution for three values of temperature  $T$  and condensate fraction  $f$ . At  $T = 63\text{ nK}$ , the population imbalance of the condensate shows that it is in a magnetized phase.[81]

this breaks the  $Z_2$  symmetry and condensate is magnetic. For  $\Omega > 4E_r$  it was found that bosons condense into the zero momentum state and displays zero magnetization [82, 83].

Fig. 1.18 shows the momentum distribution of bosons in the magnetic phase and Fig.1.19 shows the full experimentally determined phase diagram as a function of spin-orbit coupling  $\Omega$ .

**Rashba SOC:** There are various proposals to realize Rashba spin-orbit coupling in ultracold atoms. One of the ideas is to extend the Raman scheme [84, 85]. The internal states of atoms are cyclically coupled to one another through Raman transitions. The low energy manifold of the quantum gas can be described using Rashba type Hamiltonian,

$$H = \frac{k^2}{2m} + (\sigma_x k_y - \sigma_y k_x) \quad (1.43)$$

This has the advantage that there is no collisional instability but the challenge is from heating due to many laser beams. Other proposals are to use fast switching of the counter propagating Raman laser beams [86], and use magnetic fields to generate non Abelian SOC. For that magnetic fields are required to vary on the scale of the lattice spacing. This can be done using a magnetic chip in experiments [87, 88]. None of these, however, has been realized experimentally.

### 1.4.2 SOC in optical lattices

**Abelian SOC:** SOC with equal Rashba and Dresselhaus magnitudes has been realized in optical lattices using technology developed in the context of atomic clocks. The alkaline earth atoms

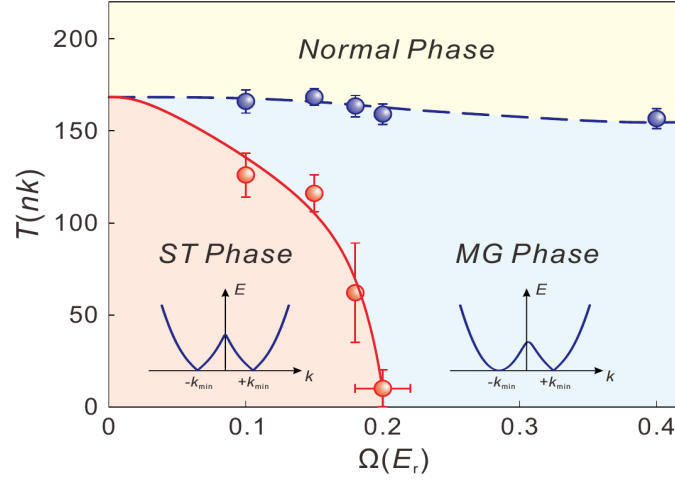


Figure 1.19: Finite temperature phase diagram of spin-orbit coupled bosons[81]

with two states, ground states ( $|g\rangle$ ) and nearby metastable state ( $|e\rangle$ ) are used. The alkaline earth atoms are trapped in optical lattice with lattice depth being same for both states  $|g\rangle$  and  $|e\rangle$ . In order to engineer SOC, coherent coupling is introduced between these states using a single photon transition from a clock laser. The clock laser leads to tunable momentum transfer along the direction of atomic chains coupling state  $|g, k\rangle$  with state  $|e, k + \delta k\rangle$  and generating spin momentum locking. The momentum transfer can be controlled by changing the angle  $\theta$  between the clock laser and optical lattice. The idea was proposed earlier [89–91] and has been realized experimentally [92, 93]. This has been used to realize Harper-Hofstadter ladder Hamiltonian [93].

**Rashba SOC:** Though Abelian spin-orbit coupling in optical lattice has been realized there are no experiments with Rashba type spin-orbit coupling. There have been various proposals to realize Rashba spin-orbit coupling in optical lattice. One of the proposals is to apply the optical potentials that give rise to spin-orbit coupling and the optical lattice [94]. Other idea is to generate lattice potentials and use light assisted tunneling processes generalizing the scheme used in simulation of Hofstadter problem to non-Abelian gauge coupling [95–97]. This scheme has an additional advantage in terms of lower loss rates and less heating. It has also been proposed to use the polarization of optical lattice to provide a spatially varying spin-dependent potential [98].



### 1.4.3 Open Issue in SOC:

On the theoretical side, Rashba spin-orbit coupling in BHM has also been studied using other approaches such as strong coupling expansion [99, 100] and real space bosonic dynamical mean field theory (BDMFT) [101]. They have unearthed a rich ground state phase diagram for these systems. Some of the unconventional phases found include those with long range magnetic order in the Mott ground state [101] and the possibility of a boson condensate at finite momentum [99, 100]. Such studies have also been supplemented by their weak-coupling counterparts in the continuum where there is no Mott transition. The weakly interacting condensates have been studied using the Bogoliubov-Hartree-Fock approximation [102].

In spite of several studies on the ground state, only limited theoretical work exists on the thermal phases of spin-orbit coupled systems. For Abelian systems with equal mixture of Rashba and Dresselhaus coupling, Ref.[103] derives an effective  $t - J$  model for the bosons and studies the thermal phases of this effective model. The study reveals a stripe superfluid order at low temperature and a two step melting upon increasing temperature, leading first to a striped normal phase of the bosons and then to a homogeneous state. However similar study for the thermal phases of Bose-Einstein condensates (BECs) in the presence of Rashba spin-orbit coupling is lacking. In the near future, experiments can probe dynamics of bosons in the presence of SOC. But there are no theoretical studies of the dynamics of bosons in the presence of SOC.

In Chapter 5 we study the thermal phases of a two species Bose-Hubbard model in the presence of a Rashba spin-orbit coupling. Our study thus involves bosons in the presence of an effective non-Abelian gauge field. We use the approach described in detail in Chapter 2 and give the detailed results in Chapter 5.

## 1.5 Disorder in an optical lattice

Sixty years ago, P. W. Anderson suggested that certain materials would undergo a metal-insulator transitions as the amount of disorder is changed [104]. He suggested a tight binding model where in the absence of disorder electron motion would be described using extended wave functions, but beyond a critical disorder the conductivity would vanish. This transition would arise from

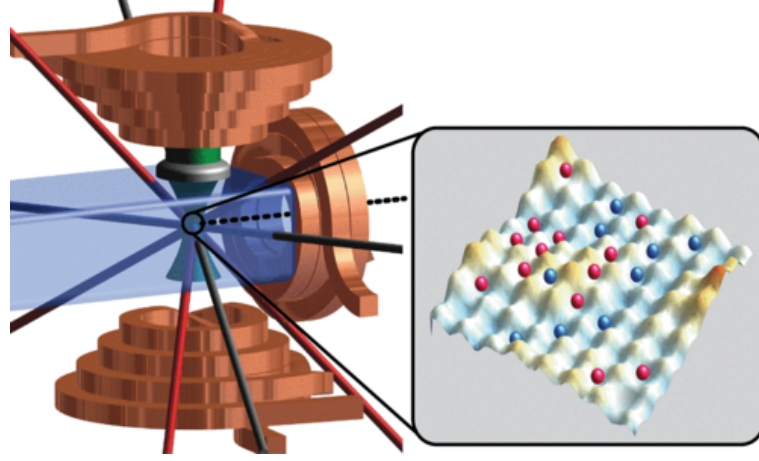


Figure 1.20: The experimental set up to introduce speckle disorder in an optical lattice [? ]. The atoms are trapped using optical dipole trap (gray lines). The lasers are superimposed to create 3D optical lattice (red). The speckle field is imposed on the atoms (green). The optical speckle field is produced by passing a 532 nm laser beam through a holographic diffuser and focusing it onto the atoms. The two dimensional representation of lattice is shown where two hyperfine states of atom are represented using different color.

the change in wavefunctions (at the Fermi level) from extended to localized, with exponentially decaying tails.

The Anderson localization in its original form is difficult to observe in the solid state due to the presence of interaction. Since in cold atoms the interaction strength can be tuned, Anderson localization can be observed in ultra cold atomic systems. [105–107].

The disorder in cold atoms is generated using speckle potentials [105–107]. When coherent laser light is scattered from a rough surface a random intensity pattern is produced. This is called a speckle pattern [108]. The speckle intensity is characterized by two parameters, standard deviation and correlation length.  $P(I) = \frac{1}{\langle I \rangle} \exp \frac{-I}{\langle I \rangle}$  with  $\langle I(\vec{r}) I(0) \rangle = I_0^2 (1 + |\gamma(\vec{r})|)^2$ ,  $\gamma(\vec{r}) = J_1(|\vec{r}|/\sigma)/(|\vec{r}|/\sigma)$  where  $J_1$  is the first order Bessel function and  $\sigma$  is the correlation length of disorder. In experiments a focused laser beam is first passed through a lens of focal length  $f$  and a diffuser is placed near the lens. The atoms are located at the focal plane of the lens. The effective dipole potential that atom feels is sum of the optical lattice potential and speckle field, leading to generation of ‘disordered optical lattice’. The disorder strength can be varied by changing the optical intensity. By changing the aperture of the lens the correlation length can be tuned. Fig.1.20 shows the schematic of an experimental set-up using optical speckle fields to introduce the random site potential in the optical lattices.

Much of the earlier studies were done using uncorrelated disorder, while speckle disorder is spatially correlated. One difference between the two is the Fourier transform of the two point correlation function of the random potential. The Fourier transform of the two point function in case of uncorrelated disorder is unbounded. In case of speckle disorder the correlation function vanishes above a momentum [109].

It is interesting to ask how spatial correlations in the disorder - as in disordered optical lattices - modify the physics. The ‘speckle disorder’ in these systems is characterised by two parameters: the scale  $V$  of potential fluctuations, and the correlation length,  $\sigma$ . Most of the optical lattice disorder experiments have been with bosons, mainly in the ‘non interacting’ regime [109–112] with only a few probing interactions [113–115]. In the non-interacting problems, the trap is switched off and the Bose gas allowed to expand in the presence of speckle disorder. In one dimension (1D), even for weak disorder [109–111] the cloud stops expanding and forms a stationary localised wave. By fitting the stationary pattern a localisation length can be extracted, and is found to increase with speckle size. For bosons in 3D [112], expansion yields a localised part and a diffusive part. For interacting bosons in a 3D optical lattice the effect of disorder on the condensate fraction has been probed [113, 114].

There are experiments on fermions probing both the non interacting [116, 117] and interacting [118, 119] regimes. In the non-interacting regime localisation has been observed in a 3D disordered potential [116]. The dependence on the correlation length of disorder was studied by adjusting the aperture of the speckle focusing lens and the mean localisation length was seen to increase linearly with speckle correlation length [117]. The effect of speckle disorder at fixed correlation length was studied on a strongly interacting Fermi superfluid [119] and its properties investigated using high resolution *in situ* imaging and ‘conductance’ measurements.

Some of the effects of spatial correlations in the disorder have been probed by theory. For non interacting systems, transport in a speckle disorder potential requires revision of many results that exist in the case of uncorrelated disorder. Several studies have been done on this [120–129] modifying the Boltzmann equation and extending the self-consistent theory of localisation. For interacting systems we are aware of two kinds of theory, (i) those which examine [130, 131] bosonic superfluids in a speckle potential, with repulsive interactions present, and (ii) studies of

Fermi systems [132, 133] with repulsive interactions and speckle disorder. Those in (i) mainly use the Gross-Pitaevskii framework, focusing on the lowest self-consistent eigenstate, while (ii) uses dynamical mean field theory (DMFT).

Most studies studying effect of disorder on fermionic superfluidity involves uncorrelated disorder. In Chapter 6, we study the impact of speckle disorder on fermionic superfluidity, in the context of attractive Fermi Hubbard model.

# Theoretical tools

## 2.1 Introduction

In the previous Chapter we discussed several experiments in ultracold systems using bosonic atoms. In this Chapter we first review the theoretical methods available to study Bose systems in the presence of strong correlation, and then go on to discuss the method we use in this thesis to study correlated bosons.

## 2.2 Bose Hubbard model

In the case of single species Bose Hubbard model (BHM), quantum Monte Carlo provides accurate results and matches excellently with experimental results in the presence of a trap. There are other methods, analytical or semi-analytical, which not as accurate as QMC but help we understand the key qualitative physics of the problem. Here we provide a brief review of theoretical tools available to study the strong correlation physics in the BHM.

### 2.2.1 Theory approaches

The superfluid to Mott insulator transition has been studied in single species Bose Hubbard model using a variety of approaches. The various methods can be classified into two parts: (i) zero temperature methods, and (ii) finite temperature methods. We provide a quick review of

these approaches below.

### 2.2.1.1 Zero temperature methods

**Mean Field + RPA:** The mean field approach [19, 23] correctly captures the qualitative physics of the BHM. It provides a  $\mu/t$  vs  $U/t$  phase diagram at zero temperature distinguishing the ground state into superfluid and Mott phase. The excitation spectrum has been studied by using the RPA approach [49, 134]. The weak coupling superfluid, as in the continuum, has a low energy linearly dispersing mode, while the Mott insulator has a gapped excitation spectrum. Increasing interaction in the superfluid leads to the appearance of a ‘negative energy’ gapless mode - which dictates the broadening of the momentum distribution from the simple  $k = 0$  peak, and gapped ‘amplitude’ modes of both positive and negative energy. As the system heads towards the Mott transition the weight shifts from the traditional Bogoliubov mode to the negative energy phase mode and the amplitude modes. The mean field overestimates the transition point, and the excitation spectrum obtained from RPA is sharp. There is no source of broadening, mean frequency observed in experiments in linear response regime qualitatively matches with that observed in ultracold experiments.

**Cluster Gutzwiller:** In cluster Gutzwiller method [64, 135–138] the lattice is partitioned into clusters, each isolated cluster is treated exactly, and intercluster hopping is treated approximately. The local superfluid order parameters is defined for each of the boundary sites of the cluster which is needed to be solved self consistently. With increasing cluster size, the superfluid Mott boundary obtained using this method approaches the exact results.

**Strong coupling expansion:** The strong coupling calculation of Monien et al [60, 61], is done in one and two spatial dimensions by systematically expanding in powers of  $t/U$  around the Mott state. These calculations not only predict the superfluid Mott phase boundary accurately but have also been used to obtain dispersion of single-particle and single-hole excitations in the Mott insulator. Though these calculations are limited to Mott phase they have been extended to superfluid phase by Krishnendu et al by using projection operator technique [63]. The hopping terms is penalized in the large  $U$  regime by creating multiple occupancy at a site. They use

projection operator on each bond to systematically distinguish between the hopping process into low energy and the high energy sector. This is done in orders of  $t/U$ . The effective Hamiltonian so obtained till  $t^2/U$  is solved using mean field ansatz. Then there are other strong coupling [139] and variational approaches [62, 140, 141]. This method accurately predicts the zero temperature phase boundary as well as the zero temperature excitation in agreement with RPA calculation.

**Variational cluster theory:** In variational cluster approach [65–68] lattice is divided into clusters. The Green's function of the cluster is obtained exactly by exactly diagonalizing the Hamiltonian of the cluster using Lanczos method. The Green's function of the exact system is obtained by solving the equation which relates the Green's function of the exact system in terms of Green's function of clusters. At zero temperature this method provides accurate estimation of phase boundary and has been used to obtain single particle excitation spectrum in both superfluid and Mott phase at zero temperature. The low energy excitation spectrum has a finite but small gap even within the superfluid phase. Overall the results for excitation spectra matches qualitatively well with RPA.

**Field theoretic approaches:** The excitation spectrum in the vicinity of the quantum critical point has been studied using the relativistic O(N) model in two spatial dimensions [40, 142, 143]. The excitation spectrum consists of of N -1 gapless Goldstone modes which behave like free particles at long wavelengths and a amplitude mode. Within mean field theory, amplitude mode is sharp and gapped. Beyond mean field, stability of Higgs mode is not guaranteed. In experiments scalar probe is used and perturbed Hamiltonian is proportional to the  $|\psi|^2$ . To the lowest order in perturbation theory self energy of amplitude mode was analysed which goes as  $\Sigma(\omega) = \omega^3$ . The low frequency superfluid susceptibility has a universal scaling form  $S(\omega, \Delta) \propto \Phi(\omega/\Delta)\Delta^{3-2/\nu}$  where  $\Phi$  is the universal scaling function and  $\Delta = (U - U_c)^\nu$  and  $\nu = 0.6717$ . Similar scaling form was also seen in the experiment.

### 2.2.1.2 Finite temperature methods

**Quantum Monte Carlo:** Quantum Monte Carlo are exact calculations which provide accurate estimation of phase boundaries and thermal scales. There are exact results in 3D

[144] and 2D [145]. Such simulations involve a stochastic evaluation of all connected and disconnected diagrams occurring in a high-temperature series expansion on a finite lattice, which is an expansion in the hopping or kinetic energy (over temperature) around the atomic limit [146, 147]. There has been QMC calculation in the presence of trap, and momentum distribution of bosons obtained from these calculations shows an excellent agreement with time of flight images obtained from experiments [28]. QMC has also been used to calculate dynamical quantities. There has not been much of the results involving single particle spectral function for dimensions greater than one [75], most of the effort has been in computation of two particle quantities [39, 47, 148] which are in agreement with those seen in experiments.

**Bosonic DMFT:** The BDMFT is generalization of mean field theory where mean field is allowed to fluctuate dynamically with no spatial fluctuations. The full many body problem is mapped on to an effective impurity problem coupled to a self-consistently determined bath. The effective impurity action is derived as an approximation to the kinetic energy functional of the lattice problem. The resulting impurity problem is solved using continuous time Monte Carlo algorithm based on a sampling of a perturbation expansion in the hybridization function and the condensate wave function. This has been used to study BHM model in 2D and 3D [71–73, 149].

In terms of the approximate method this is the only method which captures thermal scale in close agreement with QMC. The BDMFT approach has also been used to compute single particle spectral function [74] but accuracy of results are affected due to errors in analytical continuation from Matsubara frequency to real frequencies. The mean curve does agree with RPA results, but, weights and broadening could not be resolved. The issue is especially severe for small frequencies.

**Slave particle methods:** Within the path integral formalism BHM was rewritten in terms of slave bosons and was used to derive an effective action for the superfluid order parameter [69, 70]. In the slave boson formalism, for any occupation number a pair of bosonic creation and annihilation operators is introduced that create and annihilate the state with precisely that given integer number of particles. The quartic term in the original Bose-Hubbard Hamiltonian is replaced by quadratic term in the slave boson creation and annihilation operators, the hopping



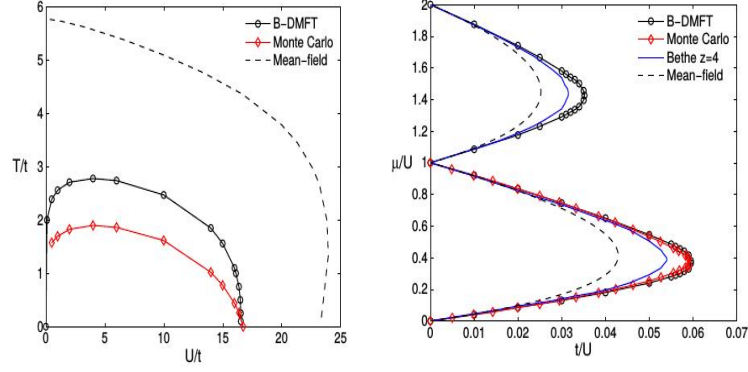


Figure 2.1: Left panel: Comparison of phase diagram of the square lattice Bose-Hubbard model in the space of interaction and temperature for  $n = 1$  using various approaches. Right panel: ground- state phase diagram in the space of  $t/U$  and  $\mu/U$ , showing the first two Mott lobes surrounded by superfluid under various approaches.

term becoming more complicated. The hopping term was decoupled using Hubbard Stratonovich transformation to write it in terms of auxiliary field (superfluid order). The slave bosons were integrated out to get an effective action of auxiliary field. This action was used to obtain phase boundaries at zero and finite temperature and excitation spectrum within the superfluid and Mott phase. Though the thermal scales obtained from this method are quantitatively off when compared to QMC, the excitation spectrum within superfluid phase is linear but in Mott phase they saw an increase in gap with rise in temperature.

### 2.2.2 Unresolved issues

While QMC provides high accuracy numerical results for the thermodynamic features, one would want methods that (i) shed light on the key physical effects, and (ii) allow access to dynamical properties. Mean field theory [19, 23], although quantitatively not very accurate, highlights the crucial effect of particle number fluctuation in the superfluid ground state. More sophisticated methods, *e.g.*, strong coupling expansion [60, 61], variational calculations [62], the projection operator technique [63], cluster Gutzwiller [64] and variational cluster schemes [65–68] improve on the mean field ground state and yield results that agree well with QMC for the zero temperature transition.

There is less insight into the finite temperature situation. Mean field theory has a finite temperature generalisation but leads to a large overestimate of  $T_c$  scales. Slave particle methods

[69, 70], dynamical mean field theory [71–73] have been used to study thermal physics. Fig. 2.1 shows the results for superfluid to normal transition for  $n = 1$  filling and ground state phase diagram in the  $t/U$  and  $\mu/U$  plane using various approaches. Among the methods above only the results of BDMFT compare reasonably with QMC in terms of thermal properties. In terms of computing dynamical quantities at finite temperature both BDMFT and QMC result becomes unreliable at very low frequency when the spectral weight is relatively small due to large errors in analytical continuation from Matsubara to real frequencies.

In cold atomic experiments there is an overall harmonic trap and recent advances in cold atomic experiments not only provide access to single site imaging but also provide information on dynamical quantities. So this calls for a real space method which not only captures thermal scales correctly but also provides information on dynamical quantities.

In this Chapter we present an alternate method, with emphasis on *spatial fluctuations*, which we believe are important in lower dimensions, and include temporal (quantum) fluctuations only approximately. Though in experiments there is an overall trap we have not done calculation in presence of trap. Our methods are general enough to include the effects of trap under LDA approximation.

### 2.2.3 Path integral formulation

We explore a new method in the context of the 2D Bose Hubbard model at unity filling:

$$H = -t \sum_{\langle ij \rangle} a_i^\dagger a_j - \mu \sum_i n_i + \frac{U}{2} \sum_i n_i(n_i - 1) \quad (2.1)$$

where  $a$  and  $a^\dagger$  are the usual second quantised bosonic operators,  $t$  is the nearest neighbour hopping amplitude,  $U$  is the onsite repulsion, and the boson density is fixed at  $n = 1$  by using a chemical potential  $\mu$ .

In order to arrive at our approximations we follow a standard path integral approach [134, 139, 150]. Within the path integral formalism the full partition function is given by

$$Z = \int \mathcal{D}b \mathcal{D}\bar{b} e^{-(S_0 + S_K)}$$

$$\begin{aligned}
S_0 &= \int_0^\beta d\tau [\sum_i \bar{b}_i (\partial_\tau - \mu) b_i + \frac{U}{2} \sum_i \bar{b}_i b_i (\bar{b}_i b_i - 1)] \\
S_K &= \int_0^\beta d\tau (-t) \sum_{\langle ij \rangle} (\bar{b}_i b_j + h.c.)
\end{aligned} \tag{2.2}$$

Here  $b$  and  $\bar{b}$  are c-number equivalent of bosonic operators  $a$  and  $a^\dagger$  respectively. The  $b_i(\tau) = \beta^{-1} \sum_n b_{i,n} e^{i\omega_n \tau}$  are space and imaginary time dependent classical fields.  $\omega_n$  are bosonic Matsubara frequencies.  $S_0$  involves the local terms and  $S_K$  the kinetic energy.

We separate the kinetic term as follows:  $S_K = S_K^a + S_K^b$ ,

$$\begin{aligned}
S_K^a &= - \sum_{\vec{k}} A_{\vec{k}} \bar{b}_{\vec{k},0} b_{\vec{k},0} \\
S_K^b &= - \sum_{\vec{k}} B_{\vec{k}} \bar{b}_{\vec{k},0} b_{\vec{k},0} - \sum_{n \neq 0, \vec{k}} t_{\vec{k}} \bar{b}_{\vec{k},n} b_{\vec{k},n}
\end{aligned} \tag{2.3}$$

where  $A_{\vec{k}} = \theta(t_{\vec{k}}) t_{\vec{k}}$  and  $B_{\vec{k}} = \theta(-t_{\vec{k}}) t_{\vec{k}}$  and  $t_{\vec{k}} = 2t(\cos k_x a + \cos k_y a)$ . Note that  $S_K^a$  involves only zero frequency modes of  $b_{\vec{k}}$ , and only  $\vec{k}$  for which the tight binding energy,  $-t_{\vec{k}}$ , is negative.  $S_K^b$  involves the rest of the contributions.

We use a Hubbard-Stratonovich transformation to decouple only  $S_K^a$ , keeping  $S_K^b$  untouched.

$$e^{-S_K^a} = \int \mathcal{D}\psi \mathcal{D}\psi^* e^{-\sum_{\vec{k}} \psi_{\vec{k}}^* \psi_{\vec{k}} + \sum_{\vec{k}} \sqrt{A_{\vec{k}}} (\psi_{\vec{k}} \bar{b}_{\vec{k},0} + h.c.)} \tag{2.4}$$

The focus on  $S_K^a$  to start with is (i) to use a ‘classical’ ( $\tau$  independent) auxiliary field, and (ii) retain positive weight in a sampling process, as we will explain soon. Collecting the terms and Fourier transforming to real space and imaginary time:

$$\begin{aligned}
Z &= \int \mathcal{D}\psi \mathcal{D}\psi^* \mathcal{D}b \mathcal{D}\bar{b} e^{-(S+S_K^b)} \\
S &= S_0[b, \bar{b}] - \sum_{ij} (C_{ij} \bar{b}_i \psi_j + hc) + \sum_i \psi_i^* \psi_i \\
C_{ij} &= \frac{1}{N} \sum_{\vec{k}} \sqrt{A_{\vec{k}}} e^{i\vec{k}(\vec{r}_i - \vec{r}_j)}
\end{aligned} \tag{2.5}$$

This is an exact representation of Bose Hubbard model. The fourfold symmetric real function  $C_{ij}$  is shown in Fig. 2.2, with respect to the reference site  $i$  taken at the origin.

We examine two approximations: (i) Drop  $S_K^b$  completely and solve for the physics arising

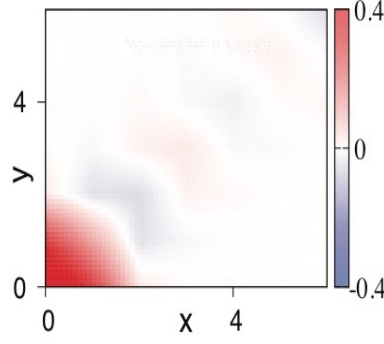


Figure 2.2: The coupling  $C_{ij}$  between the boson field  $b_i$  and the auxiliary field  $\psi_j$ . The reference site  $i$  is taken to be the origin  $(0, 0)$ . The plot highlights the rapid decay of  $C_{ij}$  with separation  $R_{ij}$ , justifying a ‘cluster treatment’ (see text) of the energy cost.

from  $S$  - this is the SPA for the partition function and treats the hybridising field as classical.

(ii) Treat the effect of dynamical fluctuations contained in  $S_K^b$  to quadratic order, this is the PSPA.

#### 2.2.4 Static path approximation (SPA)

We examine the SPA in detail. Within the SPA

$$\begin{aligned} Z &= \int \mathcal{D}\psi \mathcal{D}\psi^* \mathcal{D}b \mathcal{D}\bar{b} e^{-S} \\ &= \int \mathcal{D}\psi \mathcal{D}\psi^* e^{-\beta F\{\psi\}} \end{aligned} \quad (2.6)$$

In the expression above

$$\begin{aligned} F &= \sum_i F_i = -\frac{1}{\beta} \sum_i \log(\text{Tr}[\exp(-\beta H'_i)]) \\ H'_i &= (a_i^\dagger \Phi_i + h.c) + \frac{U}{2} n_i(n_i - 1) - \mu n_i + \psi_i^* \psi_i \\ \Phi_i &= \sum_j C_{ij} \psi_j \end{aligned} \quad (2.7)$$

In what follows we will call  $\psi_i$  the *auxiliary field*, which is what we actually update, and  $\Phi_i$  the *hybridisation field*.

The task at any temperature is to sample over configurations of  $\{\psi_i\}$ . Suppose one has a configuration  $\{\psi_i^0\}$ . The algorithm goes as follows: (i) At some site  $R_n$  one attempts an update  $\psi_n^0 \rightarrow \psi_n'$ . (ii) This modifies the hybridisation field  $\Phi_m^0$  in a neighbourhood of  $R_n$  decided by the ‘range function’  $C_{nm}$ . (iii) Given the rapidly decaying nature of  $C_{nm}$  we consider the  $\Phi$  to change

at  $N_c \sim 6^2$  sites around  $R_n$ . (iii) At these sites we compute the difference of local free energy due to the  $\Phi$  change. An atomic basis of  $N_b = 10$  states is used for the local diagonalisation. Once the free energy cost is known a Metropolis argument is used to determine acceptance of the move.

We have checked that our results are stable against an increase of  $N_c$  and  $N_b$ , down to  $U = 2t$ . The cost of the ‘local update’ is  $\sim N_c N_b^3$  and that of a ‘system update’ is  $\propto N N_c N_b^3$ , where  $N$  is the system size. The cost is *linear* in  $N$  and *no system wide diagonalisation is needed*.

After equilibration, we store  $\psi$  configurations to calculate thermodynamic averages. We adjust  $\mu$  to remain at unity filling at each temperature. At  $T = 0$  where every site sees the same hybridisation SPA reduces to mean field theory. At finite temperature both the amplitude and the phase of the  $\psi_i$  (and so the  $\Phi_i$ ) fluctuate.

### 2.2.5 Perturbed SPA

To improve the SPA one needs to build back the neglected quantum fluctuations. To derive the corrected form of free energy, we retain the  $S$  part exactly and include corrections due to  $S_K^b$  perturbatively by summing diagrams with ‘self avoiding’ paths to all order and then replacing the series sum by an exponentiated term.

#### 2.2.5.1 Derivation of PSPA

The BHM in path integral representation can be written as (see equation 2.5)

$$Z = \int \mathcal{D}\psi \mathcal{D}\psi^* \mathcal{D}b \mathcal{D}\bar{b} e^{-(S+S_K^b)} \quad (2.8)$$

Within PSPA we solve for  $S$  exactly and take into account perturbative correction due to  $S_K^b$  perturbatively.  $S_K^b$  part takes into account kinetic energy corrections due to bosons out of the condensate. Expanding in powers of  $S_K^b$

$$Z \approx \int \mathcal{D}\psi \mathcal{D}\psi^* \mathcal{D}b \mathcal{D}\bar{b} e^{-S} (1 - S_K^b + \frac{1}{2!} S_K^b{}^2 + \dots) \quad (2.9)$$

For a given  $\psi$  background, from equation 2.6 one knows that

$$\int \mathcal{D}b\mathcal{D}\bar{b} e^{-S} = \text{Tr}[e^{(-\beta H')}] \quad (2.10)$$

$$\frac{\int \mathcal{D}b\mathcal{D}\bar{b} e^{-S} S_K^b}{\text{Tr}[e^{(-\beta H')}] } = \beta X \quad (2.11)$$

$X$  includes effects of zero frequency part of positive band. One substitutes for  $S_K^b$  in terms bosonic fields in the above expression. Then one Fourier transform from imaginary frequency to imaginary time. Now if one relates, correlator in path integral formalism to that of operator formalism, one gets the expression for  $X$  in terms of energy eigenvalues and eigenvectors of  $H'$  Hamiltonian.

$$\begin{aligned} X = & \frac{\sum_{i \neq j} (t_{ij} - B_{i,j}) \text{Tr}[e^{-\beta H'_i} a_i^\dagger] \text{Tr}[e^{-\beta H'_j} a_j]}{\text{Tr}[e^{-\beta H'_i}] \text{Tr}[e^{-\beta H'_j}]} - \sum_i B_{ii} \left( \sum_{n_i} e^{-\beta E_n^i} |\langle n_i | a_i^\dagger | n_i \rangle|^2 \right. \\ & \left. - \frac{1}{\beta} \sum_{n_i \neq m_i} \langle n_i | a_i^\dagger | m_i \rangle \langle m_i | a_i | n_i \rangle \frac{e^{-\beta E_n^i} - e^{-\beta E_m^i}}{(E_m^i - E_n^i)} \right) \end{aligned} \quad (2.12)$$

Here  $i, j$  are site index and  $|n_i\rangle, |m_i\rangle$  represents eigenstates at site  $i$ .

Now to second order in  $S_K^b$  one gets,

$$\frac{\int \mathcal{D}b\mathcal{D}\bar{b} e^{-S} S_K^b{}^2}{2! \text{Tr}[e^{(-\beta H')}] } = \beta Y + \frac{(\beta X)^2}{2!} \quad (2.13)$$

Similarly while computing  $Y$ , one substitutes for  $S_K^b$  in terms of bosonic fields. Then one Fourier transform from frequency to imaginary time. Now one can relate correlation function in path integral representation to correlation function of second quantized operators with  $H'$  as unperturbed Hamiltonian. Since  $H'$  is local above term can be rewritten as convolution of site

local Green function.

$$Y = \sum_{i,j} t^2/2 (F1_{i,j;i,j+1} + F1_{i,j;i+1,j} + F2_{i,j;i+1,j} + F2_{i,j;i,j+1}) \quad (2.14)$$

Y include corrections due to kinetic energy of bosons out of the condensate till second order. Here  $(i, j)$  represent a site and  $(i \pm 1, j)$  or  $(i, j \pm 1)$  are it's nearest neighbours.  $F1$  takes into account correction due to anomalous terms and  $F2$  takes into account correction due to normal terms. The expressions for  $F1, F2$  in terms of energy eigenvalues and eigenvectors of  $H'$  Hamiltonian are given below.  $|u\rangle, |v\rangle$  are eigenvector of  $H'$  at site index  $(i, j)$  &  $|p\rangle, |q\rangle$  are eigenvector of  $H'$  at site index  $(k, m)$ .

$$\begin{aligned} F1_{i,j;k,m} &= \sum_{u \neq v; p \neq q} (\chi_{uvpq} + \bar{\chi}_{uvpq}) (A_{i,j;k,m}^{uvpq} + \frac{1}{4\beta} B_{i,j;k,m}'^{uvpq}) \\ \chi_{uvpq} &= \langle u | a_{i,j}^\dagger | v \rangle \langle v | a_{i,j}^\dagger | u \rangle \langle p | a_{k,m} | q \rangle \langle q | a_{k,m} | p \rangle \\ \bar{\chi}_{uvpq} &= \langle u | a_{i,j} | v \rangle \langle v | a_{i,j} | u \rangle \langle p | a_{k,m}^\dagger | q \rangle \langle q | a_{k,m}^\dagger | p \rangle \end{aligned} \quad (2.15)$$

The expression for  $F2$  given by

$$\begin{aligned} F2_{i,j;k,m} &= \sum_{u \neq v; p \neq q} (\chi'_{uvpq} + \bar{\chi}'_{uvpq}) (A_{i,j;k,m}^{uvpq} + \frac{1}{4\beta} B_{i,j;k,m}'^{uvpq}) \\ \chi'_{uvpq} &= \langle u | a_{i,j}^\dagger | v \rangle \langle v | a_{i,j} | u \rangle \langle p | a_{k,m} | q \rangle \langle q | a_{k,m}^\dagger | p \rangle \\ \bar{\chi}'_{uvpq} &= \langle u | a_{i,j} | v \rangle \langle v | a_{i,j}^\dagger | u \rangle \langle p | a_{k,m}^\dagger | q \rangle \langle q | a_{k,m} | p \rangle \end{aligned} \quad (2.16)$$

$$A_{i,j;k,m}^{uvpq} = \frac{e^{-\beta(\epsilon_q^{k,m} + \epsilon_v^{i,j})} - e^{-\beta(\epsilon_u^{i,j} + \epsilon_p^{k,m})}}{\epsilon_u^{i,j} + \epsilon_p^{k,m} - \epsilon_q^{k,m} - \epsilon_v^{i,j}} \text{ if } den \neq 0 \quad (2.17)$$

$$\text{else } A_{i,j;k,m}^{uvpq} = \beta e^{-\beta(\epsilon_q^{k,m} + \epsilon_v^{i,j})} \quad (2.18)$$

$$B_{i,j;k,m}'^{uvpq} = \frac{e^{-\beta\epsilon_v^{i,j}} - e^{-\beta\epsilon_u^{i,j}}}{\epsilon_u^{i,j} - \epsilon_v^{i,j}} \frac{e^{-\beta\epsilon_q^{k,m}} - e^{-\beta\epsilon_p^{k,m}}}{\epsilon_q^{k,m} - \epsilon_p^{k,m}} \quad (2.19)$$

Now  $Z$  can be approximated by,

$$Z \approx \int \mathcal{D}\psi \mathcal{D}\psi^* e^{-\beta F} (1 - \beta X + \beta Y - (\beta X)^2/2! + \dots) \quad (2.20)$$

In the above series we ignore higher order diagrams which includes more than two bosonic operator at a same site  $i$ .

$$\begin{aligned} Z &\approx \int \mathcal{D}\psi \mathcal{D}\psi^* e^{-\beta(F+X-Y)} \\ F &= -\frac{1}{\beta} \log(\text{Tr}[e^{(-\beta H')}] ) \end{aligned} \quad (2.21)$$

Here  $F$  is the contribution due to  $S$  part of the action.

$X$  depends upon a coupling  $B_{ij}$  which falls off quickly with distance so we use  $B_{ij}$  generated for a  $4 \times 4$  lattice.  $X$  can be written as the sum of contribution coming from onsite, nearest neighbour bonds, and next nearest neighbour bonds for every site whereas  $Y$  is sum of contribution from only nearest neighbour bonds. The change in the free energy, relevant for the update, is computed on a  $6 \times 6$  cluster centered on the update site. While calculating  $Y$  we sum over only the lowest four eigenstates. The rest follows as in SPA.

### 2.2.6 Static measurables

We track the following indicators to quantify the hybridisation field and bosonic properties.  $N$  is system size.

1. The structure factor:

$$S(\mathbf{q}) = \frac{1}{N^2} \sum_{ij} \langle \Phi_i \Phi_j^* \rangle e^{i\mathbf{q} \cdot (\vec{r}_i - \vec{r}_j)}$$

The  $T_c$  is extracted from the  $T$  dependence of the  $S(0, 0)$ . Angular brackets denote thermal average.



2. The spatial correlation in a single Monte Carlo snapshot:

$$C_i = \sum_{\delta} |\Phi_i| |\Phi_{i+\delta}| \cos(\theta_i - \theta_{i+\delta})$$

where  $\delta$  are the nearest neighbours of  $i$ .

3. The correlation length  $\xi(U, T)$  obtained from a fit to  $S(\mathbf{q})$ :

$$\xi(T, U) = \frac{1}{2 \sin(\pi/L)} \sqrt{\frac{S(0, 0)}{S(2\pi/L, 0)} - 1}$$

4. The distribution, and moments, of the hybridisation field:

$$P(|\Phi|) = \frac{1}{N} \sum_i \langle \delta(|\Phi| - |\Phi_i|) \rangle$$

Note that  $P$  is normalised. The distribution allows us to calculate the moments  $\langle y^n \rangle = \int dy P(y) y^n$  where  $y = |\Phi|$ .  $n = 1$  yields the mean,  $\Phi_{av}$ . We compute the standard deviation, or ‘width’ of the  $|\Phi|$  as  $\Phi_{wid} = \sqrt{\langle |\Phi|^2 \rangle - \langle |\Phi| \rangle^2}$ .

5. The momentum distribution of bosons ,

$$n(\mathbf{k}) = \frac{1}{N} \left\langle \sum_{i,j} e^{-i\mathbf{k} \cdot (\vec{r}_i - \vec{r}_j)} \text{Tr}[e^{-\beta H'} a_i^\dagger a_j] \right\rangle$$

6. The internal energy  $\mathcal{E}(T)$ . The expression for this is complicated and is shown in the Appendix A.

### 2.2.7 Estimation of $T_c$

2D models with XY symmetry do not admit finite  $T$  long range order, but only quasi long range order with algebraic decay of correlations. The change from algebraic to exponential decay of correlations with increasing  $T$  marks the BKT transition. For the 2D classical XY model,

$$H = -J \sum_{\langle ij \rangle} \vec{S}_i \cdot \vec{S}_j$$

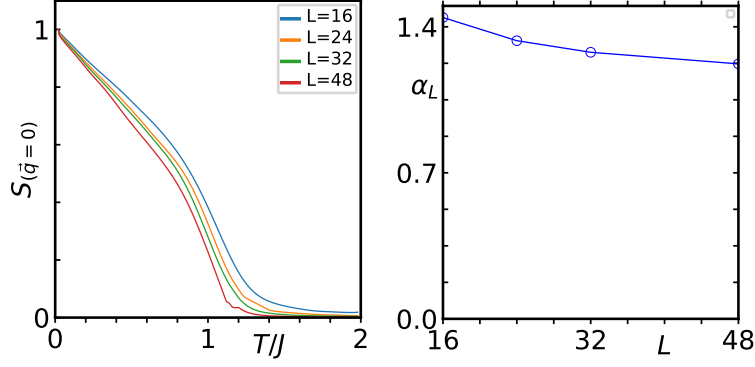


Figure 2.3: Left Panel: Plot of the  $\mathbf{q} = 0$  structure factor at various lattice sizes as a function of temperature. Right panel: plot of  $\alpha_L$  as a function of system size defined below.

where  $J$  is the coupling strength and  $\vec{S}_i$  are planar vectors of unit magnitude, the  $T_c^{XY}$  is known to be  $\approx 0.9J$ .  $k_B$  is set to 1.

In Fig. 2.3, we plot the static structure factor for the XY model at various lattice sizes, given by

$$S(\mathbf{q} = 0) = \frac{1}{N^2} \sum_{ij} \vec{S}_i \cdot \vec{S}_j$$

where  $N = L^2$ . Due to the algebraic decay of correlations in the low  $T$  phase this quantity vanishes at any finite  $T$  when the linear dimension  $L \rightarrow \infty$ . To that extent any estimate of  $T_c$  obtained by using  $S(\mathbf{q} = 0)$  is bound to be size dependent. Ideally one should compute the superfluid stiffness and locate  $T_c$  from there.

However we are interested more in the  $U$  dependence of  $T_c$  so we use a calibration of the large but finite  $L$  result on  $S(\mathbf{q} = 0)$  with respect to the ideal XY model  $T_c$ . This allows us to obtain a scale factor which we use for the Bose Hubbard model.

Specifically, we plot  $S(\mathbf{q} = 0, T)$  for various  $L$  and locate a nominal “ $T_c$ ” for each  $L$  from the extrapolated temperature at which  $S(\mathbf{q} = 0, T)$  hits zero when increasing  $T$  from low temperature.  $T_c(L)/T_c^{XY}$  gives us a scale factor  $\alpha_L$  that can be used to estimate the thermodynamic  $T_c$  from a finite size calculation. Note that in the XY model the factor  $\alpha_L$  is weakly size dependent over a large range of intermediate sizes.

The strategy above is feasible because (i) the exact XY model  $T_c$  is known, unlike for many other models, and (ii) the weak size dependence of  $\alpha_L$  allows a quick estimate of  $T_c$  from a single large  $L$  without having to do multiple sizes. For the Bose-Hubbard model we use the same scale

factor on the appropriate  $S(\mathbf{q} = 0)$  data to locate an approximate  $T_c$ .

### 2.2.8 Excitation spectra

Once the equilibrium distribution for the auxiliary field is obtained, via a Monte Carlo strategy, we can compute the boson Green's function through a real space implementation of the random phase approximation(RPA) [49]. The RPA, although not exact, interpolates between the non interacting and strong coupling limits and has been shown to yield qualitatively correct results in the ground state. We briefly outline the derivation of the RPA Green function starting from the exact Green function. The bosonic Green functions of BHM are given by

$$\begin{bmatrix} G_{11} & G_{12} \\ G_{21} & G_{22} \end{bmatrix}_{ij,n} = -\frac{1}{Z} \text{Tr} \left\{ e^{-\beta H} \begin{bmatrix} a_{i,n} a_{j,n}^\dagger & a_{i,n}^\dagger a_{j,-n}^\dagger \\ a_{i,n} a_{j,-n} & a_{i,-n} a_{j,-n}^\dagger \end{bmatrix} \right\}$$

Here  $i, j$  denotes the space labels and  $n$  represents the matsubara frequency index. One can express above correlation function in path integral formalism.

$$G_{ij,n} = -\frac{1}{Z} \int \mathcal{D}\psi \mathcal{D}\psi^* \mathcal{D}b \mathcal{D}\bar{b} e^{-(S+S_K^b)} \mathcal{G}_{ij,n}(b, \bar{b}) \quad (2.22)$$

where

$$\mathcal{G}_{ij,n}(b, \bar{b}) = \begin{bmatrix} b_{i,n} \bar{b}_{j,n} & \bar{b}_{i,n} \bar{b}_{j,-n} \\ b_{i,n} b_{j,-n} & b_{i,-n} \bar{b}_{j,-n} \end{bmatrix}$$

We solve for  $S$  exactly as previously and take into account correction in computation of Green function perturbatively due to  $S_K^b$ . The Green function evaluated using  $S$  are site local in nature. The perturbative correction due to  $S_K^b$  are leads to correction in Green function due to delocalization of bosons from site  $i$  to site  $j$ .

$$G_{ij,n} = -\frac{1}{Z} \int \mathcal{D}\psi \mathcal{D}\psi^* \mathcal{D}b \mathcal{D}\bar{b} e^{-(S)} \mathcal{G}_{ij,n}(b, \bar{b}) (1 - S_K^b + \frac{1}{2!} S_K^b{}^2 + \dots) \quad (2.23)$$

Here  $G_0$  is the Green function of  $H'$  Hamiltonian. Due to presence of non-zero hybridisation it has both normal and anomalous terms. It is site local in nature shown by  $\delta_{ij}$ .

$$-G_{0ij,n} = \int \mathcal{D}b \mathcal{D}\bar{b} e^{-(S)} \mathcal{G}_{ij,n}(b, \bar{b}) = Tr \left\{ e^{-\beta H'} \begin{bmatrix} a_{i,n} a_{j,n}^\dagger & a_{i,n}^\dagger a_{j,-n}^\dagger \\ a_{i,n} a_{j,-n} & a_{i,-n} a_{j,-n}^\dagger \end{bmatrix} \right\} \delta_{ij} \quad (2.24)$$

To first order in  $S_K^b$  one gets,

$$\int \mathcal{D}b \mathcal{D}\bar{b} e^{-(S)} \mathcal{G}_{ij,n}(b, \bar{b}) S_K^b = (G_0 * T * G_0)_{ij,n} \quad (2.25)$$

Here  $*$  represents product in the real space and  $G_0$  are the atomic Green function in SPA background.  $T$  is the hopping matrix. Similarly to second order in  $S_K^b$  one gets,

$$\int \mathcal{D}b \mathcal{D}\bar{b} e^{-(S)} \mathcal{G}_{ij,n}(b, \bar{b}) \frac{1}{2!} S_K^b{}^2 \approx (G_0 * T * G_0 * T * G_0)_{ij,n} \quad (2.26)$$

We ignore higher order terms in the above expression where more than two bosonic operators sit at the same site  $i$ .

$$G_{ij,n} \approx \frac{1}{Z_{SPA}} \int \mathcal{D}\psi \mathcal{D}\psi^* \left[ G_{0ij,n} - (G_0 * T * G_0)_{ij,n} - (G_0 * T * G_0 * T * G_0)_{ij,n} + \dots \right] \quad (2.27)$$

The partition function  $Z$  is approximated by the SPA partition function. Above series is known as ‘self-avoiding walk’, where one does not visit the same site twice. Here one does not have to evaluate Green function of higher order. Summing the above series one gets,

$$\langle G_{i\alpha;j\beta}^{RPA} \rangle = \int \mathcal{D}\psi \mathcal{D}\psi^* G_{i\alpha;j\beta}^{RPA} / \left( \int \mathcal{D}\psi \mathcal{D}\psi^* Tr[e^{-\beta H_{eff}}] \right) \quad (2.28)$$

$$\text{where } \hat{G}^{RPA} = \frac{\hat{G}_0}{(1 + T\hat{G}_0)} \text{ with } T_{i\alpha;j\beta} = t\delta_{i-j,n}\delta_{\alpha,\beta}$$

We compute the Green’s function via the ‘self avoiding walk’ method. On the mean field state it leads to the same answers as standard RPA but we are not aware of any answers in the finite temperature problem. The results are discussed in Chapter 4. We analytically continue

$G^{RPA}(i\omega_n \rightarrow \omega + i\eta)$  to obtain the retarded Green function. The RPA Green function is averaged over thermal configurations of the  $\psi$  field. The single particle spectral function is given by

$$A(\mathbf{k}, \omega) = -\frac{1}{\pi L^2} \sum_{i,j} e^{-i\vec{k} \cdot (\vec{r}_i - \vec{r}_j)} < Im(G_{i1;j1}^{RPA}) >$$

$$N(\omega) = \frac{1}{N} \sum_{\mathbf{k}} A(\mathbf{k}, \omega)$$

We solve the SPA Hamiltonian for each background configuration. Then we construct atomic Green's function matrix  $\hat{G}_0$  is a block diagonal matrix of size  $2L^2 \times 2L^2$ , where  $L^2$  is the system size. It includes the 'normal' and 'anomalous' atomic Green's function at each site.

$T$  is the hopping matrix of size  $2L^2 \times 2L^2$ . To compute the RPA Green's function for each background we add the hopping matrix to the inverted atomic Green's function for each value of  $\omega + i\eta$  where  $\eta$  is a very small number. We use the imaginary part of the RPA Green function to compute  $A(\vec{k}, \omega)$  and  $N(\omega)$ . We repeat the above procedure for each thermal configuration and take the thermal average. All our results are for system size  $L^2 = 24 \times 24$ .

Given the observed 'four peak' structure of the spectral function (with higher bands having negligible weight) we tried a four Lorentzian fit to the spectral data. These involve twelve parameters, 4 residues, 4 'center frequencies' and 4 broadenings, with the sum of the 4 residues being  $\sim 1$  acting as a sum rule check. This is a scheme that we applied at all  $T$  in the  $U < U_c$  window, while for  $U > U_c$  a two Lorentzian fit is more appropriate. Specifically, we tried:

$$A(\mathbf{k}, \omega) = \frac{1}{\pi} \sum_n r_{n,\mathbf{k}} \frac{\Gamma_{n,\mathbf{k}}}{(\omega - \Omega_{n,\mathbf{k}})^2 + \Gamma_{n,\mathbf{k}}^2}$$

Much of the analysis in Chapter 4 is based on the estimated parameter set  $\{\Omega_{n,\mathbf{k}}, r_{n,\mathbf{k}}, \Gamma_{n,\mathbf{k}}\}$  for varying  $U$  and  $T$ .

## 2.3 Spin-orbit coupled bosons

### 2.3.1 Theory approaches

The microscopic Hamiltonian that describes motion of atoms in presence of spin orbit coupling and optical lattice is

$$H = \sum_{\sigma_1, \sigma_2} \int d\vec{r} \psi_{\sigma_1}^\dagger(\vec{r}) h_{\sigma_1, \sigma_2} \psi_{\sigma_2}(\vec{r}) + \int d\vec{r} d\vec{r}' \psi_{\sigma_1}^\dagger(\vec{r}) \psi_{\sigma_1}(\vec{r}) V_{\sigma_1, \sigma_2}(\vec{r}, \vec{r}') \psi_{\sigma_2}^\dagger(\vec{r}') \psi_{\sigma_2}(\vec{r}') \quad (2.29)$$

where

$$h_{\sigma_1, \sigma_2} = -\frac{1}{2m} \nabla^2 - i\lambda(\sigma_x \partial_y - \sigma_y \partial_x) + V_0(\cos^2(k_0 x) + \cos^2(k_0 y)) \quad (2.30)$$

Let us ignore the interaction term and simplify the term contributing to the free particle Hamiltonian. The free particle term can be fitted to tight binding model by doing detailed numerics [151, 152]. The free particle term can be well simplified by rewriting this terms of well localized wannier states using an approach followed in reference [20]. In presence of deep optical lattice atoms usually experience harmonic confinement  $V_0 \propto (x - x_i)^2 + (y - y_i)^2$ . For sufficiently deep optical lattice low energy wannier states can be approximated at each site by ground state wavefunction of a spin orbit coupled particle in a single harmonic well. In the present approximation, eigenfunctions for the lowest energy level can be written in terms of polar co-ordinates [153–155]

$$\phi_{+1} \approx e^{-\frac{1}{2}(\frac{r}{l})^2} \begin{pmatrix} J_0(\gamma r/l) \\ J_1(\gamma r/l) e^{i\theta} \end{pmatrix}; \quad \phi_{-1} = i\sigma_y \phi_1^*(\vec{r}) \quad (2.31)$$

where  $J_0$  and  $J_1$  are zeroth and first order bessel function,  $\gamma = m\lambda l$  is the dimensionless spin orbit coupling strength and  $l = \frac{1}{k_0} (\frac{2mV_0}{k_0^2})^{-1/4}$

The localized boson operators can be reexpressed in terms of these wavefunctions

$$b_{i\alpha}^\dagger = \int d\vec{r} \phi_{\alpha\sigma}(\vec{r} - \vec{R}_i) \psi_\sigma^\dagger(\vec{r}) \quad (2.32)$$

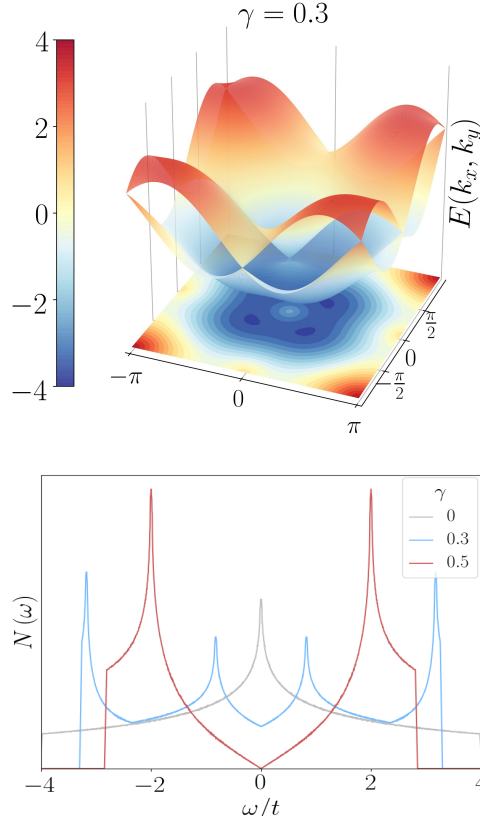


Figure 2.4: Top: The band structure for  $\gamma = 0.3$ . The dispersion has a four fold symmetry. The minima occur at finite wavevectors, as is evident from the projection of the lower band onto the x-y plane. Bottom: The noninteracting density of states for three different values of  $\gamma$ .  $\gamma = 0$  has the usual tight binding form in 2D, while for finite  $\gamma$  one observes a dip at zero along with a linearly rising behavior which is reminiscent of the Dirac cone present in the band structure at the  $\Gamma$  point. All energies are in units of  $t$ .

Because of the relative phase  $\theta$  between up and down spin components hopping amplitudes, which leads to spin flip, has spatial anisotropy.

Using above approximation motion of atoms in presence of spin-orbit coupling and optical lattice can be approximated by

$$H_{SOBHM} = H_{kin} + H_U \quad (2.33)$$

$$H_{kin} = \sum_{\langle ij \rangle; \alpha\beta} \mathcal{R}_{\alpha\beta}(i, j) b_{i\alpha}^\dagger b_{j\beta} + H.c. \quad (2.34)$$

$$H_U = \frac{U}{2} \sum_{i;\alpha} n_{i\alpha} (n_{i\alpha} - 1) + \lambda U \sum_i n_{i1} n_{i2} - \sum_{i;\alpha} (\mu + \Omega \sigma_z) n_{i\alpha} \quad (2.35)$$

Here  $\mathcal{R}(i, j) = -t \exp[i\mathbf{A} \cdot (\mathbf{i} - \mathbf{j})]/2$  is the real space hopping matrix,  $\mathbf{A} = (\gamma_x \sigma_y, \gamma_y \sigma_x, 0)$ .

For the rest of the discussion  $\Omega$  is set to be zero and  $\gamma_x = \gamma_y$ .

### 2.3.1.1 Non-interacting limit

In absence of interaction term above Hamiltonian reduces to

$$H_{SOBHM} = \sum_{\langle ij \rangle; \alpha\beta} \mathcal{R}_{\alpha\beta}(i, j) b_{i\alpha}^\dagger b_{j\beta} + H.c. \quad (2.36)$$

Above term can be diagonalized in the Fourier basis. In the Fourier basis the Hamiltonian can be reexpressed as

$$= \sum_k (b_{k1}^\dagger \ b_{k2}^\dagger) \begin{pmatrix} -2t \cos \gamma (\cos k_x + \cos k_y) & -2t \sin \gamma (-\sin k_x + i \sin k_y) \\ -2t \sin \gamma (-\sin k_x - i \sin k_y) & -2t \cos \gamma (\cos k_x + \cos k_y) \end{pmatrix} \begin{pmatrix} b_{k1} \\ b_{k2} \end{pmatrix} \quad (2.37)$$

Above term can be diagonalized by going to the chiral basis. The eigenvalues and eigenvectors are given by

$$E_{\mathbf{k}}^\pm = -2t [\cos \gamma (\cos k_x + \cos k_y) \mp (\sin \gamma \sqrt{\sin^2 k_x + \sin^2 k_y})] \quad (2.38)$$

$$\chi_{\mathbf{k}}^\pm = \frac{1}{\sqrt{2}} \begin{pmatrix} 1 \\ \pm e^{i\theta_{\mathbf{k}}} \end{pmatrix} \quad (2.39)$$

with  $\theta_{\mathbf{k}} = \tan^{-1}[\sin k_x / \sin k_y]$ .

Here  $+$ ( $-$ ) denotes the upper(lower) bands in Fig. 2.4. The band structure respects  $\pi/2$  rotational symmetry of the square lattice. Since the local interaction terms do not break this symmetry, this degeneracy should remain intact even in the many-body spectrum. For Rashba type spin-orbit coupling the band minima always lies on the diagonals of the two-dimensional (2D) Brillouin zone (BZ). The locations are at  $(\pm k_0, \pm k_0)$  where  $k_0$  is determined by the strength



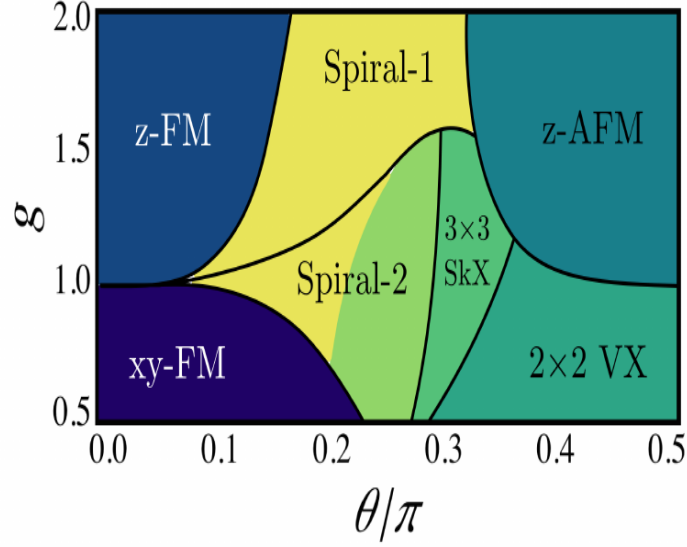


Figure 2.5: Classical magnetic phases for the classical spin model determined by Monte Carlo annealing on a  $36 \times 36$  site square lattice.[157]

of the SO coupling:  $k_0 = \tan^{-1}[\tan(\gamma)/\sqrt{2}]$ . The noninteracting density of states (DOS) has been shown in Fig.2.4. As the spin-orbit coupling strength  $\theta$  is varied from 0 to  $1/2$ , the DOS develops additional van Hove singularities at finite energies, while the singular peak at  $\omega = 0$  turns into a dip with a linear rise.

### 2.3.1.2 Mott-insulator regime

In the deep MI regime for  $U_{\sigma_1, \sigma_2} \gg t$  the physics of the system can be captured by an effective spin model obtained by second-order perturbation theory, which is given by [151, 156, 157]

$$H_{eff} = \sum_{\langle ij \rangle; a=x,y,z} J_{ij}^a S_i^a S_j^a + \vec{D}_{ij} \cdot (\vec{S}_i \times \vec{S}_j) \quad (2.40)$$

where  $S_i^a = b_i^\dagger \sigma^a b_i / 2$  with  $a=x,y,z$ . The first and second terms denote the Heisenberg and Dzyaloshinskii-Moriya type of coupling. The explicit forms of  $J_{\langle ij \rangle}^a$  and  $\vec{D}_{\langle ij \rangle}$  are given by  $J_x^x = J_y^y = -4t^2 \cos(2\gamma)/\lambda U$ ,  $J_x^y = J_y^x = -4t^2/\lambda U$ ,  $J_x^z = J_y^z = -4t^2(2\lambda - 1) \cos(2\gamma)/\lambda U$ ,  $\vec{D}_{\hat{x}} = -4t^2 \sin(2\gamma) \hat{y}/\lambda U$  and  $\vec{D}_{\hat{y}} = 4t^2 \sin(2\gamma) \hat{x}/\lambda U$

The two types of coupling favors different type of magnetic order. Heisenberg coupling

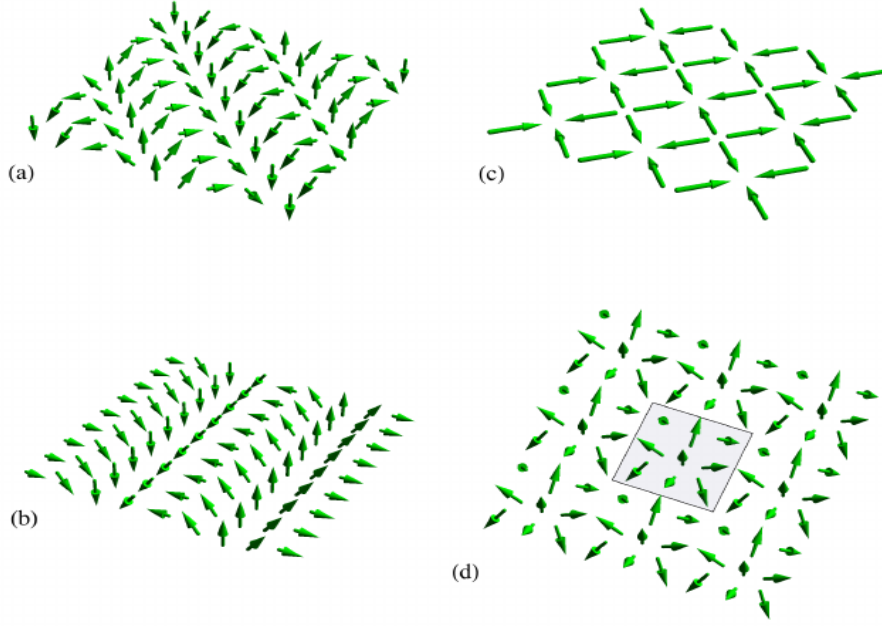


Figure 2.6: Classical magnetic states in the Mott insulating limit of the spin-orbit coupled Bose-Hubbard model. (a) Spiral-1 state; coplanar spin-orientation rotating along (11). (b) Spiral-2 state; coplanar spin-orientation rotating along (10). (c) Vortex crystal;  $2 \times 2$  unit cell with  $\pi/2$  rotation along each bond. (d) Skyrmion crystal; the  $3 \times 3$  unit cell is highlighted with a gray box. The central spin points in the positive  $z$  direction, while the remaining spins tumble outward toward  $-z$  direction.[157]

favors ferromagnetism and Dzyaloshinskii-Moriya type of coupling favors spiral orders. The competition between the two phases leads to exotic magnetic states.

Solving the above quantum mechanical model is a difficult problem. One can solve the above model by making a mean-field approximation by promoting quantum mechanical spin operators to classical spin.  $S_i \rightarrow \langle s_i | S_i | s_i \rangle$ . Under the above approximation quantum mechanical model reduces to the classical spin model. The classical Monte Carlo was used to determine the ground state phase diagram shown in 2.5. The general features of the classical phase diagram can therefore be largely understood by visualizing the various stable spin configurations, shown in 2.6.

### 2.3.1.3 Mean-field theory

The mean field approach of single species Bose Hubbard model was generalized to the case of SOBHM to locate the superfluid Mott phase boundary and to study impact of spin orbit cou-

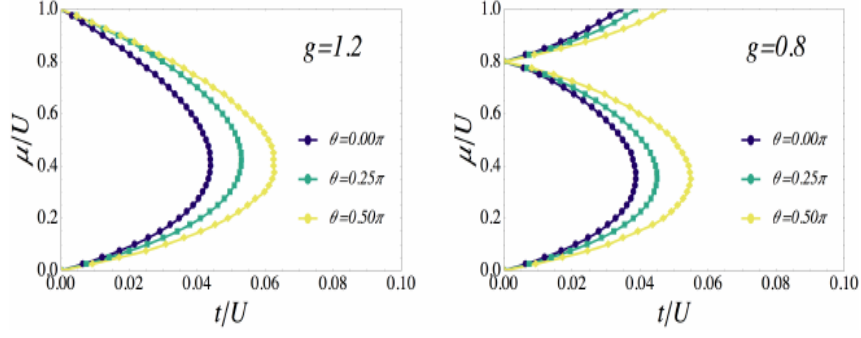


Figure 2.7: Mott lobes in the  $t/U, \mu/U$  plane for different values of spin orbit coupling and interspecies interaction strength. With increasing spin orbit coupling the Mott-superfluid phase boundary is shift to larger values of  $t/U$ . [157]

pling on phase boundary [157–159]. Under the mean field approximation creation(annihilation) operators are written in terms of expectation value plus fluctuations  $b_{i,\sigma} = \phi_{i,\sigma} + \delta b_{i,\sigma}$  where  $\phi_{i,\sigma} = \langle b_{i,\sigma} \rangle$ . The SOBHM under this approximation can be written as

$$H = H_{kin}^{MF} + H_U \quad (2.41)$$

$$H_{kin}^{MF} = \sum_{i,\alpha} \Gamma_{i,\alpha}^* b_{i,\alpha} + \Gamma_{i,\alpha} b_{i,\alpha}^\dagger - \Gamma_{i,\alpha} \phi_{i,\alpha}^* \quad (2.42)$$

$$\Gamma_{i,\alpha} = \sum_{\alpha,\beta} \mathcal{R}_{\alpha\beta}(i, i+j) \phi_{i+j,\beta} + \mathcal{R}_{\beta\alpha}^*(i-j, i) \phi_{i-j,\beta} \quad (2.43)$$

where  $j$  runs over nearest neighbour.

The above approximation has an advantage that a full Hamiltonian is now written as direct sum over lattice sites. Solving the above problem requires diagonalization for each single site where hilbert space is cut off by the maximum occupancy  $n_c$  for each species. It amounts to diagonalizing a matrix of size  $n_c^2 \times n_c^2$  and solving the  $\phi_{i,\sigma} = \langle b_{i,\sigma} \rangle$  equation self consistently.

Fig.2.7 shows the results for two values of interspecies interaction strength  $g = 0.8$  and  $g = 1.2$  and different values of spin-orbit coupling. The superfluid-Mott phase boundary is pushed to larger values of  $t/U$  with increase in spin orbit coupling strength. As the increase in spin-orbit coupling leads to reduction in bandwidth and therefore large hopping amplitude  $t$  is required at larger SOC parameter to stabilize the superfluid state.

Other approaches such as strong coupling expansion [99, 100] and real space bosonic dy-

namical mean field theory (BDMFT) [101] have also been used to study the above system. They have unearthed a rich ground state phase diagram for these systems. Some of the unconventional phases found include those with long range magnetic order in the Mott ground state [101] and the possibility of a boson condensate at finite momentum [99, 100]. Such studies have also been supplemented by their weak-coupling counterparts in the continuum where there is no Mott transition. The weakly interacting condensates have been studied using the Bogoliubov-Hartree-Fock approximation [102].

In spite of several studies on the ground state, only limited theoretical work exists on the thermal phases of spin-orbit coupled systems. For Abelian systems with equal mixture of Rashba and Dresselhaus coupling, Ref. [103] derives an effective  $t - J$  model for the bosons and studies the thermal phases of this effective model. The study reveals a stripe superfluid order at low temperature and a two step melting upon increasing temperature, leading first to a striped normal phase of the bosons and then to a homogeneous state. However similar study for the thermal phases of Bose-Einstein condensates (BECs) in the presence of Rashba spin-orbit coupling is lacking. In Chapter five we study the thermal phases of a two-species Bose-Hubbard model in the presence of a Rashba spin-orbit coupling. Our study thus involves bosons in the presence of an effective non-Abelian gauge field. We use the approach described for single species BHM and generalize it to the case of non-Abelian spin orbit coupling.

In this section, we shall present the model we use and also discuss the details of the method used for computation.

### 2.3.2 Lattice model

We begin by defining a Rashba spin-orbit coupled Bose-Hubbard Hamiltonian on a square lattice in 2D:

$$H = H_{kin} + H_U \quad (2.44)$$

$$H_{kin} = \sum_{\langle ij \rangle; \alpha\beta} \mathcal{R}_{\alpha\beta}(i, j) b_{i\alpha}^\dagger b_{j\beta} + H.c. \quad (2.45)$$

$$H_U = \frac{U}{2} \sum_{i; \alpha} n_{i\alpha} (n_{i\alpha} - 1) + \lambda U \sum_i n_{i1} n_{i2}$$

$$- \sum_{i;\alpha} (\mu + \Omega \sigma_z) n_{i\alpha}. \quad (2.46)$$

Here  $\mathcal{R}(i, j) = -t \exp[i\mathbf{A} \cdot (\mathbf{i} - \mathbf{j})]/2$  is the real space hopping matrix,  $\mathbf{A} = (\gamma \sigma_y, -\gamma \sigma_x, 0)$  is the synthetic gauge field.  $U$  is the on-site repulsion,  $\lambda$  denotes the ratio between inter-species and intra-species on-site repulsion, and  $\Omega$  is the Zeeman field which arises due to the coupling of the Raman laser to the bosonic atom [77]. This term depends on the strength of the atom-laser coupling and can be tuned to the extent that the spin-orbit physics does not get completely masked. In this work, following Refs.[157], we shall later set  $\Omega$  to zero in order to have a clean demonstration of the effects of spin-orbit coupling. In what follows, we also neglect another additional on-site term  $H \sim \delta \sigma_y/2$  which depends on the detuning parameter  $\delta$  of the Raman laser and can be made small by sufficient reduction of the detuning. For the rest of this work, we set the lattice spacing  $a_0 = 1$ .

The kinetic part  $H_{kin}$  can be mode separated and can be written as

$$H_{SOBHM} = \sum_{\langle ij \rangle; \alpha\beta} \mathcal{R}_{\alpha\beta}(i, j) b_{i\alpha}^\dagger b_{j\beta} + H.c. \quad (2.47)$$

Above term can be diagonalized in the Fourier basis. In the Fourier basis the Hamiltonian can be reexpressed as

$$= \sum_{\mathbf{k}} (b_{\mathbf{k}1}^\dagger \ b_{\mathbf{k}2}^\dagger) \begin{pmatrix} -2t \cos \gamma (\cos k_x + \cos k_y) & -2t \sin \gamma (-\sin k_x + i \sin k_y) \\ -2t \sin \gamma (-\sin k_x - i \sin k_y) & -2t \cos \gamma (\cos k_x + \cos k_y) \end{pmatrix} \begin{pmatrix} b_{\mathbf{k}1} \\ b_{\mathbf{k}2} \end{pmatrix} \quad (2.48)$$

Above term can be diagonalized by going to the chiral basis. The eigenvalues and eigenvectors are given by

$$E_{\mathbf{k}}^\pm = -2t [\cos \gamma (\cos k_x + \cos k_y) \mp (\sin \gamma \sqrt{\sin^2 k_x + \sin^2 k_y})] \quad (2.49)$$

$$\chi_{\mathbf{k}}^\pm = \frac{1}{\sqrt{2}} \begin{pmatrix} 1 \\ \pm e^{i\theta_{\mathbf{k}}} \end{pmatrix} \quad (2.50)$$

with  $\theta_{\mathbf{k}} = \tan^{-1}[\sin k_x / \sin k_y]$ .

In order to simulate the finite temperature physics of this model we follow the approach described for single species BHM. We start by writing the imaginary time coherent state path integral using the Hamiltonian above [2.44](#)

$$Z = \int \mathcal{D}[b^*, b] e^{-(S^{loc} + S^{hop})[b^*, b]} \quad (2.51)$$

$$\begin{aligned} S^{loc} = \int_0^\beta d\tau & \left[ \sum_{i;\alpha} b_{i\alpha}^* \partial_\tau b_{i\alpha} + \frac{U}{2} \sum_{i;\alpha} n_{i\alpha} (n_{i\alpha} - 1) \right. \\ & \left. + \lambda U \sum_i n_{i1} n_{i2} - \sum_{i;\alpha} (\mu + \Omega \sigma_z) n_{i\alpha} \right] \end{aligned} \quad (2.51a)$$

$$S^{hop} = \int_0^\beta d\tau \sum_{\mathbf{k}; \sigma \in \{\pm\}} \psi_{\mathbf{k}\sigma}^\dagger E_{\mathbf{k}}^\sigma \psi_{\mathbf{k}\sigma} \quad (2.51b)$$

$$\psi_{\mathbf{k}}^+ = e^{i\theta_{\mathbf{k}}} b_{\mathbf{k}1} + b_{\mathbf{k}2} \quad (2.51c)$$

$$\psi_{\mathbf{k}}^- = e^{-i\theta_{\mathbf{k}}} b_{\mathbf{k}1} - b_{\mathbf{k}2} \quad (2.51d)$$

Next, we wish to implement a Hubbard-Stratonovich decomposition of the hopping part of the action. To this end, we segregate the negative energy part of the bands ( $\tilde{E}_{\mathbf{k}}^\pm$ ), and introduce an auxiliary field decomposition of the negative-band action using two fields  $\{\phi_{i,n}^+\}$ ,  $\{\phi_{i,n}^-\}$  for each lattice point and Matsubara frequency,  $(i, n)$ . The effects of the positive energy part of the bands can be built back perturbatively, and should not affect the low-energy physics significantly. The resulting action is given by

$$\begin{aligned} S &= S^{loc} + \tilde{S}^{hop} \\ \tilde{S}^{hop} &= - \sum_{k, \sigma, n} \left( \sqrt{-\tilde{E}_{k\sigma}} \psi_{k\sigma n}^* \phi_{k\sigma n} + H.c. + |\phi_{k\sigma n}|^2 \right) \end{aligned} \quad (2.52)$$

Next, we note that an effective Hamiltonian can be derived from Eq. [2.52](#) if we retain only the zero Matsubara frequency mode of the auxiliary fields  $\{\phi_{i,0}^+\}$ ,  $\{\phi_{i,0}^-\}$ . For the single species problem this approximation reproduces the mean-field [\[23\]](#) ground state exactly, and captures thermal scales which agree well with full quantum Monte-Carlo as seen in Chapter 3. The

effects of the finite-frequency modes can be built back perturbatively as quantum corrections over the static background. This has been accomplished for the single species problem and such corrections are known to leave the qualitative nature of the thermal phase and phase transitions unchanged. For bosons coupled via spin-orbit coupling, this turns out to be more cumbersome and we defer computation of such corrections to future work.

The effective Hamiltonian obtained by retaining only  $\{\phi_{i,0}^+\}, \{\phi_{i,0}^-\}$  fields is given by

$$H^{\text{eff}} = H_{\text{kin}}^{\text{eff}} + H_U \quad (2.53)$$

$$H_U = \frac{U}{2} \sum_{i;\alpha} n_{i\alpha} (n_{i\alpha} - 1) + \lambda U \sum_i n_{i1} n_{i2} - \sum_{i;\alpha} (\mu + \Omega \sigma_z) n_{i\alpha} \quad (2.54)$$

$$H_{\text{kin}}^{\text{eff}} = \sum_i (\Gamma_i^\dagger \Psi_i + \Psi_i^\dagger \Gamma_i + |\Phi_i|^2), \text{ with} \quad (2.55)$$

$$\Gamma_i = \frac{1}{\sqrt{2}} \sum_j \mathcal{M}_{ji} \Phi_j \quad (2.56)$$

$$\mathcal{M}_{ji} = \sum_{\mathbf{k}} e^{i\mathbf{k} \cdot (\mathbf{j} - \mathbf{i})} \begin{pmatrix} \sqrt{-\tilde{E}_{\mathbf{k}}^+} & \sqrt{-\tilde{E}_{\mathbf{k}}^-} \\ \sqrt{-\tilde{E}_{\mathbf{k}}^+} e^{-i\theta_{\mathbf{k}}} & -\sqrt{-\tilde{E}_{\mathbf{k}}^-} e^{-i\theta_{\mathbf{k}}} \end{pmatrix}$$

where  $\Phi_i \equiv \begin{pmatrix} \phi_i^+ \\ \phi_i^- \end{pmatrix}$  is a local spinor composed of zero mode of the auxiliary fields  $\{\phi_0^+\} \equiv \{\phi^+\}$  and  $\{\phi_0^-\} \equiv \{\phi^-\}$ .  $\Psi_i \equiv \begin{pmatrix} b_i^1 \\ b_i^2 \end{pmatrix}$  is a local spinor involving the bosons of the two spin states.

$\mathcal{M}_{ji}$  are 2x2 matrices which couple the chiral auxiliary fields with the spinor bosonic fields, with coefficients picked up in the band truncation process. The information of the spin-orbit coupling enters the effective Hamiltonian through these coefficient matrices. Here  $H_U$  is the local interaction part as in the original Hamiltonian 2.46 and  $\Omega$  has been set to zero in the subsequent calculations. The details of the procedure leading to  $H_{\text{eff}}$  can be found in the Appendix C.

### 2.3.3 Computational method

The effective Hamiltonian obtained in the last section, can be treated using several approximation schemes. In this work, we are going to use two such schemes. The first of these, used to obtain zero temperature phases of the system, involves treating  $\{\Phi_i\}$  as variational parameters and subsequent minimization of the energy obtained from the effective Hamiltonian. In this scheme, the energy for a configuration of  $\Phi$ s is obtained by diagonalizing the boson Hamiltonian  $H_{eff}[\Phi_i]$ . This yields the optimal ground state configuration of  $\Phi_i$  fields. In this work, we restrict ourselves to four families of such variational wave functions given by

**1. Single mode:**

$$\Phi_i = \begin{pmatrix} \phi_{k_0}^+ \\ \phi_{k_0}^- \end{pmatrix} \exp(i\mathbf{k}_0 \cdot \mathbf{r}_i)$$

**2. Two mode:**

$$\Phi_i = \begin{pmatrix} \phi_{k_0}^+ \\ \phi_{k_0}^- \end{pmatrix} \cos(\mathbf{k}_0 \cdot \mathbf{r}_i)$$

**3. Four mode:**

$$\Phi_i = \begin{pmatrix} \phi_{k_0}^+ \\ \phi_{k_0}^- \end{pmatrix} \cos(k_0^x x_i) \cos(k_0^y y_i)$$

**4. Vortex:**

$$\Phi_i = \begin{pmatrix} \phi_{k_0}^+ \\ \phi_{k_0}^- \end{pmatrix} [\cos(k_0^x x_i + k_0^y y_i) + \cos(k_0^x y_i - k_0^y x_i)]$$

where  $\mathbf{r}_i = (x_i, y_i)$  are the coordinates of site  $i$ . We note that the local Hilbert space for the bosons needs to be restricted for the problem to be numerically tractable. This is done by choosing a cutoff,  $N_i$ , in the number of boson occupation per site. In what follows, we have ensured that the cut-off is chosen such that including more states beyond it does not have any effect on the energy of the system, up to a desired accuracy. The variational calculation gives us the mean field ground state of our effective model 2.53.



Having obtained the ground state configuration of the bosons, the second method we use yields information about its thermal behavior. To this end, we use a classical Monte-Carlo scheme by starting from the ground state configuration and successively increasing the temperature. The free energy for a configuration of  $\{\Phi_i\}$ s is again obtained by diagonalizing the boson Hamiltonian  $H_{eff}$  for every attempted update of the auxiliary fields. The equilibrium  $\{\Phi_i\}$  configurations are generated by implementing a Metropolis based update scheme. In this scheme, at any given site  $i$ , we have two complex scalar auxiliary fields,  $\phi_i^+$  and  $\phi_i^-$ . For each of the fields, the amplitude fluctuations are considered to be within twice their ground state amplitude. In contrast, arbitrary phase fluctuations of these fields are allowed. The local hybridization  $\Gamma_i$  depends on the  $\Phi_i$  configurations on all sites, as defined in equation 2.56. For a given  $\{\Phi_i\}$  configuration the bosonic Hamiltonian is written in Fock space after truncating the local Hilbert space within  $N_i$  particle states, as in the variational calculation. The resulting matrix is then diagonalized exactly to obtain the free energy for the configuration.

### 2.3.4 Measurables

To detect the presence of spatial order we compute the structure factor:

$$S_{\mathbf{q}} = \left\langle \frac{1}{zV} \sum_{i,j} Tr \left[ \Phi_i^\dagger \Phi_j \right] e^{i\mathbf{q} \cdot (\mathbf{i}-\mathbf{j})} \right\rangle \quad (2.57)$$

where  $V$  is the volume of the system,  $z$  is the coordination number and  $\Phi_i$ s are the auxiliary fields introduced in sec.2.3.2.

The local magnetic texture is defined by the vector,

$$\mathbf{m}_i = \left\langle \frac{1}{Z} \sum_{\mu,\nu} Tr \left[ e^{-\beta H_{eff}} b_{i\mu}^\dagger \boldsymbol{\sigma}_{\mu\nu} b_{i\nu} \right] \right\rangle \quad (2.58)$$

where  $Z$  is the partition function and the angular brackets denote thermal averaging.

The momentum distribution of the bosons given by:

$$n_{\mathbf{k}} = \frac{1}{N} \left\langle \frac{1}{ZV} \sum_{i,j,\mu} Tr \left[ e^{-\beta H_{eff}} b_{i\mu}^\dagger b_{j\mu} \right] e^{i\mathbf{k} \cdot (\mathbf{i}-\mathbf{j})} \right\rangle \quad (2.59)$$

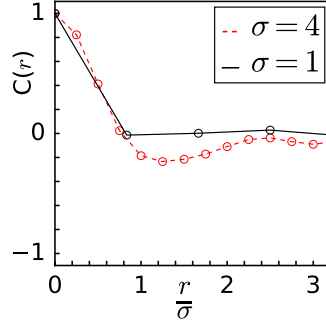


Figure 2.8: The speckle correlation function ( $\langle V(\vec{x})V(\vec{x} + \vec{r}) \rangle - \langle V(\vec{x}) \rangle^2 / \langle V(\vec{x})^2 \rangle$ ) for  $V = 1$ , plotted as a function of  $r/\sigma$ , by actually sampling our disorder configurations. The function should be universal, and die off for  $r/\sigma \gg 1$ , but sampling on a  $24 \times 24$  lattice leads to the non universal features at large  $\sigma$ .

where  $N$  is the total no. of bosons,  $Z$  is the partition function,  $V$  is system volume, and the angular brackets denote thermal averaging.

## 2.4 Disordered Fermi superfluids

### 2.4.1 Microscopic model

We study the attractive Hubbard model in two dimensions (2D), in the presence of a speckle potential,  $V_i$  in Chapter 6:

$$H = -t \sum_{\langle ij \rangle \sigma} c_{i\sigma}^\dagger c_{j\sigma} + \sum_{i\sigma} (V_i - \mu) n_{i\sigma} - |U| \sum_i n_{i\uparrow} n_{i\downarrow} \quad (2.60)$$

$t$  is the nearest neighbour hopping term,  $U$  is the onsite attraction,  $\mu$  the chemical potential. We set  $t = 1$  and fix the fermion density at  $n \approx 0.9$ . We set  $U = 4t$  where, for the 2D model at the density we use, the  $T_c$  has a peak as a function of  $U/t$ . This is the crossover between the weak coupling BCS regime and the strong coupling BEC window and the coherence length is small enough for our system size  $\sim 24 \times 24$ . In the discussion section we show a result on  $T_c(U)$ .

### 2.4.2 Speckle disorder

Speckle disorder is spatially correlated. We start by generating a spatially uncorrelated complex random field,  $v_i = v_{1,i} + iv_{2,i}$ , on the lattice. The  $v_a$  are picked from independent gaussian

distributions and  $\langle v_{a,i} \rangle = 0$  and  $\langle v_{a,i} v_{b,j} \rangle = \delta_{ab} \delta_{ij}$ , where  $a, b$  can take value 1 and 2. The speckle disorder variable is then defined as

$$\begin{aligned}
V_i &= V_0 \left| \sum_{\vec{k}} v(\vec{k}) W(\vec{k}) e^{i\vec{k} \cdot \vec{r}_i} \right|^2 \\
v(\vec{k}) &= \frac{1}{L} \sum_i v_i e^{-i\vec{k} \cdot \vec{R}_i} \\
W(\vec{k}) &= 1 \quad (k < 2\pi/\sigma) \\
&= 0 \quad (k > 2\pi/\sigma)
\end{aligned} \tag{2.61}$$

$V_0 > 0$  and the potential  $V_i$  is positive definite. It has a distribution  $P(V) = \frac{1}{V_0} e^{-V/V_0}$  and a correlation:

$$\langle V(\vec{x}) V(\vec{x} + \vec{r}) \rangle_{\vec{x}} = V^2 (1 + |\gamma(\vec{r})|^2) \tag{2.62}$$

where  $\gamma(\vec{r}) = J_1(|\vec{r}|/\sigma)/(|\vec{r}|/\sigma)$  with  $J_1$  the first order Bessel function and  $\sigma$  the speckle size (correlation length). Fig.2.8 shows the two point function generated on our finite lattice, for two  $\sigma$  values. At large  $\sigma$  the long distance behaviour of the correlation function deviates from the ideal form on our  $24 \times 24$  lattice.

### 2.4.3 Monte Carlo strategy

The Hubbard interaction cannot be treated exactly so we follow the approach used in [160]. We write the partition function for the model as an imaginary time path integral:

$$\begin{aligned}
Z &= \int D(\bar{\psi}, \psi) e^{-S[\bar{\psi}, \psi]} \\
S &= \int_0^\beta d\tau \left[ \sum_{i,\sigma} \bar{\psi}_{i,\sigma} \partial_\tau \psi_{i,\sigma} + H(\psi, \bar{\psi}) \right]
\end{aligned} \tag{2.63}$$

The  $\psi_i(\tau)$  are Grassmann fields. The quartic term in the action prevents exact evaluation of  $Z$ . To proceed it is usual to introduce auxiliary fields to ‘decouple’ the interaction. This Hubbard–Stratonovich transformation, in terms of (a) a complex scalar ‘pairing field’  $\Delta_i =$

$|\Delta_i|e^{i\theta_i}$ , and (b) a real scalar field  $\phi_i$ , is accomplished by writing:

$$\begin{aligned} \exp(U \int d\tau \bar{\psi}_{i\uparrow}(\tau) \psi_{i\uparrow}(\tau) \bar{\psi}_{i\downarrow}(\tau) \psi_{i\downarrow}(\tau)) \\ = \int d\Delta_i d\Delta_i^* d\phi_i e^{-S_{HS}} \\ S_{HS} = \int d\tau [\rho_i \phi_i + (\psi_{i\uparrow} \psi_{i\downarrow} \Delta_i + h.c.) + \frac{1}{U} (|\Delta_i(\tau)|^2 + \phi_i^2)] \end{aligned} \quad (2.64)$$

The action is now quadratic in the fermions. Quantum Monte Carlo (QMC) proceeds to sample the fields  $\Delta_i(\tau)$ ,  $\phi_i(\tau)$ , or their Matsubara components  $\Delta_i(i\Omega_n)$ ,  $\phi_i(i\Omega_n)$ . We employ a ‘static path approximation’ (SPA) wherein these fields are assumed to be ‘ $\tau$  independent’ (or, alternately, having only a  $\Omega_n = 0$  component), but fluctuating spatially. The SPA approach retains all the classical amplitude and phase fluctuations in the model and has been elaborately benchmarked in the BCS-BEC crossover problem. We show its match with QMC in the discussion section.

When the auxiliary fields are assumed to be static,  $Z$  becomes:

$$\begin{aligned} Z &= \int \mathcal{D}\Delta \mathcal{D}\Delta^* \mathcal{D}\phi \text{Tr}[e^{-\beta H_{eff}}] \\ H_{eff} &= H_0 + H_{coup} + \frac{1}{|U|} \sum_i (|\Delta_i|^2 + \phi_i^2) \\ H_0 &= -t \sum_{\langle ij \rangle} \sum_{\sigma} c_{i\sigma}^\dagger c_{j\sigma} + \sum_{i\sigma} (V_i - \mu) n_{i\sigma} \\ H_{coup} &= \sum_i (\Delta_i c_{i\uparrow}^\dagger c_{i\downarrow}^\dagger + h.c.) + \sum_i \phi_i n_i \end{aligned} \quad (2.65)$$

This is a model of quadratic fermions coupled to classical fields. The Boltzmann weight for the fields can be inferred from the top equation:  $e^{-\beta H(\Delta, \Delta^*, \phi)} \propto \text{Tr}[e^{-\beta H_{eff}}]$ . The strategy, like in QMC, would be to pick the auxiliary fields following their Boltzmann weight, solve the corresponding fermion problem, and average over configurations.

Consider the  $T = 0$  and the finite  $T$  cases separately. (i) As  $T \rightarrow 0$ , the system is pushed towards the maximum probability configuration, *i.e.*, the minimum of  $H(\Delta, \Delta^*, \phi)$ . The conditions,  $\partial H / \partial \Delta_i = 0$ ,  $\partial H / \partial \phi_i = 0$ , *etc.*, define the usual mean field HFBdG ground state. (ii) At  $T \neq 0$ , the fields fluctuate and we generate the equilibrium  $\{\Delta_i, \phi_i\}$  configurations by using a Metropolis algorithm. For each attempted update of the  $\Delta_i, \phi_i$  we diagonalise the fermionic problem on a  $8 \times 8$  cluster around the update site and compute the energy cost of the

move [161].

## 2.4.4 Measurables

We keep track of the following:

1. The  $\mathbf{q} = (0, 0)$  component of the pairing field structure factor,

$$S(\mathbf{q}) = \frac{1}{N^2} \sum_{ij} \langle \Delta_i^* \Delta_j \rangle e^{i\mathbf{q} \cdot (\vec{r}_i - \vec{r}_j)} \quad (2.66)$$

both to determine the presence of superfluidity and also to locate the  $T_c$  scale. Angular brackets indicate thermal average.

2. The overall density of states:

$$N(\omega) = \frac{1}{N} \sum_n \langle |u_n|^2 \delta(\omega - E_n) + |v_n|^2 \delta(\omega + E_n) \rangle \quad (2.67)$$

The  $u_n$  and  $v_n$  are components of the HFBdG eigenfunctions, and  $E_n$  are the eigenvalues, in individual equilibrium  $(\Delta_i, \phi_i)$  configurations. Since the configurations arise following a Boltzmann weight, thermal average is same as average over equilibrium configurations.

3. Localisation effects are tracked via the inverse participation ratio. For a normalised state  $|n\rangle$ , the inverse participation ratio (IPR) is  $P(n) = \sum_i |\langle i|n\rangle|^4$ . Averaged over an energy interval this leads to:

$$P(\omega) = \frac{1}{N(\omega)} \sum_n \delta(\omega - \epsilon_n) P(n) \quad (2.68)$$

$P(\omega)$  is a inverse measure of the number of sites over which eigenstates at energy  $\omega$  are spread.

# A classical fluctuation approach to correlated bosons

## 3.1 Introduction

The experimental realization [26, 55, 56, 58] of a quantum phase transition from a superfluid (SF) to a Mott insulator for bosons in an optical lattice bridged the gap [1, 2] between condensed matter and cold atom physics. The quantitative features of the transition are captured by quantum Monte Carlo (QMC) simulations in both two dimensions [144] and three dimensions [145]. These have established the phase diagram involving (i) the interaction,  $U$ , driven superfluid to Mott insulator transition in the ground state at integer filling, and (ii) the thermally driven superfluid to normal Bose liquid transition.

While QMC provides high accuracy numerical results for the thermodynamic features, one would want methods that (i) shed light on the key physical effects, and (ii) allow access to dynamical properties. Mean field theory [19, 23], although quantitatively not very accurate, highlights the crucial effect of particle number fluctuation in the superfluid ground state. More sophisticated methods, *e.g.*, strong coupling expansion [60, 61], variational calculations [62], the projection operator technique [63], the cluster Gutzwiller approach [64], and variational cluster schemes [65, 66] improve on the mean field ground state and yield results that agree well with QMC for the zero temperature transition.

There is less insight into the finite temperature situation. Mean field theory has a finite temperature generalisation but leads to a large overestimate of  $T_c$  scales. Slave particle methods [69, 70] and a self consistent standard basis operator [162] approach have been used to study the thermal physics. Recently a bosonic version of dynamical mean field theory (BDMFT) [71–73] has been developed - retaining all local quantum fluctuations but ignoring spatial correlations. Among the methods above only the results of BDMFT compare reasonably with QMC in terms of thermal properties.

In this chapter we will use the SPA and PSPA methods to probe the thermal physics of the Bose Hubbard model, and compare with QMC results wherever possible. As discussed before our method incorporates *classical spatial fluctuations* exactly and temporal (quantum) fluctuations only approximately. We implement the methods via Monte Carlo for the two dimensional (2D) Bose Hubbard model (BHM) at filling  $n = 1$ . We focus on the results of the numerically more accurate PSPA scheme for most physical indicators, occasionally showing SPA results for comparison. Our main results, based on the PSPA scheme, are the following:

1. Ground state: Our scheme generates a superfluid-Mott phase boundary that is indistinguishable from full QMC. However, QMC indicates a second order transition while we obtain a weak first order transition.
2. Thermal scales: we obtain a maximum superfluid  $T_c$  that is  $T_c^{max} \sim 2.5t$  (where  $t$  is the hopping scale). Within QMC  $T_c^{max} \sim 2t$  while mean field theory predicts  $T_c^{max} = 6t$ .
3. Momentum distribution: our momentum distribution results in the low temperature superfluid closely mimics available QMC data, except for a somewhat larger  $\mathbf{k} = (0, 0)$  occupancy. In the low temperature Mott phase our scheme performs poorer since it underestimates quantum fluctuation effects.
4. Thermal energy and  $C_V$ : We have computed the temperature dependence of the internal energy and obtained an excellent match with QMC data in the superfluid. For  $U \sim U_c$  in the superfluid we observe low temperature  $C_V$  akin to the XY model, arising from phase fluctuations. At weaker  $U$ , amplitude and phase contributions cannot be separated.

5. Simplified model: our approach already simplifies the Bose Hubbard model, but a further simplification is possible when  $U \rightarrow U_c$ . Retaining only phase fluctuations we construct an explicit XY model that accounts very well for the  $T_c$  scales. This can serve as a starting point for including amplitude fluctuations in a more complete free energy functional.

The chapter is organized as follows: Section 3.2 briefly discusses our model and method, Section 3.3 discusses our results for the ground state, and Section 3.4 the thermal behaviour. Section 3.5 provides an analysis in terms of an XY model, and discusses computational checks.

## 3.2 Model and method

The Bose Hubbard model is given by:

$$H = -t \sum_{\langle ij \rangle} a_i^\dagger a_j - \mu \sum_i n_i + \frac{U}{2} \sum_i n_i(n_i - 1) \quad (3.1)$$

where  $a$  and  $a^\dagger$  are the usual second quantised bosonic operators,  $t$  is the nearest neighbour hopping amplitude,  $U$  is the onsite repulsion, and the boson density is fixed at  $n = 1$  by using a chemical potential  $\mu$ .

The method to solve the BHM has been described in detail in Chapter 2 and we recapitulate very briefly here. We use a path integral representation and separate the kinetic term into zero frequency and finite frequency parts. We use a Hubbard-Stratonovich transformation to decouple the static part of the kinetic term. The original model in path integral representation can be rewritten as (see section 2.2.3):

$$\begin{aligned} Z &= \int \mathcal{D}\psi \mathcal{D}\psi^* \mathcal{D}b \mathcal{D}\bar{b} e^{-(S+S_K^b)} \\ S &= S_0[b, \bar{b}] - \sum_{ij} (C_{ij} \bar{b}_i \psi_j + hc) + \sum_i \psi_i^* \psi_i \\ C_{ij} &= \frac{1}{N} \sum_{\vec{k}} \sqrt{A_{\vec{k}}} e^{i\vec{k}(\vec{r}_i - \vec{r}_j)} \end{aligned} \quad (3.2)$$

This is an exact representation of Bose Hubbard model.

We use two approximations: (i) Drop  $S_K^b$  completely and solve for the physics arising from



$S$  - this is the SPA for the partition function and treats the hybridising field as classical. (ii) Treat the effect of dynamical fluctuations contained in  $S_K^b$  to quadratic order, this is the PSPA.

### 3.2.0.1 Static path approximation (SPA)

After dropping  $S_K^b$  completely, within the SPA approximation we get

$$\begin{aligned} Z &= \int \mathcal{D}\psi \mathcal{D}\psi^* \mathcal{D}b \mathcal{D}\bar{b} e^{-S} \\ &= \int \mathcal{D}\psi \mathcal{D}\psi^* e^{-\beta F\{\psi\}} \end{aligned} \quad (3.3)$$

In the expression above

$$\begin{aligned} F &= \sum_i F_i = -\frac{1}{\beta} \sum_i \log(\text{Tr}[\exp(-\beta H'_i)]) \\ H'_i &= (a_i^\dagger \Phi_i + h.c.) + \frac{U}{2} n_i(n_i - 1) - \mu n_i + \psi_i^* \psi_i \\ \Phi_i &= \sum_j C_{ij} \psi_j \end{aligned} \quad (3.4)$$

In what follows we will call  $\psi_i$  the *auxiliary field*, which is what we actually update, and  $\Phi_i$  the *hybridisation field*.

### 3.2.0.2 Perturbed static path approximation (PSPA)

Within PSPA we retain the  $S$  part exactly and include corrections due to  $S_K^b$  perturbatively by summing diagrams with ‘self avoiding’ paths to all order and then replacing the series sum by an exponentiated term. The full partition function is approximated by

$$\begin{aligned} Z &\approx \int \mathcal{D}\psi \mathcal{D}\psi^* e^{-\beta(F+X-Y)} \\ F &= -\frac{1}{\beta} \log(\text{Tr}[\exp(-\beta H')]) \end{aligned} \quad (3.5)$$

Here  $F$  is the contribution due to  $S$  part of the action. The expressions for  $X$  and  $Y$  are given in appendix A.  $X$  depends upon a coupling  $B_{ij}$  which falls off quickly with distance so we use  $B_{ij}$  generated for a  $4 \times 4$  lattice.  $X$  can be written as sum of contribution coming from onsite, nearest neighbour bonds, and next nearest neighbour bonds for every site whereas  $Y$  is sum of

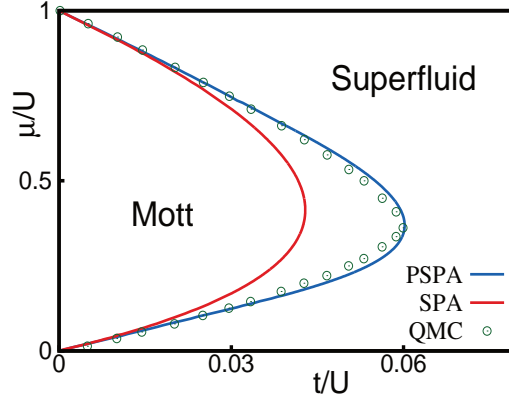


Figure 3.1: The ground state of the 2D Bose Hubbard model for varying  $\mu/t$  and  $U/t$ . The region within the lobe is a Mott insulator with  $n = 1$ . The inner lobe, with a smaller  $(t/U)_c$  is SPA result (and same as mean field theory). The outer lobe, with larger  $(t/U)_c$ , is the PSPA result and is indistinguishable from QMC.

contribution from only nearest neighbour bonds.

The task at any temperature is to sample over configurations of  $\{\psi_i\}$ . Suppose one has a configuration  $\{\psi_i^0\}$ . The algorithm goes as follows: (i) At some site  $R_n$  one attempts an update  $\psi_n^0 \rightarrow \psi_n'$ . (ii) This modifies the hybridisation field  $\Phi_m^0$  in a neighbourhood of  $R_n$  decided by the ‘range function’  $C_{nm}$ . (iii) Given the rapidly decaying nature of  $C_{nm}$  we consider the  $\Phi$  to change at  $N_c \sim 6^2$  sites around  $R_n$ . (iii) At these sites we compute the difference of local free energy due to the  $\Phi$  change. An atomic basis of  $N_b = 10$  states is used for the local diagonalisation. Once the free energy cost is known a Metropolis argument is used to determine acceptance of the move.

We have checked that our results are stable against increase of  $N_c$  and  $N_b$ , down to  $U = 2t$ . The cost of the ‘local update’ is  $\sim N_c N_b^3$  and that of a ‘system update’ is  $\propto N N_c N_b^3$ , where  $N$  is the system size. The cost is *linear* in  $N$  and *no system wide diagonalisation is needed*.

After equilibration, we store  $\psi$  configurations to calculate thermodynamic averages. We adjust  $\mu$  to remain at unity filling at each temperature. At  $T = 0$  where every site sees the same hybridisation. At finite temperature both the amplitude and the phase of the  $\psi_i$  (and so the  $\Phi_i$ ) fluctuate. When calculating  $Y$  we sum over only the lowest four eigenstates.

While we emphasize the PSPA results in this chapter, due to its quantitative accuracy, we often compare and contrast it to SPA - given the conceptual simplicity of the SPA scheme.

### 3.3 Results on the ground state

Fig3.1 shows the comparison between ground state obtained using the SPA and PSPA schemes. The value of the uniform hybridisation  $\Phi$  is zero inside the Mott lobe and increases with increase in  $t/U$ . The critical value at the tip of the Mott lobe, is found to be  $(t/U)_c = 0.0428$  within SPA, the same as the mean field result. The critical point is at  $(t/U)_c = 0.0595$  within PSPA, very close to the QMC value.

Fig3.2 compares the SPA and PSPA energy functions for uniform hybridisation. Numerical data are shown by open circles, at  $U/t = 10, 15, 16$  and  $18$ , and even order polynomial fits to them are shown by firm lines. The minimum of the respective function decides the  $T = 0$  order parameter within that scheme. In the following discussion we ignore the angle dependence of  $\Phi$  since it is irrelevant at  $T = 0$ .

In the  $U = 10t - 18t$  window shown the SPA ground state is superfluid. There is a local maximum in  $E_{SPA}(\Phi)$  at  $\Phi = 0$ , and a  $\Phi \neq 0$  minimum that moves to smaller value with increasing  $U/t$ . The SPA leads to a second order transition from superfluid to Mott insulator at  $U/t \approx 24$ . For the PSPA there is always a minimum at  $\Phi = 0$ . The  $\Phi \neq 0$  minimum is deeper for  $U \lesssim 17t$  - leading to a superfluid state. At  $U = 18t$ , panel (d) in Fig3.2, the PSPA minimum at finite  $\Phi$  is no longer visible. There is a weak first order SF to Mott transition within the PSPA at  $U \sim 17.5t$ .

We analysed the energy functions in terms of their Landau expansion. The SPA energy at  $T = 0$  has a Landau expansion of the form:  $E_{SPA}(\Phi) = \sum_m a_m \Phi^m$  where  $\Phi$  is the uniform hybridisation field. Naturally only even powers arise in the expansion. The coefficients  $a_m$  can be estimated as

$$\begin{aligned} a_0 &= (U/2)n(n-1) - \mu n \\ a_2 &= (1/4) + t G_{ii}(0) \\ a_4 &= -(t^2/4)G_{ii}^{2c} \end{aligned} \tag{3.6}$$

where  $G_{ii}(0) = -\int_0^\beta d\tau \langle T_\tau b(\tau)b^\dagger(0) \rangle$  and  $G_{ii}^{2c} = \int_0^\beta d\tau_1 \dots d\tau_3 \langle T_\tau b(\tau_1)b(\tau_2)b^\dagger(0)b^\dagger(\tau_3) \rangle - 2\beta G_{ii}^2(0)$  The  $G_{ii}$  are correlators in the  $\Phi = 0$  problem. For PSPA the expansion is similar, of

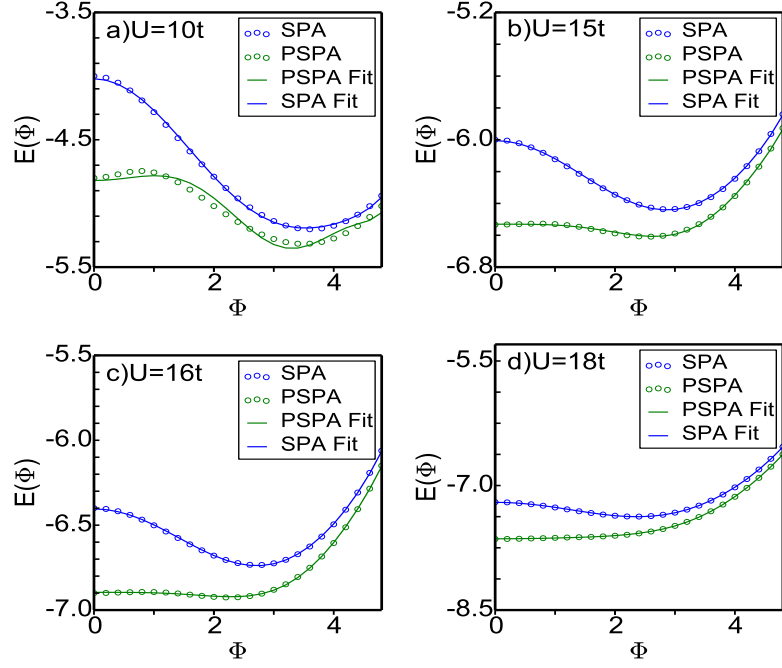


Figure 3.2: Energy functions in SPA and PSPA. The open circles show the SPA and PSPA energy functions, plotted for an uniform order parameter,  $\Phi$ , for the values of  $U/t$  indicated. The SPA and PSPA minima match with each other in panels (a) and (b), in panel (c) the difference is noticeable, while in (d) the SPA minimum is at finite  $\Phi$  while the PSPA minimum has shifted to zero. The firm lines are even order Landau fits to the energy functions to  $\mathcal{O}(\Phi^6)$

the form  $E_{PSPA}(\Phi) = \sum_m a'_m \Phi^m$  but an analytic derivation of the coefficients is more involved and is described in the Appendix A.

Fig3.3 shows the Landau parameters obtained by fitting the SPA and PSPA energy functions. For SPA the coefficient  $a_4$  is always positive,  $a_6$  is small and positive, and the SF to Mott transition is driven by  $a_2$  changing from negative to positive. For PSPA  $a_2 > 0$  and  $a_6 > 0$  throughout. There is always a minimum at  $\Phi = 0$ .  $a_4$  is large and negative at small  $U/t$ , generating the SF minimum. With increasing  $U/t$  the coefficient  $a_4 \rightarrow 0$  and the finite  $\Phi$  minimum becomes higher in energy than the  $\Phi = 0$  minimum. This drives a weak first order SF to Mott transition. We found a slight disagreement between fit parameters and the analytic estimate for coefficients of SPA functional:  $a_0$  and  $a_2$  match well but  $a_4$  deviates when  $(U_c - U) \gg t$ .

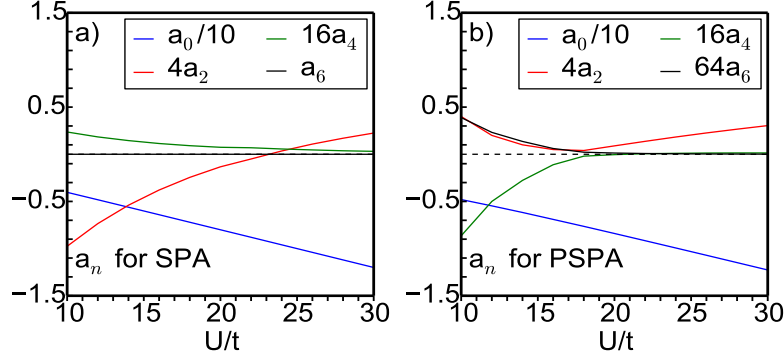


Figure 3.3: Landau parameters for (a) SPA and (b) PSPA. In SPA  $a_4 > 0$  for all  $U/t$ ,  $a_6$  is negligible, and the second order transition is driven by sign change in  $a_2$ . For PSPA  $a_2, a_6 > 0$  at all  $U/t$ . There is always a minimum at  $\Phi = 0$ , and the transition is driven by a decreasing  $a_4$ .

### 3.4 Finite temperature behaviour

#### 3.4.1 Phase diagram

We now turn to the thermal phase diagram shown in Fig3.4 and discuss it in more detail. The figure compares the  $T_c(U)$  obtained from SPA and PSPA with mean field theory and full QMC. The SPA  $T_c$  is already a significant improvement over mean field theory and compares reasonably with QMC in the intermediate  $U/t$  regime. The  $T_c$  of the superfluid should vanish as  $U \rightarrow 0$  since there is no phase stiffness in the absence of interactions. We do obtain a non monotonic dependence of  $T_c$  on  $U/t$  with a maximum located at  $U/t \sim 4$ , consistent with QMC, but the  $U/t \rightarrow 0$  limit is not captured correctly. The PSPA scheme leads to  $T_c$ 's that are close to the SPA results for  $U/t \lesssim 14$ , beyond which the PSPA  $T_c$  quickly drops to zero. However even PSPA does not correctly capture the asymptotic behaviour as  $U/t \rightarrow 0$ .

We will show detailed results for four representative  $U/t$  values: (i)  $U = 6t$  where the system is a moderate coupling superfluid, (ii)  $U = 15t$  where it is a strongly interacting superfluid, (iii)  $U = 20t$  - a ‘weak Mott state’, just beyond  $U_c$ , and (iv)  $U = 30t$  - a deep Mott state. We highlight spatial maps and distributions at four temperatures,  $T = 0.2t, t, 2t$  and  $3t$ . We first discuss the superfluid regime in the next subsection, and then the Mott and normal regime.

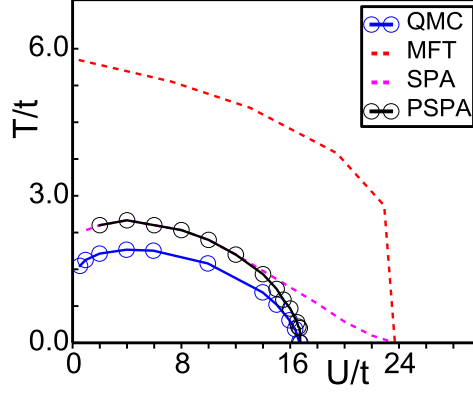


Figure 3.4: Superfluid  $T_c$  from different methods for the 2D Bose Hubbard model at filling  $n = 1$ . We use  $U_c(0)$ , the  $T = 0$  critical interaction, and  $T_c^{max}$ , the maximum superfluid  $T_c$ , to characterise each scheme. (i) Mean field theory (MFT) yields  $U_c(0) = 24t$  and  $T_c^{max} = 6t$ , (ii) for our simplest method, the SPA,  $U_c(0) = 24t$  and  $T_c^{max} \sim 2.5t$ , (iii) for the PSPA,  $U_c(0) \sim 17t$  and  $T_c^{max} \sim 2.5t$ . For full quantum Monte Carlo (iv)  $U_c(0) \sim 17t$  and  $T_c^{max} \sim 2t$ .

### 3.4.2 Superfluid phase

#### 3.4.2.1 Hybridisation field backgrounds

The Monte Carlo generates hybridisation field backgrounds  $\{\Phi_i\}$  following their Boltzmann weight. The configurations can be characterised via their spatial order, encoded in the structure factor  $S(\mathbf{q})$ , the distribution  $P(|\Phi|)$  of the field magnitude, and the phase correlation  $C_i$ .

Fig3.5 shows the correlation  $C_i$  for single Monte Carlo snapshots, at  $U = 6t$  (top) and  $U = 15t$  (bottom). At the lowest temperature shown there is only weak amplitude and angular fluctuation, hence  $C_i$  is only weakly inhomogeneous. The second column,  $T = t$ , corresponds to  $\sim 0.5T_c$  at  $U = 6t$  but is above  $T_c$  at  $U = 15t$ . As a result the top panel still shows a connected pattern while the  $U = 15t$  case shows only small correlated droplets in an otherwise uncorrelated background. The trend continues to higher  $T$ , with the correlation length for  $U = 6t$  (which we show later) being larger than that for  $U = 15t$  at a given temperature.

We have analysed the hybridisation field magnitude in detail. Fig3.6(a) and 3.6(b) shows the distribution  $P(|\Phi|)$  in the superfluid regime. At  $T = 0$  the  $|\Phi|$  is homogeneous across the system and the distribution is a delta function. At finite  $T$  we see that  $\log P(|\Phi|)$  has a parabolic character,  $\log P(|\Phi|) \sim Q(T) - (|\Phi| - \bar{\Phi}(T))^2/R(T)$ , where  $Q(T)$  is a normalisation constant,  $\bar{\Phi}(T)$  refers to the amplitude with maximum probability, and  $R(T)$  is a measure of the width of the distribution. As is obvious from the plots, for the superfluid  $\bar{\Phi}(T)$  falls with

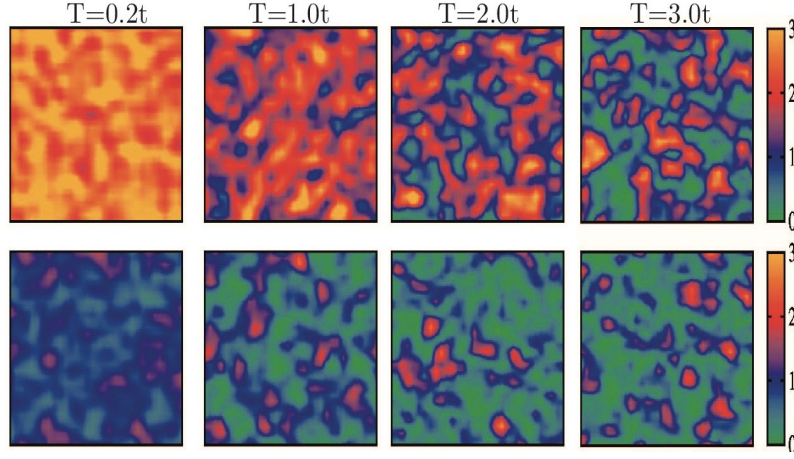


Figure 3.5: MC snapshot of spatial correlations in the superfluid. Top:  $U = 6t$ , bottom:  $U = 15t$ . The maps indicate the correlation  $C_i$  of the hybridisation at a site with its four neighbours.  $C_i = \sum_{\delta} |\Phi_i| |\Phi_{i+\delta}| \cos(\theta_i - \theta_{i+\delta})$ . The patterns are quasi homogeneous at low  $T$ , with a larger value for  $U = 6t$ . The  $U = 6t$  pattern fragments slower with temperature. Even for  $T > T_c$  small spontaneous clusters with large correlation are present. System size  $32 \times 32$ .

increasing  $T$ , while  $R(T)$  rises from zero as  $T$  increases. By the time  $T \sim T_c$  for both the weak and strongly interacting superfluids the width of the distribution is comparable to the mean.

*Amplitude fluctuations are significant all across the high  $T$  superfluid.*

Fig3.6(c)-(d) show the detailed  $T$  dependence of the mean and width of the distributions, computed from the moments. For the weak coupling SF, with  $T_c \sim 2t$ , the mean value starts dropping sharply as  $T \rightarrow T_c$ , and the width at  $T_c$ , in Fig.7(d), is  $\sim 0.5$  the mean value. In the strong coupling case, where  $T_c \sim t$ , the mean value at  $T \gtrsim T_c$  is  $\gtrsim 80\%$  of the  $T = 0$  value, although the width is comparable to the weak coupling case. The width, both at  $U = 6t$  and  $15t$ , behaves roughly  $\propto \sqrt{T}$  at low temperature.

Fig3.8 shows the spatial correlation scale  $\xi(T, U)$  extracted from an analysis of the  $\mathbf{q}$  dependence of  $S(\mathbf{q})$  about  $\mathbf{q} = (0, 0)$ . The correlation length grows smoothly as  $T \rightarrow 0$ , and at all  $T$  is larger for the  $U = 6t$  superfluid than for  $U = 15$ . This is a consequence of the larger phase stiffness at  $U = 6t$ .

### 3.4.2.2 Momentum distribution of bosons

Fig3.8 shows our result for  $n(k_x, k_y)/N$  at  $U = 6t$  and  $U = 15t$  for varying temperature. Since the low  $T$  state has a large  $\mathbf{k} = (0, 0)$  occupancy, which becomes comparable to the finite  $\mathbf{k}$  occupancy only at high  $T$ , we have used a changing colour scale to show the data. As expected,

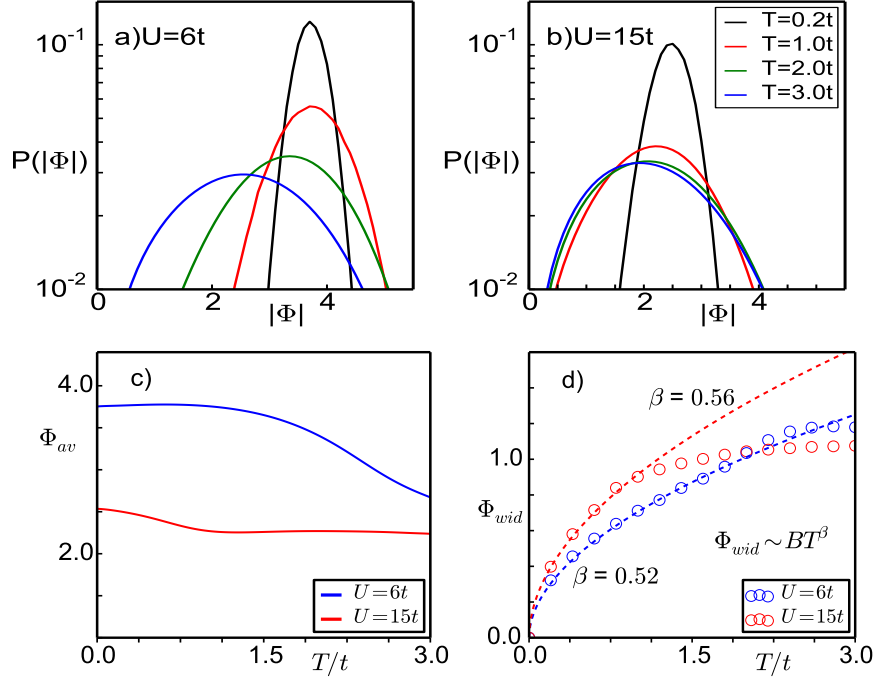


Figure 3.6: (a)-(b): Distribution of the magnitude of the local hybridisation in the superfluid regime. The lowest temperature in the data set is  $T = 0.2t$  at which amplitude fluctuations are already visible. The distributions appear gaussian in the weaker  $U$  systems. (c)-(d): Mean and standard deviation of  $|\Phi|$ . In the superfluid ( $U/t \lesssim 16$ ) the mean falls only weakly between  $T = 0$  and  $T_c$ , and somewhat faster for  $T \gtrsim T_c$ . The fluctuation ‘width’ is fitted to a form  $\Phi_{wid} = BT^\beta$  at low  $T$ . We find  $\beta \approx 0.5$  at both  $U = 6t$  and  $15t$ .

at any  $T$  the  $\mathbf{k} = (0, 0)$  occupancy is lower at  $U = 15t$  than at  $U = 6t$ . The ‘width’ of the distribution is bigger at  $U = 15t$ . These trends are quantified in Fig3.9.

Fig3.9(a)-(b) compares 2D QMC results [163], at low  $T$  ( $T \ll T_c$ ), effectively ground state data, with our results. Fig3.9(a) shows  $(1/N)n(\mathbf{k})$  along the  $k_x$  axis obtained via QMC for

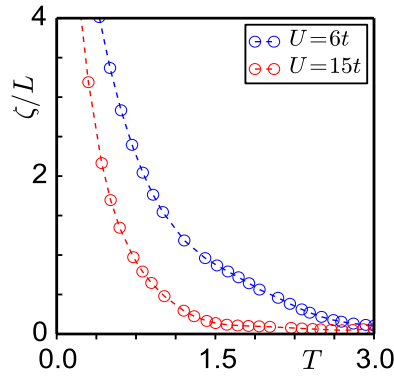


Figure 3.7: The correlation length  $\xi(T)/L$  inferred from  $\mathbf{q}$  dependence of  $S(\mathbf{q})$ , at  $U = 6t, 15t$ .  $\xi$  ‘diverges’ as  $T \rightarrow 0$  and is larger at  $U = 6t$  than at  $15t$  at all temperature. This is consistent with the spatial patterns in Fig.6.



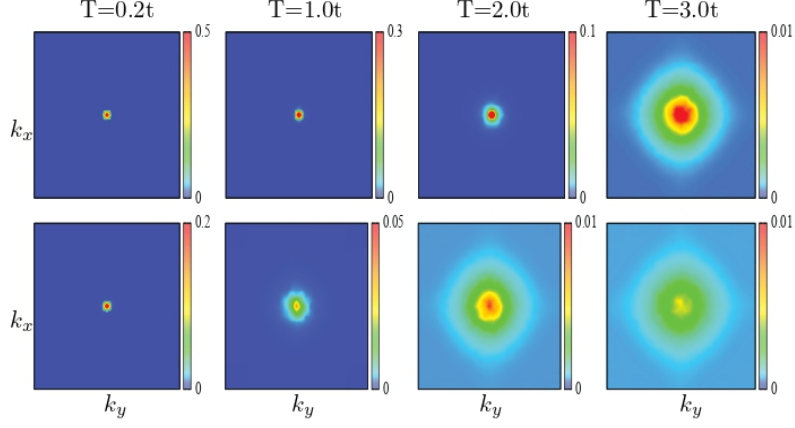


Figure 3.8: The momentum distribution,  $n(\mathbf{k})/N = \langle \langle a_{\mathbf{k}}^\dagger a_{\mathbf{k}} \rangle \rangle / N$ , for varying interaction strength and temperature in the superfluid phase. The intensity scale is linear and varies across the panel to simultaneously capture the condensate peak in the superfluid state and show the particle distribution in high temperature normal phase.

several values of  $U/t$ . The data is in the superfluid regime. The main observations are on (a) the value of  $n(\mathbf{k})$  at  $\mathbf{k} = (0, 0)$  for changing  $U$ , and (b) the sharp drop in  $n(\mathbf{k})$  as  $\mathbf{k}$  moves away from  $(0, 0)$  to the first non zero  $\mathbf{k}$  value. Fig3.9(b) shows our PSPA result for the same parameters and system size. Our  $\mathbf{k} = (0, 0)$  values are expectedly somewhat larger than QMC, at  $U = 10t$  the QMC value is about 28% smaller than ours. The  $\mathbf{k}$  dependence is similar in the two schemes.

Since the  $\mathbf{k} = (0, 0)$  and finite  $\mathbf{k}$  occupancy cannot be seen readily on a linear scale, panels (c)-(d) show the  $(1/N)n(\mathbf{k})$  at  $U = 6t$  and  $U = 15t$  on a log scale at finite  $T$ . In our  $32 \times 32$  system, the total number of bosons, at density  $n = 1$ , is  $\sim 10^3$ . For  $T \gg T_c$  we expect  $n_{\mathbf{k}} \sim 1$  at all  $\mathbf{k}$  so  $n_{\mathbf{k}}/N \rightarrow 1/N \sim 10^{-3}$ .

### 3.4.2.3 Energy and specific heat

We calculated the internal energy and specific heat, both to test out against QMC and use as a reference for the approximate ‘phase only’ model. In 2D we could find only limited QMC results, Fig3.10(a) compares our results for the kinetic energy with the result from QMC. The PSPA result is an excellent match, SPA much less so. Fig3.10(b) shows the energy  $E(T)$  within our scheme for several  $U$  values while Fig3.10(c) shows the associated specific heat.

The  $E(T)$  curves are not very illuminating, mainly indicating a quick increase in slope at  $T \sim 2t$  for  $U = 6t, 10t$ , corresponding to the  $T_c$  in these cases. At  $U = 15t$  the  $E(T)$  result is

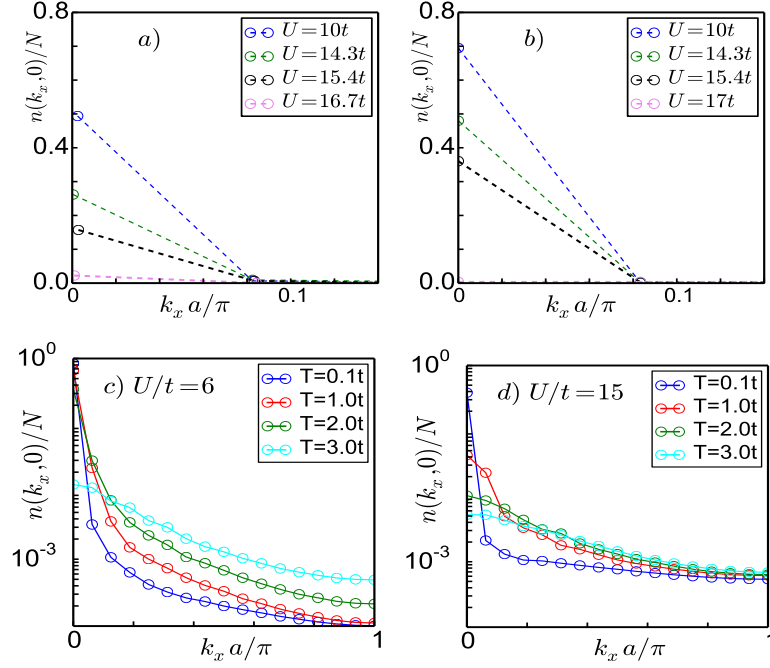


Figure 3.9: Momentum distribution in the superfluid. (a) Low  $T$  data from QMC [163], (b) data at same parameter points from PSPA. (c)-(d) Scan of  $n_k$  for  $\mathbf{k}$  from  $(0, 0) \rightarrow (0, \pi)$ , at  $U = 6t$  and  $15t$ . We have shown these results on a log scale to highlight behaviour over the large  $k$  window.

almost featureless, the corresponding  $C_v$  shows a mild bump around  $T \sim t$  - the  $T_c$  - and a very broad maximum associated with amplitude fluctuations at higher  $T$ . In fact only as  $U \rightarrow U_c$  can we separate out in the  $C_v$  the effects of (i) a phase fluctuation dominated thermal transition at low  $T$ , described roughly by standard XY physics, and (ii) high  $T$  amplitude fluctuations in a phase disordered background. At the lower  $U$  values the effect of amplitude and phase fluctuations

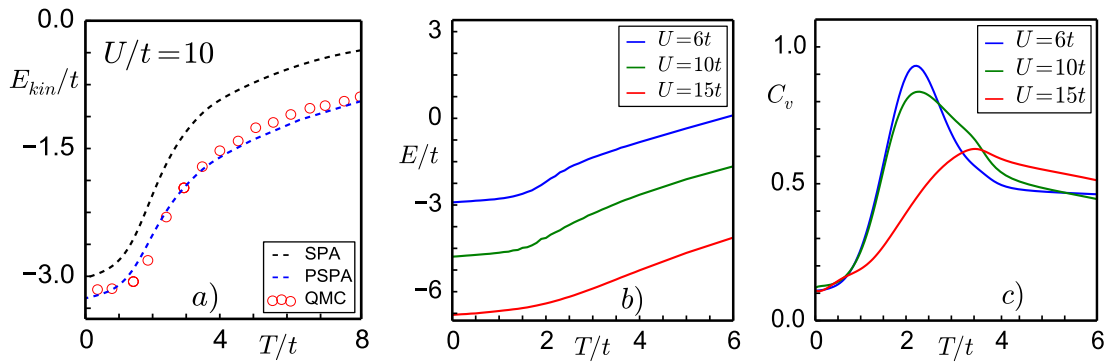


Figure 3.10: Energy and specific heat in the superfluid. (a) Compares the  $T$  dependence of the kinetic energy at  $U = 10t$  between QMC and PSPA. The match is excellent. SPA energies are significantly higher. (b) Shows the internal energy  $E(T)$  at three  $U$  values, the change in slope suggestive of a thermal transition. (c) The  $C_v$  showing the broad peak at low  $U$  associated with the thermal transition, and a two peak at feature at  $U = 15t$  - one at  $T \sim t$  associated with the thermal transition, another at  $T \sim 4t$  associated with amplitude fluctuations.

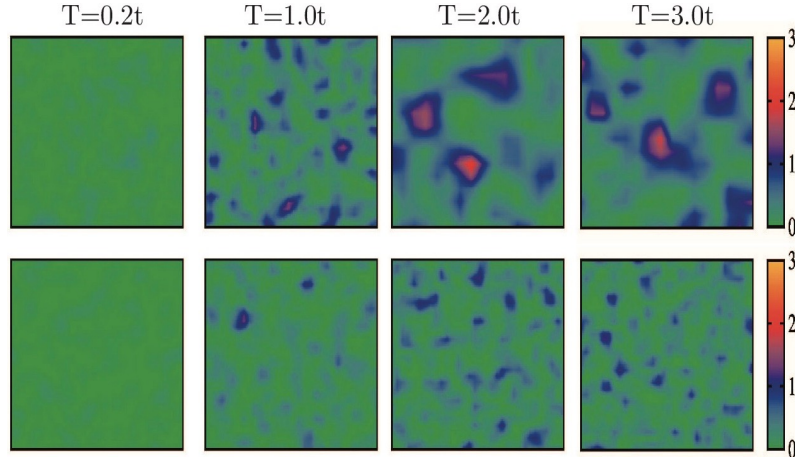


Figure 3.11: Spatial map of  $C_i = \sum_{\delta} |\Phi_i| |\Phi_{i+\delta}| \cos(\theta_i - \theta_{i+\delta})$  in the Mott insulator. Top row  $U = 20t$ , bottom  $U = 30t$ .  $C_i$  vanishes as  $T \rightarrow 0$  since the  $\Phi_i \rightarrow 0$ . Thermal fluctuations generate finite  $\Phi_i$  when  $T \neq 0$  and these can correlate over a small neighbourhood. The tendency is stronger at  $U$  near  $U_c$  rather than in the deep Mott phase at  $U = 30t$ . System size  $32 \times 32$ .

cannot be separated out in the thermal transition.

### 3.4.3 Mott insulator

#### 3.4.3.1 Hybridisation field backgrounds

Fig3.11 shows snapshots of  $C_i$ , the correlation of the hybridisation at  $R_i$  with its four neighbours in the Mott phase. At  $T = 0$  all  $C_i = 0$ . At finite  $T$  there are thermally generated  $\Phi_i$ , following the distribution shown in Fig3.12, that correlate via a coupling that we describe in the next section. Since the fluctuation induced amplitudes are unlikely to be simultaneously large over a wide neighbourhood the patches are small and randomly distributed. The thermally induced amplitudes are much smaller at  $U = 30t$  than at  $U = 20t$ .

Fig3.12(a)-(b) shows the distribution of hybridisation for  $U = 20t$  and  $U = 30t$  while Fig3.12(c)-(d) shows  $\Phi_{av}$  and  $\Phi_{wid}$ . In the Mott phase the hybridisation is zero at  $T = 0$ . With rise in temperature  $P(|\Phi|)$  picks up weight at non zero  $\Phi$ . In panels (c)-(d) both the mean and width of  $\Phi$  grow roughly as  $\sqrt{T}$ . The finite  $T$  Mott state has thermally induced particle number fluctuations but increase in  $U$  leads to suppression of these number fluctuations.

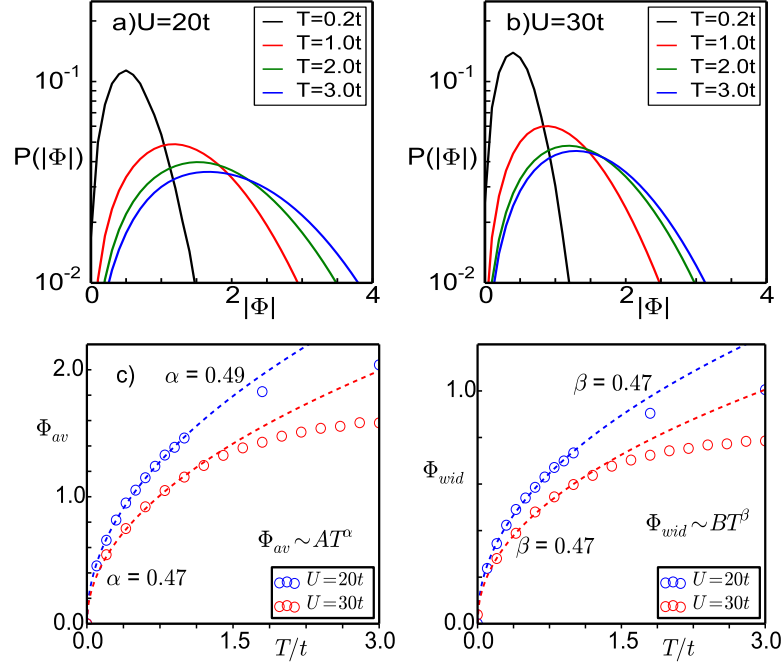


Figure 3.12: (a)-(b) Distribution of  $|\Phi|$  in the Mott insulator. The lowest temperature is  $T = 0.2t$  at which amplitude fluctuations are already visible. (c) Mean and (d) standard deviation of  $|\Phi|$ . In the Mott phase the mean is zero at  $T = 0$  but rises quickly attaining a value  $\sim 0.5$  that of the weak  $U$  superfluid at  $T \sim 3t$ . Both the mean value and width increase as  $\sqrt{T}$ .

### 3.4.3.2 Momentum distribution of bosons

The overall character of the momentum distribution in the Mott state is shown in Fig3.13. The top row shows  $n(k_x, k_y)/N$  at  $U = 20t$ , and the bottom row shows results at  $U = 30t$ . In a ‘trivial’ Mott state, where the wavefunction would be of the form  $\prod_i a_i^\dagger |0\rangle$ , one would obtain  $n_{\mathbf{k}} = 1$  at all  $\mathbf{k}$ . Inclusion of gaussian fluctuation on this state captures hopping effects to  $\mathcal{O}(t_{\mathbf{k}}/U)$ . This  $\mathbf{k}$  dependent modulation is visible in the leftmost panels in Fig3.13, with the  $U = 30t$  case having a weaker modulation as expected.

As temperature increases, small regions with thermally induced hybridisation emerge and the  $\mathbf{k} = (0, 0)$  feature in  $n_{\mathbf{k}}$  actually enhances. At even higher  $T$  the  $n_{\mathbf{k}}$  flattens out once again. The trend is similar at both  $U = 20t$  and  $30t$  with both the quantum and thermal fluctuation effects being weaker at  $30t$ . More quantitatively, as we show in the Appendix, one can write  $n(\mathbf{k})$  at low  $T$  as

$$\begin{aligned} n(\mathbf{k}, T) &= n(\mathbf{k}, 0) + \delta n(\mathbf{k}, T) \\ n(\mathbf{k}, 0) &= 1 + 4t_{\mathbf{k}}/U \end{aligned}$$

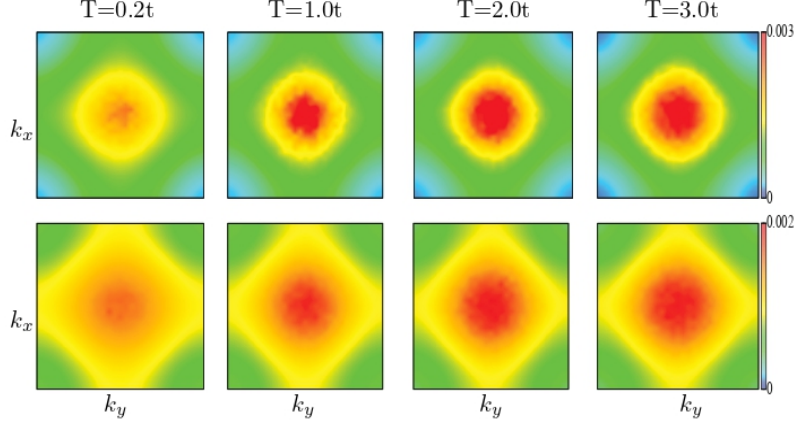


Figure 3.13: Momentum distribution  $n(k_x, k_y)/N$  in the Mott regime. Top row:  $U = 20t$ , bottom:  $U = 30t$ . In the mean field Mott state  $n(k_x, k_y) = 1$  at all  $T$ . Here, quantum fluctuations generate a correction of  $\mathcal{O}(t_k/U)$  at  $T = 0$  and finite  $T$  brings in additional corrections. At a given  $T$  the correction weakens with increasing  $U/t$

$$\delta n(\mathbf{k}, T) \propto \gamma(U, \mu) \langle |\Phi_{\mathbf{k}}|^2 \rangle \quad (3.7)$$

$\gamma(U, \mu)$  can be derived from the atomic problem, and  $\langle |\Phi_{\mathbf{k}}|^2 \rangle$  at low  $T$  can be derived from a gaussian theory (see later). Both  $t_k/U$  and  $\gamma(U, \mu)$  decreases with increasing  $U$ , suppressing both quantum and thermal fluctuations.

Fig3.14 shows  $n(k_x, 0)/N$  for varying  $U$  and  $T$ . Panel (a) shows QMC data [163] at low  $T$  while panel (b) shows our results for the same parameters. There is a scale difference by a factor of 10 between the two panels and certainly at  $U$  just greater than  $U_c$  our results are very different from QMC. Our gaussian approach is a poor approximation to the quantum fluctuations near  $U_c$ . At  $U = 25t$  our results are still off, but now by a factor of 2.

We have not been able to locate  $T$  dependent QMC data on the momentum distribution so we show only our own results in (c)-(d). All the data show a peak at  $\mathbf{k} = (0, 0)$  falling off monotonically as  $\mathbf{k} \rightarrow (\pi, 0)$ . The temperature dependence however is non monotonic at small  $\mathbf{k}$  at  $U = 20t$ . As  $T$  increases from  $0.1t$  to  $T = t$ , the  $\mathbf{k} = (0, 0)$  value rises quickly but beyond that increasing  $T$  leads to a gentle decline in the low  $\mathbf{k}$  value. The increase at low  $T$  is related to the behaviour of  $\langle |\Phi_{\mathbf{k}}|^2 \rangle$ , which is proportional to  $T$  and is peaked at  $\mathbf{k} = (0, 0)$ . The turnaround at high  $T$  is related to the homogenisation of  $n(\mathbf{k})$  where the occupancy of all  $\mathbf{k}$  states tends to 1. The scale beyond which the  $\mathbf{k} = (0, 0)$  occupancy decreases with increasing  $T$  increases with  $U$ .

Overall, the comparison with QMC reveals that our approach is poor at low  $T$  for  $U$  near  $U_c$

in the Mott regime. We believe the results improve with increasing  $T$ , although we do not have access to QMC data to demonstrate this.

### 3.4.4 Normal Bose liquid

The normal Bose liquid has no long range order,  $\langle \Phi(\mathbf{q} = (0, 0)) \rangle = 0$ , where the angular brackets denote thermal average. A ‘mean field theory’ would trivialise in this limit, leading to an isolated atomic description. We want to highlight how our approach, which reduces to mean field theory at  $T = 0$ , leads to a non trivial description of the normal state as well. We provide a visual description in terms of two indicators in Fig3.15, and a more quantitative description in Fig3.16.

The upper row in Fig3.15 shows the nearest neighbour correlation  $C_i$ , described earlier, for  $U/t = 6, 15, 20, 30$ . The results are at  $T = 3t$ , above the highest  $T_c$  in Fig. 3.4 The first two panels in the row arise from heating up a low  $T$  superfluid state, while the next two arise from heating up a Mott state. The correlation  $C_i$  depends both on  $|\Phi|$  in the neighbourhood of  $R_i$  and also the angular correlation. The panels indicate that the correlation weakens systematically as

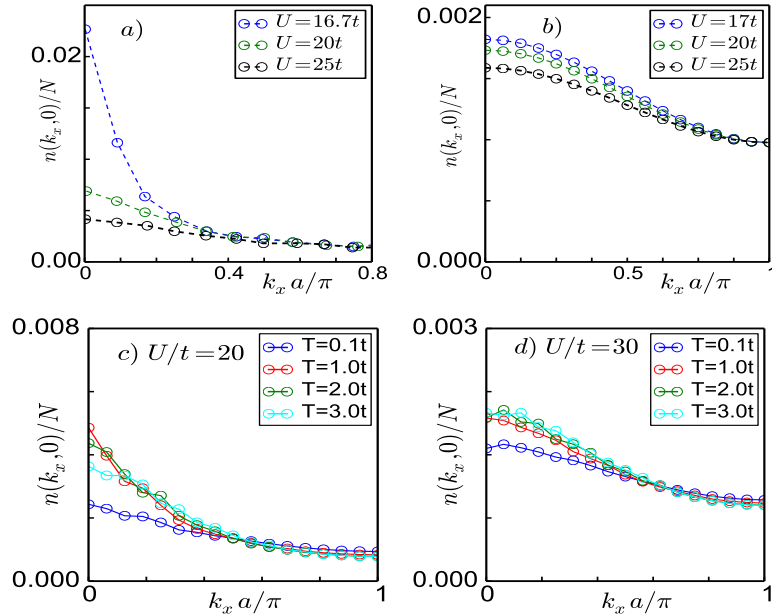


Figure 3.14:  $n(k_x, 0)/N$  for varying  $U$  and  $T$  in the Mott regime. (a) Low  $T$  QMC data [163] on a  $24 \times 24$  lattice, *i.e.*,  $N = 576$ . In a mean field state occupancy would have been  $\mathbf{k}$  independent and  $\sim 0.002$ . The QMC number at  $U = 16.7t$ , just into the Mott state is 10 times larger at  $\mathbf{k} = (0, 0)$ . (b) Our result for the parameters comparable to QMC. The  $\mathbf{k}$  dependence is much weaker than QMC and the  $\mathbf{k} \rightarrow 0$  values much smaller. (c)-(d) Show  $T$  dependence of our results at  $U = 20t$  and  $30t$  respectively for system size  $32 \times 32$  lattice, *i.e.*,  $N = 1024$ .

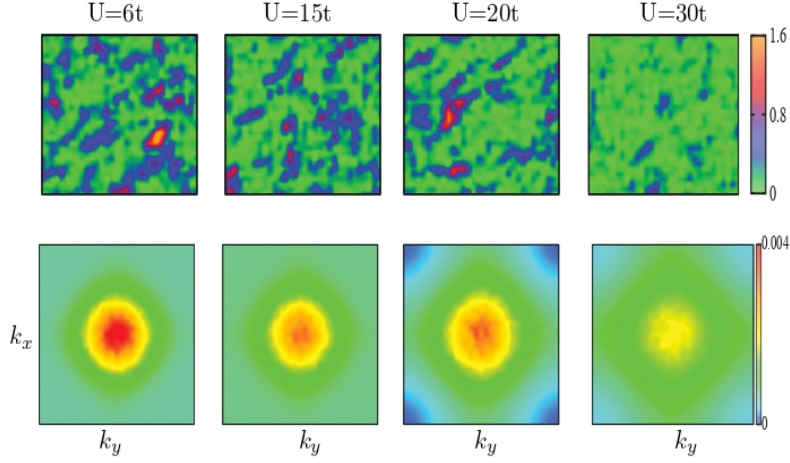


Figure 3.15: Behaviour in the normal Bose liquid. Top row: spatial map of  $C_i = \sum_{\delta} |\Phi_i| |\Phi_{i+\delta}| \cos(\theta_i - \theta_{i+\delta})$  from MC snapshots. The spatial correlation weakens as one moves from  $U = 6t$  to higher values. Bottom row: the thermally averaged momentum distribution  $n(k_x, k_y)$ . At  $U = 6t$  the distribution is still reasonably peaked, with the  $\mathbf{k} = (0, 0)$  value being  $\sim 8$  times the mean value (0.001). Increasing  $U$  reduces the peak and flattens out the distribution but there is no dramatic difference between  $U = 15t$  and  $U = 20t$  which evolved, respectively, from a superfluid and a Mott insulator.

we move from  $U = 6t$  to  $U = 30t$ . This is because both the typical magnitude of  $|\Phi|$  as well as the correlation length  $\xi$  reduce with increasing  $U/t$  as we show later.

The lower row shows  $n(k_x, k_y)/N$ , thermally averaged, for the same  $U$  and  $T$  values. The data is on a  $32^2$  system so  $1/N \sim 0.001$ . For a completely  $\mathbf{k}$  independent high  $T$  distribution the occupation would be  $n(k_x, k_y) = 1$ . The maximum of the color bar is 0.004 and at  $U = 6t$  the peak in  $n(k_x, k_y)/N$ , at  $\mathbf{k} = (0, 0)$ , is  $\sim 0.004$  and the momentum distribution has a reasonable sharp peak despite being in the normal state. The  $T_c \sim 2.3t$  while we are at  $T = 3t$ . The value at small  $\mathbf{k}$  decreases monotonically with  $U/t$  till at  $U = 30t$  the modulation is quite weak.

Fig3.16 quantifies the high  $T$  state in some detail. Panel (a) shows the mean amplitude  $\Phi_{av}(U)$ , (b) shows the fluctuation width  $\Phi_{wid}(U)$ , (c) shows the correlation length  $\xi(U)$ , and (d) shows  $n(k_x, 0)$  at some  $U$  values over the window  $6t - 30t$ . Although the systems at  $U = 6t$  and  $30t$  have very distinct ground states - one a SF with a high  $T_c$  and another a large gap Mott insulator - the difference in their high temperature behaviour is quite modest. The  $U = 30t$  case had  $\Phi_{av} = 0$  at  $T = 0$ . By  $T = 3t$ , the  $\Phi_{av}$  is  $\sim 50\%$  of the  $U = 6t$  value. The fluctuation width  $\Phi_{wid} \sim 0.5\Phi_{av}$  in this  $T$  regime.

The spatial correlations display some difference.  $U = 6t$  has a correlation length  $\sim 2$  lattice



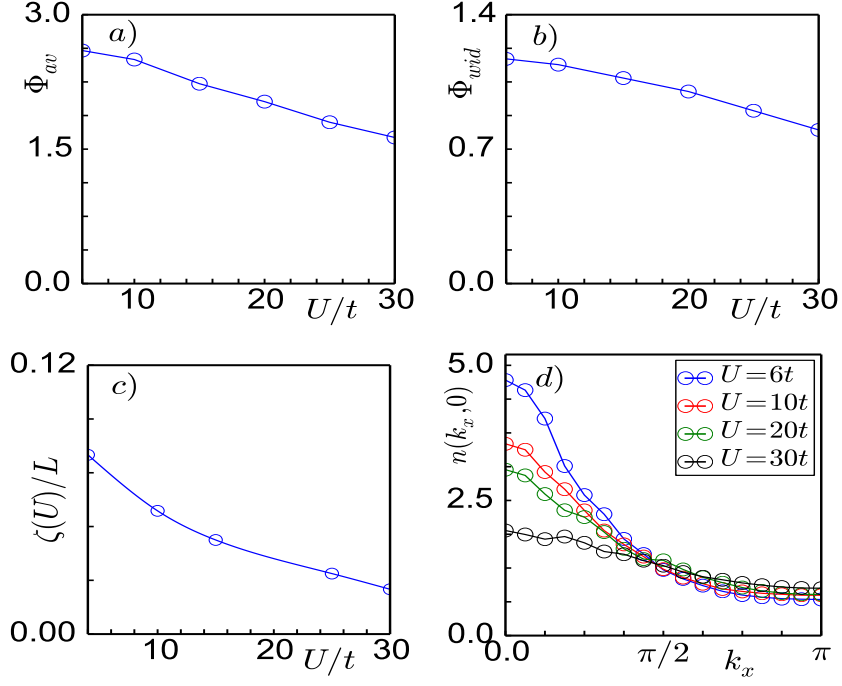


Figure 3.16: Indicators for the normal Bose ‘liquid’ at  $T = 3t$ . (a) Mean amplitude  $\Phi_{av}$ , (b) fluctuation width  $\Phi_{wid}$ , (c) correlation length  $\xi(U)$ , and (d) momentum distribution  $n(k_x, 0)$ . Note that although  $U = 6t$  and  $U = 30t$  are a ‘strong superfluid’ and a ‘deep Mott insulator’ at  $T = 0$ , their  $\Phi_{av}$  and  $\Phi_{wid}$  are within a factor of 2 at  $T = 3t$ . The correlation length, on this  $L = 32$  system is  $\gtrsim 2$  lattice spacing at  $U = 6t$  and  $\lesssim 1$  at  $U = 30t$ .  $n(\mathbf{k} = (0, 0))$  differs only by a factor of 2 between the extreme  $U$  values.

spacings, while at  $U = 30t$  the fluctuations are essentially atomic, *i.e.*, spatially uncorrelated. As a result the momentum distribution at  $U = 6t$  is relatively strongly peaked at  $\mathbf{k} = (0, 0)$  while at  $U = 30t$  it is much flatter. The more subtle differences in behaviour show up in spectral features which we will discuss elsewhere.

## 3.5 Discussion

### 3.5.1 The thermal transition

The BHM is invariant under global rotations of the phase ( $\theta_i$ ) of  $\Phi_i$ , so any effective model should have XY symmetry. The  $T$  dependence of the mean  $\Phi_{av} = \langle |\Phi_i| \rangle$ , Fig3.6(c) is weak for  $U \sim U_c$  and much stronger at small  $U$ . This allows us to explore an amplitude frozen ‘phase only’ model at large  $U$ . We highlight the method for the simpler SPA scheme.

The Landau expansion of the SPA functional, assuming a homogeneous order parameter,  $\Phi$ ,



has the form

$$E(\Phi) = a_0 + a_2|\Phi|^2 + a_4|\Phi|^4 \quad (3.8)$$

as we have already seen. The coefficients  $a_n$  depend on  $\{U, \mu\}$  and lead to the minimised value  $\Phi_0(U) = 0$  for  $U > 24t$  at  $n = 1$ . A similar result, with shifted  $U_c$  holds for PSPA. The general finite  $T$  form, where the  $\Phi_i = \sum_j C_{ij}|\psi_j|e^{i\theta_j}$  has to be treated like a field, can be obtained via a cumulant expansion of the free energy. This has the general  $U(1)$  invariant form in terms of  $\psi$ :

$$\begin{aligned} F\{\Phi\} &= F_0 + F_2 + F_4 + \dots \\ F_0 &= F\{\psi = 0\} \\ F_2 &= \sum_{ij} f_{2,ij}|\psi_i||\psi_j|\cos(\theta_i - \theta_j) \\ F_4 &= \sum_{ijkl} f_{4,ijkl}|\psi_i||\psi_j||\psi_k||\psi_l|g(\theta_i, \dots, \theta_l) \end{aligned} \quad (3.9)$$

The coefficients  $f$  can be calculated in a hopping expansion.

To capture the qualitative physics we simplify as follows: (i) We drop the fluctuation of the amplitudes with  $T$ , treating them as  $\psi_0(U) = \Phi_0(U)/2$ , the mean field value at  $T = 0$ . This is consistent with our result for the finite  $T$  mean  $\Phi$ . So, we replace all  $|\psi_i|$  by  $\Phi_0$ . (ii) We drop the spatial dependence of the  $g(\theta_i, \dots, \theta_l)$  term. After this, the only variables in  $F$  are in  $F_2$ , and the only relevant fluctuations are in the phase  $\theta_i$ , as in the XY model. Note that for computational simplicity we are working with the phases of  $\psi_i$ , not  $\Phi_i$ .

The effective model in this approximation becomes:

$$F\{\Phi\} = \sum_{ij} f_{2,ij}\Phi_0^2\cos(\theta_i - \theta_j) \quad (3.10)$$

The function  $f_2$  has a spatial dependence, which we call  $a_{ij}$ , and an overall pre-factor  $\alpha$  that

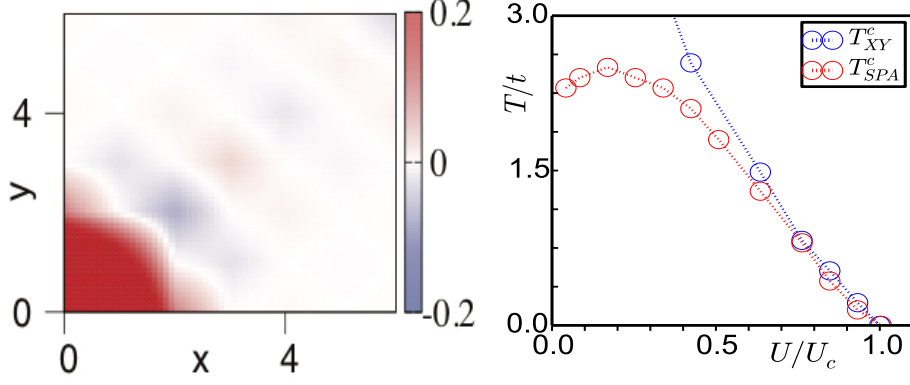


Figure 3.17: Left: the coupling function  $a_{ij}$  that enters the effective XY model. It depends only on the band structure of the non interacting system. Right: Comparison of  $T_c$  obtained from the effective XY model with  $T_c$  from the SPA based Monte Carlo. For  $U \gtrsim 0.5U_c$ , the match is reasonable. At smaller  $U$  the mean amplitude suppression with increasing temperature is a significant effect.

depends on  $U/t$ ,  $\mu/t$ , i.e  $f_{2,ij} = \alpha a_{ij}$ . This leads to a XY model

$$F\{\theta\} = -J \sum_{ij} a_{ij} \cos(\theta_i - \theta_j) \quad (3.11)$$

where  $J = \alpha(U/t, \mu/t) \Phi_0^2(U/t, \mu/t)$ . The  $T_c$  would be controlled by  $J$  and the spatial character of  $a_{ij}$  (which depends only on the band structure). In Fig3.17(right panel) we show a comparison of  $T_c$  obtained from the XY model above with the actual  $T_c$  within the SPA scheme. Beyond  $U \gtrsim U_c/2$  the two results match reasonably.

We came across another real space scheme known as bosonic auxiliary-field Monte Carlo method [164]. They have used this method to study hard core bosons on square and triangular lattice.

### 3.5.2 Size dependence

Fig3.18 shows the size dependence of our results. We did the calculation for four system sizes  $L = 16, 24, 32, 40$  for SPA and  $L = 16, 24, 32$  for PSPA scheme and show the SPA results for the ordering feature in the structure factor. We find that in the superfluid phase, even at moderate coupling ( $U = 4t$ ), a system size  $L = 24$  is large enough to probe ‘bulk’ behaviour.  $L = 32$  is hard to distinguish from  $L = 24$ . For larger interaction strength,  $U \gtrsim 15t$ ,  $L = 16$  seems to capture the behaviour reasonably. This is related to the behaviour of the correlation length

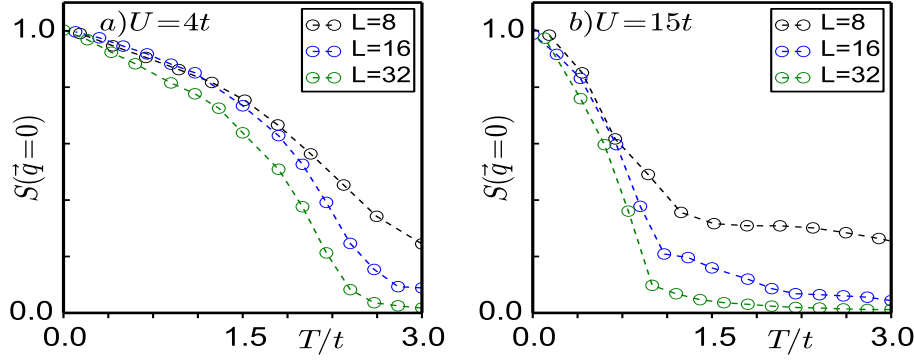


Figure 3.18: Size dependence of the  $\mathbf{q} = (0, 0)$  structure factor at  $U = 4t, 15t$ . At both these  $U$  values the function, and the superfluid onset temperature is almost size independent for  $L \gtrsim 24$ .

$\xi(T, U)$  shown in Fig3.7.

### 3.5.3 Computational cost

Conventional QMC [146, 147] can handle  $N = 10^4$  bosons at temperature  $T \sim 0.1t$  and  $N \sim 10^6$  at  $T \sim 6t$ , where  $t$  is the hopping scale. Crudely, for a fixed resource the accessible system size is  $N \propto 1/T$ . Looking at numbers available in the literature the typical run time  $\tau_{QMC}$  for the QMC algorithm for  $10^4$  bosons, for  $T \sim t$ , is about one hour on a single processor. The corresponding time,  $\tau_{SPA}$ , for our algorithm to handle  $10^4$  bosons *at any*  $T$  is  $\sim 6$  hours on a single processor. The QMC cost, however, has a prefactor  $\propto 1/T$ , to handle fluctuations in imaginary time, while the SPA cost is  $T$  independent. At high  $T$  QMC is a very efficient method, but the temperature integrated cost, when one goes down from high  $T$  towards the ground state, can be large.

### 3.5.4 Three dimensions

We have studied the zero temperature SPA and PSPA theory in the case of 3D Bose Hubbard model. At zero temperature we computed the superfluid Mott boundary for unity filling. The SPA result, as in 2D, matches with mean field theory, while the PSPA critical point is almost indistinguishable from the QMC result. We have not checked the finite temperature results in case of 3D but believe our thermal scales would lie within 20% of QMC results.

### 3.5.5 Future applications

Our technique is general enough to handle any kind of diagonal disorder as in case of diagonal disorder the only change is in the exactly handled local Hamiltonian. We can also handle hopping disorder through a change in coupling between the auxiliary field and the bosons. We can of course handle smooth potentials like traps. We can also study spin-orbit coupling or artificial gauge fields in multispecies bosons. Finally, given the equilibrium classical backgrounds we can compute Green's functions of the Bose theory via a strong coupling expansion.

## 3.6 Conclusions

We have computed the finite temperature phase diagram of the two dimensional Bose Hubbard model at integer filling. The mainstay of our work is the inclusion of all classical thermal fluctuations, and gaussian quantum fluctuations, to which the local bosonic degree of freedom is subject. Our method yields transition scales,  $T_c(U)$ , that compare favourably with full quantum Monte Carlo and has a computational cost that scales linearly with system size. The method is framed in real space, unlike dynamical mean field theory. As a result it can capture the amplitude and phase fluctuations on a specific lattice, disordered background, or the presence of a trap. It allows access to spectral information, and generalises readily to multispecies bosons, both difficult within standard quantum Monte Carlo.

# Finite temperature spectra of the Bose Hubbard model

## 4.1 Introduction

In the previous Chapter we have discussed our results on the thermodynamics of the single species Bose Hubbard model. The focus of this Chapter is on computation of spectral properties.

In presence of weak repulsive interactions, a Bose gas has a dispersion [32]  $\omega_{\mathbf{k}} = v_s k$ , where  $k = |\mathbf{k}|$ ,  $\mathbf{k}$  is the momentum of an excitation, and  $v_s$  is the critical superfluid (SF) velocity. This differs from the  $\omega_{\mathbf{k}} \propto k^2$  result for free particles and is responsible for supporting ‘superflow’ upto a velocity  $\sim v_s$  in the system. This result was arrived at by using a method suggested by Bogoliubov [33]. In a lattice with integer density of bosons, increasing the interaction strength drives the quantum phase transition from superfluid to Mott insulator. Even in presence of the lattice, however, the low energy excitations of the superfluid are linearly dispersive and gapless, as in the continuum, but the Mott insulator - a phase specific to the lattice - has a gapped spectrum.

Starting with the realization of a superfluid to Mott transition [1, 2] in an optical lattice one can now access the dynamical properties of the bosons. The excitation spectra has been probed via Bragg spectroscopy [56, 58], which accesses the dynamical structure factor, and lattice spectroscopy [41], which probes the kinetic energy correlator. These measurements have revealed the existence of the sound (Bogoliubov) mode [56] and also the more exotic amplitude

mode [58].

Motivated by the experiments, there have been theoretical efforts to calculate the single particle spectral properties. At zero temperature, the methods employed include the strong coupling expansion [139], Schwinger-boson mean field theory [59], the random phase approximation [49], the quantum rotor approach [165], and a variational cluster method [65–68]. Broadly, a ‘four mode’ character defines the momentum dependence of the spectra in the superfluid ground state. At weak interaction one observes only the positive energy phase mode. With increasing interaction one sees (i) the appearance of a negative energy gapless feature, and (ii) the emergence of gapped ‘amplitude’ modes of both positive and negative energy. As the system heads towards the Mott transition the weight shifts from the positive energy phase mode, *i.e.*, the traditional Bogoliubov mode, to the negative energy phase mode and the amplitude modes. There have been attempts to go beyond the RPA formalism but those were limited to the Mott phase [141, 166].

At finite temperature there are only a few results available, mainly from QMC in 1D and BDMFT in 3D. The results of both the methods agree well with the RPA at low temperature but the weight and width of the modes could not be resolved accurately due to analytical continuation problems.

In this Chapter we discuss our results for single particle spectra in the Bose Hubbard model (BHM). We adopt a two step process: (i) we solve the BHM by using the SPA method described earlier, and (ii) on the equilibrium configurations of this theory, which captures  $T_c$  quite well, we use a real space generalisation of the ‘random phase approximation’ (RPA) for the boson Green’s function (described in detail in Chapter 2). Since the method is formulated in real frequency, it avoids analytic continuation problems.

The RPA approach has been well studied at  $T = 0$  so we quickly describe the understanding there before summarising our finite temperature results. In the superfluid ground state, *i.e.*, when  $U < U_c$ , the single particle spectral function at a momentum  $\mathbf{k}$  has a four peak structure - characterised by the energy  $\Omega_{n,\mathbf{k}}$  and residue  $r_{n,\mathbf{k}}$ . The residue and the dispersion depend strongly on  $U$ . Within RPA the damping  $\Gamma_{n,\mathbf{k}}$  of these modes is zero at  $T = 0$ . Two of the modes are ‘phase modes’ (or Bogoliubov-Goldstone modes), with  $\Omega_{\mathbf{k}} \sim |\mathbf{k}|$  as  $|\mathbf{k}| \rightarrow 0$ . One is of positive energy and another negative. The two other modes, again one of positive energy and

another negative, have  $\Omega_{\mathbf{k}} \rightarrow \text{const}$  as  $|\mathbf{k}| \rightarrow 0$ . These are the ‘amplitude’ (or Higgs) modes. In the Mott phase ( $U > U_c$ ) there are only two modes - one a positive energy ‘particle’ mode and another a negative energy ‘hole’ mode. Both of these are gapped.

With these  $T = 0$  results as reference we summarise our main results on the thermal behaviour of the spectra. We work in two dimensions at density  $n = 1$ . We vary the interaction  $U$  from weak coupling through  $U_c$  to the Mott regime and the temperature from  $T = 0$  to well above the SF to normal transition at  $T_c(U)$ .

1. *Low temperature superfluid:* We find that over the interval  $0 < T \lesssim 0.7T_c$  the  $\Omega_{n,\mathbf{k}}$  and  $r_{n,\mathbf{k}}$  are essentially temperature independent.  $\Gamma_{n,\mathbf{k}}$  behaves approximately as  $\sim \sqrt{T} f_{n,\mathbf{k}}$  where the  $f_{n,\mathbf{k}}$  are weakly momentum dependent.
2. *Superfluid to Bose liquid transition:* Close to  $T_c$  it is hard to distinguish between the gapless and gapped band, as the peaks merge to produce a single band each at positive and negative frequency. The structure is similar to what we observe in the normal Bose liquid.
3. *Low temperature Mott regime:* The Mott phase has two gapped modes, one at positive energy and another at negative energy. The  $\mathbf{k} = 0$  gap between these modes increases with  $U$ , and for a fixed  $U$  it increases with  $T$  - with the rate of change being larger near  $U_c$ . The residue has a weak  $T$  dependence and for both modes we find  $\Gamma \propto \sqrt{T}$ , with a coefficient that reduces with increasing  $U$ .
4. *High temperature Bose liquid:*
  - (a) In the high temperature normal state we discern only one positive mode and one negative mode since the amplitude and phase bands merge. The bandwidth of excitations increases monotonically with  $U$ , the damping peaks at  $U \sim 4t - 5t$  (around which  $T_c$  also peaks).
  - (b) For  $0.9U_c \lesssim U \lesssim U_c$ , the ‘normal Bose liquid’ is gapped above a temperature  $T_g > T_c$ , with progressive increase of the gap with increasing temperature, a feature that it shares with the finite temperature Mott insulator.

The Chapter is organized as follows: Section 4.2 discusses our method for computing the spectra. Section 4.3 discusses our spectral results for the ground state, and Section 4.4 discusses spectra at finite temperature. Section 4.5 provides a semi-analytic framework for understanding the spectral results obtained numerically.

## 4.2 Model and method

We solve the Bose Hubbard model given by:

$$H = -t \sum_{\langle ij \rangle} (b_i^\dagger b_j + h.c.) - \mu \sum_i n_i + \frac{U}{2} \sum_i n_i(n_i - 1) \quad (4.1)$$

where  $t$  is the nearest neighbour hopping, set to  $t = 1$ ,  $U$  is the interaction strength, and  $\mu$  the chemical potential. We decouple the zero frequency part of the kinetic term, described in detail in Chapter 2, to derive an effective Hamiltonian,  $H_{eff}$ . It is a sum of ‘single site’ Hamiltonians with a local hybridising field  $\Phi_i$ .

$$H_{eff} = \sum_i \left[ \frac{U}{2} n_i(n_i - 1) - \mu n_i - (\Phi_i b_i^\dagger + h.c.) + \psi_i^* \psi_i \right] \quad (4.2)$$

The field  $\Phi_i$  is a weighted spatial sum over the original auxiliary field  $\psi_i$ :

$$\Phi_i = \sum_j C_{ij} \psi_j, \quad C_{ij} = \frac{1}{N} \sum_{\vec{k}} \sqrt{A_{\vec{k}}} e^{i\vec{k}(\vec{r}_i - \vec{r}_j)}$$

Once the equilibrium distribution for the auxiliary field  $\{\Phi\}$  is obtained we can compute the boson Green’s function using the following real space implementation of the random phase approximation(RPA) [49]. We briefly recapitulate the RPA approximation below. The Green’s functions for the Bose Hubbard model are given by:

$$\begin{bmatrix} G_{11} & G_{12} \\ G_{21} & G_{22} \end{bmatrix}_{ij,n} = -\frac{1}{Z} Tr \left\{ e^{-\beta H} \begin{bmatrix} b_{i,n} b_{j,n}^\dagger & b_{i,n}^\dagger b_{j,-n}^\dagger \\ b_{i,n} b_{j,-n} & b_{i,-n} b_{j,-n}^\dagger \end{bmatrix} \right\} \quad (4.3)$$



Here  $i, j$  denotes the space labels and  $n$  represents the matsubara frequency index. We compute the Green's function via the 'self avoiding walk' method proposed in the context of the strong coupling expansion. On the mean field state it leads to the same answers as standard RPA but we are not aware of any answers in the finite temperature problem. The detailed method is discussed in the Chapter 2, we only quote the final answer here.

$$\langle G_{i\alpha;j\beta}^{RPA} \rangle = \int \mathcal{D}\psi \mathcal{D}\psi^* G_{i\alpha;j\beta}^{RPA} / \left( \int \mathcal{D}\psi \mathcal{D}\psi^* Tr[e^{-\beta H_{eff}}] \right) \quad (4.4)$$

$$\text{where } \hat{G}^{RPA} = \frac{\hat{G}_0}{(1 + T\hat{G}_0)} \text{ with } T_{i\alpha;j\beta} = t\delta_{i-j,nn}\delta_{\alpha,\beta}$$

$$\begin{bmatrix} G_{11}^0 & G_{12}^0 \\ G_{21}^0 & G_{22}^0 \end{bmatrix}_{ij,n} = -\frac{1}{Z} Tr \left\{ e^{-\beta H_{eff}} \begin{bmatrix} b_{i,n} b_{j,n}^\dagger & b_{i,n}^\dagger b_{j,-n}^\dagger \\ b_{i,n} b_{j,-n} & b_{i,-n} b_{j,-n}^\dagger \end{bmatrix} \right\} \delta_{ij}$$

where  $\hat{G}_0$  is Green's function of the atomic problem and  $T$  is the hopping matrix. We analytically continue  $G^{RPA}(i\omega_n \rightarrow \omega + i\eta)$  to obtain the retarded Green's function. The RPA Green's function is averaged over thermal configurations of the  $\psi$  field. The single particle spectral function is given by

$$A(\mathbf{k}, \omega) = -\frac{1}{\pi} \sum_{i,j} e^{-i\vec{k} \cdot (\vec{r}_i - \vec{r}_j)} \langle Im(G_{i1;j1}^{RPA}) \rangle, \quad N(\omega) = \frac{1}{N} \sum_{\mathbf{k}} A(\mathbf{k}, \omega) \quad (4.5)$$

where  $N(\omega)$  is single particle density of states.

We solve the SPA hamiltonian for each background configuration. Then we construct atomic Green's function matrix,  $\hat{G}_0$ . The atomic Green's function,  $\hat{G}_0$ , is a block diagonal matrix of size  $2L^2 \times 2L^2$ , where  $L^2$  is the number of lattice sites in the system. It includes the 'normal' and 'anomalous' atomic Green's function at each site.

$T$  is the hopping matrix of size  $2L^2 \times 2L^2$  To compute the RPA Green's function for each background we add the hopping matrix to the inverted atomic Green's function for each value of  $\omega + i\eta$  where  $\eta$  is a very small number. We use the imaginary part of RPA Green's function to compute  $A(\vec{k}, \omega)$  and  $N(\omega)$ . We repeat the above procedure for each thermal configuration and take the thermal average. All our results are for system size  $L^2 = 24 \times 24$ .

Given the observed structure of the spectral function as described in the introduction, we tried a four Lorentzian fit to the spectral data in the low temperature superfluid. This involves twelve parameters, 4 residues, 4 ‘center frequencies’ and 4 broadenings, with the sum of the 4 residues being  $\sim 1$  acting as a sum rule check. Elsewhere, *e.g.*, close to  $T_c$ , in the Mott regime, or for the Bose liquid, we have used a two Lorentzian fit. The fitting function has the form

$$A(\mathbf{k}, \omega) = \frac{1}{\pi} \sum_n r_{n,\mathbf{k}} \frac{\Gamma_{n,\mathbf{k}}}{(\omega - \Omega_{n,\mathbf{k}})^2 + \Gamma_{n,\mathbf{k}}^2} \quad (4.6)$$

with  $n$  taking 4 or 2 values as appropriate. Much of the analysis in this paper is based on the estimated parameter set  $\{\Omega_{n,\mathbf{k}}, r_{n,\mathbf{k}}, \Gamma_{n,\mathbf{k}}\}$  for varying  $U$  and  $T$ .

## 4.3 Spectrum at zero temperature

### 4.3.1 Superfluid ground state

Fig.4.1 shows the evolution of the spectrum in the superfluid phase from weak interaction,  $U = 2t$ , to intermediate,  $U = 10t$ , and then to  $U = 15t$ . The critical coupling is  $U_c \approx 24t$  in the problem. The first row shows a map of  $|A(\mathbf{k}, \omega)|$ , for  $\mathbf{k}$  varying from  $(0, 0) \rightarrow (\pi, \pi)$ . The second row shows the lineshape of  $|A(\mathbf{k}, \omega)|$ , since some features are not clear in the spectral map, while the third row shows the DOS  $N(\omega)$ . We note that  $A(\mathbf{k}, \omega) = \theta(\omega)|A(\mathbf{k}, \omega)| - \theta(-\omega)|A(\mathbf{k}, \omega)|$  therefore  $|A(\mathbf{k}, \omega)|$  contains the same information as  $A(\mathbf{k}, \omega)$ .

In the weak coupling superfluid at  $T = 0$  the only mode that has substantial weight is the positive energy gapless mode. This is the Bogoliubov mode associated with the broken symmetry - the Goldstone mode in this problem. When the dominant occupancy is still that of  $\mathbf{k} = (0, 0)$ , the negative energy spectra has very small residue at all  $\mathbf{k} \neq (0, 0)$  since  $\int_{-\infty}^0 d\omega A(\mathbf{k}, \omega) = n_{\mathbf{k}}$  and  $n_{\mathbf{k}} \rightarrow 0$  for all  $\mathbf{k} \neq 0$  as  $\frac{U}{t} \rightarrow 0$ .

Looking at the spectral map, top row in Fig.4.1, already at  $U = 2t$  (left panel) one sees three more bands in addition to the traditional gapless Bogoliubov band. These include a negative energy gapless mode, with linear dispersion, and gapped amplitude bands of positive and negative energy. The negative energy gapped band has very small weight and is visible

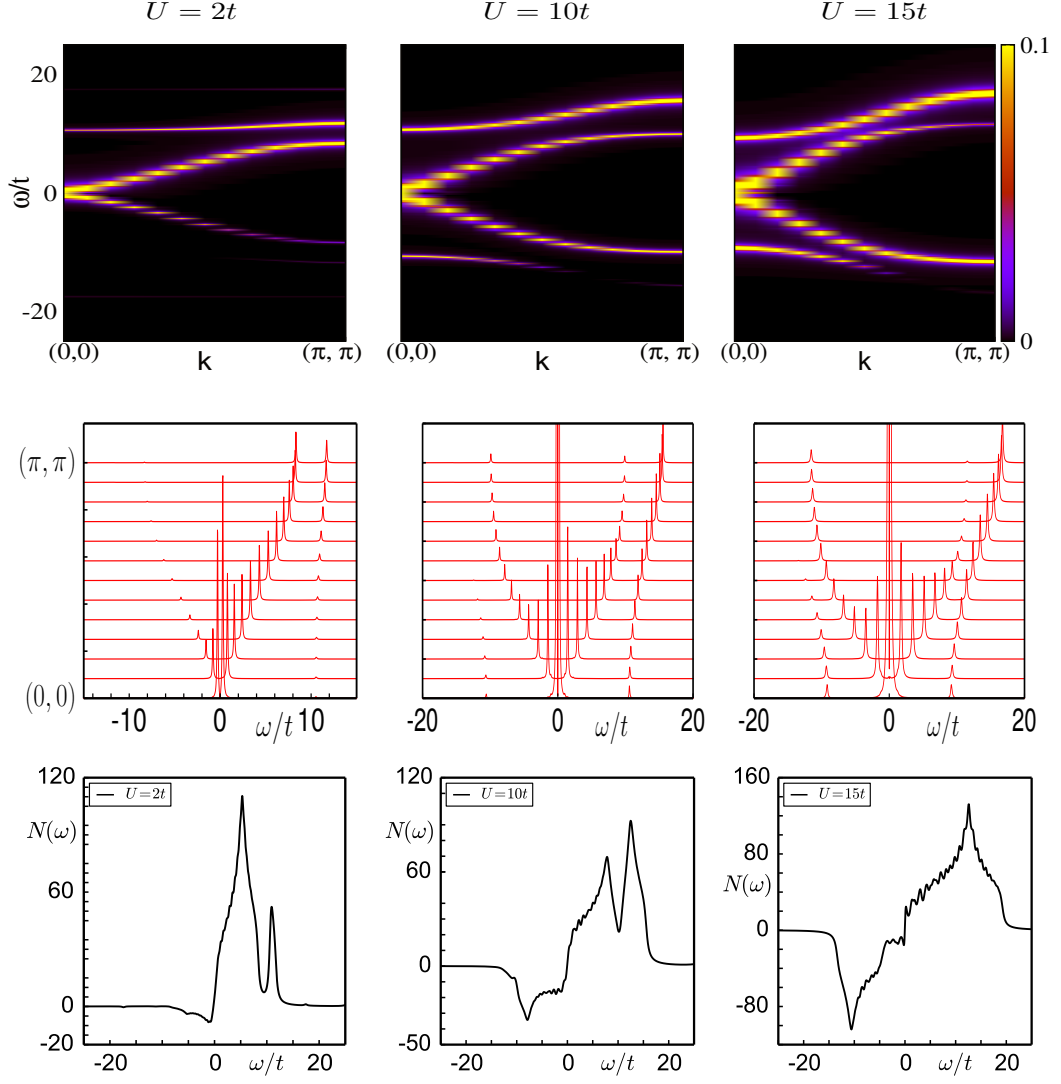


Figure 4.1: Spectral function and density of states in the superfluid ground state. From left to right along each row,  $U = 2t$ ,  $10t$ ,  $15t$ . First row: A map of  $|A(\mathbf{k}, \omega)|$ , where  $A(\mathbf{k}, \omega)$  is the spectral function, for the diagonal scan  $\mathbf{k} : (0, 0) \rightarrow (\pi, \pi)$ . Second row: the lineshape of  $|A(\mathbf{k}, \omega)|$ , highlighting the variation in the residue, and the resolution limited lineshape. Third row: the density of states  $N(\omega)$ . Note the growing negative energy weight as  $U/t$  increases.

only near  $\mathbf{k} = (0, 0)$ . Increasing interaction, middle panel,  $U = 10t$ , and right panel,  $U = 15t$ , makes the weight in the negative energy gapless mode visibly larger (signifying a broader  $n_{\mathbf{k}}$  distribution) as well as more prominent amplitude modes.

The middle row in Fig. 4.1 shows the lines associated with  $|A(\mathbf{k}, \omega)|$ , which are essentially resolution limited at  $T = 0$ . The momenta values in these panels increase from  $(0, 0)$  for the line in the front to  $(\pi, \pi)$  along the diagonal for the line at the back. The patterns reveal the relatively large ‘mass gap’ of the amplitude mode at  $U = 2t$  and its progressive reduction as  $U$  increases

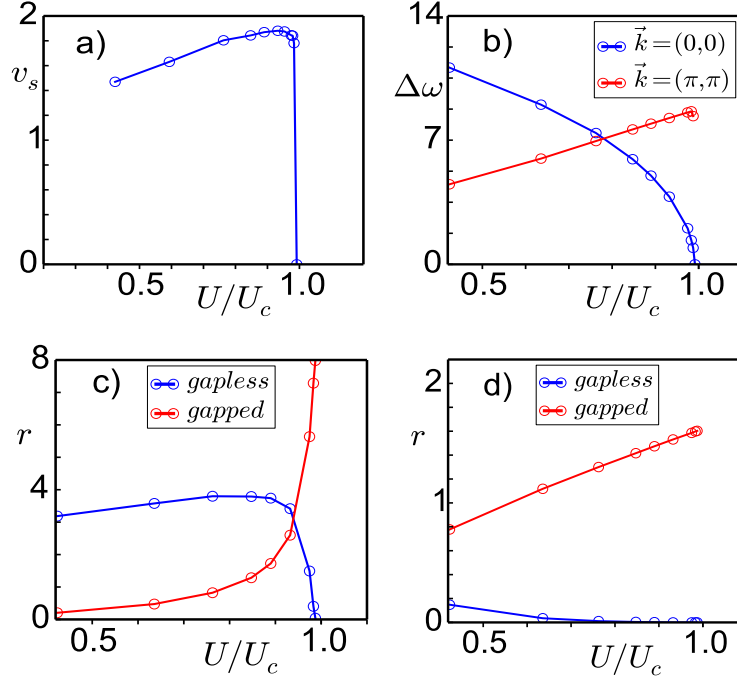


Figure 4.2: Key features of the  $T = 0$  spectrum. (a) Superfluid velocity, (b) difference in energies at  $\mathbf{k} = (0,0)$  and  $(\pi, \pi)$  for the gapless positive mode and the gapped positive mode, (c) dependence of the residue at  $\mathbf{k} = (0,0)$  on  $U/t$ , (d) same at  $\mathbf{k} = (\pi, \pi)$

to  $15t$  (where it is still finite). As interaction strength is increased further, the gap in the positive energy gapped band reduces and ultimately vanishes as one moves close to  $U_c$ .

It also shows that at low  $U$  and low  $\mathbf{k}$  the only relevant mode is continuum like, since weak interaction and low  $\mathbf{k}$  are equivalent to the Nozieres-Leggett [32] theory. However, increasing momentum even at  $U = 2t$  leads to a sizable residue in the amplitude mode, while increasing interaction takes one farther away from the weak coupling continuum picture.

The third row in Fig.4.1, shows the evolution of DOS as a function of interaction strength in the superfluid phase. On the negative frequency axis, the DOS increases with increase in interaction strength. This is related to the condensate depletion as we argued for the spectral map. At positive frequency for small  $U$ , we see a dip in density of states and then again a rise. This arises from the separation of the amplitude and phase bands at small  $U$ . This dip is not visible at large  $U$ , as Goldstone and amplitude mode being close to one another at small momentum and at large  $\vec{k}$ , amplitude mode carries the significant weight and Goldstone mode has an insignificant weight.

In Fig.4.2 we plot some indicators extracted from the  $U$  and  $\mathbf{k}$  dependence of the spectral

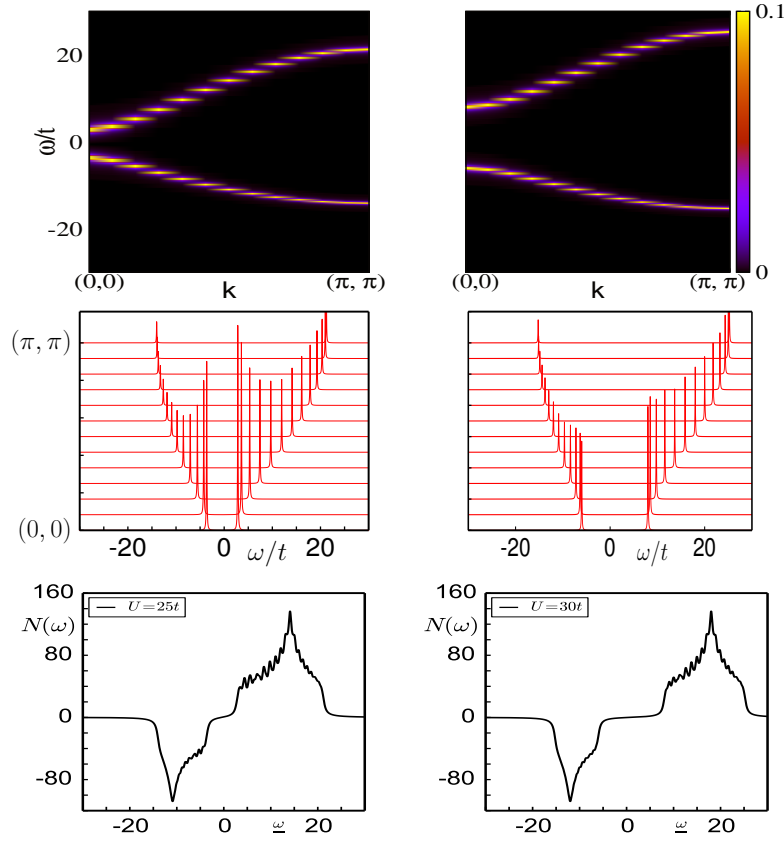


Figure 4.3: Spectral function and density of states in the Mott ground state. From left to right along each row,  $U = 25t, 30t$ . First row:  $|A(\mathbf{k}, \omega)|$  second row: the lineshape of  $|A(\mathbf{k}, \omega)|$ , and third row: density of states  $N(\omega)$ .

functions at more  $U$  values than we have shown in Fig.4.2. The superfluid velocity, panel (a), is calculated as the slope of the dispersion of the positive energy gapless mode as  $\mathbf{k} \rightarrow 0$ . The slope increases with  $U$ . The superfluid velocity increases moderately from  $U = U_c/2$  to  $U \sim U_c$ . Panel (b) shows the separation between the positive energy amplitude and phase modes at  $\mathbf{k} = (0, 0)$  (blue) and  $\mathbf{k} = (\pi, \pi)$  (red). The phase mode is anyway zero energy at  $\mathbf{k} = 0$  so the blue curve basically shows the collapse of the mass gap of the amplitude mode as  $U \rightarrow U_c$ . Panel (c) shows the variation of the small  $\mathbf{k}$  residue with  $U$  for the positive amplitude and phase bands. The amplitude residue is vanishingly small as  $U \rightarrow 0$ , where the phase mode dominates, but overcomes the phase residue as  $U \rightarrow U_c$ . At  $\mathbf{k} = (\pi, \pi)$ , however, the amplitude residue is much larger than the phase residue for the window  $0.5U_c < U < U_c$ . In the discussion section, we try to obtain the analytic expression for dispersions and residue for the superfluid phase close to the superfluid Mott boundary .

### 4.3.2 Mott ground state

In Fig.4.3 the first row shows the map of  $|A(\mathbf{k}, \omega)|$ , the second row shows the lineshape and the third row the DOS for a ‘weak’ Mott insulator,  $U = 25t$  and a ‘deep’ Mott state,  $U = 30t$ . There are only two modes - termed the ‘particle mode’ at positive frequency and the ‘hole mode’ at negative frequency. At  $U = U_c$  both the modes are gapless. As one moves into the Mott phase, both the modes become gapped, the gap between them at  $\mathbf{k} = 0$  increases with  $U$  as  $\sqrt{\epsilon_{\vec{k}=0}^2 + 6U\epsilon_{\vec{k}=0} + U^2}$ , where  $\epsilon_{\vec{k}} = -2t(\cos(k_x a) + \cos(k_y a))$ . The weight of the modes, for fixed  $U$ , decreases as one goes to larger momentum. The reduction of weight with increasing momentum becomes slower at larger  $U/t$ . The weight of modes, at fixed momentum, decrease with increase in  $U$ . We derive expressions for the dispersion and residue later.

Fig.4.3 third row shows the density of states in the Mott phase at  $U = 25t$  and  $U = 30t$ . The gap in the DOS increases with  $U$ . The DOS deep in the Mott phase has a tight binding shape with van Hove feature on both side of the frequency axis.

## 4.4 Spectra at finite temperature

In the previous section, we described the excitation spectra in the superfluid and Mott phase at  $T = 0$ . In this section we describe our results for the excitation spectra at finite temperature. But finite temperature the Bose system can be a superfluid, a normal Bose liquid, or ‘Mott insulator’ (the finite  $T$  Mott phase has no symmetry difference with respect to the Bose liquid).

### 4.4.1 Low temperature superfluid

Fig.4.4 shows the plot of  $|A(\mathbf{k}, \omega)|$  and  $N(\omega)$  for  $U/t = 2, 10, 15$  and varying  $T$ . For  $U = 2t$ , at very low temperature three bands are visible. The increase in temperature leads to reduction in weight and broadening of the excitations. The weight reduction is significant for the negative energy gapless band and positive energy amplitude band. Most of the weight is still being carried by the Bogoliubov band for all momenta at finite temperatures. With rising temperature, as the bands broaden, the positive energy gapless mode and the amplitude mode begin to merge. For superfluid phase at intermediate ( $U = 10t$ ) and strong interaction ( $U = 15t$ ) the spectra has a

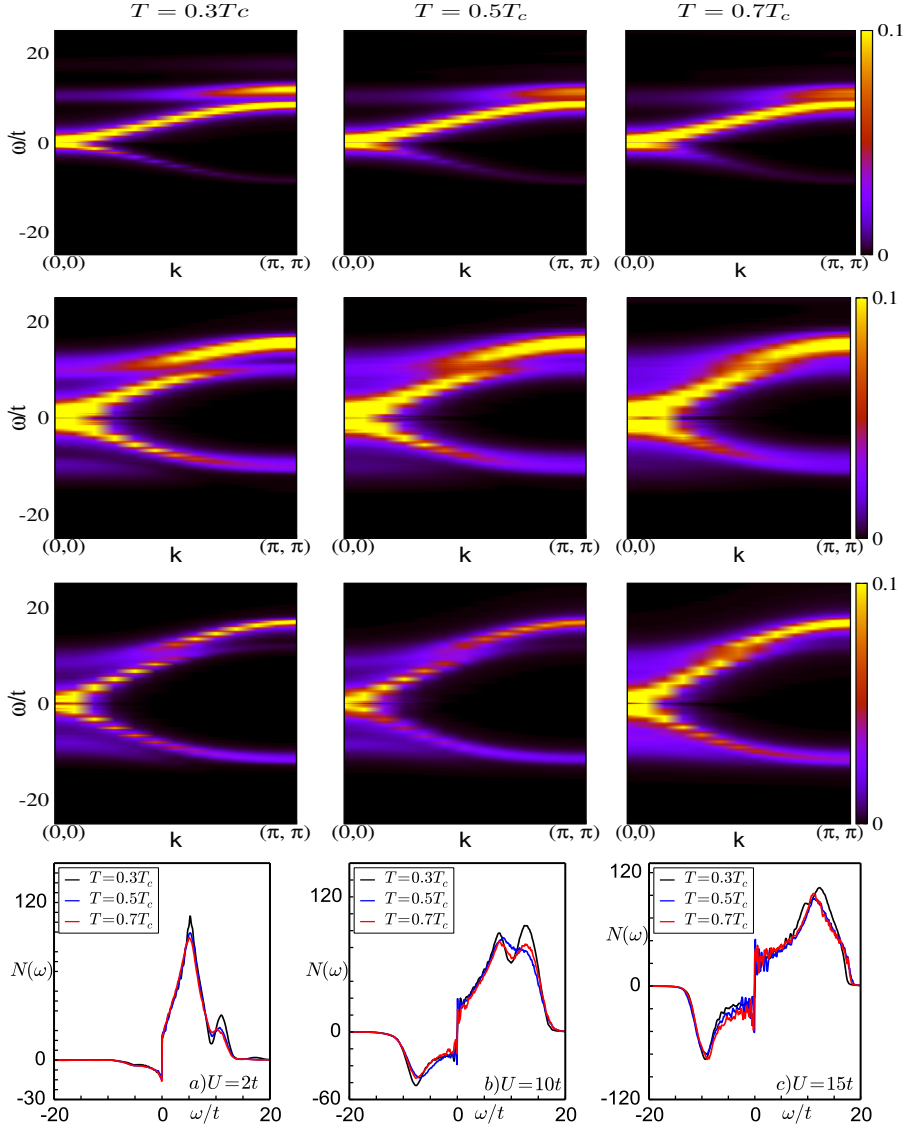


Figure 4.4: Spectral function and density of states in the superfluid phase at finite temperature. Upper rows:  $|A(\mathbf{k}, \omega)|$  with increasing temperature for  $U = 2t$  (first row),  $U = 10t$  (second row) and  $U = 15t$  (third row). Bottom row: density of states  $N(\omega)$ . Notice the merger of the Goldstone mode with the weakly dispersive upper branch as  $T$  is increased, and the loss in weight of the negative frequency branch for  $U = 2t$  and  $10t$ .

four mode structure at low temperature.

Increasing  $T$  leads to broadening of the modes and so a reduction in peak intensity. The reduction seems to be stronger for the negative gapless band and the positive gapless band for  $k$  values above  $(\pi/2, \pi/2)$ . For the positive gapped band the reduction is more severe below  $(\pi/2, \pi/2)$ . By  $0.3T_c$ , the negative energy gapless band at all momenta, except the very small, is only faintly visible. Similarly, positive energy gapless band is faintly visible for large momenta and positive energy gapped band is faintly visible for small momenta.

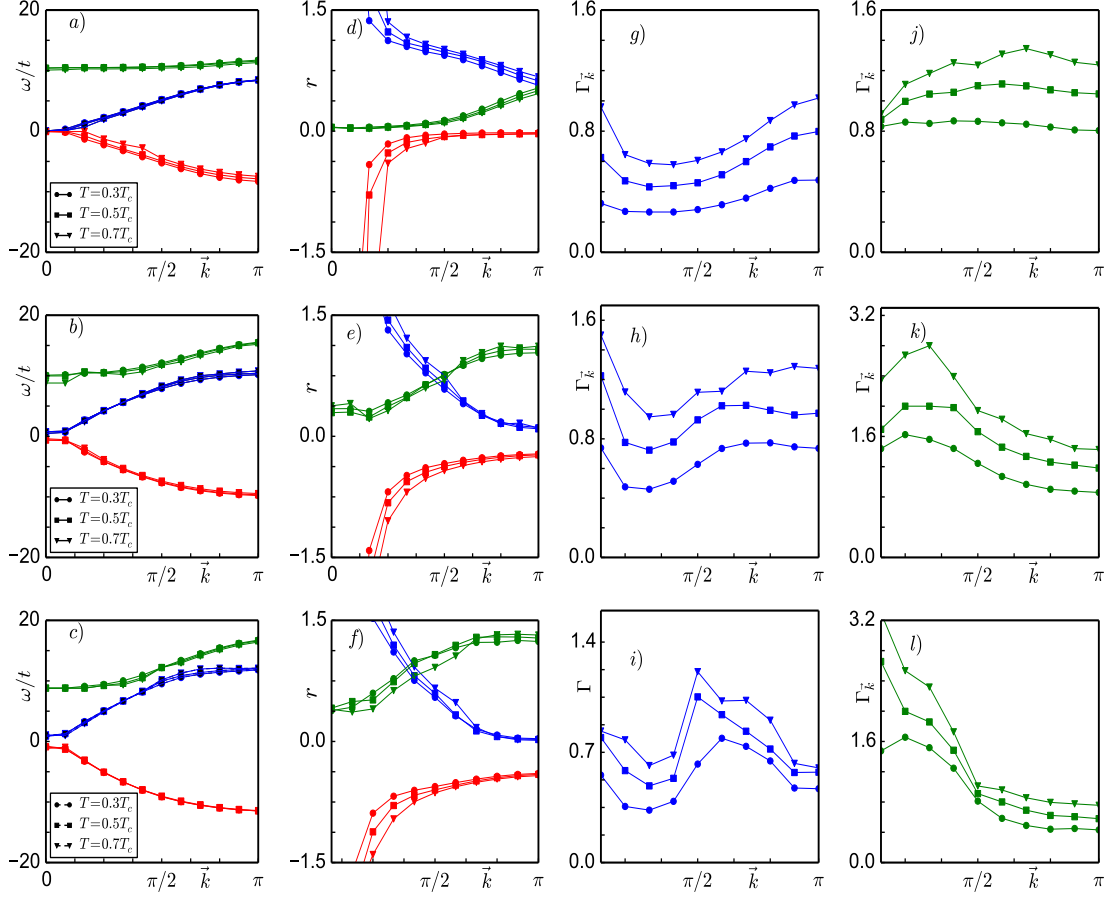


Figure 4.5: Parametrisation of the finite  $T$  spectral data in the superfluid regime. First column: mean dispersion, second column: residue, third column: broadening for the gapless band at positive energy, fourth column: broadening for amplitude band at positive energy. From first row to last row,  $U$  varies from  $2t$ ,  $10t$ ,  $15t$ .

In the last row in Fig.4.4, we show the DOS  $N(\omega)$  for  $U = 2t, 10t$  and  $15t$ . For  $U = 2t$ , there is not much change in the density of states on the negative frequency side with temperature till  $0.7T_c$ . On the positive frequency side, the dip in the density of states at larger  $\omega$  seen at  $T = 0$  is reduced. This is due to broadening of amplitude and gapless mode with temperature. Overall, there is small suppression of DOS on the positive frequency side. Similar features are seen for  $U = 10t$  and  $U = 15t$ .

We track the average dispersion and broadening of the bands by fitting the data to a four peak Lorentzian. We show the results for mean dispersion, residue and broadening for  $\vec{k}$  from  $(0, 0) \rightarrow (\pi, \pi)$  along the diagonal, Fig.4.5. Panels (a)-(c) shows the result for mean dispersion and panels (d)-(f) show the associated residue, for  $U = 2t, 10t, 15t$  respectively. The mean dispersion and residue does not show any significant temperature dependence. The mode



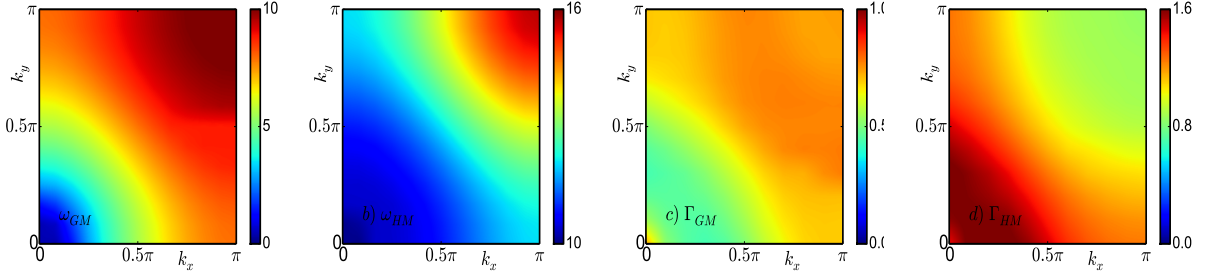


Figure 4.6: Map of the  $k$  dependence of  $\omega_k$  and  $\gamma_k$  for the positive phase band and amplitude band at  $U = 10t$  at  $T = 0.3T_c$  in the first quadrant of Brillouin zone. (a) dispersion  $\omega_{k_x, k_y}$  for the positive gapless band (GM) (b) dispersion  $\omega_{k_x, k_y}$  for the positive amplitude band (HM), (c) broadening  $\Gamma_{k_x, k_y}$  for the positive gapless band (GM), (d) broadening  $\Gamma_{k_x, k_y}$  for the positive amplitude band (HM)

structure remains the same, except, for the superfluid close to  $U_c$ .

The insensitivity of the dispersion and residue to temperature change can be understood roughly as follows. In the RPA Green's function the main input is the atomic Green's functions (see section 4.2). This depends on the energy eigenvalues and eigenvectors of the atomic problem. The energy eigenvalues can be written as an expansion in terms of hybridisation as  $\epsilon_n = a_{0n} + a_{2n}|\Phi_i|^2 + a_{4n}|\Phi_i|^4 + \dots$ . At low temperatures change in mean and width of the hybridisation is small (see fig. 3.6(c) and 3.6(d)). This means that there is a small change in eigenvalues of atomic problem across the site. The residue of the normal component of atomic Green's function, also just depends on amplitude  $\Phi_i$  and not on phase. It is the anomalous part of atomic Green's function that depends on both amplitude and phase of  $\Phi_i$ . At low temperature, the system has large correlation length. So, the change in atomic Green's function is such that one can still think in terms of zero temperature mode structure. The main effect of temperature is on the mode broadening.

Figs.(g), (h), and (i) shows the broadening for the positive gapless band and Figs.(j), (k) and (l) shows the result for broadening for positive gapped band for  $U = 2t, 10t, 15t$  respectively. The broadening seems to grow with temperature. The broadening follows a power law behaviour,  $\Gamma_k \sim T^\alpha$ , for all values of  $U$ , for both the gapless and gapped bands. For  $U = 2t$ , the broadening is roughly  $k$  independent for both the positive gapless and gapped band. At  $U = 10t$ , the broadening shows some  $k$  dependence. The broadening for the positive gapless band has a maximum at small  $k$ , then it decreases and again rises at intermediate  $k$ , and remains constant

till  $k = (\pi, \pi)$ . But for positive gapped band broadening scale decreases with increase in  $k$ . Similar trends are seen at  $U = 15t$ . But  $k$  dependent features become more prominent for both the positive gapless and gapped bands. The broadening scales are comparable for both the gapless and gapped bands at  $U = 2t$ . With increase in interaction strength, broadening scales for gapped bands becomes larger as compared to gapless band. The difference between broadening for gapless and gapped bands is larger for small  $k$  values.

Fig.4.6 shows the map of the  $k$  dep of  $\omega_k$  and  $\Gamma_k$  for the positive amplitude and phase bands, in the first quadrant of the BZ, at  $T = 0.3T_c$  for  $U = 10t$ . Figs (a) and (b) shows the plot of  $\omega_{\vec{k}}$  for positive gapless and positive gapped band and Figs.(c) and (d) shows the plot of  $\Gamma_{\vec{k}}$  for the positive gapless and gapped band respectively. Even at finite temperature dispersion are function of  $|\vec{k}|$ . In the discussion section, we obtain the dispersion for gapless and gapped band in the superfluid phase close to  $U_c$ . Using that as a hint, we find that dispersion could be fit using function  $\sqrt{A + B(1 - \epsilon_{\vec{k}}) + C(1 - \epsilon_{\vec{k}})^2}$ , where A, B and C are fit parameters. For the gapless band,  $A = 0$  and at small momentum  $\omega_{GM}$  is a linear function of momentum. For the amplitude band, we find that,  $A \neq 0$  away from the critical point and dispersion goes as  $A + C|\vec{k}|^2$  for small momentum. Similarly for the broadening also, we find that, it also shows  $|\vec{k}|$  dependence for both gapless and gapped band. For the positive gapless band,  $|\Gamma_{\vec{k}}|$  increases with increase in momentum and for gapped band it decreases with increase in momentum.

To track the  $T$  dependence of broadening at a fix  $\vec{k}$  value, we fit  $\Gamma_{\vec{k}}$  to a power law form  $AT^\alpha$ . Fig.4.7 shows the  $T$  dependence of  $\Gamma$ , for few  $k$  values, for the positive amplitude and phase bands, and  $U = 4t$  and  $10t$ , between 0 to  $0.7T_c$ . Figs.(a) and (b) shows the plot of  $T$  dependence of  $\Gamma_k$  for the positive energy gapless band for  $U = 4t$  and  $10t$  respectively. Similarly Figs.(d) and (e) shows the plot of  $T$  dependence of  $\Gamma_k$  for the positive energy gapped band for  $U = 4t$  and  $10t$ . Symbols are the exact data point, dotted lines are the best fit with power law behaviour  $AT^\alpha$ . In the Figs.(c) and (f), we show the plot of exponent  $\alpha$  as a function of  $\vec{k}$ , for positive gapless and gapped band respectively. For the positive gapless band Fig.(c), the exponent  $\alpha$  is independent of  $k$  and approximately close to 0.6 for  $U = 4t$ . But for  $U = 10t$  the exponent  $\alpha$  changes with  $k$  and varies from 0.75 at small  $k$  to 0.5 at large  $k$ . Again in Fig.(f), for the positive gapped band, the exponent  $\beta$  for  $U = 4t$  remains independent of  $k$  and close to 0.5. For  $U = 10t$

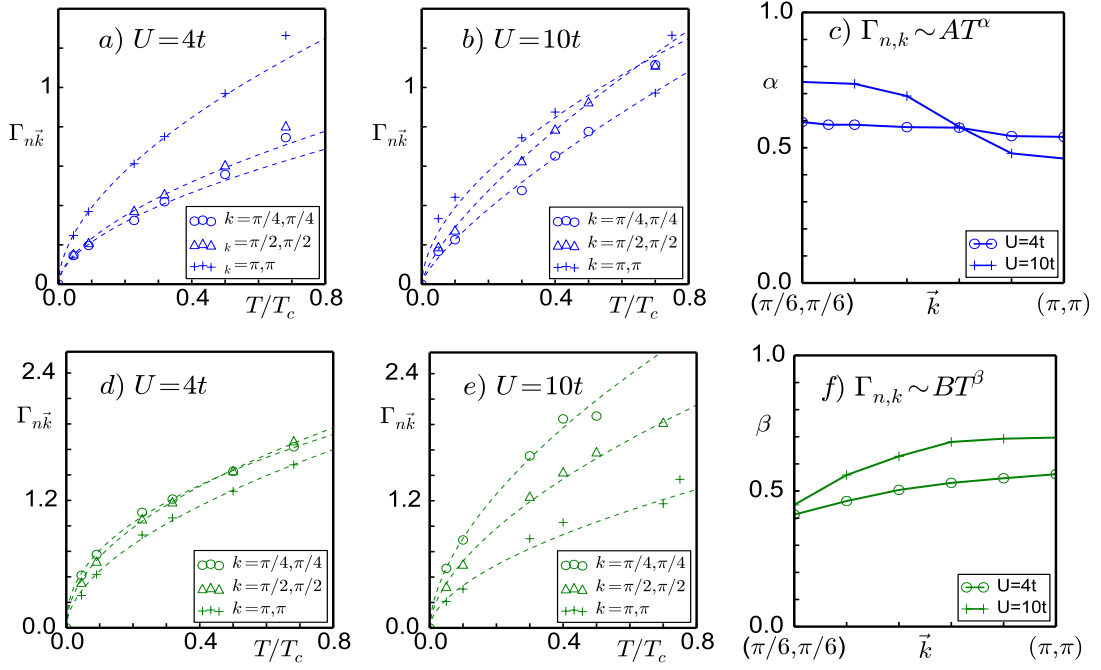


Figure 4.7: Temperature dependence of  $\Gamma_k$  for few  $k$  values. (a)-(b) Positive gapless band, and (d)-(e) positive gapped band.  $U = 4t$  and  $U = 10t$  and  $0 < T < 0.7T_c$ . Symbols are the exact data points and dotted line is the fit using power law form  $\Gamma_k \sim AT^\alpha$ . (c) Exponent  $\alpha$  as a function of  $k$  for  $U = 4t$  and  $10t$  for the positive gapless band. Similarly (f) shows the exponent for the positive gapped band.

the exponent goes from below 0.5 at small  $k$  to close to 0.6 at large  $k$ .

#### 4.4.2 Superfluid to Bose liquid transition

In the low temperature superfluid phase, we find that mode structure remains unchanged and effect of temperature is mainly in the broadening. However, as one moves close to  $T_c$  we know that the mean of the auxiliary field begins to drift quickly from zero temperature value (Fig.3.6(c)). The width of the auxiliary field is also close to 50% of the mean value (Fig.3.6(d)). This suggests that bosons are moving in a strongly ‘disordered’ background. The system can no longer be described as fluctuating around the minima of the mexican hat potential.

Fig.4.8 shows the continuous evolution of the spectral map from  $0.6T_c$  to  $1.2T_c$  at fixed  $U$  value,  $U = 10t$ . At  $0.6T_c$  and  $0.8T_c$  gapless and gapped bands have broadened but not merged completely. The contribution to spectral map due gapless and gapped band can still be distinguished. But as one goes near or above,  $0.9T_c$  this distinction is not possible. The four mode structure seen at low temperature is no longer visible close to  $T_c$ . Now only two broad

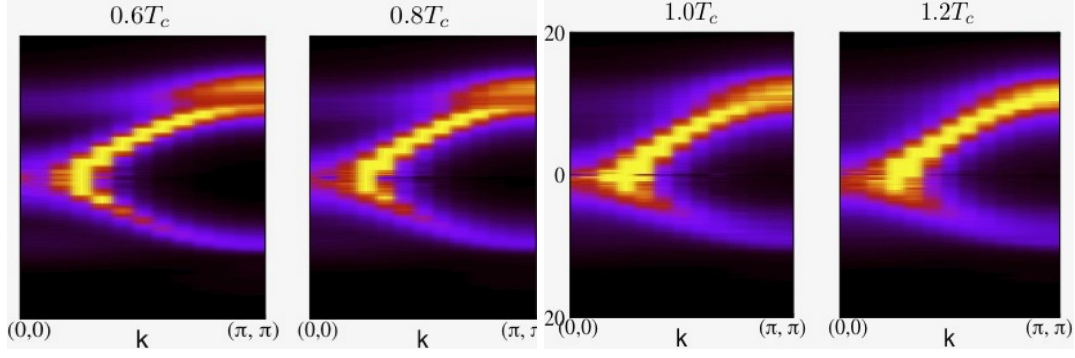


Figure 4.8: Evolution of spectral map for  $U = 10t$  from  $0.6T_c$  to  $1.2T_c$ . Notice the merging of gapless and gapped band as temperature rises.

bands can be seen, one on the positive side of the frequency axis and one on the negative side frequency axis.

In Fig.4.9, we show the evolution of the spectral map as one goes from below  $T_c$  to above  $T_c$ . The spectral map evolves continuously as one goes above the critical temperature. No sharp features are visible. At  $U = 2t$ , the reminiscent gapless and gapped band on the positive side of the frequency axis can be seen, close to  $T_c$ . But for other values of  $U$ , only single band on both the positive and negative side of the frequency axis can be seen.

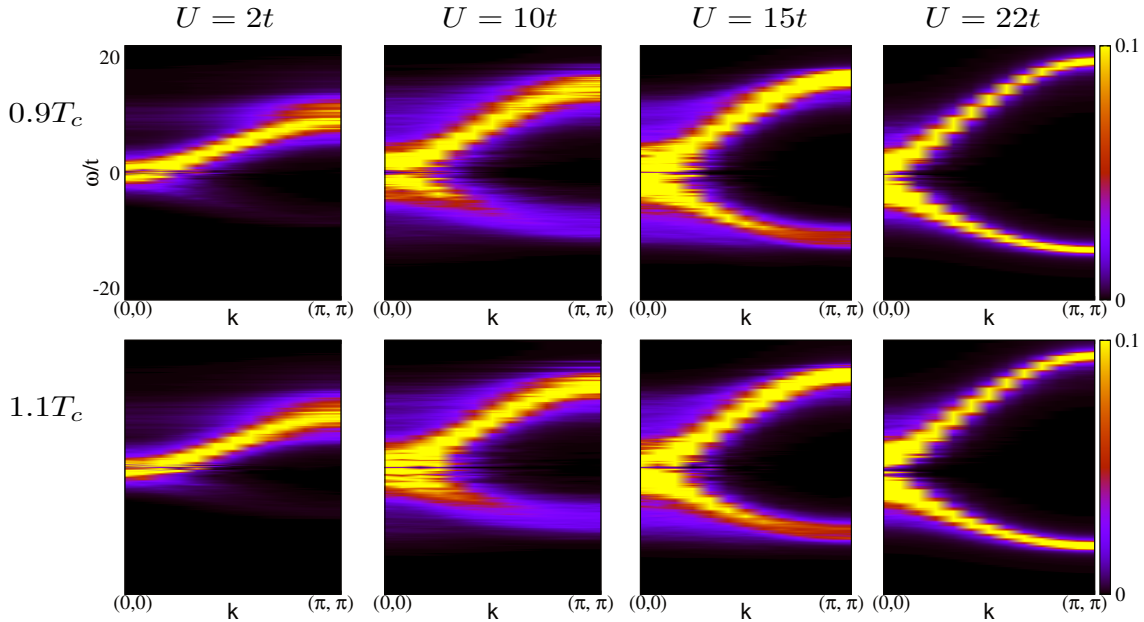


Figure 4.9: Spectral map for  $U = 4t, 10t, 15t, 22t$  close to  $T_c$ . There is continuous evolution of spectral map as one goes from below  $T_c$  to above  $T_c$ . No sharp features are seen in the spectral map as one goes above the transition temperature.

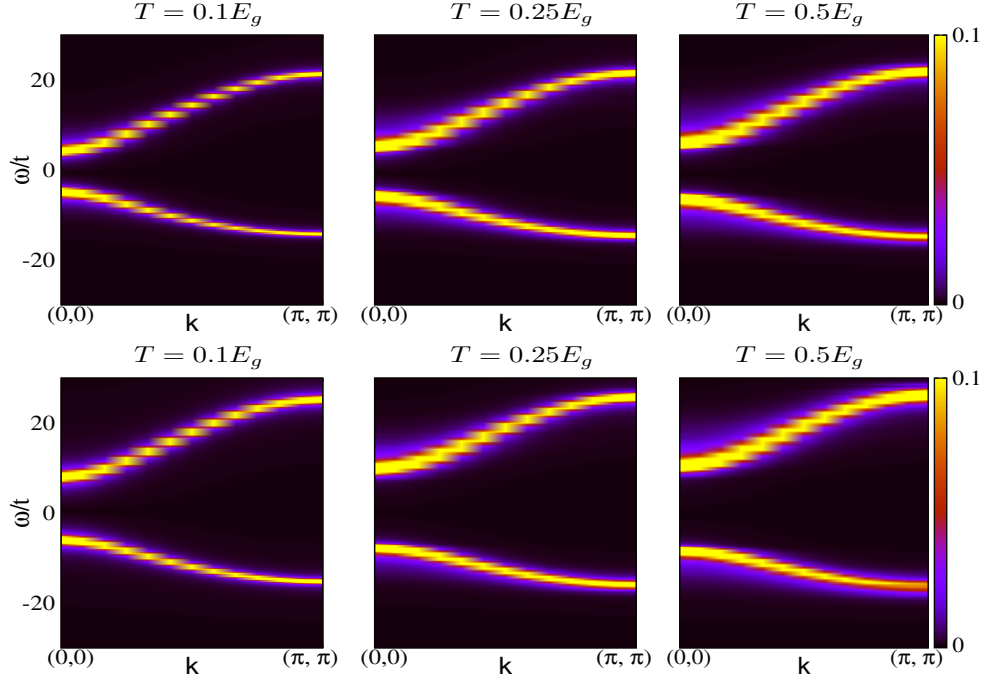


Figure 4.10: Spectra in the finite temperature Mott state.  $|A(\mathbf{k}, \omega)|$  with increasing temperature. First row:  $U = 25t$ , second row:  $U = 30t$ .

#### 4.4.3 Low temperature Mott phase

In the previous section, we studied the evolution of excitation spectra from superfluid to normal phase. In this section, we would look at the finite temperature results in the Mott phase. Fig.4.10 shows the plot of  $|A(\mathbf{k}, \omega)|$  for  $U = 25t$  and  $U = 30t$ . We have probed the Mott phase till temperature of the scale 0.5 times the Mott gap. Even till such high temperature, excitation spectra show two mode structure and no thermally generated extra mode is visible. The mode structure consists of particle mode on the positive side of the frequency axis and hole mode on the negative side of the frequency axis. The weight of the particle and hole mode is seen decreasing with temperature. The magnitude of the gap grows with rise in temperature.

Fig.4.11 shows the plot of  $N(\omega)$  for  $U = 25t$  and  $U = 30t$ . The effect of temperature on  $N(\omega)$  is sharp reduction of van-Hove like peak, increase in gap with both  $U$  and  $T$ . But overall DOS retains its feature at all temperatures.

We fit the data to the two peak Lorentzian and obtain residue, mean, dispersion and broadening scales shown in Fig.4.12. For low  $\vec{k}$  average dispersion again indicates an increase in gap with increase in temperature. But for intermediate to large  $\vec{k}$ , dispersion does not show much temperature dependence. The residue depletes with temperature but the depletion is small.

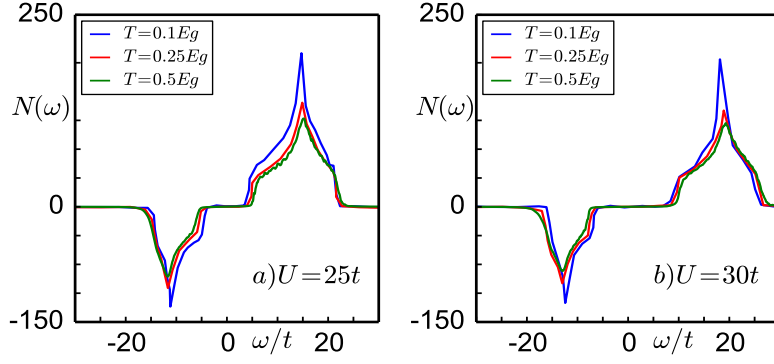


Figure 4.11: Density of states  $N(\omega)$  (a)  $U = 25t$  and (b)  $U = 30t$ . The increase in gap and suppression of van-Hove like peak with temperature is visible

The broadening is seen increasing with temperature and has small momentum dependence. The broadening scales roughly goes as  $T^{1/2}$ . Above results could be understood in terms of distribution of auxiliary field. Since,

$$H_{eff}^i = \underbrace{\left[ \frac{U}{2} n_i (n_i - 1) - \mu n_i \right]}_{H_0} - \underbrace{(\Phi_i b_i^\dagger + h.c.)}_{H_p} + \psi_i^* \psi_i \quad (4.7)$$

At zero temperature the value of hybridisation is zero in the Mott phase. The eigenvalues of  $H_0$  are  $-\mu, 0, U - \mu$  with 1, 0, 2 particle eigenstate. So the poles of atomic Green's function are at  $-\mu$  and  $U - \mu$  with residue -1 and 2 respectively. Temperature leads to generation of non-zero

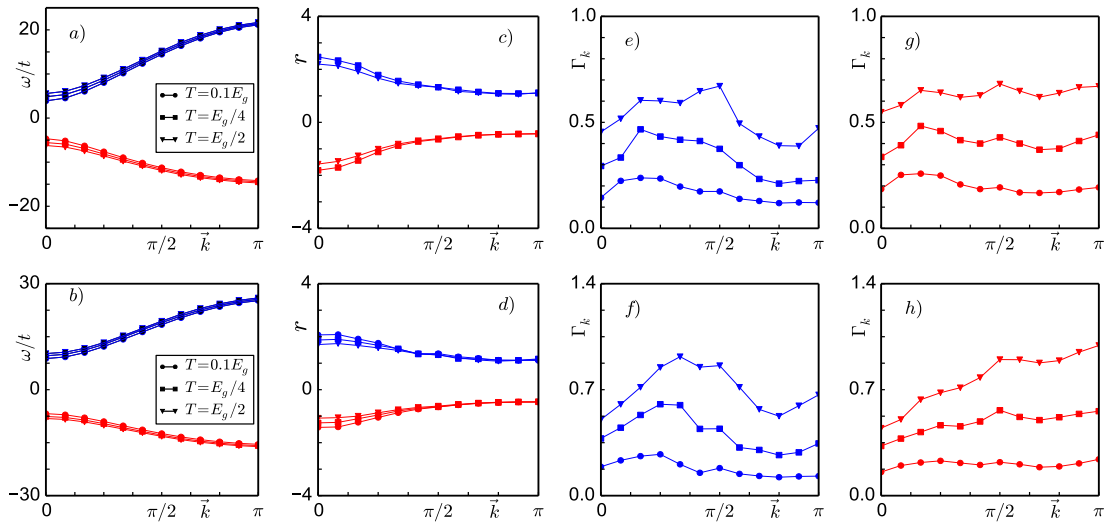


Figure 4.12: Parametrisation of the spectral data. First column: mean dispersion, second column: residue, third column: broadening for the particle band, fourth column :broadening for hole band. Top row:  $U = 25t$ , Bottom row:  $U = 30t$ .

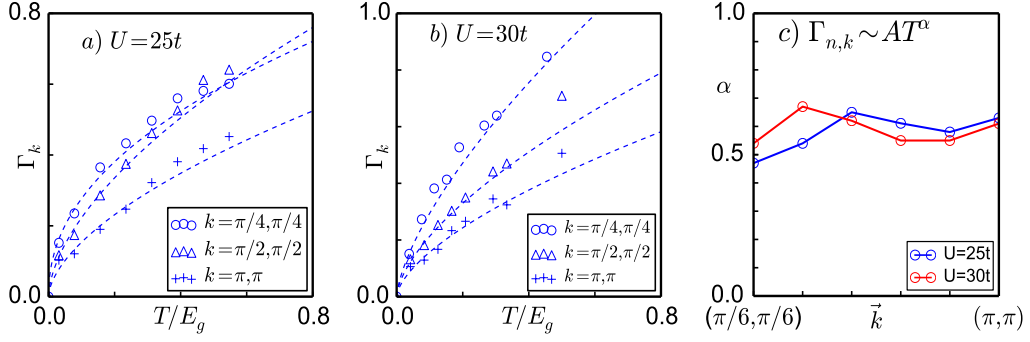


Figure 4.13: Temperature dependence of  $\Gamma_k$  for few  $k$  values for the positive gapped band shown in (a) for  $U = 25t$  and (b) for  $U = 30t$  between 0 to  $0.5E_g$ . Symbols are the exact data points and dotted line is the fit using power law form  $\Gamma_k \sim AT^\alpha$ . (c) shows the plot of exponent  $\alpha$  as a function of  $k$  for  $U = 25t$  and  $30t$  for the positive gapped band.

hybridisation. In the presence of non-zero hybridisation, energy eigenvalues and eigenstates of  $H_{eff}$  can be obtained by including perturbative corrections due to  $H_p$  on eigenstates of  $H_0$ . If one corrects the energy eigenvalues to second order in  $\Phi_i^2$ , the effect of non-zero hybridisation leads to shifts in the pole of atomic Green's function to  $-\mu - \alpha(U, \mu)|\Phi_i|^2$  and  $U - \mu + \beta(U, \mu)|\Phi_i|^2$  and residue has a weaker dependence on hybridisation. Here  $\alpha$  and  $\beta$  are positive definite functions.

In the Mott phase, both mean and width of the auxiliary field go as  $T^{1/2}$  (Fig.3.12). Since mean is non zero and increases as a function of temperature. So effectively, the gap between poles of the normal part of atomic Green's increases with temperature. As we know the RPA Green's function, is derived out of atomic Green's function (see section 4.2). The correlation length in Mott phase is one atomic spacing. This implies anomalous Green's function is approximately zero. The changing hybridisation with temperature only affects the diagonal component of the Green's function. Since the gap between poles of atomic Green's function increases with increase in temperature, this leads to an increase in gap in the mean value of dispersion at small  $\vec{k}$ . The width of the auxiliary field controls the broadening. Thus broadening shows power law behaviour similar to  $\Phi_{wid}$  (Fig.3.12(d)).

In Fig.4.13 we show the temperature dependence of  $\Gamma_k$  for the particle band for a few  $k$  values. We fit  $\Gamma_k$  to power law form  $\alpha T^{1/2}$ . Symbols are the exact data points and dotted lines are the best fit. Figs (a) and (b) show the result for  $\Gamma_k$  for  $U = 25t$  and  $U = 30t$  respectively. Figs (c) shows the plot of exponent  $\alpha$  as a function of  $\vec{k}$ . The exponent  $\alpha$  is roughly close to 0.5



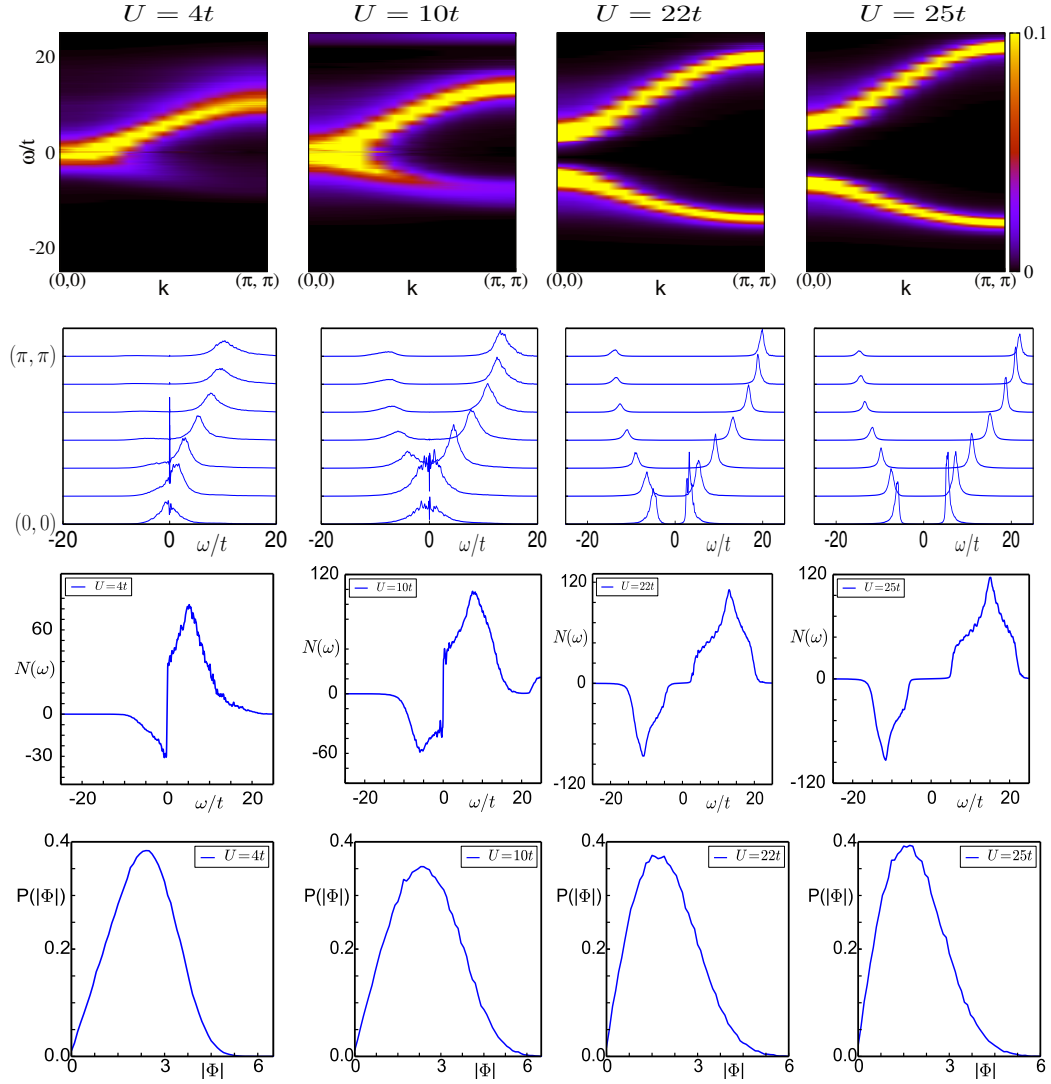


Figure 4.14: The effect of increasing interaction in the  $T > T_c$  normal Bose liquid. First row:  $|A(\mathbf{k}, \omega)|$  second row: lineshapes, third row:  $N(\omega)$  Fourth row:  $P(|\Phi|)$ . From left to right  $U = 2t, 10t, 22t, 25t$ . The opening of gap with increasing interaction strength is visible. The temperature is  $T = 3t$ .

upto fairly large temperature for both  $U = 25t$  and  $U = 30t$ . The broadening scales are similar for the hole band as well.

#### 4.4.4 High temperature Bose liquid

We show the effect of increasing interaction strength in the normal phase in Fig.4.14. The temperature we chose is  $T = 3.0t$ , this is above the  $T_c^{max} \approx 2.4t$ . Fig.4.14 shows the plot of  $|A(\mathbf{k}, \omega)|$ , lineshapes, density of states and  $P(\Phi)$  for increasing interaction at  $T = 3.0t$ . At  $T = 3.0t$  the normal Bose liquid shows two mode structure. For the weakly ( $U = 4t$ ) and



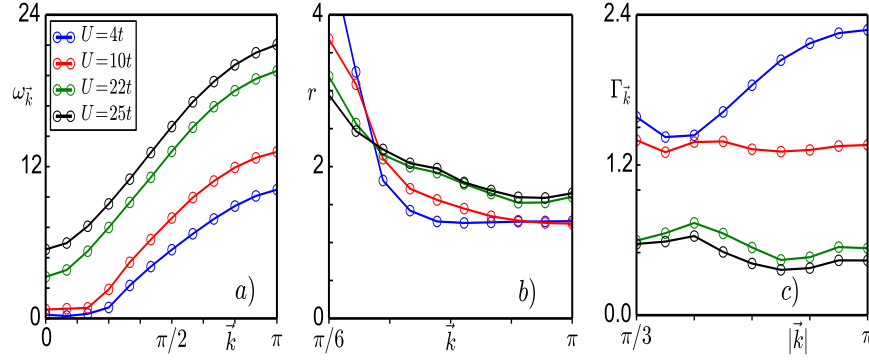


Figure 4.15: (a) Dispersion, (b) residue and (c) damping for the  $U$  variation at  $T = 3t$ .

intermediate interacting ( $U = 10t$ ) bose liquid excitation spectrum is gapless. But for a Bose liquid close to  $U_c$  ( $U = 22t$ ), a gap opens up in the single particle excitation spectra. The magnitude of the gap increases with increase in interaction strength. This can be clearly seen from spectral map and density of states. The asymmetry in density of states between positive and negative frequency axis also reduces with increasing interaction. The width of the distribution is roughly same across the interaction strength at  $T = 3t$ .

Fig.4.15(a) shows the plot of dispersion in the normal phase at  $T = 3.0t$ . All plots are for the positive energy band as a function of wavevectors for few  $U$  values. Fig (b) shows the plot of residue. At small values of interaction strength there is a sharp decrease in residue with increase in wavevector. As one increases interaction strength this decrease becomes more gradual. Fig (c) shows the broadening in the normal phase. The broadening decreases as one increases interaction strength. The variation in broadening with interaction strength at large  $\vec{k}$  is more pronounced as compared to small wave vectors. Fig.4.16 shows the broadening at few  $\vec{k}$  values as a function of interaction strength. The broadening behaves non-monotonically with increasing interaction

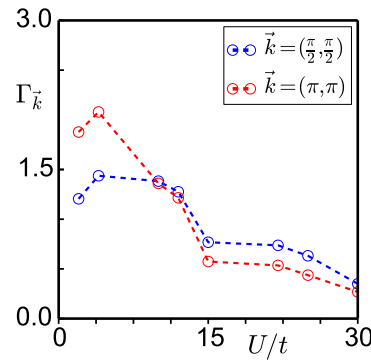


Figure 4.16:  $U$  dependence of the positive mode damping for few  $k$  values at  $T = 3t$ .

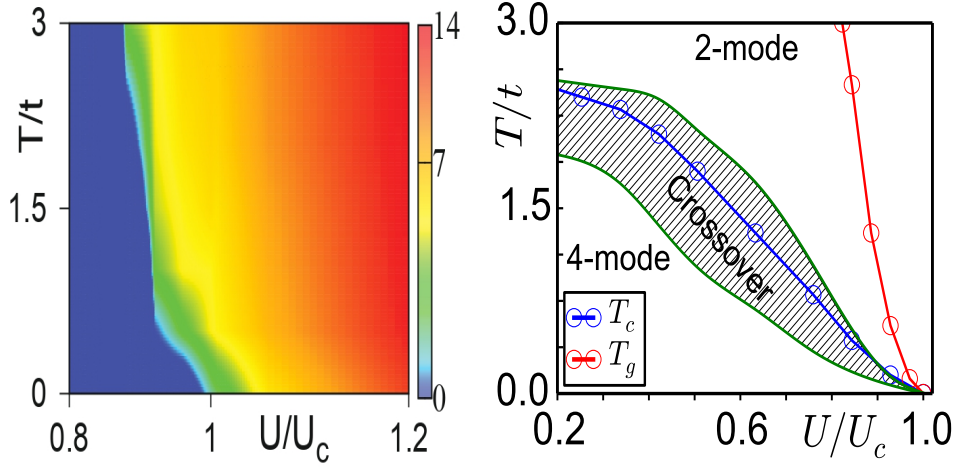


Figure 4.17: Left Panel: Map of the single particle gap in the spectrum between  $0.8U_c$  to  $1.2U_c$  for temperature between 0 to  $3t$ . The temperature rise leads to opening of gap even below  $U_c$ . With increase in temperature single particle gap begins to increase. Right Panel: ‘Phase diagram’ of the 2D-BHM in terms of its spectral properties. Shows the superfluid to normal transition temperature,  $T_c$ , the temperature  $T_g$  above which the spectrum shows a gap. Below the shaded area the spectrum is four mode and four mode fit works well. Above the shaded area, spectrum has two bands one on the positive side of the frequency axis and another on the negative side of the frequency axis. Within the shaded area transition from four mode to two mode occurs due to merging of gapped and gapless band with rising temperature.

strength. The maxima of broadening occurs at  $U = 4t$ .

#### 4.4.5 Finite temperature phase diagram

On the basis of the results in the previous section, we draw a finite temperature phase diagram in terms of (i) Low energy spectral gap (ii) Nature of mode structure. The results are shown in Fig.4.17. The left panel in Fig.4.17 shows the plot of magnitude of the gap in the single particle density of states, as a function of temperature, for  $U$  values between  $0.8U_c$  and  $1.2U_c$ . Even for  $U < U_c$  the gap begins to show up. The magnitude of the gap rises with increase in temperature.

Depending on the nature of spectral function at finite temperature, we draw a  $U - T$  phase diagram in the right panel of Fig.4.17. The  $T_c$  curve demarcates the superfluid phase from normal phase. The normal phase is further separated into a gapped and gapless phase using  $T_g$ . There is a smooth crossover from gapless normal liquid phase to the left of  $T_g$ , to the gapped normal liquid phase, to the right of  $T_g$ . The phase diagram is further characterised in terms of mode structure of the spectral function. Below the shaded region mode structure is essentially four peaked. There is a smooth crossover from four peaked spectral function to two peaked spectral function above

the shaded area. The shaded region belongs to the transition region. Here excitation spectra has hints of four mode structure. One can reasonably fit the spectral data in the shaded region, using both four mode and two mode.

## 4.5 Discussion

In this section we try to understand the zero temperature and finite temperature results in terms of an effective model.

### 4.5.1 Analysing the $T = 0$ results

At  $T = 0$  the field  $\phi_i$  is uniform,  $\phi_0$  say, so the Green's function is:

$$G(\vec{k}, \omega) = \frac{1}{G_{at}^{-1}(\omega, \phi_0) - \epsilon(\vec{k})} \quad (4.8)$$

where  $G_{at}(\omega, \phi_0)$  is the atomic Green's function in the presence of a 'hybridisation'  $\phi_0$ .  $G_{at}(\omega, \phi_0)$  is a sum of simple poles at  $T = 0$ . RPA Green's function also has a set of undamped excitations for each  $\vec{k}$ . Very close to superfluid-Mott transition phase boundary order parameter  $|\phi_0|^2$  is small.

For small  $|\phi_0|^2$  one can approximate,

$$G_{at}(\omega, \phi)^{-1} \approx G_{at}(\omega, 0)^{-1} - \Sigma \quad (4.9)$$

where  $\Sigma$  is the self energy due to the presence of non-zero value of hybridisation. The details are given in Appendix B. When the value of hybridisation is zero, occupation number basis forms the good eigen states. The presence of non-zero hybridisation creates mixing in number basis states. It leads to generating a non-zero self energy.

$$\Sigma = \begin{bmatrix} g\phi_0^2/f & g\phi_0^2/2f \\ g\phi_0^2/2f & g\phi_0^2/f \end{bmatrix} \quad (4.10)$$

where  $f = (\frac{1}{\mu} - \frac{2}{-U+\mu})^2$  and we have included only zero frequency part in the self energy.  $g$  is

the static contribution due to four point function.

So RPA Green's function can be approximated by,

$$\bar{G}(\vec{k}, \omega) \approx \frac{1}{[\bar{G}_{at}(\omega, 0)]^{-1} - \Sigma - \epsilon(\vec{k})} \quad (4.11)$$

#### 4.5.1.1 Mott phase

Within the Mott phase  $\phi_0 = 0$ , which implies  $\Sigma = 0$ .

$$G(\vec{k}, \omega)_{1,1} = \frac{1 - z_{\vec{k}}}{\omega - E_{\vec{k}}^-} + \frac{z_{\vec{k}}}{\omega - E_{\vec{k}}^+} \quad (4.12)$$

where

$$E_{\vec{k}}^{\pm} = \epsilon_{\vec{k}} + U - 2\mu \pm \sqrt{\epsilon_{\vec{k}}^2 + 6\epsilon_{\vec{k}}U + U^2}/2$$

and

$$z_{\vec{k}} = \frac{E_{\vec{k}}^+ + \mu + U}{E_{\vec{k}}^+ - E_{\vec{k}}^-}$$

The Mott phase has two branches namely particle and hole mode. where  $E_{\vec{k}}^+$  is the dispersion of particle mode and  $E_{\vec{k}}^-$  is the dispersion of hole mode.  $z_{\vec{k}}$  and  $1 - z_{\vec{k}}$  are the residue of particle and hole mode respectively.

#### 4.5.1.2 Superfluid phase

If we solve for the approximated RPA Green's function in presence of  $\Sigma$ , instead of two modes in the Mott phase, presence of non-zero hybridisation leads to four mode structure. The (1, 1) component of  $G(\vec{k}, \omega)$  is given by,

$$G(\vec{k}, \omega)_{1,1} = \frac{z_{\vec{k},gm}^+}{\omega - E_{\vec{k},gm}^+} + \frac{z_{\vec{k},hm}^+}{\omega - E_{\vec{k},hm}^+} + \frac{z_{\vec{k},gm}^-}{\omega - E_{\vec{k},gm}^-} + \frac{z_{\vec{k},hm}^-}{\omega - E_{\vec{k},hm}^-} \quad (4.13)$$

Where,  $E_{\vec{k},gm}^+$  and  $E_{\vec{k},hm}^+$  are the dispersion for positive energy gapless and gapped bands, and,  $E_{\vec{k},gm}^-$  and  $E_{\vec{k},hm}^-$  for the negative energy gapless and gapped bands.

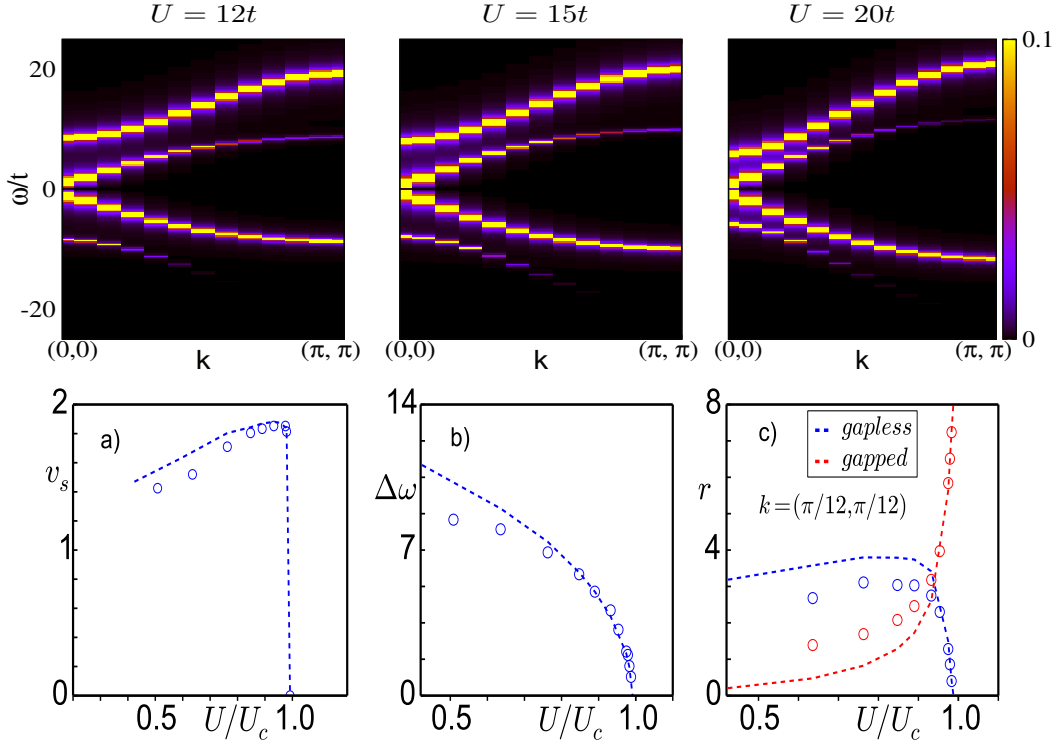


Figure 4.18: Spectral results obtained by approximating the atomic Green's function to order  $|\Phi|^2$ . Top row: Spectral map in the superfluid phase. Along the row  $U = 12t, 15t, 18t$ . Bottom row: Comparison between exact RPA in the groundstate with the approximate calculation. Dotted line is the exact result and open circles are result from approximate calculation. (a) superfluid velocity obtained from slope of dispersion of gapless band (b) amplitude mode gap at  $\vec{k} = (0, 0)$  (c) residue of gapless and gapped band at  $\vec{k} = (\pi/12, \pi/12)$ .

$$E_{k,gm}^+ = \sqrt{-\frac{F_{\vec{k}}}{2} - \frac{1}{2}(F_{\vec{k}}^2 - 4C_{\vec{k}})^{1/2}}$$

$$E_{k,gm}^- = -\sqrt{-\frac{F_{\vec{k}}}{2} - \frac{1}{2}(F_{\vec{k}}^2 - 4C_{\vec{k}})^{1/2}}$$

$$E_{k,hm}^+ = \sqrt{-\frac{F_{\vec{k}}}{2} + \frac{1}{2}(F_{\vec{k}}^2 - 4C_{\vec{k}})^{1/2}}$$

$$E_{k,hm}^- = -\sqrt{-\frac{F_{\vec{k}}}{2} + \frac{1}{2}(F_{\vec{k}}^2 - 4C_{\vec{k}})^{1/2}}$$

where  $|E_{k,gm}^+| = |E_{k,gm}^-|$  and  $|E_{k,hm}^+| = |E_{k,hm}^-|$ . The dispersions are symmetric around  $\omega = 0$

$$z_{\vec{k}}^{\pm} = \frac{D_{\vec{k}}}{2} \pm (D_{\vec{k}}^2 - 4H_{\vec{k}})^{1/2}$$

$$D_{\vec{k}} = 2\mu - U + g\phi_0^2/f + \epsilon_{\vec{k}}$$

$$H_{\vec{k}} = (2\mu - U)^2/4 - U^2/4 + (g\phi_0^2/f + \epsilon_{\vec{k}})(\mu + U)$$

$$F_{\vec{k}} = 2H_{\vec{k}} - D_{\vec{k}}^2 + (g\phi_0^2/2f)^2$$

$$C_{\vec{k}} = H_{\vec{k}}^2 - (g\phi_0^2/2f)^2(\mu + U)^2$$

$z_{k,gm}^+$  and  $z_{k,hm}^+$  are the residue for the positive energy gapless and gapped bands ,and,  $z_{k,gm}^-$  and  $z_{k,hm}^-$  are the residue for the negative energy gapless and gapped bands.

$$\begin{aligned} z_{\vec{k},gm}^+ &= -\frac{(E_{k,gm}^+ + U + \mu)(E_{k,gm}^+ - z_{\vec{k}}^+)(E_{k,gm}^+ - z_{\vec{k}}^-)}{2E_{k,gm}^+(E_{k,hm}^{+2} - E_{k,gm}^{+2})} \\ z_{\vec{k},gm}^- &= -\frac{(E_{k,gm}^+ - U - \mu)(E_{k,gm}^+ + z_{\vec{k}}^+)(E_{k,gm}^+ + z_{\vec{k}}^-)}{2E_{k,gm}^+(E_{k,hm}^{+2} - E_{k,gm}^{+2})} \\ z_{\vec{k},hm}^+ &= \frac{(E_{k,hm}^+ + U + \mu)(E_{k,hm}^+ - z_{\vec{k}}^+)(E_{k,hm}^+ - z_{\vec{k}}^-)}{2E_{k,hm}^+(E_{k,hm}^{+2} - E_{k,gm}^{+2})} \\ z_{\vec{k},hm}^- &= \frac{(E_{k,hm}^+ - U - \mu)(E_{k,hm}^+ + z_{\vec{k}}^+)(E_{k,hm}^+ + z_{\vec{k}}^-)}{2E_{k,hm}^+(E_{k,hm}^{+2} - E_{k,gm}^{+2})} \end{aligned}$$

Top row in Fig.4.18 shows the result for spectra obtained from the above approximate calculation for  $U = 12, 15t, 20t$ . To make comparison in the bottom row, we plot (a)superfluid velocity, (b)amplitude mode gap and (c)residue of gapless and gapped band at  $\vec{k} = (\pi/12, \pi/12)$ . We plot exact RPA results and approximate results together. The exact results are given by dotted line and approximate results are given by open circles. Close to the SF-Mott boundary match is excellent. The results begin to deviate as one moves away from the transition point.

#### 4.5.2 A model for finite $T$ spectra

Our method is a generalisation of the RPA to finite temperature. It has two key differences with respect to the  $T = 0$  scheme. We emphasize these and then set up an approximation that provides some analytic insight into the numerical answers.

(i) At  $T = 0$  the field  $\phi_i$  is uniform,  $\phi_0$  say, so the Green's function is:

$$G(\vec{k}, \omega) = \frac{1}{G_{at}^{-1}(\omega, \phi_0) - \epsilon(\vec{k})} \quad (4.14)$$

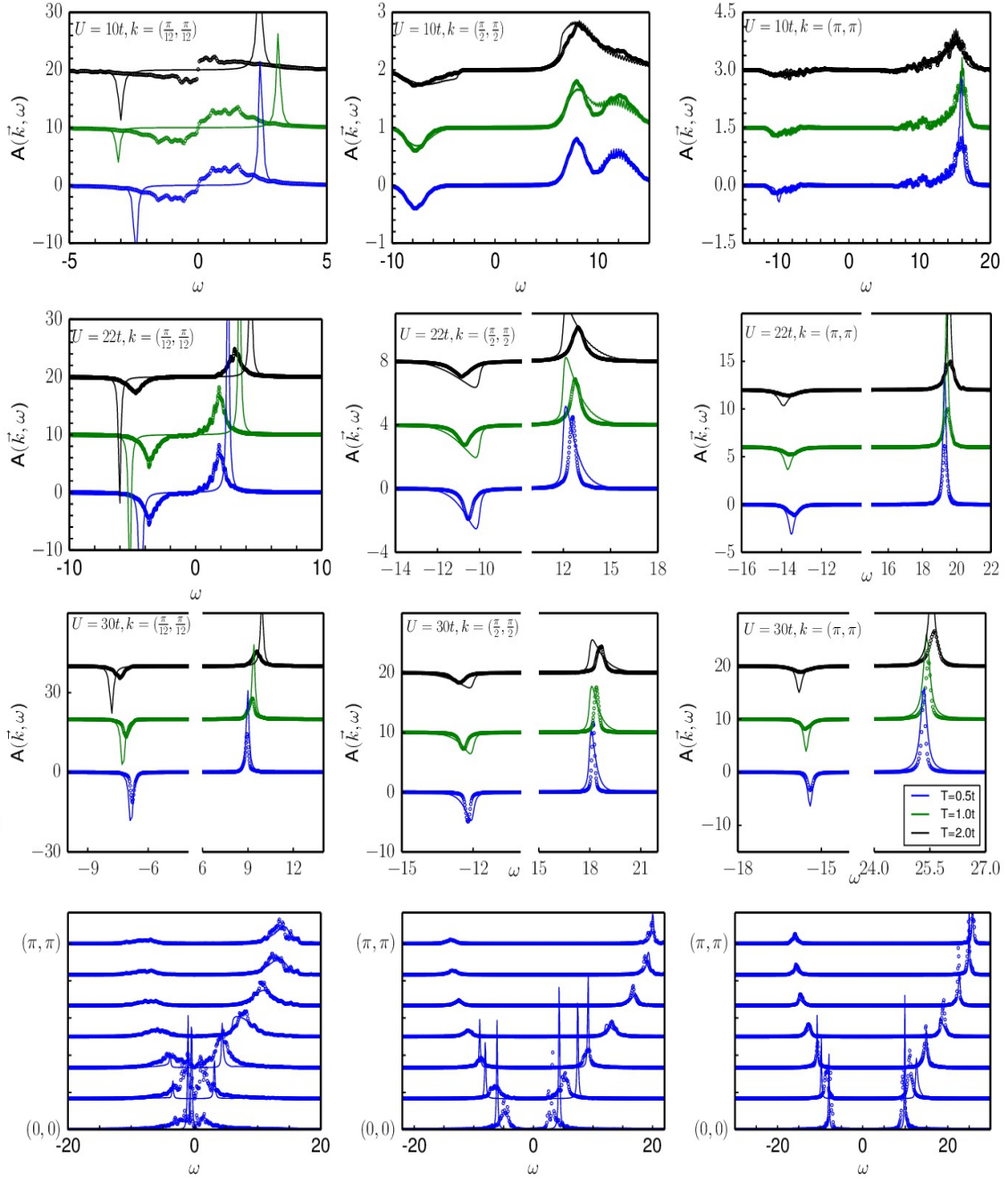


Figure 4.19: Comparison between spectra obtained from exact RPA calculation and approximate calculation at three  $U$  values and for three  $\vec{k}$  as a function of temperature. Top row  $U = 10t$ , Middle row  $U = 22t$  and Third row  $U = 30t$ . For each of these comparison is shown at three temperature values  $T = 0.5t, 1.0t, 2.0t$ . The match between two calculation is good at large  $\vec{k} = (\pi/2, \pi/2)$  and  $(\pi, \pi)$  but at  $(\pi/12, \pi/12)$  match is bad except deep in the Mott phase. Last row shows the comparison of lineshapes obtained from two calculation in the normal state  $T = 3.0t$ .  $U$  values are  $10t, 22t, 30t$  as one moves along the row. Solid lines are approximate calculation and open circles are exact results.

where  $G_{at}(\omega, \phi_0)$  is the atomic Green's function in the presence of a 'hybridisation'  $\phi_0$ . At finite  $T$  the  $\phi_i$  are spatially fluctuating so for *each configuration*  $\{\phi\}$  one has to use the real space

version of the Green's function expression:

$$G_{ij}(\omega, \{\phi\}) = G_{at}^{ii}(\omega) [\mathcal{I} - t_{ij} G_{at}^{jj}(\omega)]^{-1} \quad (4.15)$$

where the atomic Green's functions depend on the  $\phi$  at the respective site. The calculation is implemented in real space and retains information about the site to site variation of the  $\phi_i$ . The expression above should be interpreted as a series summed to infinite order:

$$G_{ij}(\omega, \{\phi\}) = G_{at}^{ii}(\omega) \delta_{ij} + G_{at}^{ii}(\omega) t_{ij} G_{at}^{jj}(\omega) + G_{at}^{ii}(\omega) t_{i\alpha} G_{at}^{\alpha\alpha}(\omega) t_{\alpha j} G_{at}^{jj}(\omega) + .. \quad (4.16)$$

(ii) The  $G_{ij}(\omega, \{\phi\})$  needs to be averaged over the equilibrium distribution  $P\{\phi\} \sim e^{-\beta H_{eff}\{\phi\}}$ ,

$$\bar{G}_{ij}(\omega) = \langle G_{ij}(\omega, \{\phi\}) \rangle_{\{\phi\}}$$

This averaging is implemented numerically by computing  $G_{ij}$  via matrix inversion for each  $\{\phi\}$  and performing an average over equilibrium configurations. The momentum resolved, thermally averaged Green's function is:

$$\bar{G}(\vec{k}, \omega) = \frac{1}{N} \sum_{i,j} \bar{G}_{ij}(\omega) e^{i\vec{k} \cdot (\vec{r}_i - \vec{r}_j)} \quad (4.17)$$

The two non trivial steps therefore are (i) the inversion of a  $2N \times 2N$  matrix for each  $\{\phi\}$ , and (ii) averaging the Green's function over a correlated  $\{\phi\}$  distribution.

To devise an approximation we note that:

$$\begin{aligned} \bar{G}_{ij}(\omega) &= \langle G_{at}^{ii}(\omega) \delta_{ij} + G_{at}^{ii}(\omega) t_{ij} G_{at}^{jj}(\omega) + G_{at}^{ii}(\omega) t_{i\alpha} G_{at}^{\alpha\alpha}(\omega) t_{\alpha j} G_{at}^{jj}(\omega) + .. \rangle_{\{\phi\}} \\ &= \langle G_{at}^{ii}(\omega) \rangle \delta_{ij} + t_{ij} \langle G_{at}^{ii}(\omega) G_{at}^{jj}(\omega) \rangle + t_{i\alpha} t_{\alpha j} \langle G_{at}^{ii}(\omega) G_{at}^{\alpha\alpha}(\omega) G_{at}^{jj}(\omega) \rangle + .. \end{aligned} \quad (4.18)$$

Since the distribution  $P\{\phi\}$  is spatially correlated the averages over products of Green's functions *do not factorise*. Let us, nevertheless, try that as a starting approximation, *i.e.*,

$$\langle G_{at}^{ii}(\omega) G_{at}^{jj}(\omega) \rangle = \langle G_{at}^{ii}(\omega) \rangle \langle G_{at}^{jj}(\omega) \rangle, \text{ etc}$$



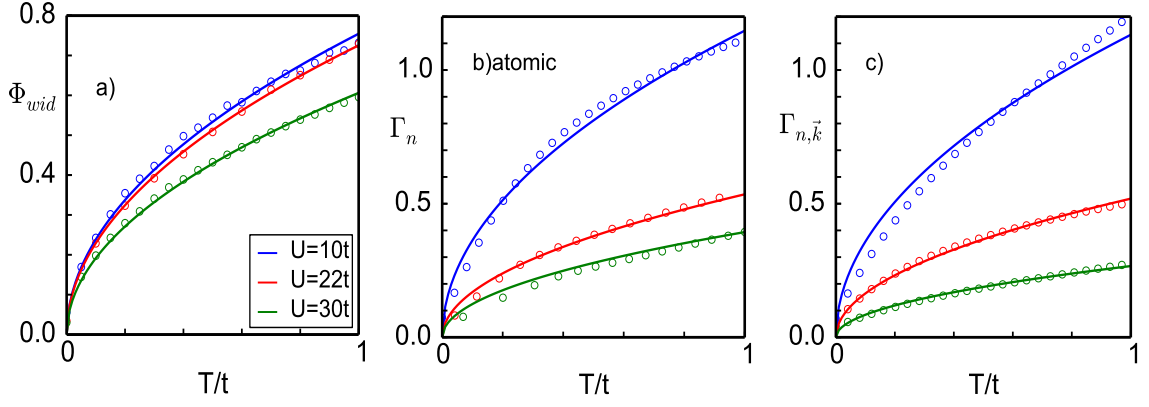


Figure 4.20: Temperature dependence of amplitude ‘width’ and damping scales. a)  $\Phi_{wid}$  b) width of atomic Green’s function around one of the  $T = 0$  pole. c) width of positive band obtained from exact RPA calculation at  $\vec{k} = (\pi/2, \pi/2)$ . The results are shown for  $U = 10t, 22t, 30t$ . Open circles are exact results and firm lines are  $T^{1/2}$  fit, indicating the tempearture behaviour is same for all these quantities.

For our translation invariant system  $\langle G_{at}^{ii}(\omega) \rangle = \bar{G}_{at}(\omega)$  independent of the site  $i$ , where

$$\bar{G}_{at}(\omega) = \int d\phi P(\phi) G_{at}(\omega, \phi) \quad (4.19)$$

Note that the thermally averaged  $G_{at}$  above, in a crucial difference from the  $T = 0$  result, has *branch cuts* rather than simple poles. The series sum for  $\bar{G}_{ij}(\omega)$  is now trivial, and after Fourier

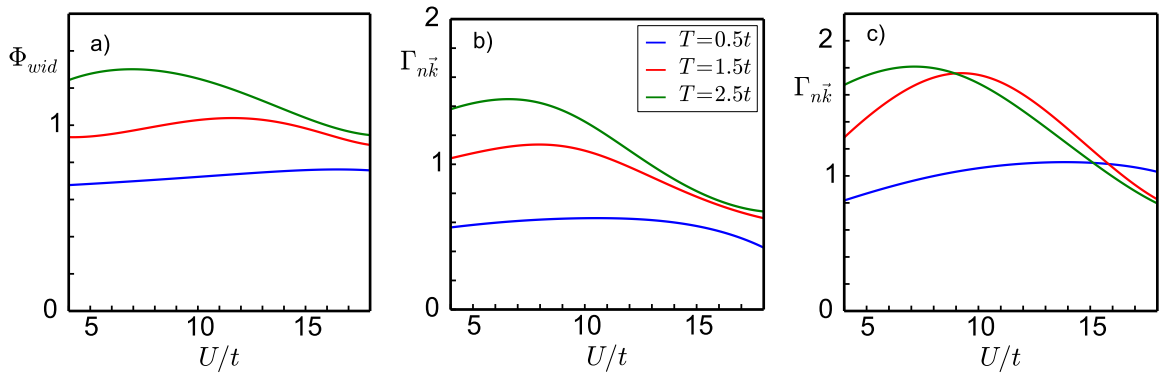


Figure 4.21:  $U$  dependence of amplitude ‘width’ and damping scales. a)  $\Phi_{wid}$  b) width of positive gapless band. c) width of gapped positive band obtained from exact RPA calculation at  $\vec{k} = (\pi/2, \pi/2)$ . The results are shown for  $T/t = 0.5t, 1.5t, 2.5t$ . The curves are non-monotonic as a function of interaction strength with point of maxima shifting to lower  $U$  values as temperature rises.

transforming one obtains:

$$\bar{G}(\vec{k}, \omega) = \frac{1}{[\bar{G}_{at}(\omega)]^{-1} - \epsilon(\vec{k})} \quad (4.20)$$

The  $T = 0$  RPA had already generated a dispersion, the point of this exercise is get a handle on the damping of the excitations.

Where is the damping?  $P(\Phi)$  is characterised by mean and width. A width in  $P(\phi)$ , as would happen at finite  $T$ , leads to an associated  $\Gamma$  in  $\bar{G}_{at}(\omega)$  and via this to a damping in  $\bar{G}(\vec{k}, \omega)$ .

Let us compare the results obtained in this scheme to that of full matrix inversion in the MC backgrounds. Fig.4.19 reproduces the full spectral function data (open circles), at three  $U$ , three temperatures, and  $\vec{k} = (\pi/12, \pi/12)$ ,  $(\pi/2, \pi/2)$ ,  $(\pi, \pi)$ . The approximate results are shown as firm lines. In our reading, the match is poor at  $\vec{k} = (\pi/12, \pi/12)$  (left column), good at  $(\pi/2, \pi/2)$  (centre) and reasonable at  $(\pi, \pi)$  (right). We note that the full calculation at low  $\vec{k}$  has problems of its own, related to normalisation.

If we accept this as a reasonable first approximation some analytic progress can be made in understanding the damping. We proceed in two steps: (i) connecting the observed broadening of the  $P(\Phi)$  distribution, which encodes some information about inhomogeneity in the background, to the thermally averaged atomic Green's function  $\bar{G}_{at}(\omega)$ , and (ii) relating the features of  $\bar{G}_{at}(\omega)$  to the features of  $\bar{G}(\vec{k}, \omega)$ .

The atomic Green's function for some hybridisation  $\phi$  is obtained by diagonalising the local problem in the occupation number basis. This leads to a form

$$G_{at}(\omega, \phi) = \sum_n \frac{\alpha_n(\phi)}{(\omega - \epsilon_n(\phi))} - \frac{\beta_n(\phi)}{(\omega + \epsilon_n(\phi))} \quad (4.21)$$

Averaging this numerically over  $P(\phi)$  leads to a complicated  $\omega$  dependence. We *parametrise* it by the form:

$$\bar{G}_{at}(\omega) = \sum_n \frac{\bar{\alpha}_n}{(\omega - \bar{\epsilon}_n) + i\Gamma_{n+}} - \frac{\bar{\beta}_n}{(\omega + \bar{\epsilon}_n) + i\Gamma_{n-}} \quad (4.22)$$

Similar parametrisation can be done for other components of atomic Green's function. The  $\bar{\alpha}$ ,  $\bar{\epsilon}$ ,  $\bar{\beta}$  need not be close to their  $T = 0$  value (although they usually are), while  $\Gamma_n$  is an explicitly  $T \neq 0$  feature due to thermal fluctuations.

The parametrisation allows us to analyse the RPA Green's function. Using the expression above, let's analyse the RPA Green's function in the Mott phase where the off diagonal component of  $G_{at}$  can be dropped off. Though similar analysis would hold for superfluid phase

$$\bar{G}(\vec{k}, \omega) = \frac{1}{[\bar{G}_{at}(\omega)]^{-1} - \epsilon(\vec{k})} \quad (4.23)$$

and

$$\bar{G}_{at}(\omega) = \sum_n \frac{\bar{\alpha}_n}{(\omega - \bar{\epsilon}_n) + i\Gamma_{n+}} - \frac{\bar{\beta}_n}{(\omega + \bar{\epsilon}_n) + i\Gamma_{n-}} \quad (4.24)$$

This expression, by definition, captures the  $T = 0$  RPA result, *i.e.*, real poles of  $\bar{G}(\vec{k}, \omega)$ . We label these roots  $\omega_{n,\vec{k}}$ . What happens when  $\Gamma_n \neq 0$ , but small? We can track the locus of each of the  $\omega_{n,\vec{k}}$  in a perturbation expansion in the  $\Gamma$ . The algebra is straightforward, and it leads to an expression of the form

$$\omega_{n,\vec{k}}^{\pm} \rightarrow \omega_{n,\vec{k}} + i \sum_m \Gamma_{m\pm} A_k^{mn} = \omega_{n,\vec{k}} + i\Gamma_{n,\vec{k},\pm} \quad (4.25)$$

The functions  $A_k^{mn}$  depend on the location of the RPA real roots. In this limit, the  $T$  dependence of quasiparticle damping,  $\Gamma_{n,\vec{k}}$ , will be the same as that of the  $\Gamma_n$ . We observe that at low  $T$  the  $\Gamma_n \propto \sqrt{T}$  and find that the  $\Gamma_{n,\vec{k}}$  also indeed behave like  $\sqrt{T}$  shown in Fig.4.20. In fact, the full spectral function also has a  $\sqrt{T}$  damping up to fairly high temperature and it saturates beyond  $T_c$ . Fig.4.21 shows the plot of  $\Phi_{wid}$  and broadening for positive gapless and positive gapped band at a fixed  $\vec{k}$  value as a function of interaction strength at three temperature values. The three panels shows similar qualitative behaviour with point of maxima shifting to smaller  $U$  values with rise in temperature.

## 4.6 Conclusions

We have presented results on the single particle spectral function of the Bose Hubbard model at integer filling as the interaction drives the system from a superfluid to the Mott state. Our generalisation of the standard mean field theory retains all the classical thermal fluctuations in the problem. This, as we have discussed in the previous Chapter, is an excellent method for computing the thermal transition scale in the problem. In the thermally fluctuating backgrounds we implement a real space ‘RPA’, equivalent to the ‘self avoiding walk’ method of strong coupling theory. We classify the spectral behaviour in terms of ‘four mode’ and ‘two mode’. Four mode spectra is seen only in the low temperature superfluid. Everywhere else, in the higher temperature superfluid, the normal Bose liquid, and the Mott phase, the momentum resolved spectrum has only two peaks. We establish the detailed behaviour of the spectral function in terms of their dispersion, weight, and damping. Among the striking finite temperature results we observe a ‘gapped’ spectrum in what is supposed to be a strongly correlated ‘Bose liquid’. We suggest an approximate scheme to understand the finite temperature results.

# Spin-orbit coupled correlated bosons in an optical lattice

## 5.1 Introduction

In Chapters 3-4 we studied the physics of strong correlation in the single species Bose Hubbard model. Several recent cold atomic experiments tune Raman processes to create artificial spin-orbit couplings in multicomponent Bose systems [167–169]. Most of these experimental procedures produce an equal mixture of Rashba and Dresselhaus coupling, which leads to an effective Abelian gauge field for the bosons. However, there have been concrete proposals to experimentally realize purely Rashba type spin-orbit coupling [170]. This is equivalent to a non-Abelian gauge-field for two component bosons.

The ground state phase diagram of such systems have been theoretically studied [99–101, 157, 158]. These studies employed several theoretical techniques such as mean field theories[158], simulated annealing of effective quantum spin models[157], real space bosonic dynamical mean field theory (BDMFT) [101], and strong coupling expansion [99, 100]. They have unearthed a rich ground state phase diagram for these systems. Some of the unconventional phases found include those with long range magnetic order in the Mott ground state [157] and the possibility of a boson condensate at finite momentum [99, 100]. Such studies have also been supplemented by their weak-coupling counterparts in the continuum where there is no Mott transition. The weakly

interacting condensates have been studied using the Bogoliubov-Hartree-Fock approximation [102].

In spite of several studies on the ground state, only limited theoretical work exists on the thermal phases of spin-orbit coupled systems. For Abelian systems with equal mixture of Rashba and Dresselhaus coupling, Ref. [103] derives an effective  $t - J$  model for the bosons and studies the thermal phases of this effective model. The study reveals a stripe superfluid order at low temperature and a two step melting upon increasing temperature, leading first to a striped normal phase of the bosons and then to a homogeneous state. Similar studies were carried out for two component fermions in optical lattices [171]. However the thermal phases of Bose-Einstein condensates (BECs) in the presence of Rashba spin-orbit coupling have not been studied before. This is particularly pertinent since an equal mixture of Rashba and Dresselhaus terms breaks the four-fold rotation symmetry of the lattice, while the Rashba spin-orbit term keeps it intact. This leads to the possibility of superfluid phases with lower symmetry than that of the lattice.

In this chapter, we study the thermal phases of a two-species Bose-Hubbard model in the presence of a Rashba spin-orbit coupling. Our study thus involves bosons in the presence of an effective non-Abelian gauge field. In what follows, we use an auxiliary field decomposition of the kinetic energy followed by a ‘classical’ approximation to the auxiliary field described in detail in chapter 2. We then carry out a Monte-Carlo study of the resulting model, sampling the auxiliary field configurations.

We start by deriving an effective Hamiltonian whose mean field ground state coincides, in the main, with earlier results [157]. Our results on this problem are the following: (i) We find that the ground state is either a Mott insulator, or a superfluid with condensation either at a single wavevector ( $\mathbf{k}_0$ ) or two wavevectors ( $\pm\mathbf{k}_0$ ). The  $\pm\mathbf{k}_0$  condensate constitutes a spin density wave, while the finite  $\mathbf{k}_0$  condensate is a phase twisted superfluid [100]. (ii) The superfluid has associated ‘magnetic’ textures - related to the spatially varying spin state occupancy. (iii) Increasing temperature leads to the simultaneous loss of superfluidity and order in the magnetic textures. We establish the  $T_c$  scale for varying Hubbard interaction, interspecies coupling and spin-orbit interaction using our Monte Carlo scheme. (iv) The momentum distribution function,  $n_{\mathbf{k}}$ , evolves from its ‘low symmetry’ character at low temperature to four-fold symmetry as

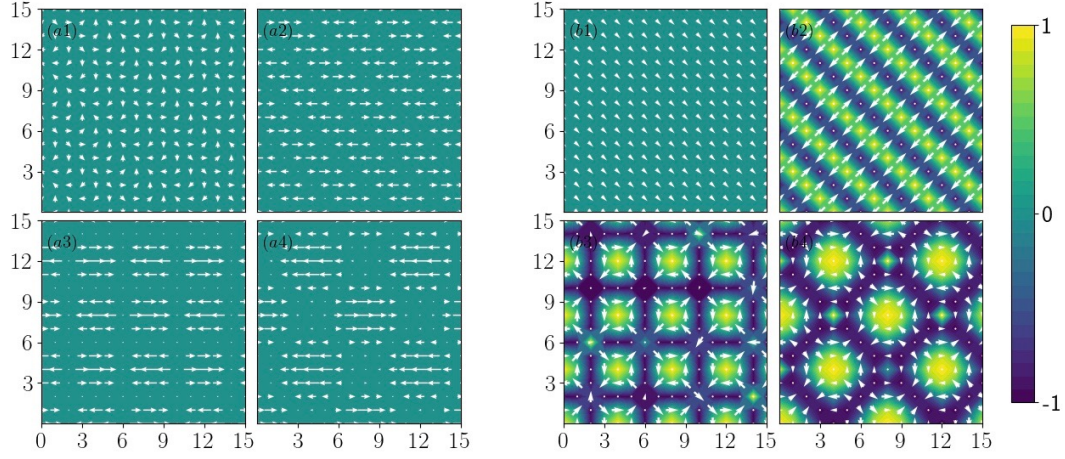


Figure 5.1: Left panels (a1-a4): The variational families chosen for minimization. The ratio  $|\phi_{k_0}^+|/|\phi_{k_0}^-|$  has been plotted in color and  $(\text{Re}[\phi_{k_0}^-], \text{Im}[\phi_{k_0}^-])$  has been plotted using arrows. Right panels (b1-b4): the magnetic textures corresponding to the left panels. The  $(m_x, m_y)$  components have been plotted using arrows, while the  $m_z$  component has been plotted in color. (a1, b1) represent a typical single mode configuration, (a2, b2) a two mode, (a3, b3) a four mode, and (a4, b4) a vortex configuration. The single mode and the two mode configurations arise in the ground state but the four mode and the vortex configurations do not.

$T \rightarrow T_c$ , providing a detectable thermal signature of Rashba coupling. Finally, (v) we construct an effective Landau theory which provides some analytic understanding of the thermal scales, and discuss experiments which can test our theory.

The plan of the rest of this work is as follows. In Sec. 5.3, we study the ground state phase diagram. We study the finite temperature effect on different phases in Sec. 5.4 and construct an effective Landau theory in Sec. 5.5. Finally, we discuss our main results, chart out experiments which can test our theory, and conclude in Sec. 5.6. Some details of our calculation and the construction of the effective Landau theory are presented in the Appendices.

## 5.2 Model and method

In this section, we shall present the model we use and also discuss the details of the method used for computation.

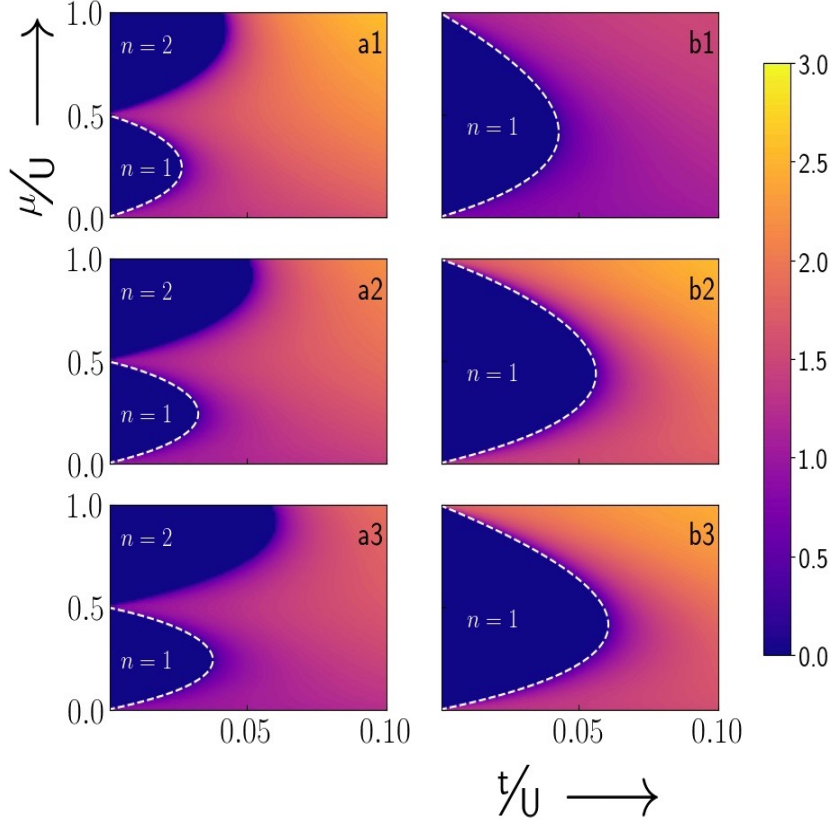


Figure 5.2: Variational ground state phase diagram. The variation of superfluid order parameter is shown in color. Left panel a1-a3 shows the results for  $\lambda=0.5$ , at  $\gamma = 0, 0.3\pi$  and  $0.5\pi$  respectively. The superfluid phase in these cases is a plane wave state with homogeneous FM order. The right panel b1-b3 shows the same plot for  $\lambda=1.5$ . In this case, the superfluid phase has a two mode superposition which leads to a stripe like magnetic texture - FIG.5.6. The dashed lines demarcate the superfluid and Mott phase boundaries as calculated from the effective Landau functional described in section 5.5.

### 5.2.1 Model

We begin by defining a Rashba spin-orbit coupled Bose-Hubbard Hamiltonian on a square lattice in 2D:

$$H = H_{kin} + H_U \quad (5.1)$$

$$H_{kin} = \sum_{\langle ij \rangle}^{\alpha\beta} \mathcal{R}_{\alpha\beta}(i, j) b_{i\alpha}^\dagger b_{j\beta} + H.c. \quad (5.1a)$$

$$H_U = \frac{U}{2} \sum_{i;\alpha} n_{i\alpha} (n_{i\alpha} - 1) + \lambda U \sum_i n_{i1} n_{i2} - \sum_{i;\alpha} (\mu + \Omega \sigma_z) n_{i\alpha}. \quad (5.1b)$$

Here  $\mathcal{R}(i, j) = -t \exp[i\mathbf{A} \cdot (\mathbf{i} - \mathbf{j})]/2$  is the real space hopping matrix,  $\mathbf{A} = (\gamma\sigma_y, -\gamma\sigma_x, 0)$  is the synthetic gauge field.  $U$  is the on-site repulsion,  $\lambda$  denotes the ratio between inter-species



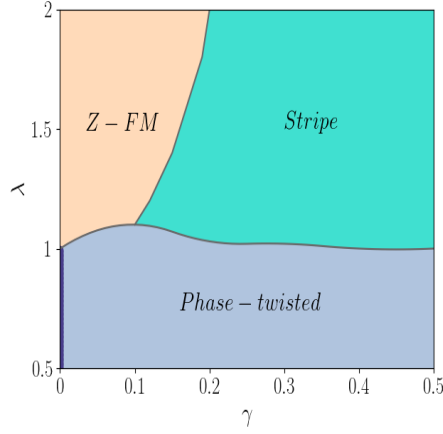


Figure 5.3: Classification of the ground state superfluid phases for  $U/t = 10$ . For  $\lambda < 1$  and  $\gamma = 0$  we get a homogeneous superfluid in which  $\langle b_{i\alpha}^\dagger \rangle$  remains constant throughout the system. The phase-twisted superfluid has homogeneous amplitude of  $\langle b_{i\alpha}^\dagger \rangle$ , but its phase modulates from site to site. The Z-FM is a homogeneous phase in which there is condensation in only one of the spin state. The stripe phase supports spatial modulation in both the amplitude and the phase of  $\langle b_{i\alpha}^\dagger \rangle$ , and is characterized by stripe-like patterns in the magnetic texture, FIG. 5.6. For  $\gamma > 0.4$  the stripe phase shows a  $(\pi, \pi)$  order, which is the Z-AFM phase mentioned in Ref. [157].

and intra-species on-site repulsion, and  $\Omega$  is the Zeeman field which arises due to the coupling of the Raman laser to the bosonic atom [169]. This term depends on the strength of the atom-laser coupling and can be tuned to the extent that the spin-orbit physics does not get completely masked. In this work, following Refs. [157], we shall later set  $\Omega$  to zero in order to have a clean demonstration of the effects of spin-orbit coupling. In what follows, we also neglect another additional on-site term  $H \sim \delta\sigma_y/2$  which depends on the detuning parameter  $\delta$  of the Raman laser and can be made small by sufficient reduction of the detuning. For the rest of this work, we set the lattice spacing  $a_0 = 1$ .

### 5.2.2 Effective Hamiltonian

In order to simulate the finite temperature physics of this model we introduce auxiliary fields and implement a Hubbard-Stratonovich decomposition of the hopping part of the action using two fields  $\{\phi_{i,n}^+\}$ ,  $\{\phi_{i,n}^-\}$  for each lattice point and Matsubara frequency,  $(i, n)$ , described in detail in Chapter 2. We retain only the zero Matsubara frequency mode of the auxiliary fields  $\{\phi_{i,0}^+\}$ ,  $\{\phi_{i,0}^-\}$ .

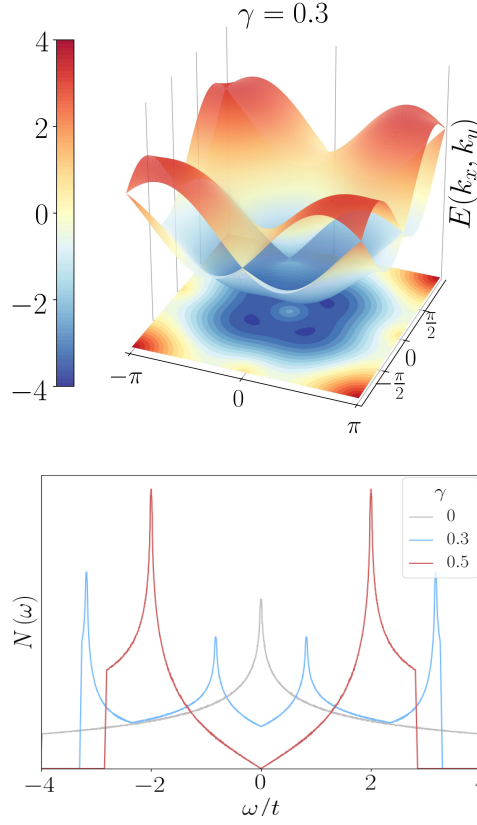


Figure 5.4: Top: The band structure for  $\gamma = 0.3$ . The dispersion has a four fold symmetry. The minima occur at finite wavevectors, as is evident from the projection of the lower band onto the x-y plane. Bottom: The noninteracting density of states for three different values of  $\gamma$ .  $\gamma = 0$  has the usual tight binding form in 2D, while for finite  $\gamma$  one observes a dip at zero along with a linearly rising behavior which is reminiscent of the Dirac cone present in the band structure at the  $\Gamma$  point. All energies are in units of  $t$ .

The effective Hamiltonian obtained by retaining only  $\{\phi_{i,0}^+\}$ ,  $\{\phi_{i,0}^-\}$  fields is given by

$$H^{\text{eff}} = H_{\text{kin}}^{\text{eff}} + H_U \quad (5.2)$$

$$H_U = \frac{U}{2} \sum_{i;\alpha} n_{i\alpha} (n_{i\alpha} - 1) + \lambda U \sum_i n_{i1} n_{i2} - \sum_{i;\alpha} (\mu + \Omega \sigma_z) n_{i\alpha} \quad (5.3)$$

$$H_{\text{kin}}^{\text{eff}} = \sum_i (\Gamma_i^\dagger \Psi_i + \Psi_i^\dagger \Gamma_i + |\Phi_i|^2), \text{ with} \quad (5.4)$$

$$\Gamma_i = \frac{1}{\sqrt{2}} \sum_j \mathcal{M}_{ji} \Phi_j$$

$$\mathcal{M}_{ji} = \sum_{\mathbf{k}} e^{i\mathbf{k} \cdot (\mathbf{j} - \mathbf{i})} \begin{pmatrix} \sqrt{-\tilde{E}_{\mathbf{k}}^+} & \sqrt{-\tilde{E}_{\mathbf{k}}^-} \\ \sqrt{-\tilde{E}_{\mathbf{k}}^+} e^{-i\theta_{\mathbf{k}}} & -\sqrt{-\tilde{E}_{\mathbf{k}}^-} e^{-i\theta_{\mathbf{k}}} \end{pmatrix}$$

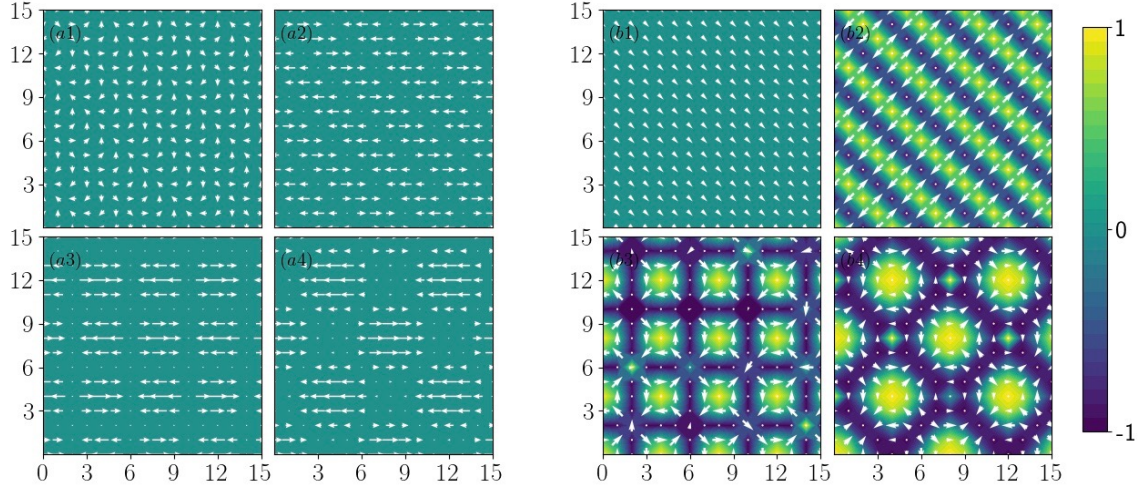


Figure 5.5: Left panels (a1-a4): The variational families chosen for minimization. The ratio  $|\phi_{k_0}^+|/|\phi_{k_0}^-|$  has been plotted in color and  $(\text{Re}[\phi_{k_0}^-], \text{Im}[\phi_{k_0}^-])$  has been plotted using arrows. Right panels (b1-b4): the magnetic textures corresponding to the left panels. The  $(\mathbf{m}_x, \mathbf{m}_y)$  components have been plotted using arrows, while the  $\mathbf{m}_z$  component has been plotted in color. (a1, b1) represent a typical single mode configuration, (a2, b2) a two mode, (a3, b3) a four mode, and (a4, b4) a vortex configuration. The single mode and the two mode configurations arise in the ground state but the four mode and the vortex configurations do not.

where  $\Phi_i \equiv \begin{pmatrix} \phi_i^+ \\ \phi_i^- \end{pmatrix}$  is a local spinor composed of zero mode of the auxiliary fields  $\{\phi_0^+\} \equiv \{\phi^+\}$  and  $\{\phi_0^-\} \equiv \{\phi^-\}$ .  $\Psi_i \equiv \begin{pmatrix} b_i^1 \\ b_i^2 \end{pmatrix}$  is a local spinor involving the bosons of the two species.  $\mathcal{M}_{ji}$  are 2x2 matrices which couple the chiral auxiliary fields with the bosonic spinor, with coefficients picked up in the band truncation process. The information of the spin-orbit coupling enters the effective Hamiltonian through these coefficient matrices. Here  $H_U$  is the local interaction part as in the original Hamiltonian 5.1b and  $\Omega$  has been set to zero in the subsequent calculations. The details of the procedure leading to  $H_{\text{eff}}$  can be found in the Appendix C.

### 5.2.3 Methods

The effective Hamiltonian obtained in the last section, can be treated using several approximation schemes. In this work, we are going to use two such schemes. The first of these, used to obtain zero temperature phases of the system, involves treating  $\{\Phi_i\}$  as variational parameters and subsequent minimization of the energy obtained from the effective Hamiltonian. In this scheme, the energy for a configuration of  $\Phi$ s is obtained by diagonalizing the boson Hamiltonian  $H_{\text{eff}}[\Phi_i]$ .

This yields the optimal ground state configuration of  $\Phi_i$  fields. In this work, we restrict ourselves to four families of such variational wavefunctions given by

**1. Single mode:**

$$\Phi_i = \begin{pmatrix} \phi_{k_0}^+ \\ \phi_{k_0}^- \end{pmatrix} \exp(i\mathbf{k}_0 \cdot \mathbf{r}_i)$$

**2. Two mode:**

$$\Phi_i = \begin{pmatrix} \phi_{k_0}^+ \\ \phi_{k_0}^- \end{pmatrix} \cos(\mathbf{k}_0 \cdot \mathbf{r}_i)$$

**3. Four mode:**

$$\Phi_i = \begin{pmatrix} \phi_{k_0}^+ \\ \phi_{k_0}^- \end{pmatrix} \cos(k_0^x x_i) \cos(k_0^y y_i)$$

**4. Vortex:**

$$\Phi_i = \begin{pmatrix} \phi_{k_0}^+ \\ \phi_{k_0}^- \end{pmatrix} [\cos(k_0^x x_i + k_0^y y_i) + \cos(k_0^x y_i - k_0^y x_i)]$$

where  $\mathbf{r}_i = (x_i, y_i)$  are the coordinates of site  $i$ . A sketch of these variational profiles of  $\Phi_i$  and the corresponding magnetic texture of the bosons is given in Fig.5.3. We note that the local Hilbert space for the bosons needs to be restricted for the problem to be numerically tractable. This is done by choosing a cutoff,  $N_i$ , in the number of boson occupation per site. In what follows, we have ensured that the cut-off is chosen such that including more states beyond it does not have any effect on the energy of the system, up to a desired accuracy. The variational calculation gives us the mean field ground state of our effective model5.2.

Having obtained the ground state configuration of the bosons, the second method we use yields information about its thermal behavior. To this end, we use a classical Monte-Carlo scheme by starting from the ground state configuration and successively increasing the temperature. The free energy for a configuration of  $\{\Phi_i\}$ s is again obtained by diagonalizing the boson Hamiltonian  $H_{eff}$  for every attempted update of the auxiliary fields. The equilibrium  $\{\Phi_i\}$  configurations are

generated by implementing a Metropolis based update scheme. In this scheme, at any given site  $i$ , we have two complex scalar auxiliary fields,  $\phi_i^+$  and  $\phi_i^-$ . For each of the fields, the amplitude fluctuations are considered to be within twice their ground state amplitude. In contrast, arbitrary phase fluctuations of these fields are allowed. The local hybridization  $\Gamma_i$  depends on the  $\Phi_i$  configurations on all sites, as defined in equation 5.5. For a given  $\{\Phi_i\}$  configuration the bosonic Hamiltonian is written in Fock space after truncating the local Hilbert space within  $N_i$  particle states, as in the variational calculation. The resulting matrix is then diagonalized exactly to obtain the free energy for the configuration.

#### 5.2.4 Indicators

To detect the presence of spatial order we compute the structure factor:

$$S_{\mathbf{q}} = \left\langle \frac{1}{zV} \sum_{i,j} \text{Tr} \left[ \Phi_i^\dagger \Phi_j \right] e^{i\mathbf{q} \cdot (\mathbf{i}-\mathbf{j})} \right\rangle \quad (5.5)$$

where  $V$  is the volume of the system,  $z$  is the coordination number and  $\Phi_i$ s are the auxiliary fields introduced in sec.5.2.1.

The local magnetic texture of the is defined by the vector,

$$\mathbf{m}_i = \left\langle \frac{1}{Z} \sum_{\mu,\nu} \text{Tr} \left[ e^{-\beta H_{eff}} b_{i\mu}^\dagger \boldsymbol{\sigma}_{\mu\nu} b_{i\nu} \right] \right\rangle \quad (5.6)$$

where  $Z$  is the partition function and the angular brackets denote thermal averaging.

The momentum distribution of the bosons given by:

$$n_{\mathbf{k}} = \frac{1}{N} \left\langle \frac{1}{ZV} \sum_{i,j,\mu} \text{Tr} \left[ e^{-\beta H_{eff}} b_{i\mu}^\dagger b_{j\mu} \right] e^{i\mathbf{k} \cdot (\mathbf{i}-\mathbf{j})} \right\rangle \quad (5.7)$$

where  $N$  is the total no. of bosons,  $Z$  is the partition function,  $V$  is system volume, and the angular brackets denote thermal averaging.

### 5.3 Variational ground state

In this section, we shall use the variational scheme outlined earlier to obtain the mean-field ground state phase diagram of the bosons. In what follows, we have numerically implemented this scheme on a  $16 \times 16$  unit cell with  $4 \leq N_i \leq 10$  hybridization states per site. The chosen value of  $N_i$  depending on the value of the on-site interaction  $U$ . For every parameter point  $N_i$  have been fixed at its optimal value, so that increasing it does not affect the results. Unless otherwise mentioned, the filling should be considered as fixed to one boson per site.

Due to the symmetry in the problem, we can restrict  $\gamma$  to the interval  $[0, 0.5]$ . Moreover, we notice that in the atomic limit, where the problem becomes independent of  $\gamma$ , the level schemes differ qualitatively if one tunes  $\lambda$  across unity, as shown in section 5.5 (see Fig. 5.12). This allows us to segregate the two parameter regimes -  $\lambda < 1$  and  $\lambda > 1$ . We present our results for a characteristic value of  $\lambda$  in each of these intervals ( $\lambda = 0.5$  and  $1.5$  respectively), and expect qualitatively similar trends for other values of  $\lambda$  in the respective intervals. At each parameter point we first classify the ground state phases using expectation values of linear bosonic operators like  $\langle b_{i\alpha}^\dagger \rangle$ . This allows us to demarcate the ground state superfluid (SF) - Mott insulator (MI) phase boundary (FIG. 5.2). The order parameter vanishes in the MI phase, as a result, the kinetic part of the Hamiltonian has no contribution in the energy and we recover the atomic limit. In the SF phase a non-vanishing amplitude of  $\langle b_{i\alpha}^\dagger \rangle$  survives throughout the system, while in the MI phase it vanishes on all sites. We further classify the superfluid phases by using expectation values of bosonic bilinears as defined in Sec 5.2.4. This yields a classification of the superfluid phases into the following subcategories:

- *Homogeneous* - where  $\langle b_{i\alpha}^\dagger \rangle$  and the bilinears remain constant throughout the system.
- *Phase-twisted* - where the amplitude of  $\langle b_{i\alpha}^\dagger \rangle$  as well as the bilinears remain constant throughout the system, but the phase of  $\langle b_{i\alpha}^\dagger \rangle$  varies from site to site.
- *Z-FM* - in which  $\langle b_{i1}^\dagger \rangle$  retains a homogeneous nonzero value, but  $\langle b_{i2}^\dagger \rangle$  vanishes throughout the system;  $m_z$  remains pinned to 1, while  $m_x$  and  $m_y$  vanish.
- *Stripe* - in which both the amplitude as well as the phase of  $\langle b_{i\alpha}^\dagger \rangle$  vary from site to site, and the bilinears show stripe like patterns across the system.

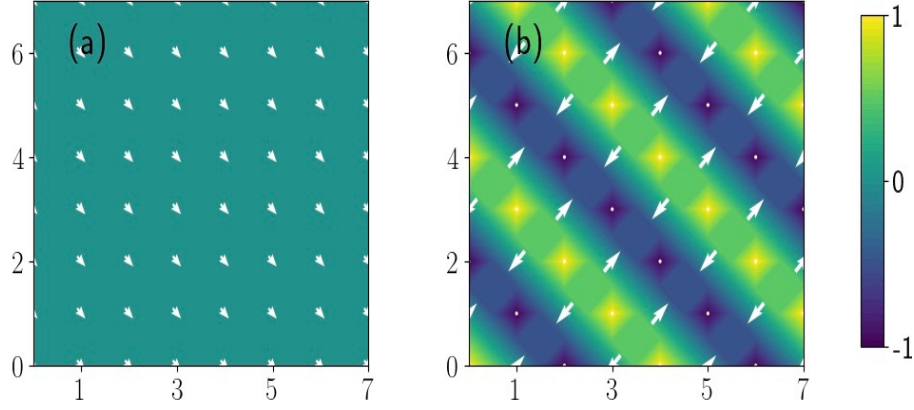


Figure 5.6: Real space snapshot of magnetic texture in the ground state at  $\gamma=0.3$  for (a)  $\lambda = 0.5$  and (b)  $\lambda = 1.5$ . The  $m_z$  component has been shown in color while the  $m_x - m_y$  components have been denoted via vectors. The  $\lambda=0.5$  state is a phase-twisted superfluid with no magnetic component out of the plane, whereas all the in-plane vectors get aligned at  $-\frac{\pi}{4}$  to the x axis. The  $\lambda=1.5$  state shows a stripe-like magnetic pattern whose pitch is controlled by the spin-orbit coupling.

The effect of increasing  $\gamma$  at fixed  $U$  and  $\lambda$  can be understood as follows. The effective bandwidth of the system varies with  $\gamma$  as  $W(\gamma) = 4t\sqrt{2(1 + \cos^2 \gamma)}$ . Thus one requires progressively larger bare hopping  $t/U$  to compensate for the  $\cos^2 \gamma$  term in order to stabilize the superfluid phase. Thus we expect  $t_c$  to increase with  $\gamma$  for fixed  $U$  and  $\lambda$ . This expectation is verified in our numerics as can be seen from both panels of Fig.5.2. Within the superfluid phase, the phase diagram can be broadly classified into three separate regimes. In the first of these, where  $\lambda < 1$  (FIG.5.2(a)), single mode variational profile minimizes  $H_{\text{eff}}$ . For any finite value of  $\gamma$  this leads to a phase-twisted superfluid with uniform density for both the species throughout the system, while for  $\gamma = 0$  it reduces to the homogeneous superfluid phase. The fact that any finite  $\gamma$  would necessarily lead to a phase twisted superfluid can be understood in terms of an effective Landau functional, which will be discussed in section 5.5.

In the second regime where  $\lambda > 1$  (FIG. 5.2(b)), for low values of  $\gamma$  we get condensation in only one of the spin species, leading to a  $z$ -polarized ferromagnetic texture. In contrast, for larger values of  $\gamma$ , the two mode variational state wins over others in the superfluid phase, leading to a stripe-like order with modulating density in each spin species. The pitch of the spin density wave depends on  $\gamma$ , and for  $\gamma > 0.4$  it leads to a Z-AFM order. The complete phase diagram in the superfluid phase as a function of  $\gamma$  and  $\lambda$  is shown in Fig.5.3. The superfluid-Mott phase boundary is governed by the vanishing of the second order coefficient of the Landau functional



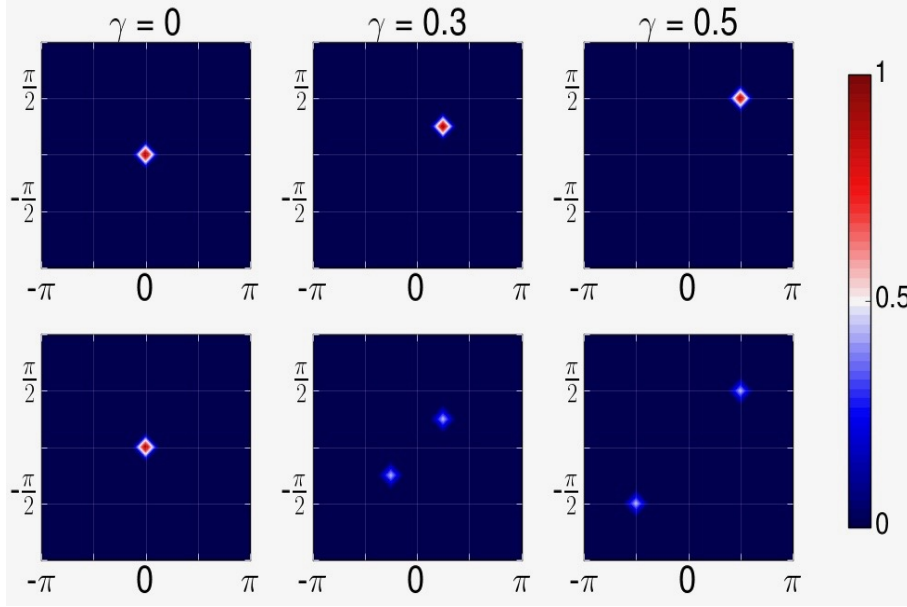


Figure 5.7: The ground state momentum distribution as a function of spin-orbit  $\gamma$  has been plotted columnwise for  $\gamma = 0, 0.3$  and  $0.5$ . The top row shows the plots for  $\lambda = 0.5$  with  $U$  fixed at 10. With increasing  $\gamma$  the condensation wave-vector moves from  $(0,0)$  to  $(k_0, k_0)$ , accompanied by slight depletion of the peak. The bottom row represents  $\lambda = 1.5$  with  $u = 4t$ . In this case, as  $\gamma$  is tuned from zero, the condensate splits from a single peak feature at  $(0,0)$  to two peaks at  $(-k_0, -k_0)$  and  $(k_0, k_0)$  with equal no. of particles at both points. The total condensate fraction, which has contributions from both the peaks, gets slightly depleted with increasing  $\gamma$

obtained by tracing out the bosons in the strong coupling limit. We discuss this procedure in detail and chart out the analytic intuition obtained from it in section 5.5.

We note here that in our calculations we find that the four mode and vortex configurations do not feature in the ground state, although at certain parameter points their energies come very close to the ground state energy. This is in contrast to the phase diagram obtained in previous works [101, 157] using other techniques. This might be an artifact of band truncation in our implementation of the mean-field approximation, although it is not entirely clear whether other mean-field approaches can actually capture those phases [158]. Nevertheless, at larger values of  $\lambda$  ( $\gtrsim 1.5$ ), our ground state phase diagram matches qualitatively with that in Ref. [157]. In this region, we wish to highlight our finite temperature results, since the merit of our technique is in capturing the thermal scales nonperturbatively, which could not have been possible, to this extent, using other techniques.

Next, we study the magnetic structure of the ground state. The magnetic texture, shown in Fig. 5.6 arises from the relative boson density modulation between the two species over different



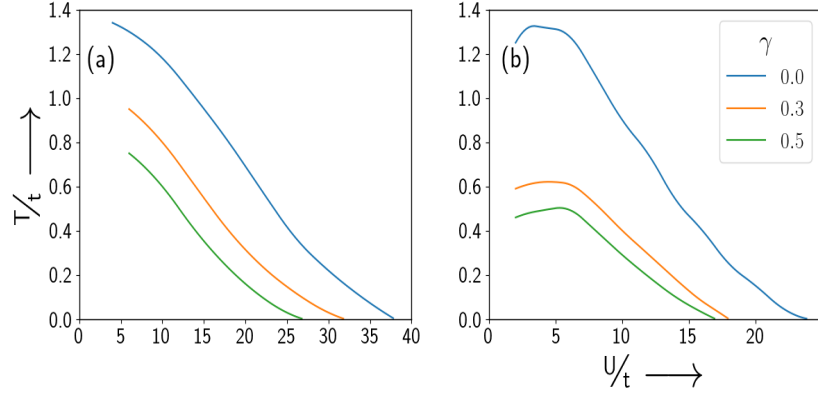


Figure 5.8: The thermal phase transition scales for (a)  $\lambda = 0.5$  and (b)  $\lambda = 1.5$ . The  $T_c(U)$  result for different  $\gamma$  are shown in color. The low temperature phase is a superfluid with condensation at a wavevector governed by  $\gamma$ . Beyond  $T_c(U, \gamma)$  the system is a normal Bose liquid. For a fixed  $U$ ,  $T_c$  decreases with increase in  $\gamma$  due to renormalization of the bandwidth.

lattice sites. We find that in the ground state, for  $\lambda < 1$ ,  $m_{zi} = 0$  which indicates that there is no local population imbalance between the two spin species throughout the lattice as shown in Fig.5.6(a). The planar components, which encapsulate the relative phase between the two species, are also same on all sites. In contrast, for  $\lambda > 1$ , the ground state, for  $\gamma = 0$ , has  $|m_{zi}| = 1$  which means that the bosons condense in only one of the spin state and the density of the other spin state remains zero on all sites. Increasing  $\gamma$  leads to a diagonal stripe-like order with  $|m_{zi}| < 1$  indicating population imbalance between the two spin species. This imbalance varies in space leading to the stripe-like order as shown in Fig.5.6(b).

At  $T = 0$  and in the superfluid phase,  $n_k$  is sharply peaked as shown in Fig.5.7. The peak height represents the condensate fraction, which depends on the strength of interaction  $U$  and the spin-orbit coupling  $\gamma$ . The condensate gets depleted with increasing  $U$  (keeping  $\gamma$  and  $\lambda$  fixed) leading to diminished peak height. For  $\lambda < 1$ , the position of the momentum distribution peak shifts from  $k = 0$  to  $(k_0, k_0)$  where  $k_0$  is given by the band minima. This is shown in the top panel of Fig.5.7. Note that the position of this minima is controlled by the spin-orbit coupling. For  $\lambda > 1$  the single peak at  $\gamma = 0$  splits into two peaks at  $(\pm k_0, \pm k_0)$  with equal heights as shown in the bottom panel of Fig.5.7. This indicates that the ground state is a superposition of Bose condensates at two distinct wavevectors. The peak heights diminish with increasing  $\gamma$ , keeping  $U$  fixed. This can be attributed to the fact that the band stiffness about the minimum decreases as the spin-orbit strength is increased. We note that such a superposition state may be

unstable in the presence of a trap potential and we shall not address this issue further here.

## 5.4 Finite temperature results

In this section we chart out the finite temperature phases starting from the variational mean-field ground states obtained in the previous section. We use the classical Monte Carlo scheme described in Sec. 5.2.3 and run the simulation on a  $16 \times 16$  lattice with two fluctuating fields,  $\phi^{\pm i}$  and  $\phi^-$  at each site  $i$ . Both the amplitude and the phase interval of the fields are discretized in hundred subintervals. The amplitude interval is restricted to twice the saddle point value while full phase fluctuation has been allowed. The real space  $\{\Phi_i\}$  configurations are obtained by sampling over four thousand MC sweeps for each temperature. In each these sweeps, all the sites of the system are updated once. A total of  $N_0 = 100$  configurations are saved at every temperature, which are subsequently used to calculate thermal averages of observables.

The finite temperature phase diagram is shown below in Fig. 5.8. The low temperature state is the variational ground state which we have discussed at length in Sec. 5.3. As we heat up the system it gets thermally disordered and finally makes transition to a normal state. The normal state is a Bose liquid with no long range order, but short range spatial correlations. The critical temperature  $T_c$  varies non-monotonically with  $U$ . As  $U$  is lowered starting from  $U_c$ ,  $T_c$  grows linearly up to quite low values of  $U$  ( $\sim 2 - 6$  depending on  $\lambda$  and  $\gamma$ ) after which it falls suddenly. For  $\gamma = 0$  the fall is sharp and is easily discernible in Fig. 5.8, while for finite  $\gamma$ , it is quite gradual. The low  $U$  part of the phase diagram is numerically inaccessible due to large number fluctuations in the condensate, for which one needs to retain enormously high number of local hybridization states. For this reason we could access results only starting from  $U/t = 2$ . With increasing  $\gamma$  the  $T_c$  scales get suppressed at all values of  $\lambda$  and  $U$ . This can again be attributed to suppression of effective bandwidth by the spin orbit coupling as discussed in Sec. 5.3.

Next, we address the effect of finite temperature on the momentum distribution functions. The results are shown in Fig. 5.9. The peaks in the ground state momentum distribution show significant thermal broadening with increasing  $T$ . This is best appreciated by looking at the  $\gamma = 0$  behavior (top panel in Fig. 5.9). The condensate fraction remains almost constant up to

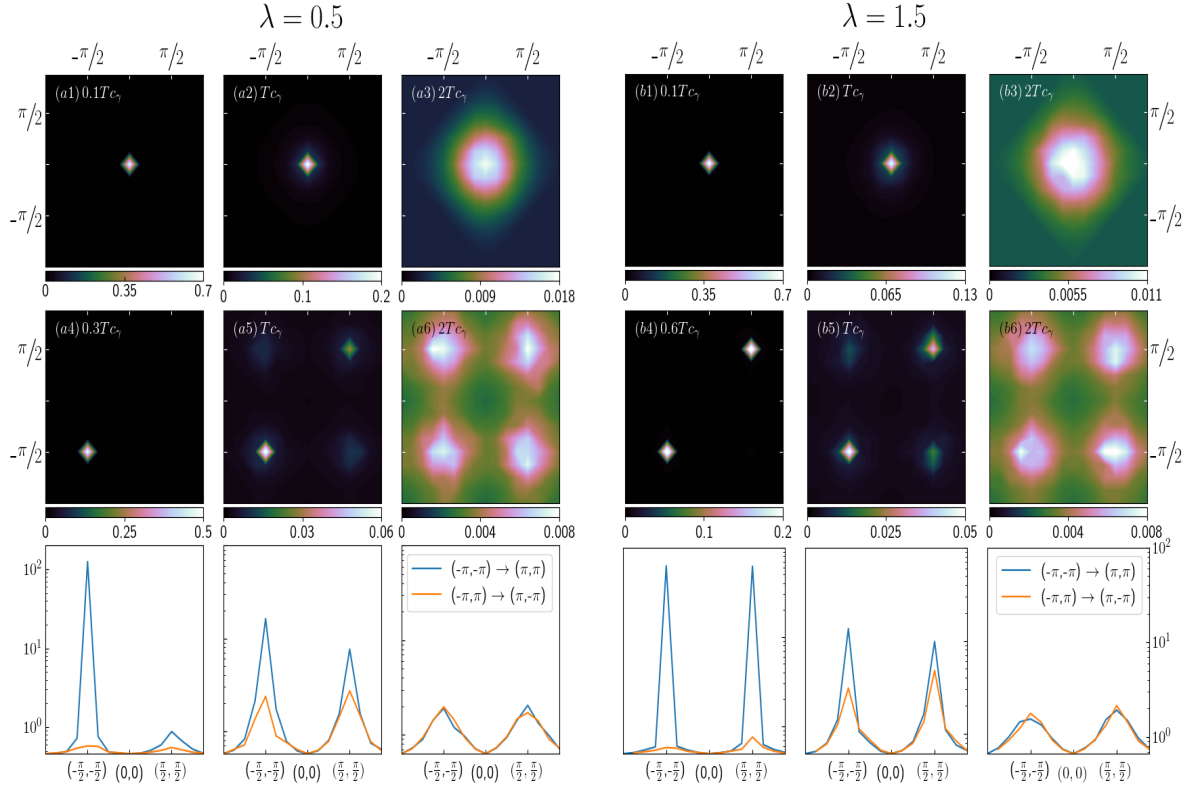


Figure 5.9: The thermal evolution of the momentum distribution function ( $n_{\mathbf{k}}$ ) has been plotted in the left panel for  $\lambda = 0.5$  at  $U = 14t$ , and in the right panel for  $\lambda = 1.5$  for  $U = 10t$ . The first two rows show evolution of the normalized  $n_{\mathbf{k}}$  for  $\gamma = 0$  and  $0.5$  respectively. The columns show thermal broadening of the  $n_{\mathbf{k}}$  peaks as the system is heated up from a low temperature (a1, a4) to the critical temperature  $T_c$  (a2, a5), and finally to a high temperature (a3, a6) where the superfluidity has been lost. The right panel shows the same sequence for  $\lambda = 1.5$ . The last row shows the  $n_{\mathbf{k}}$  projection along the two diagonals of the square BZ for  $\gamma = 0.5$ . For finite  $\gamma$  the low temperature distribution is sharply peaked at  $(k_0, k_0)$  and  $(-k_0, -k_0)$  (b4). As the temperature reaches close to  $T_c$  small weights appear at the symmetry related points  $(k_0, -k_0)$  and  $(-k_0, k_0)$  in the BZ due to thermal fluctuations (b5). In the high temperature state one can observe significant thermal broadening of the features at relevant  $k$ -points (b6).

$T = 0.1T_c$ , after which particles start getting excited out of the condensate. For  $T \simeq T_c$  there is significant broadening of the peak even though the superfluid order still survives. Beyond  $T_c$  phase fluctuations destroy the coherence giving uniform Bose liquid. For finite  $\gamma$  one can notice thermal weights developing in the symmetry related  $k$ -points when the system is close to  $T_c$ , for both the  $\lambda$  values. These weights signify the presence of low energy states at certain  $k$ -points, which is reminiscent of the band structure symmetry. At temperatures close to  $T_c$  thermal fluctuations excite particles out of the condensate to these low energy states, without destroying the overall phase coherence in the system. As the system is heated up further the populations in these symmetry related  $k$ -points tend to homogenize at the cost of destroying superfluidity.

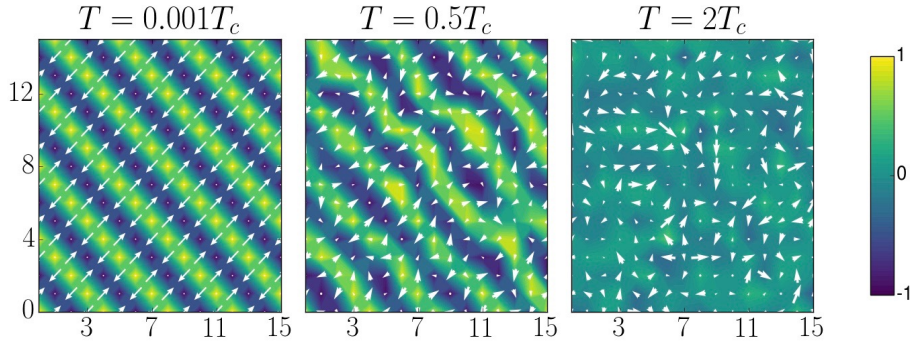


Figure 5.10: Spatial snapshots of  $\mathbf{m}_i$  for  $\lambda = 1.5$  at  $U = 10$  illustrating the temperature variation of the magnetic textures across the thermal transition. The spin density wave survives to intermediate temperatures and vanishes for  $T \gg T_c$ . The planar components get disordered at a lower temperature scale as compared to the  $z$ -component. All energies are in units of  $t$ .

Next, we consider the behavior of the magnetic texture as a function of temperature. As the system is heated from the ground state the magnetic textures start getting disordered. The thermal behavior of the magnetic texture is shown in Fig. 5.10. We observe that for a temperature  $T < T_c$  the planar moments become more disordered as compared to  $m_z$  (shown in color). This can be attributed to the fact that the planar moments capture the gapless phase fluctuations of the superfluid, whereas  $m_z$  captures their population difference. Finally, for  $T > T_c$ , we find that the planar moments become completely disordered while the  $z$  component homogenizes.

We track the peak in the structure factor  $S_q$  with temperature to locate the onset of long range order as shown in Fig. 5.11. We find that as the system is heated from its ground state, the auxiliary fields start fluctuating about their saddle point; consequently, the distribution of the  $\{\Phi_i\}$ s broaden. At each site the two variables (per species), i.e. the amplitude and the phase of the auxiliary field  $\phi_{i\sigma}$  get disordered with temperature. It is the fluctuations of the phase degree of freedom which ultimately kill superfluidity in the system. The transition temperature  $T_c(\lambda, \gamma, U)$  can be inferred from the "knee" of the  $S_q$  peak vs temperature curve. Thus this measurements allow us to locate  $T_c$  which may be relevant in realistic experiments.

## 5.5 Understanding of thermal scales

We derive an effective spin model for the bosons in the SF phase near the SF-MI transition. To this end, note that at large  $U/t$ , close to the Mott phase, the original boson fields can be integrated out to give an effective description of the bosons in terms of the auxiliary fields. It leads to a

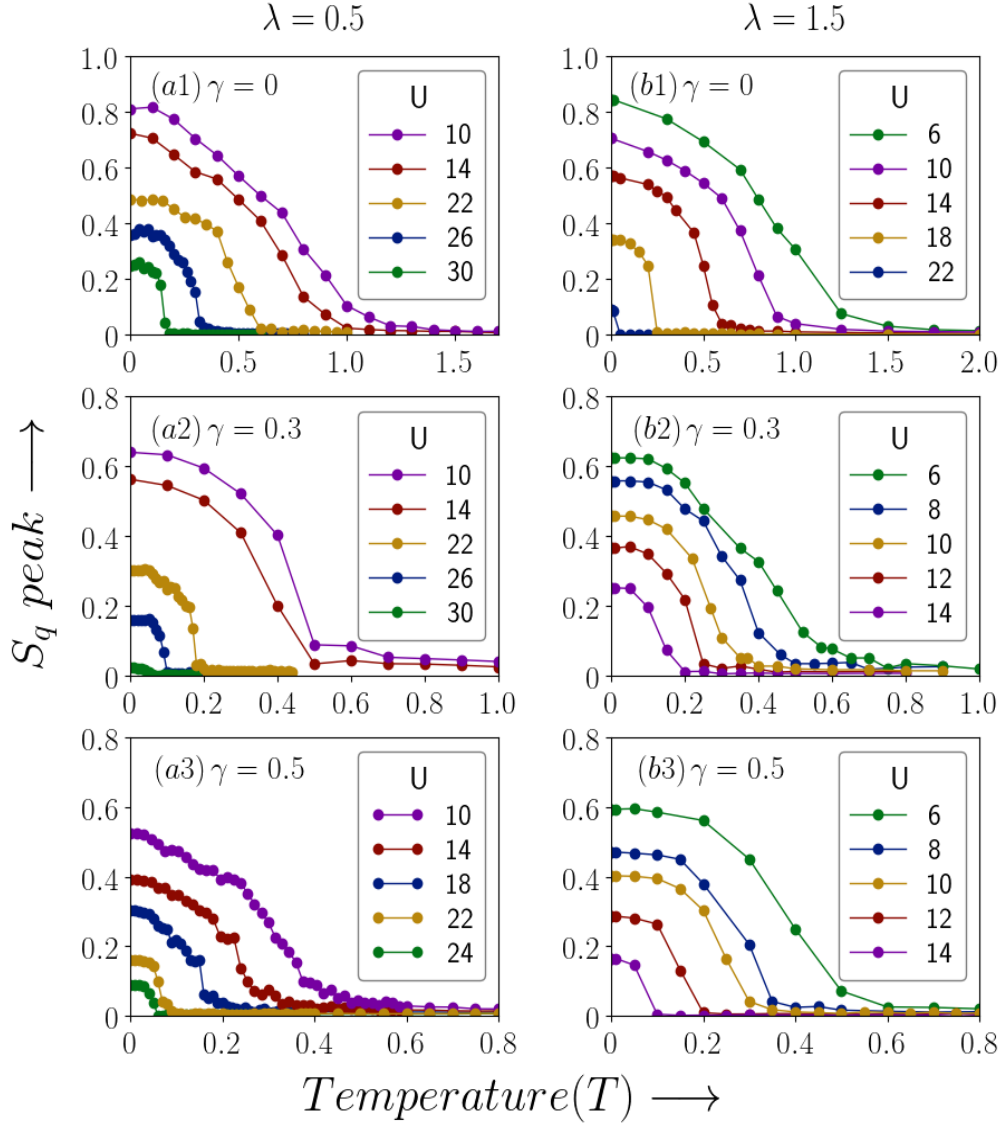


Figure 5.11: Thermal evolution of the structure factor peak has been plotted for a  $16 \times 16$  lattice at  $\lambda = 0.5$  in the first column (a1-a3), and for  $\lambda = 1.5$  in the second column (b1-b3). All energies are in units of  $t$ .

Landau energy functional, with coefficients depending on the parameters of the theory.

For the single species problem one can derive the free energy functional by performing a cumulant expansion of the SPA functional A. In the two-species problem the ground state in the atomic limit is degenerate as shown in Fig.5.12. Thus one needs to use degenerate perturbation theory about the atomic limit. The Landau energy functional after second order correction in  $\{\Gamma_{i\alpha}\}$  is given by:

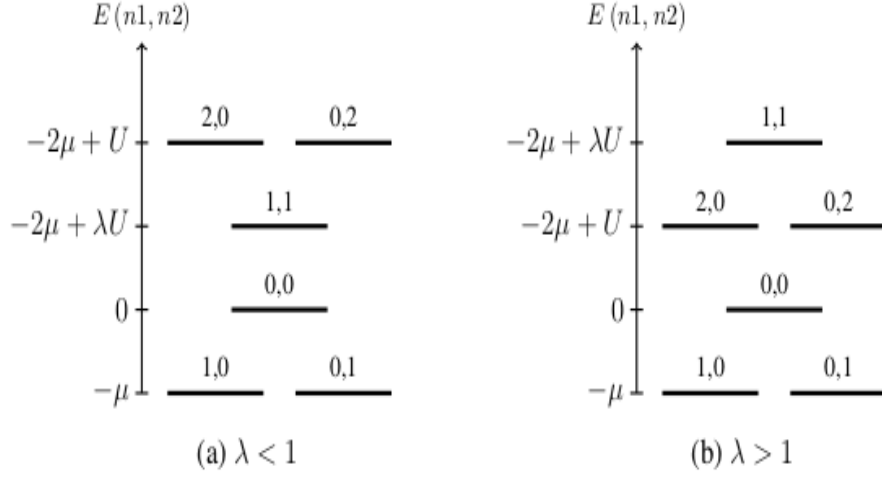


Figure 5.12: Schematic level scheme of two-species bosons in the atomic limit.

$$\begin{aligned} \delta E^{(2)} = & -\frac{1}{2U\tilde{\mu}} \sum_i \left[ f(\tilde{\mu}, \lambda) (|\Gamma_{i1}|^2 + |\Gamma_{i2}|^2) \right. \\ & \left. + \sqrt{\left( g(\tilde{\mu}, \lambda) (|\Gamma_{i1}|^2 - |\Gamma_{i2}|^2) \right)^2 + \left( \frac{2\lambda\tilde{\mu}|\Gamma_{i1}\Gamma_{i2}|}{\lambda - \tilde{\mu}} \right)^2} \right] + \sum_{i\sigma} |\phi_{i\sigma}|^2 \end{aligned} \quad (5.8)$$

with  $\tilde{\mu} \equiv \frac{\mu}{U}$ , and

$$\begin{aligned} f(\tilde{\mu}, \lambda) & \equiv \left( \frac{1 + \tilde{\mu}}{(1 - \tilde{\mu})} + \frac{\tilde{\mu}}{\lambda - \tilde{\mu}} \right) \\ g(\tilde{\mu}, \lambda) & \equiv \left( \frac{1 + \tilde{\mu}}{(1 - \tilde{\mu})} - \frac{\tilde{\mu}}{\lambda - \tilde{\mu}} \right). \end{aligned} \quad (5.9)$$

Notice that the square root term lifts the degeneracy of the ground state. We now express the hybridization fields  $\{\Gamma_{i\alpha}\}$  in terms of the auxiliary fields  $\{\phi_{i\sigma}\}$  using Eq. 5.5.

$$\begin{aligned} |\Gamma_{i\alpha}|^2 = & \sum_{j\sigma; l\delta; \mathbf{k}, \mathbf{q}} \left( (\mathcal{M}_{\mathbf{k}}^{\alpha\sigma})^* \mathcal{M}_{\mathbf{q}}^{\alpha\delta} \right) e^{i(\mathbf{k}-\mathbf{q}) \cdot \mathbf{i} + i(\mathbf{q} \cdot \mathbf{l} - \mathbf{k} \cdot \mathbf{j})} \\ & \times |\phi_{j\sigma}| |\phi_{l\delta}| e^{-i(\theta_{j\sigma} - \theta_{l\delta})} \end{aligned} \quad (5.10)$$

If we choose the  $\{\phi_{i\sigma}\}$  from the single mode variational family and use the fact that the amplitude for the  $\{\phi_+\}$  field vanishes in the ground state, then the energy functional can be

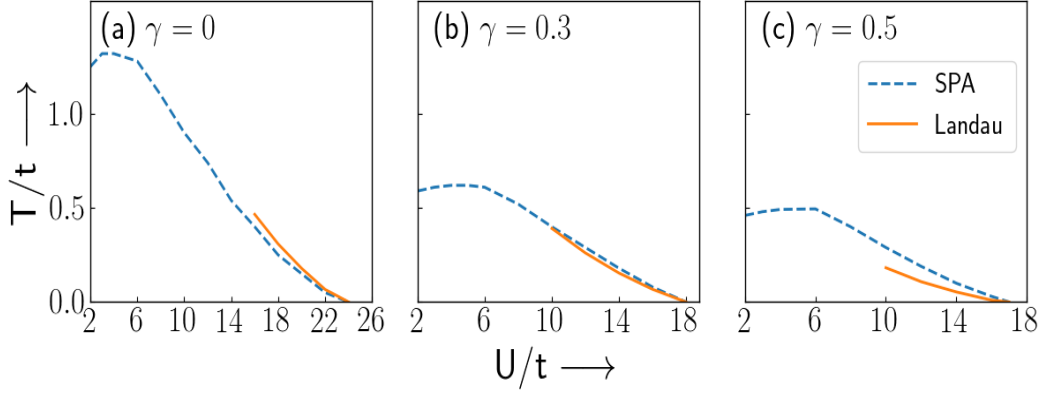


Figure 5.13: Comparison of ordering temperatures as obtained from the SPA based monte-carlo scheme ( $T_c$ ) with that obtained from the second order Landau functional ( $T^*$ ), at  $\lambda = 1.5$  for (a)  $\gamma = 0$ , (b)  $\gamma = 0.3$  and (c)  $\gamma = 0.5$ .

written as:

$$\begin{aligned} \frac{\delta E^{(2)}}{V} &= \alpha^{(2)}(U, \tilde{\mu}, \lambda, \gamma) |\phi_-|^2 \\ \alpha^{(2)}(U, \tilde{\mu}, \lambda, \gamma) &\equiv 1 - \frac{|\tilde{E}_{\mathbf{k}_0(\gamma)}^-|}{2U\tilde{\mu}} \left( \frac{1 + \tilde{\mu}}{(1 - \tilde{\mu})} + \frac{\tilde{\mu}(1 + \lambda)}{\lambda - \tilde{\mu}} \right) \end{aligned} \quad (5.11)$$

where  $V$  is the volume of the system. The condensation wavevector in the ground state is given by the  $\mathbf{k}_0$  for which  $\alpha^{(2)}$  becomes maximally negative. In the expression of  $\alpha^{(2)}$  the factor in brackets remains positive definite for the region of parameter space in which the single mode solution dominates. Hence, the maximally negative value of  $\alpha^{(2)}$  occurs at the minima of the lower band, which are given by  $(\pm k_0, \pm k_0)$ , with  $k_0 = \tan^{-1} [\tan \gamma / \sqrt{2}]$ . From this, we can also conclude that the presence of an arbitrarily small  $\gamma$  would lead to a phase-twisted superfluid. At the optimal  $\mathbf{k}_0$ , the SF-Mott phase boundary is determined by the zeros of  $\alpha^{(2)}$ . At  $\lambda = 0.5$ , for which the single mode variational state dominates, we have matched the phase boundary obtained through numerical minimization, with that obtained from the effective Landau theory. We find excellent agreement between the two, as is evident in Fig. 5.13. A similar match was also found for  $\lambda = 1.5$  where we have stripe and z-FM like order in the ground state.

Notice that at this level we have truncated the Landau expansion to second order. The energy functional obtained above is quadratic in  $\{|\phi_{i\sigma}|\}$ , and hence the amplitudes would vanish at the minimum. So, unless we compute the  $\delta E^{(4)}$  correction, this scheme cannot be used to optimize over the amplitudes. However, once the optimal amplitudes are fixed from the variational

calculation, this functional may be used to anneal the phase of the auxiliary fields, assuming that the amplitude variation with temperature is small close to  $U_c$ . This would allow us to compare the  $T_c(U)$  curves of the bosonic theory with the effective spin model. For a crude estimate, one can ignore the terms inside the square root to derive a more explicit looking functional in terms of the phase degrees of freedom.

$$\begin{aligned} \tilde{E}^{(2)} = & -\frac{1}{2U} f(\tilde{\mu}, \lambda) \left[ \sum_{ij} \mathcal{A}_{ij} |\phi_i^+| |\phi_j^+| \cos(\theta_i^+ - \theta_j^+) \right. \\ & \left. + \sum_{ij} \mathcal{B}_{ij} |\phi_i^-| |\phi_j^-| \cos(\theta_i^- - \theta_j^-) \right] + \sum_{i\sigma} |\phi_{i\sigma}|^2 \end{aligned} \quad (5.12)$$

$$\mathcal{A}_{ij} \equiv \sum_{\mathbf{k}\alpha} ((\mathcal{M}_{\mathbf{k}}^{\alpha+})^* \mathcal{M}_{\mathbf{k}}^{\alpha+}) e^{-i\mathbf{k}\cdot(\mathbf{i}-\mathbf{j})} \quad (5.12a)$$

$$\mathcal{B}_{ij} \equiv \sum_{\mathbf{k}\alpha} ((\mathcal{M}_{\mathbf{k}}^{\alpha-})^* \mathcal{M}_{\mathbf{k}}^{\alpha-}) e^{-i\mathbf{k}\cdot(\mathbf{i}-\mathbf{j})} \quad (5.12b)$$

The couplings  $\mathcal{A}$  and  $\mathcal{B}$  depend on the band structure, and rapidly decay to zero with increasing distance. This allows us to approximate the lattice sum by just the sum over nearest neighbors (or the next-nearest neighbors, in case the nearest neighbor coupling vanishes). Hence, under all these assumptions, one can extract an effective exchange scale which would allow us to calculate an effective ordering temperature ( $T^*$ ) for each point in our parameter space. A comparison of  $T^*$  with the  $T_c$  obtained from the monte-carlo has been shown in Fig. 5.13. The approximation gets better at lower  $\gamma$  (where neglecting the terms within the square root in Eq. 5.8 can be easily justified) as expected. The match seems reasonably good, given the drastic nature of approximations made for extracting a  $T^*$  out of the effective Landau functional.

## 5.6 Discussion

In this work we have studied the thermal phases and phase transitions for bosons with Rashba spin-orbit coupling. Our starting point has been a strong coupling mean-field phase of these bosons in the SF phase near the SF-MI critical point. We find that the result of our mean-field



study lead to homogeneous, phase-twisted, and spin density-wave ordered SF phases depending on the strength of spin-orbit coupling. The phase diagram that we find agrees qualitatively with earlier studies using more sophisticated methods [157]. Using these ground states as the starting point, we then perform a finite temperature Monte Carlo study of the thermal properties of the bosons. The thermal phase diagram for the bosons shows reduction of the critical temperature  $T_c$  with increasing strength of the spin orbit coupling  $\gamma$  at a fixed value of the Hubbard interaction  $U$ . This can be interpreted as spin-orbit coupling introducing an effective frustration in the system leading to reduction of order parameter stiffness and hence  $T_c$ . We also obtain the thermal broadening in the momentum distribution and the presence of satellite peaks at the band minima which reflects the four-fold symmetry of the Rashba term. We note that such four-fold symmetric momentum distribution would be absent in earlier studies which studies an effective Abelian theory involving an equal mixture of Dresselhaus and Rashba spin-orbit terms. We find that the spin density waves survive to temperatures close to  $T_c$ . Finally, we also study the magnetic textures of these bosons via computation of the magnetization  $\mathbf{m}_i$ . In particular, we provide a clear description of the thermal evolution of these textures and their subsequent homogenization for  $T > T_c$ .

The present study neglects the quantum fluctuations of the auxiliary fields completely. This leads to an overestimation of  $U_c$  on one hand, but more importantly, leads to loss of any dynamics in the Mott phase at zero temperature. A scheme for building back the finite frequency quantum modes already exists, and has been used to capture quantum dynamics in the single species problem. Using that method, in this problem one hopes to recover the vortex-like magnetic textures close to the Mott phase[157]. We leave this issue as a subject of future study.

The simplest experimental verification of our work would be measurement of the momentum distribution of the bosons in the SF phase at finite temperature. We provide a detailed thermal broadening of the momentum distribution function which could be verified by standard experiments. In addition, we also predict that  $n_{\mathbf{k}}$  would reflect the four-fold symmetry of the Rashba coupling term at finite temperature. This property involves peak positions of the momentum distribution which is easily measured in standard experiments.

In the presence of spin orbit coupling, the dispersion in the non-interacting problem is given

by,

$$\epsilon^\pm(k_x, k_y) = -2t[\cos(\gamma)(\cos(k_x) + \cos(k_y)) \mp (\sin(\gamma)\sqrt{\sin^2 k_x + \sin^2 k_y})]$$

On the lattice,  $\vec{k} = k_x \hat{x} + k_y \hat{y}$ , where  $k_x = \frac{2\pi j}{L}$  and  $k_y = \frac{2\pi m}{L}$ . Here  $j$  and  $m$  are integers with  $j$  and  $m \in [0, N - 1]$ .  $L$  is the lattice size with  $L = Na$  and  $a$  being the lattice constant. Taking the thermodynamic limit [172],  $L \rightarrow \infty$ , leads to  $k_x$  and  $k_y$  becoming continuous variables  $\in [0, 2\pi/a]$ . This does not change the nature of dispersion, which in the thermodynamic limit would have four degenerate minima.

It is only when one takes the continuum limit ( $a \rightarrow 0$ ), that the above dispersion changes to

$$\epsilon^\pm(k_x, k_y) = -2t[\cos(\gamma)(2 - (k_x^2 + k_y^2)/2) \mp (\sin(\gamma)\sqrt{k_x^2 + k_y^2})]$$

and the four degenerate minima turn into a whole line of minima. In the study by E. Kawasaki and M. Holzmann [173], they observe that systems show the BKT phase transition when the non-interacting dispersion has discrete minima. It is only when there are a continuum of minima in the non-interacting dispersion, that there is no phase transition in the thermodynamic limit. Our results are consistent with the results of reference [173].

## 5.7 Conclusion

We have studied strongly correlated two-component bosons on a square 2D lattice in the presence of Rashba spin-orbit coupling. We focus on the finite temperature problem and use a recently developed auxiliary field based Monte Carlo tool, that retains all the classical thermal fluctuations in this correlated system, to address the thermal state. We establish the superfluid critical temperature  $T_c$  for varying intra- and inter-species repulsion and spin orbit coupling. We study the momentum distribution and ‘magnetic textures’ as the temperature is increased through  $T_c$  and highlight the loss of coherence and spatial order. We have predicted experimentally verifiable signatures of the Rashba coupling in the finite temperature superfluid.

# Impact of speckle disorder on Fermi superfluids

## 6.1 Introduction

Having studied bosonic superfluids in previous chapter, here we study the effect of disorder on fermi superfluids. Fermi superfluids with  $s$ -wave symmetry are robust to the presence of weak disorder [174, 175]. In two dimensions, where all states are localised in the presence of arbitrarily weak disorder [176], and the non interacting system would be an insulator, the presence of pairing interaction leads to a superfluid (SF) state [177]. The interplay of disorder and pairing on the survival of a superfluid ground state has been extensively explored both theoretically [178–182] and experimentally [183–186]. Most of the earlier experiments are on the solid state, where multiple interactions may be at play, but artificially engineered optical lattices [2, 20, 187] now provide a controlled option.

Weak coupling superfluidity in the presence of disorder was first examined by Anderson [174], leading to what is called ‘Anderson’s theorem’ about the insensitivity of the SF state to weak disorder. This insight has been put on firmer ground by solution [178] of the Bogoliubov-de Gennes (BdG) equations for disordered SF’s, explicitly solving for the spatially modulated pairing amplitude. This leads to significant predictions about cluster formation and survival of the spectral gap across the disorder driven SF to insulator transition (SIT). Thermal effects can

be reasonably accessed within the BdG scheme at weak coupling. Complications arise when one moves beyond the weak coupling ‘BCS’ window [160, 188–190].

It is interesting to ask how spatial correlations in the disorder - as in disordered optical lattices - modify the physics. The ‘speckle disorder’ in these systems is characterised by two parameters: the scale  $V$  of potential fluctuations, and the correlation length,  $\sigma$ . Some of the effects of spatial correlations in the disorder have been probed by theory. For non interacting systems, transport in a speckle disorder potential requires revision of many results that exist in the case of uncorrelated disorder. Several studies have been done on this [121–129] modifying the Boltzmann equation and extending the self-consistent theory of localisation. For interacting systems we are aware of two kinds of theory, (i) those which examine [130, 131] bosonic superfluids in a speckle potential, with repulsive interactions present, and (ii) studies of Fermi systems [132, 133] with repulsive interactions and speckle disorder. Those in (i) mainly use the Gross-Pitaevskii framework, focusing on the lowest self-consistent eigenstate, while (ii) uses dynamical mean field theory (DMFT).

Most of the optical lattice disorder experiments have been with bosons, mainly in the ‘non interacting’ regime [109–112] with only a few probing interactions [113–115]. In the non-interacting problems, the trap is switched off and the Bose gas allowed to expand in the presence of speckle disorder. In one dimension (1D), even for weak disorder [109–111] the cloud stops expanding and forms a stationary localised wave. By fitting the stationary pattern a localisation length can be extracted, and is found to increase with speckle size. For bosons in 3D [112], expansion yields a localised part and a diffusive part. For interacting bosons in a 3D optical lattice the effect of disorder on the condensate fraction has been probed [113, 114].

There are experiments on fermions probing both the non interacting [116, 117] and interacting [118, 119] regimes. In the non-interacting regime localisation has been observed in a 3D disordered potential [116]. The dependence on the correlation length of disorder was studied by adjusting the aperture of the speckle focusing lens and the mean localisation length was seen to increase linearly with speckle correlation length [117]. The effect of speckle disorder at fixed correlation length was studied on a strongly interacting Fermi superfluid [119] and its properties investigated using high resolution *in situ* imaging and ‘conductance’ measurements.

In this chapter we study the effect of speckle correlated disorder on a Fermi superfluid by using the tools developed for uncorrelated disorder. We use the two dimensional attractive Hubbard model and work at a mean density  $n = 0.9$  per site and intermediate coupling,  $U = 4t$  (where the  $T_c$  peaks as a function of coupling). We derive an effective SPA functional for fermi superfluids in presence of disorder and solve the resulting problem using auxiliary field monte carlo described in detail section 2.4 Our main results are the following.

1. *Superfluid-insulator boundary at  $T = 0$ :* The critical disorder for the superfluid to insulator transition [191] increases with speckle size  $\sigma$ :  $V_c(\sigma) - V_c(0) \propto \sigma^\alpha$ , where we estimate  $2.0 \lesssim \alpha \lesssim 2.5$ .
2. *Gap and coherence peak:* At  $T = 0$ , increasing the disorder at a fixed speckle size leads to suppression of the coherence peak and the gap. Increasing the speckle size at fixed disorder sharpens the coherence peaks but again *suppresses* the gap.
3. *Critical temperature:* At fixed disorder strength an increase in speckle size increases  $T_c$ . We find that for  $V \lesssim V_c(0)$ ,  $T_c(\sigma) - T_c(0) \propto \sigma^\nu$ , where  $\nu \sim 1$ . Increasing  $\sigma$  can convert an insulator to a superfluid. In such cases, where  $V > V_c(0)$ , we find  $T_c(V, \sigma) \sim (\sigma - \sigma_c)\theta(\sigma - \sigma_c)$ , where  $\sigma_c$  depends on  $V$ .
4. *Thermal pseudogap:* While the  $T_c$  increases with speckle size, the ‘gap temperature’  $T_g$  at which the low temperature gap converts to a pseudogap, reduces with increasing speckle size.
5. *Spatial behaviour and localisation:* At large speckle size the order parameter  $\Delta_i$  in the ground state is small in the ‘hill’ and ‘valley’ regions of the effective potential and is large only over a small fraction of system volume. The phase stiffness coupling the  $\Delta_i$  is however large due to the delocalisation promoted by the smooth potential.

The chapter is organised as follows. Section 6.2 describe the model and method used. In section 6.3 describes our ground state results within the Hartree-Fock-Bogoliubov-de Gennes (HFBdG) scheme, starting with the speckle correlation driven smoothening of the order parameter field, the possibility of an ‘insulator-superfluid transition’, and the unusual low energy features

that emerge in the single particle density of states. Section 6.4 is on the finite temperature results, incorporating the effect of thermal amplitude and phase fluctuations. It shows the increase in superfluid  $T_c$  and the suppression of pseudogap temperature with speckle size. Section 6.5 tries to create an understanding of the results in terms of the Hartree renormalised effective potential, the fermionic eigenstates in that potential, and the effective - spatially inhomogeneous - phase stiffness that arises in the problem. Many of these require numerical calculations of their own, but have a simple connect with localisation theory and XY model physics. We conclude in section 6.6

## 6.2 Model and method

We study the attractive Hubbard model in two dimensions (2D), in the presence of a speckle potential,  $V_i$ :

$$H = -t \sum_{\langle ij \rangle \sigma} c_{i\sigma}^\dagger c_{j\sigma} + \sum_{i\sigma} (V_i - \mu) n_{i\sigma} - |U| \sum_i n_{i\uparrow} n_{i\downarrow} \quad (6.1)$$

$t$  is the nearest neighbour hopping term,  $U$  is the onsite attraction,  $\mu$  the chemical potential. We set  $t = 1$  and fix the fermion density at  $n \approx 0.9$ . We use  $U = 4t$  since the  $T_c$  is large, and the coherence length is small enough for system size  $\sim 24 \times 24$  to access the physics.

Our disorder  $V_i$  has the two point correlation:

$$\langle V(\vec{x}) V(\vec{x} + \vec{r}) \rangle_{\vec{x}} = V^2 (1 + |\gamma(\vec{r})|^2) \quad (6.2)$$

with  $\gamma(\vec{r}) = J_1(|\vec{r}|/\sigma)/(|\vec{r}|/\sigma)$ , where  $J_1$  is the first order Bessel function and  $\sigma$  is the speckle size (correlation length). Fig.6.1 shows the two point function generated on our finite lattice, for two  $\sigma$  values. At large  $\sigma$  the long distance behaviour of the correlation function deviates from the ideal form on our  $24 \times 24$  lattice.

The Hubbard interaction cannot be treated exactly so we follow the approach used in [160]. We decouple the interaction by using two auxiliary fields: (a) a complex scalar ‘pairing field’  $\Delta_i = |\Delta_i| e^{i\theta_i}$ , and (b) a real scalar field  $\phi_i$ . When these fields are assumed to be static, we

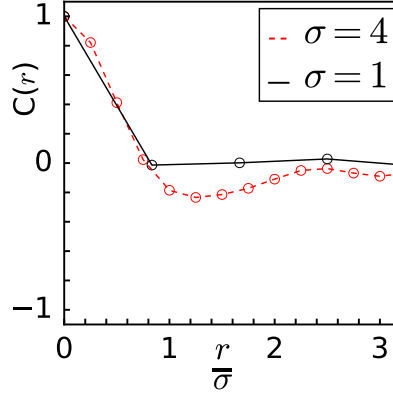


Figure 6.1: The speckle correlation function  $\langle V(\vec{x})V(\vec{x} + \vec{r}) \rangle - \langle V(\vec{x}) \rangle^2$  for  $V = 1$ , plotted as a function of  $r/\sigma$ , by actually sampling our disorder configurations. The function should be universal, and die off for  $r/\sigma \gg 1$ , but sampling on a  $24 \times 24$  lattice leads to the non universal features at large  $\sigma$ .

obtain the following effective model:

$$\begin{aligned}
 H_{eff} &= H_0 + H_{coup} + \frac{1}{|U|} \sum_i (|\Delta_i|^2 + \phi_i^2) \\
 H_0 &= -t \sum_{\langle ij \rangle} \sum_{\sigma} c_{i\sigma}^\dagger c_{j\sigma} + \sum_{i\sigma} (V_i - \mu) n_{i\sigma} \\
 H_{coup} &= \sum_i (\Delta_i c_{i\uparrow}^\dagger c_{i\downarrow}^\dagger + h.c.) + \sum_i \phi_i n_i
 \end{aligned} \tag{6.3}$$

The auxiliary fields follow the probability distribution  $P[\Delta, \phi] \propto \text{Tr}[e^{-\beta H_{eff}}]$  obtained by tracing over fermions.

At zero temperature  $P$  picks the  $\Delta_i, \phi_i$  corresponding to the lowest total energy. This is the mean field Hartee-Fock-Bogoliubov-de Gennes (HFBdG) state. At finite temperature we sample  $\{\Delta_i, \phi_i\}$  configurations by using a Metropolis algorithm. For each attempted update of the  $\Delta_i, \phi_i$  we solve the HFBdG problem on a  $8 \times 8$  lattice around the update site and compute the energy cost of the move [161]. To calculate properties of the system as a whole we solve the HFBdG model on the full lattice for equilibrium configurations, compute fermionic properties, and average over configurations of  $\{\Delta_i, \phi_i\}$ . We keep track of the following:

1. The  $\mathbf{q} = (0, 0)$  component of the pairing field structure factor,

$$S(\mathbf{q}) = \frac{1}{N^2} \sum_{ij} \langle \Delta_i^* \Delta_j \rangle e^{i\mathbf{q} \cdot (\vec{r}_i - \vec{r}_j)} \tag{6.4}$$

both to determine the presence of superfluidity and also to locate the  $T_c$  scale.

2. The overall density of states:

$$N(\omega) = \frac{1}{N} \sum_n \langle |u_n|^2 \delta(\omega - E_n) + |v_n|^2 \delta(\omega + E_n) \rangle \quad (6.5)$$

where  $u_n$  and  $v_n$  are components of the HFBdG eigenfunctions,  $E_n$  are the eigenvalues, and the angular brackets indicate thermal and disorder average.

3. Localisation effects are tracked via the inverse participation ratio. For a normalised state  $|n\rangle$ , the inverse participation ratio (IPR) is  $P(n) = \sum_i |\langle i|n\rangle|^4$ . Averaged over an energy interval this leads to:

$$P(\omega) = \frac{1}{N(\omega)} \sum_n \delta(\omega - \epsilon_n) P(n) \quad (6.6)$$

$P(\omega)$  is a inverse measure of the number of sites over which eigenstates at energy  $\omega$  are spread.

## 6.3 Ground state

The ground state of disordered superfluids is characterised by two spatially varying averages,  $\langle n_i \rangle$  and  $\langle c_{i\uparrow}^\dagger c_{i\downarrow}^\dagger \rangle$ . They are related, in our approach, to the fields  $\phi_i$  and  $\Delta_i$ . At  $T = 0$  within our scheme (and mean field theory) the phase  $\theta_i$  is same at every site. Let us start with the spatial behaviour.

### 6.3.1 Spatial behaviour

Fig.6.2 shows the spatial behaviour in the ground state for changing speckle size and disorder strength. The top row shows the pattern of the bare disorder  $V_i$  for fixed  $V$  and four speckle sizes. Realisations with larger  $V$ , but same  $\sigma$ , can be generated by simply scaling the potential in the top row.



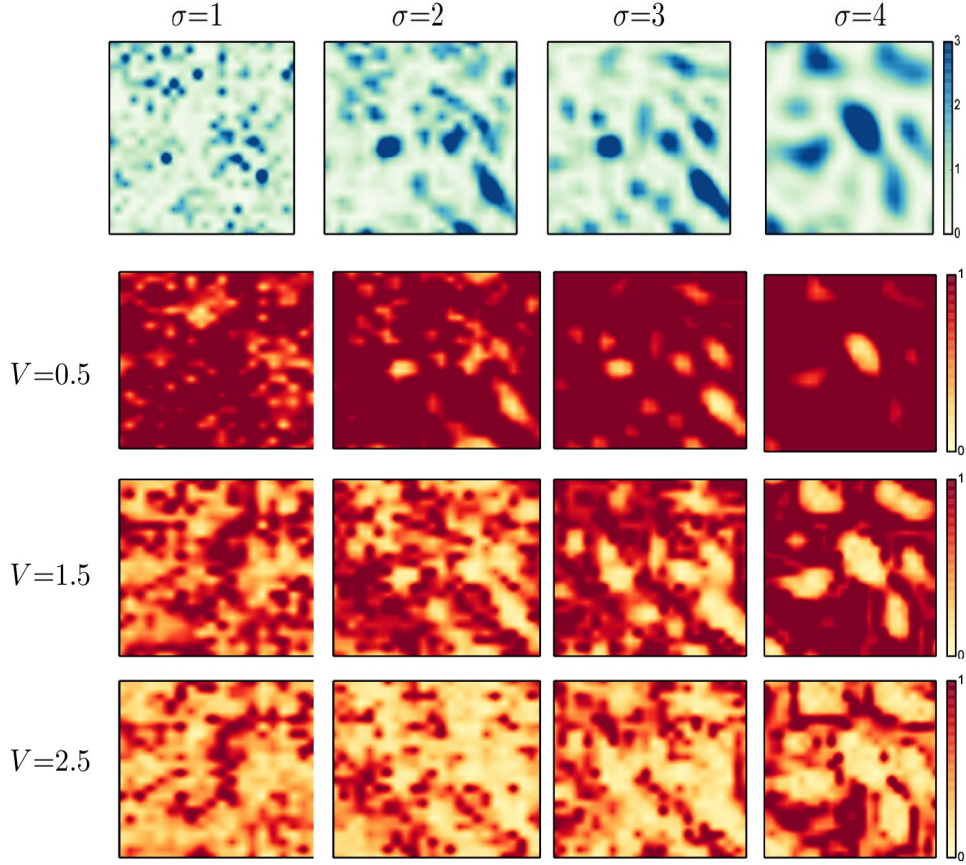


Figure 6.2: Maps for spatial patterns in the ground state. The top row shows the disorder potential  $V_i$  for fixed  $V$  and four speckle sizes  $\sigma$ . Patterns for different  $V$  can be generated by simply scaling these up. Notice the more random  $V_i$  landscape at small  $\sigma$  and the progressively smoother variation at larger  $\sigma$ . The lower set of panels shows the amplitude  $|\Delta_i|$  for varying  $V$  and  $\sigma$ . From the top row down  $V = 0.5t, 1.5t, 2.5t$ . The small  $V$  large  $\sigma$  pattern has the strongest order while the large  $V$  small  $\sigma$  panel has the weakest order. Spatially,  $|\Delta_i|$  anti-correlates with the extremes in  $V_i$ .

As expected, the  $V_i$  shows a rapid site to site variation at  $\sigma = 1$  and a progressively smoother, island like structure, at  $\sigma = 4$ . The lower set of panels shows the amplitude,  $|\Delta_i|$ , of the pairing field that emerges for different combinations of  $V$  and  $\sigma$ . The  $V$  values are chosen to capture behaviour at weak disorder ( $V = 0.5t$ ), close to critical ( $V = 1.5t$ ), and in the insulating regime ( $V = 2.5t$ ) in the uncorrelated limit. Expectedly, the  $|\Delta_i|$  is large and quasi homogeneous at small  $V$  and large  $\sigma$  (top right) and rapidly varying and of small average value when  $V$  is large and  $\sigma$  is small (bottom left). The  $|\Delta_i|$  also ‘anti correlates’ with the extremes  $V_i$ , since these regions - with  $n_i$  close to 0 or 2 - suppress charge fluctuation.

While it seems that an increase in  $V$  can be ‘compensated’ by an increase in  $\sigma$ , to retain the same degree of overall order, the situation is more subtle. From Fig 6.3(a) we located  $(V, \sigma)$

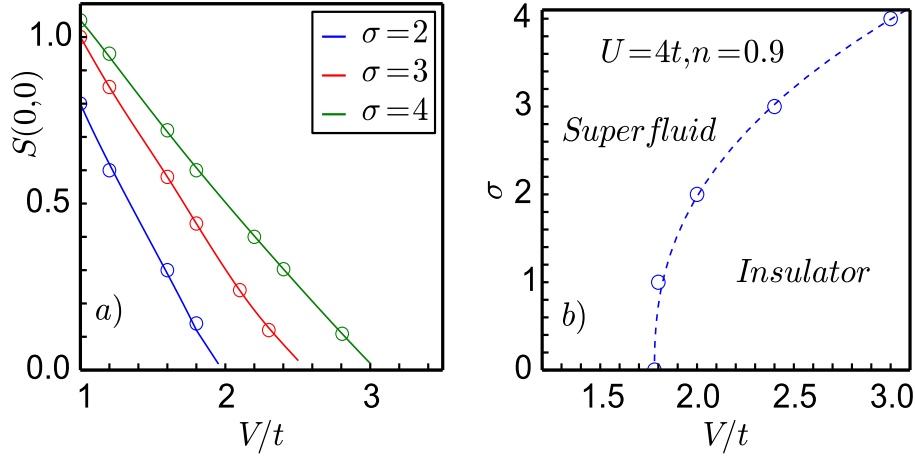


Figure 6.3: Order in the ground state: (a). The superfluid order parameter, *i.e.*, the pairing field structure factor  $S(\mathbf{q} = (0, 0))$ , extrapolated down to  $T = 0$ , as a function of disorder strength  $V$  at various speckle size  $\sigma$ . The critical disorder for SF to insulator transition increases with  $\sigma$ . (b) The ground state phase diagram at  $U = 4t$  and  $n = 0.9$  that emerges from the data in panel (a). The dotted line is a fit  $V_c(\sigma) - V_c(0) \propto \sigma^{2.4}$ .

pairs where the overall magnitude of the order is same at  $T = 0$ . The pair  $(V = 1.5t, \sigma = 2)$  and  $(V = 2.5t, \sigma = 4)$  above satisfy this. Spatial similarity? The small  $V$  small  $\sigma$  pattern, while inhomogeneous, has a more ‘space filling’ character in the order parameter compared to the large  $V$  large  $\sigma$  case where a small fraction of the total area has large  $\Delta_i$  and large areas have  $\Delta_i \rightarrow 0$ . The large hills and valleys created by the strong  $V$  large  $\sigma$  make the  $\Delta_i$  pattern more filamentary. *An increase in  $\sigma$  is not simply like a decrease in  $V$ .*

### 6.3.2 Phase diagram

While the local distribution follows  $P(v) \propto e^{-v/V}$ , the introduction of a correlation length  $\sigma$  makes the critical disorder  $V_c$  dependent on  $\sigma$ . Fig 6.3(a) shows how the SF order parameter at  $T = 0$  (obtained by extrapolating the finite  $T$  result) falls with  $V/t$  for different  $\sigma$ . The intersection of these lines with the  $x$  axis maps out  $V_c(\sigma)$ .

Fig 6.3.(b) shows the  $V - \sigma$  ground state phase diagram obtained by the method above. For uncorrelated exponential disorder we find  $V_c \sim 1.8t$ . With increase in  $\sigma$  the  $V_c$  increases - widening the SF window - and we find that  $V_c(\sigma) - V_c(0) \propto \sigma^\alpha$  with  $\alpha \sim 2.4$ . We call the phase without SF order an ‘insulator’ since it has an interaction induced gap in the spectrum.

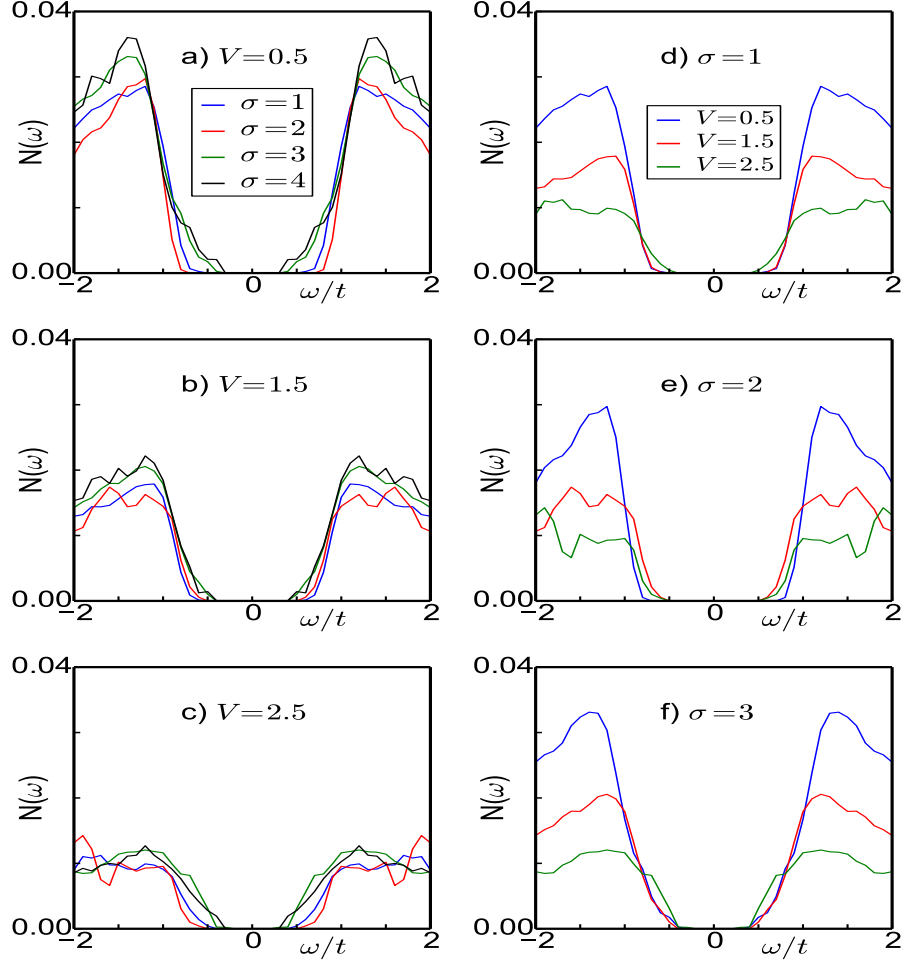


Figure 6.4: Density of states in the ground state. Panels (a)-(c) show the DOS at three strengths of disorder  $V$  and for four  $\sigma$  at each  $V$ . Increase in  $\sigma$  sharpens the coherence peak but also suppresses the gap. Panels (d)-(f) show the same data as in (a)-(c) now highlighting the variation with  $V$  at fixed  $\sigma$ . Here increasing  $V$  suppresses both the coherence peak and the gap.

### 6.3.3 Density of states

We now examine the DOS in the ground state for varying  $V$  and  $\sigma$ , Fig 6.4, the left column shows results at fixed  $V$ , while the right column shows the same data organised in terms of fixed  $\sigma$ . Panel (a) shows the  $\sigma$  dependence at weak disorder. There are three effects that emerge on increasing  $\sigma$ : (i) the ‘coherence peak’ sharpens, (ii) the gap in the DOS reduces, and (iii) the rise from the gap edge to the coherence peak shows a reducing slope - unlike the sharp rise that one sees in a clean system. Panels (b) and (c) show behaviour similar to (a) except for an overall suppression in magnitude (the bandwidths are much larger here) and a rather tenuous coherence feature.

Feature (i) above would be expected also in terms of a decrease in the effective disorder, (ii)

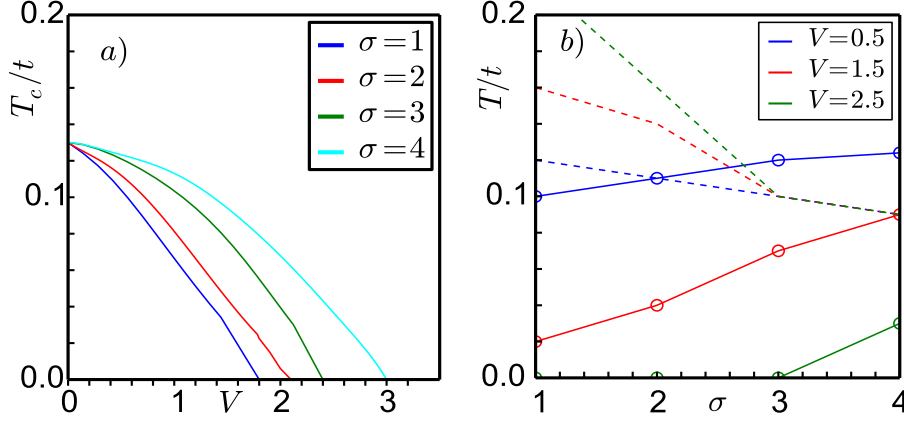


Figure 6.5: Variation of the superfluid  $T_c$  with disorder and speckle correlation length. (a) Disorder dependence for various  $\sigma$ . At  $V = 0$  we have the ‘clean’  $T_c$ . The rate of fall with  $V$  decreases with increasing  $\sigma$ . (b) Firm lines:  $T_c$  for varying  $\sigma$  and three values of  $V$ . Dotted lines:  $T_g$  - low  $T$  gap to high  $T$  pseudogap crossover temperature.

and (iii) however contradict that interpretation. As we will see, an increase in  $\sigma$  does not make the  $|\Delta_i|$  large and homogeneous, it makes the  $|\Delta_i|$  distribution very broad, with large weight at small  $|\Delta|$ . This leads to the low energy weight and unusual shape in  $N(\omega)$ .

The disorder dependence at fixed  $\sigma$  is more traditional. Increasing  $V$  suppresses the coherence peak and increases low energy spectral weight - effectively reducing the gap. The feature is visible in panels (d)-(f).

## 6.4 Thermal fluctuations

To understand how speckle correlations affect the  $T_c$  and spectral properties we do a Monte Carlo on  $H_{eff}$ , annealing the variables  $\phi_i$  and  $\Delta_i$ , which now pick up a distribution at each site. We compute spatial correlations and DOS averaged over equilibrium configurations.

### 6.4.1 Phase diagram

Tracking the ordering peak,  $S(\mathbf{q} = 0)$  in the pairing structure factor allows us to locate a transition scale. For our density and interaction choice that scale is  $\sim 0.13t$  in the clean limit. We choose several  $V$  for  $\sigma = 1 - 4$ , and about 10 realisations for each  $(V, \sigma)$  combination, and cool the system from high temperature. We save equilibrium configurations of  $\{\Delta_i, \phi_i\}$ , the

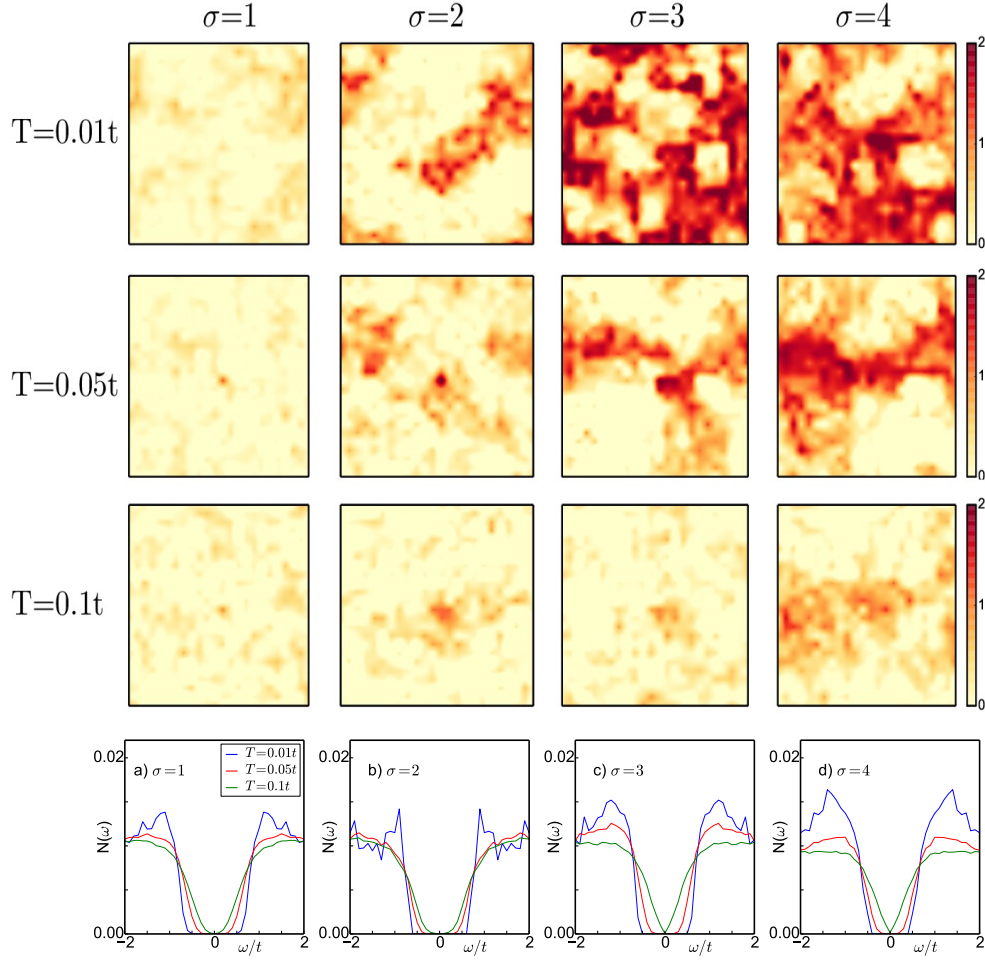


Figure 6.6: Speckle size and temperature dependence of  $\Delta_0 \cdot \Delta_i$  at strong disorder.  $\Delta_0$  is the pairing field at a reference (corner) site. The overlap is based on a single MC configuration at  $V = 2t$  and the  $\sigma, T$  indicated. Increasing  $\sigma$  augments intersite correlation, with the largest  $\sigma$  lowest  $T$  panel (top right) having the strongest correlation. Bottom row: Density of states at  $V = 2t$ , showing  $\sigma$  and  $T$  dependence. At low  $\sigma$  the low  $T$  state shows no coherence peak, and a broad gap that smears out with increasing  $T$ . At  $\sigma = 4$  there is a reasonable coherence feature, and a smaller gap at low  $T$ . The gap fills more quickly with rising  $T$  than at  $\sigma = 1$ . The behaviour in panels (b)-(c) interpolate between (a) and (d).

pairing structure factor  $S(\mathbf{q})$ , and the DOS.

The  $T_c$  scale that emerges is shown in Fig 6.5. Panel (a) shows the  $V$  dependence for different  $\sigma$  while panel (b) shows the  $\sigma$  dependence at fixed  $V$ . In (a) all the  $T_c$  curves start at the clean value when  $V = 0$ . The drop with  $V/t$  is relatively quick at  $\sigma = 1$ , hitting  $T_c = 0$  at  $V \sim 1.8t$ , while at  $\sigma = 4$  the fall is much slower and the critical disorder is  $V \sim 3t$ . These numbers lead to the phase diagram in Fig 6.3.

Panel (b) shows the effect of increasing  $\sigma$  on the  $T_c$ , for fixed values of  $V$ . At weak disorder,  $V = 0.5t$ , the  $T_c$  rises slowly with increasing  $\sigma$  and tends to reach the clean limit value for  $\sigma \gtrsim 4$ .

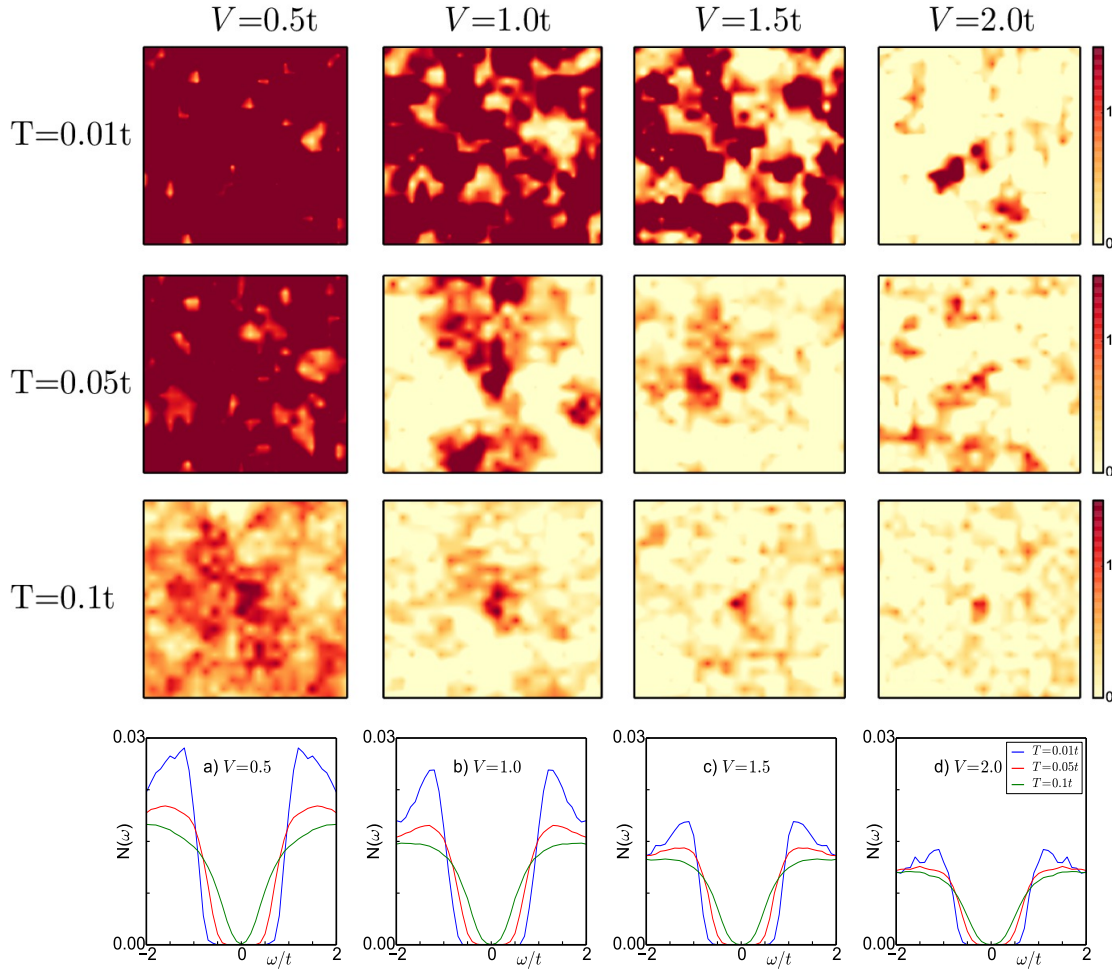


Figure 6.7: Disorder and temperature dependence of  $\Delta_0 \cdot \Delta_i$  at moderate speckle size,  $\sigma = 2$ . At fixed temperature along the row the correlation decreases with increase in  $V$ . The correlation is strongest at  $V = 0.5t$  and  $T = 0.01t$  and decreases with increasing  $V$  or  $T$ . Bottom row: DOS at  $\sigma = 2$ , showing  $V$  and  $T$  dependence. The suppression in coherence peak is seen with increasing temperature and disorder strength. The gap in the density of states reduces with increasing temperature. This effect is more pronounced at small disorder strength.

At  $V = 1.5t$ , where for uncorrelated disorder the system is close to a SF-insulator transition, increasing  $\sigma$  leads to a quicker rise in  $T_c$ . The third case, at  $V = 2.5t$  is the most interesting. Here the system remains insulating upto  $\sigma \sim 3$  and only at  $\sigma = 4$  do we see a small finite  $T_c$ . This is a speckle size induced insulator to SF transition - the bottom right panel in Fig 6.2 suggests that this occurs via percolation. The dotted lines indicate a crossover from the low  $T$  ‘gapped’ regime to a higher  $T$  pseudogap regime. The corresponding  $T_g$  scale reduces with increasing  $\sigma$ .



### 6.4.2 Speckle variation

Fig 6.6 shows the spatial correlations of the pairing field at  $V = 2t$  (where the uncorrelated disorder problem would be insulating) for four speckle sizes and three temperatures. To keep track of both amplitude and phase correlations we plot the scalar  $C_i = \Delta_0 \cdot \Delta_i$ , where  $\vec{R}_0$  is a reference (corner) site and  $\vec{R}_i$  is the site under consideration, treating  $\Delta$  like a two dimensional ‘vector’. At the lowest  $T$  there is hardly any pairing correlation at  $\sigma = 1$ , some trace at  $\sigma = 2$ , and percolative patterns at  $\sigma = 3 - 4$ . Naturally the finite  $T$  systems at  $\sigma = 1, 2$  do not have any SF correlations, the  $\sigma = 3$  system seems to lose global correlation at  $T < 0.05t$ , while the  $\sigma = 4$  system loses its order somewhere between  $T = 0.05t$  and  $T = 0.1t$ . One can draw a  $T_c(\sigma)$  plot akin to Fig 6.5(b) that shows the onset of SF order for  $\sigma > 2$  and a gradual enhancement of  $T_c$  with  $\sigma$ . With increase in  $\sigma$  the low  $T$  gap in the DOS reduces while the coherence peak sharpens. Increase in  $T$  leads to a quicker closure of the gap in the large  $\sigma$  system.

### 6.4.3 Disorder variation

Fig 6.7 shows data that is complementary to Fig 6.6, now focusing on results at a fixed speckle size  $\sigma = 2$ . As expected the low  $T$  system shows SF order for  $V \lesssim 1.5t$  and insulating character for  $V = 2t$ . The  $V = 2t$  system continues to remain insulating at all  $T$  while the weaker disorder cases show a fragmentation of the spatial order, and its loss at a scale  $T_c(V)$ , with increasing  $T$ . The associated  $T_c$  are given in Fig 6.5(a).

The change in DOS with  $V$  and  $T$  is as anticipated. At low  $V$  the low  $T$  DOS has a large gap with sharp edge and reasonable coherence peaks. With increasing  $T$  there is a transfer of weight to low energy and a smearing of the coherence feature. With increase in  $V$  the low  $T$  DOS shows a smaller gap and for  $V \gtrsim 1.5t$  no coherence peaks are visible. However, the transfer of spectral weight to low frequency, due to increasing  $T$ , is weaker in the larger  $V$  case compared to weak disorder.

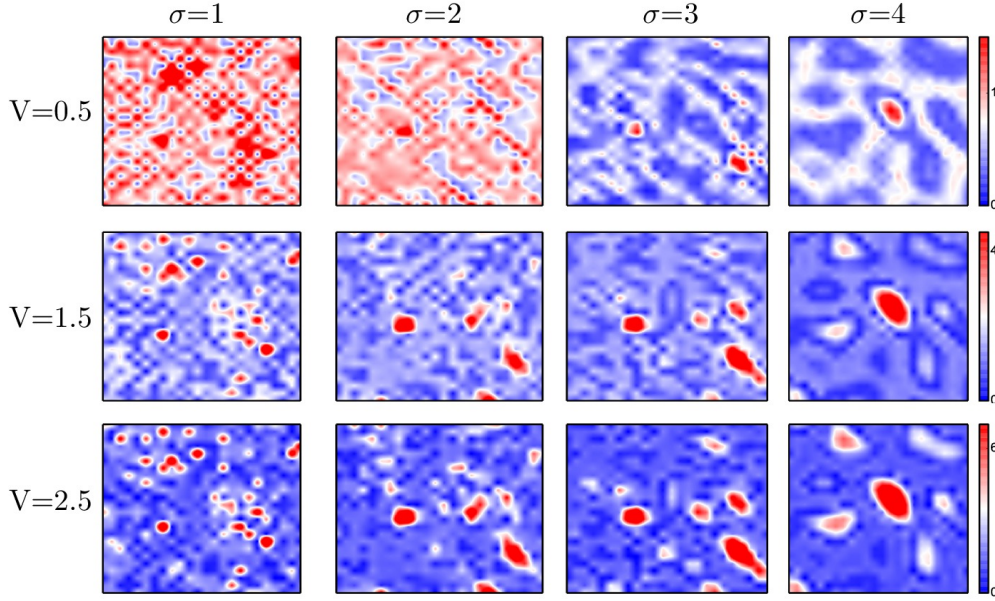


Figure 6.8: Maps for the effective potential  $V_{eff}$  for varying speckle size and disorder strength. The disorder is  $V = 0.5t, 1.5t, 2.5t$  from top to bottom, while the speckle size is  $\sigma = 1, 2, 3, 4$  from left to right. The bottom left panel - large  $V$  and small  $\sigma$  - has the most fluctuating pattern while the top right panel - small  $V$  and large  $\sigma$  - has the smoothest profile.

## 6.5 Discussion

Having seen the results of increasing speckle size on the ground state and thermal properties of the superfluid, we want to suggest how these effects arise from the renormalised effective potential that emerges in this problem.

### 6.5.1 Ground state properties

#### 6.5.1.1 Nature of the effective disorder

From previous studies on uncorrelated disorder[178] we know that the presence of the Hartree term in HFBdG Hamiltonian enhances the effect of disorder. At  $U \gg t$  and in the presence of disorder the density field become strongly inhomogeneous due to the Hartree feedback from the interaction term. As a result, the effective potential to which the fermions react is not  $V_i$  but  $V_{eff} = V_i + \phi_i = V_i + \frac{U}{2}\langle n_i \rangle$ . In contrast to a weakly interacting system with uncorrelated disorder the pairing in the present problem would involve fermions in an effective potential that is (i) strongly renormalised due to the large  $U$ , and (ii) spatially correlated due to the fermionic feedback and finite  $\sigma$ . The combination of  $V$  and  $U$  enhances localisation, while increasing  $\sigma$



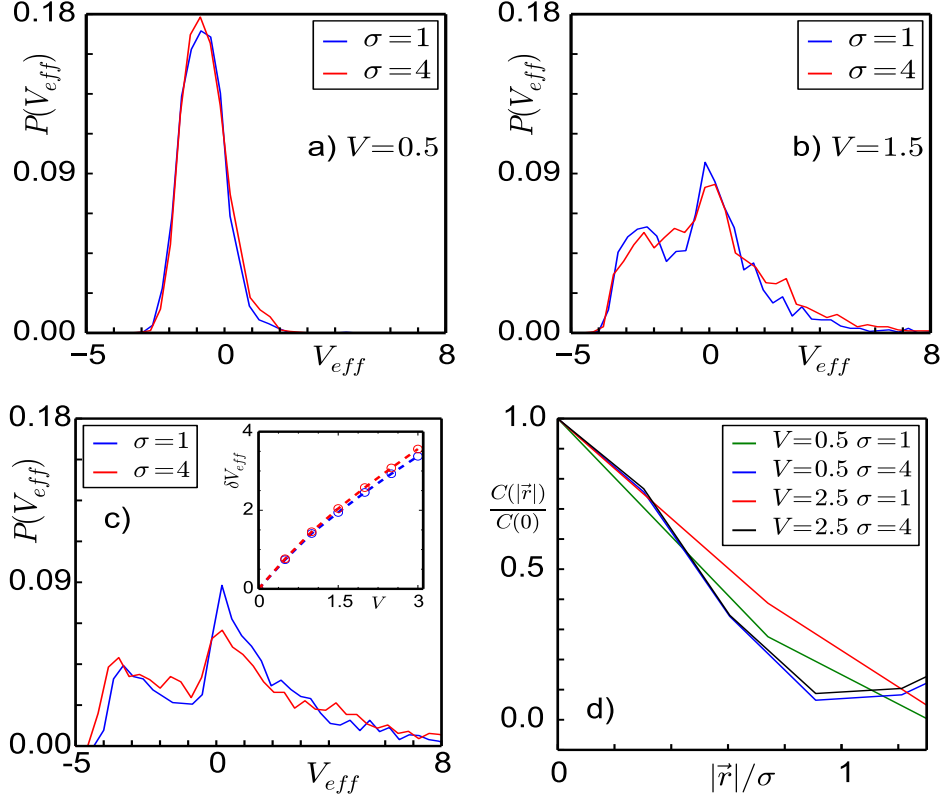


Figure 6.9: (a)-(c) shows  $P(V_{eff})$  at  $V = 0.5t, 1.5t, 2.5$ , respectively, comparing  $\sigma = 1$  with  $\sigma = 4$ . Inset of Panel (c) shows the variance  $\delta V_{eff}$  with respect to  $V$  at  $\sigma = 1, 4$ . At a given  $V$  the variance is slightly larger at  $\sigma = 4$  compared to  $\sigma = 1$ . (d) The normalised  $C(\vec{r})$  as a function of disorder for two speckle sizes. The behaviour suggests that the spatial correlation in  $V_{eff}$  is dictated by just  $\sigma$  and is unaffected  $V$ .

at fixed  $(V, U)$  weakens localisation. These effects in turn impact on the phase stiffness which dictates the  $T_c$  scales of the superfluid [192].

With this in mind, Fig 6.8 shows maps of the effective potential  $V_{eff}$  for varying  $V$  and  $\sigma$ . The  $\phi$  that enters  $V_{eff}$  is obtained via the full HFBdG minimisation. As expected the  $V_{eff}$  at small  $\sigma$  is rapidly fluctuating while at large  $\sigma$  the variation is much smoother. The main impact of  $\phi_i$  is to increase the width of the effective disorder leaving the spatial correlation more or less as in  $V_i$ . This is borne out by comparing Fig 6.8 with the top row in Fig 6.2

We show the distribution of  $V_{eff}$  at three values of  $V$  in Fig 6.9(a)-(c), comparing results at  $\sigma = 1$  and  $\sigma = 4$ . The distributions show marginally greater weight at large  $V_{eff}$  for the larger  $\sigma$  case. The inset of Fig 6.9(c) compares the standard deviation  $\delta V_{eff} = \sqrt{\langle V_{eff}(\vec{r})^2 \rangle - \langle V_{eff}(\vec{r}) \rangle^2}$  for two values of  $\sigma$ . The  $\delta V_{eff}$  at  $\sigma = 4$  is only slightly larger than that at  $\sigma = 1$ . We conclude that the local distribution of  $V_{eff}$  is mainly independent of speckle size.

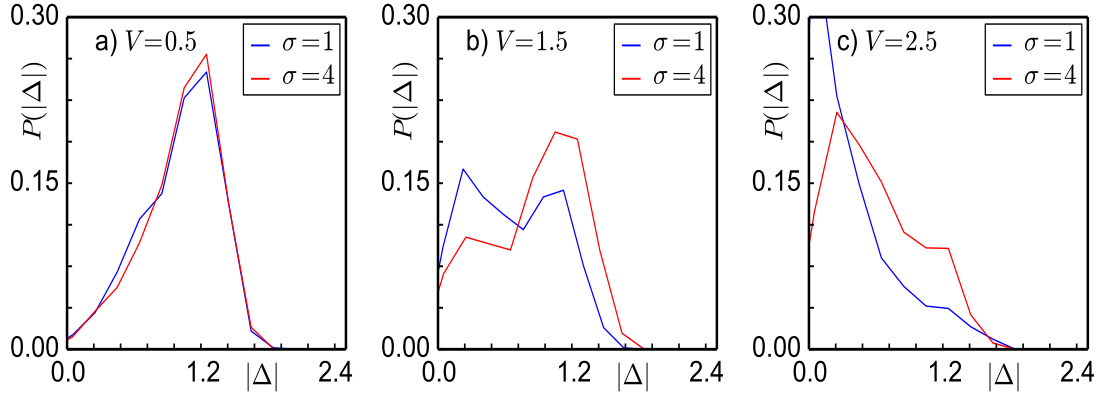


Figure 6.10: The distribution of  $|\Delta_i|$  in the ground state comparing the  $\sigma$  dependence at  $V = 0.5t, 1.5t, 2.5t$ . At larger  $V$  the effect of  $\sigma$  is to create a distribution with large weight at low amplitude.

To characterise the spatial correlations in  $V_{eff}$  panels 6.9(d) show the plot of

$$C(|\vec{r}|) = \langle V_{eff}(\vec{x} + \vec{r}) V_{eff}(\vec{x}) \rangle - \langle V_{eff}(\vec{x}) \rangle^2 \quad (6.7)$$

for speckle sizes 1 and 4. These indicate that the spatial correlations depend on  $\sigma$  but are essentially  $V$  independent. Overall, Fig 6.9 suggests that the strength of  $V_{eff}$  is dictated by  $V$  and  $U$  while the correlations in  $V_{eff}$  are dictated by  $\sigma$  only.

### 6.5.1.2 Order parameter in the ground state

Fig 6.10 shows the distribution of  $|\Delta_i|$  in the ground state for three values of  $V$  and two speckle size. While  $\sigma$  has little effect in the distribution at  $V = 0.5t$ , there is a distinct  $\sigma$  dependence at larger disorder - for a given  $V$  the distribution at larger  $\sigma$  has much greater weight at low amplitude. This correlates with the behaviour of the spatial patterns and the DOS that we have seen earlier.

### 6.5.1.3 Localisation effects

While the  $V_{eff}$  and the resulting  $\Delta_i$  control features like the DOS, to understand intersite coupling between the  $\Delta_i$  we need to understand the spatial extent of the wavefunctions in the  $V_{eff}$  background.

First the case of bare disorder, to set a reference. Fig 6.11 shows the DOS (upper row) and

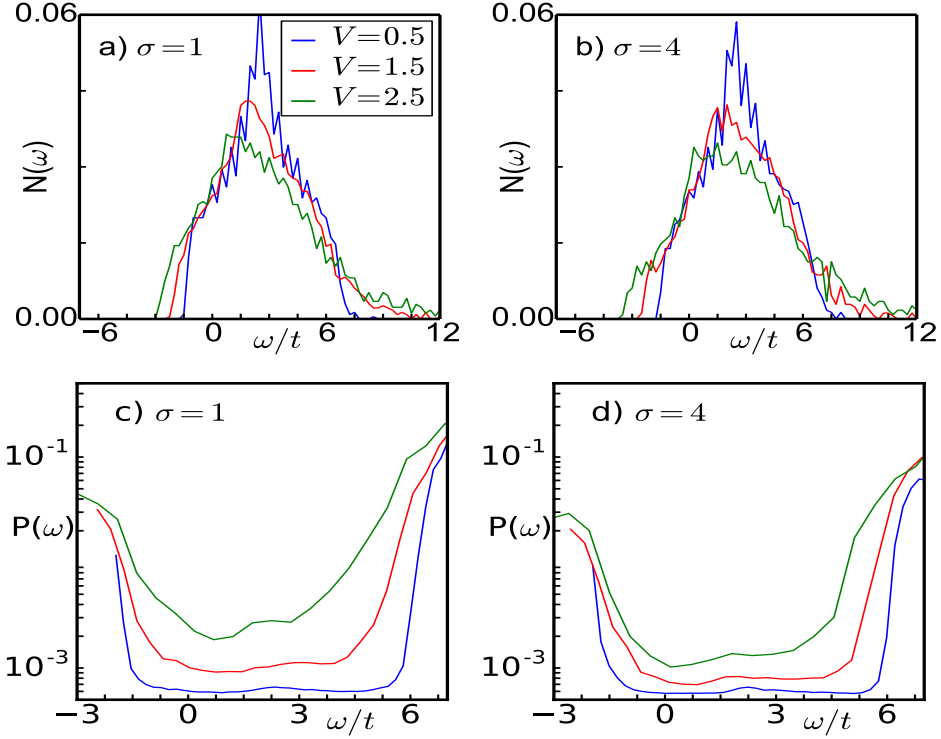


Figure 6.11: DOS and IPR in the background of the bare disorder,  $V_i$ . The DOS naturally broadens with  $V$  but is not very sensitive to  $\sigma$ . The IPR however is sensitive to  $\sigma$  and shows weaker localisation (smaller IPR) at larger  $\sigma$ .

the IPR (lower row) in the presence of only  $V_i$ . The model is solved with  $U$  set to zero. We show results for  $V = 0.5t, 1.5t, 2.5t$  and  $\sigma = 1, 4$ . Since  $P(v) \sim e^{-v/V}$  has a finite positive mean the DOS and IPR plots are asymmetric about  $\omega = 0$ . The greater width of the disorder distribution at larger  $V$  leads to a correspondingly broader DOS. Comparing panels (a) and (b) the speckle size does not make a significant difference to the DOS. The IPR shows a more significant  $\sigma$  dependence, particularly at large  $V$ . At  $V = 0.5t$  the IPR at the band center is  $\ll 10^{-3}$ , suggesting a localisation length  $> \sqrt{10^3}$ , larger than our system size ( $24 \times 24$ ). At  $V = 2.5t$ , however, there is a visible difference between the band center IPR at  $\sigma = 1$  and  $\sigma = 4$ . Nevertheless the numbers for the IPR are still  $\sim 10^{-3}$ , indicating a large localisation length.

Fig 6.12 shows results on the DOS and IPR based on a  $V_{eff}$  extracted from the solution of the HFBdG equation. The effective model that is solved to obtain the results in the figure is

$$H = -t \sum_{\langle ij \rangle} c_i^\dagger c_j + \sum_i V_i^{eff} n_i \quad (6.8)$$

As in Fig 6.11 the disorder values are  $0.5t, 1.5t, 2.5t$ . The fermions are subject to a larger

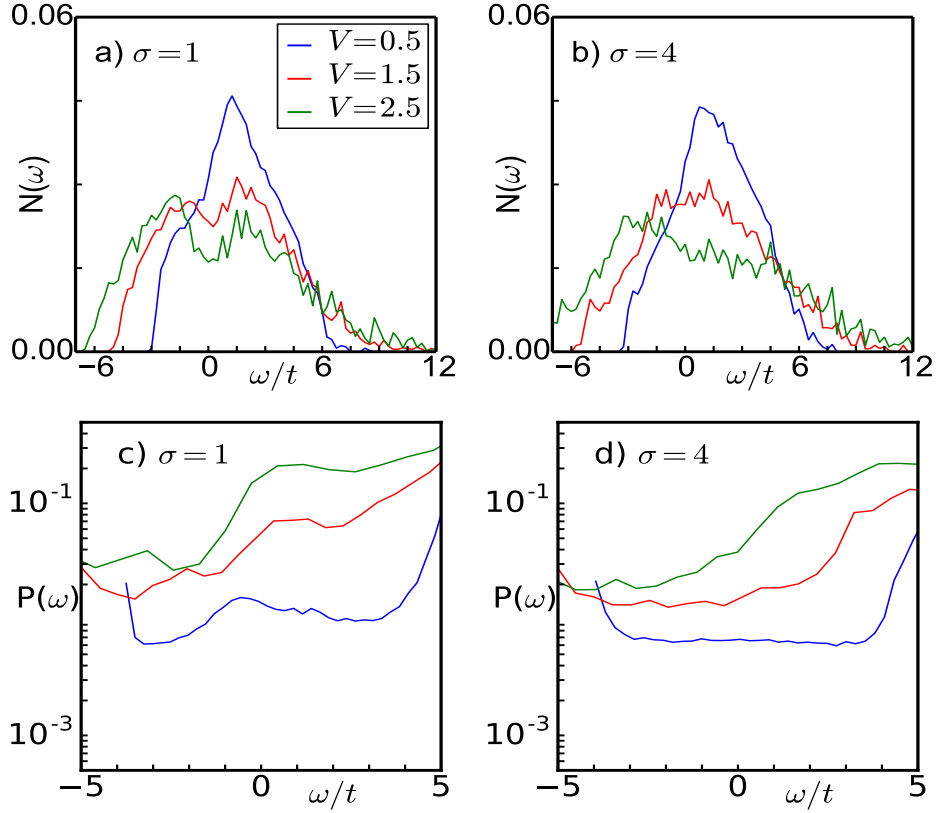


Figure 6.12: DOS and IPR in the presence of the effective disorder  $V_i^{eff} = V_i + \phi_i$ . We have ignored the pairing effects in this calculation. The  $V_i^{eff}$  problem has larger bandwidth, due to the larger effective disorder, and greater localisation compared to the bare disorder. The IPR is much larger than in the  $V_i$  problem, and much larger at  $\sigma = 1$  compared to  $\sigma = 4$ .

effective disorder than in Fig 6.11. As a result the weight spreads over a larger frequency window. Here again the the effect of disorder is somewhat weaker in (b) compared to (a).

The most interesting feature is the contrast between the IPR in Fig 6.11 with that in Fig 6.12. Note the following: (i) the IPR in the  $V_{eff}$  problem, near  $\omega = 0$  or near the band edges, is at least an order of magnitude larger than the corresponding value in the bare disorder problem, and (ii) between Fig 6.12(c) and Fig 6.12(d) the larger  $\sigma$  case shows a clearly smaller IPR. For example around  $\omega = 0$  the IPR at  $V = 2.5t$  and  $\sigma = 1$  is  $\sim 2 \times 10^{-1}$ , while at  $\sigma = 4$  the corresponding IPR is  $\sim 3 \times 10^{-2}$ . The associated ‘localisation length’ would be  $\sim 2$  lattice spacings at  $\sigma = 1$  and  $\sim 5$  lattice spacings at  $\sigma = 4$ . These are well below our system size, and significantly different from one another. This feature of the single particle eigenfunctions enters the fermionic Green’s function  $G_{ij}(i\omega_n)$  and through that the phase stiffness and  $T_c$  scales. We discuss this next.

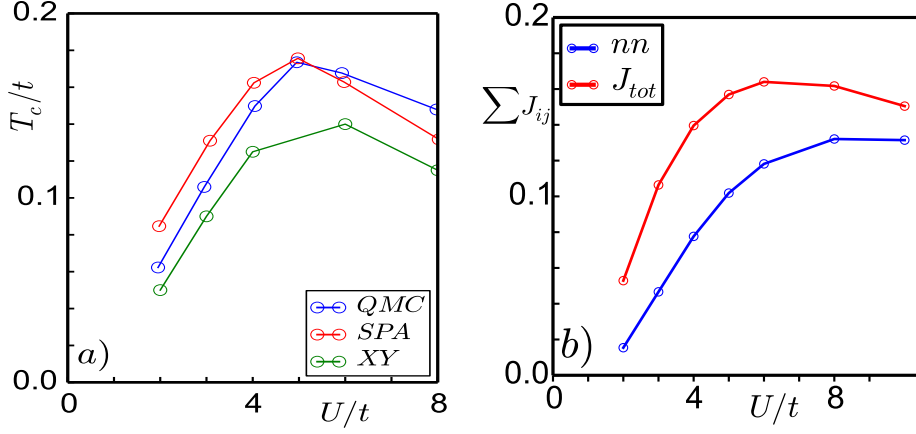


Figure 6.13: (a) The comparison of  $T_c$  scales in the clean limit, between full QMC, our MC result (SPA) and the XY model in the text. We operate near the peak  $T_c$ , the BCS-BEC crossover regime. The SPA well approximates the QMC answer. The XY model also succeeds in capturing the non-monotonic dependence of  $T_c$  on  $U/t$ . (b) Sum of nearest neighbour XY couplings versus sum of all couplings including nearest neighbour. For small to moderate  $U$  the model has significant long range couplings and it is only at very large  $U$  that it can be truncated to nearest neighbour.

### 6.5.2 Phase coupling scales

To understand the intersite coupling between the pairing fields we derive an effective XY model and benchmark it with respect to full MC results. A study of the couplings  $J_{ij}$  of this model with disorder and speckle size provides some insight on the phase transitions we observe in the parent problem. Postponing a detailed justification to the Appendix D, the approximate model we use is of the form:

$$\begin{aligned}
 H_{XY} &= - \sum_{ij} J_{ij} \cos(\theta_i - \theta_j) \\
 J_{ij} &= J_{ij}^0 \Delta_{i0} \Delta_{j0} \\
 J_{ij}^0 &= \frac{1}{\beta} \sum_n [F_{ij}(i\omega_n) F_{ji}(i\omega_n) + G_{ij\uparrow}(i\omega_n) G_{ij\downarrow}(-i\omega_n)]
 \end{aligned} \tag{6.9}$$

The  $\Delta_{i0}$ , etc, are the pairing field amplitude in the  $T = 0$  HFBdG state.  $G_{ij}$  is the ‘normal’ Green’s function and  $F_{ij}$  is the ‘anomalous’ Green’s function computed on the HFBdG state. Via these Green’s functions  $J_{ij}$  contains information about *excitations* on the HFBdG ground state. Note that  $J_{ij}$  is not limited to nearest neighbours.

First a benchmark in the ‘clean’ problem. Fig 6.13(a) compares the  $T_c$  scales obtained from

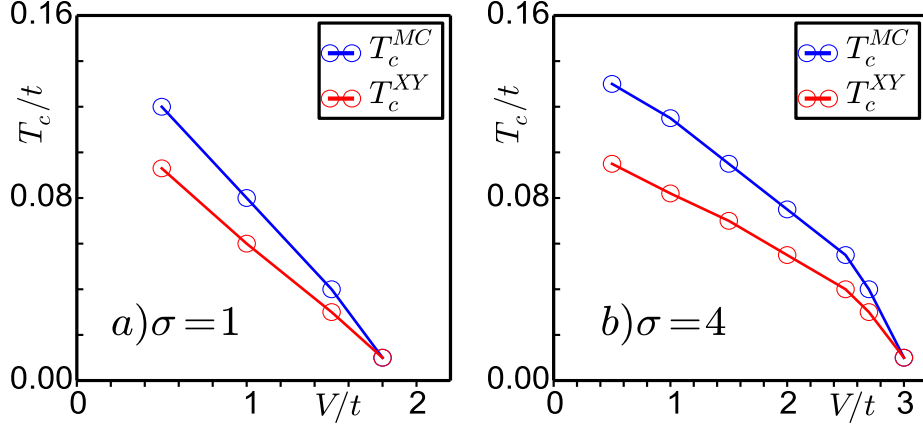


Figure 6.14: Comparison of  $T_c$  scales obtained from exact MC with the XY model for two speckle sizes. Fig a) shows the comparison for speckle size 1 and Fig b) shows the comparison for speckle size 4. The difference in the results of the two calculation increases with decrease of disorder.

the full MC with results from  $H_{XY}$  as  $U/t$  is varied across the BCS to BEC crossover. Given that no explicit finite temperature corrections have been included in the parameters of  $H_{XY}$ , the match is reasonable - and gets better at large  $U$ . Fig 6.13(b) focuses on the couplings that contribute to the  $T_c$ . At weak to intermediate coupling, in this clean limit, couplings beyond nearest neighbour have significant weight. This is demonstrated by the difference between the blue and red curves, for the NN coupling and the sum of all couplings, respectively. However when  $U/t \gg 1$  the nearest neighbour coupling dominates.

At small  $U$ , one can drop the dependence of the  $J_{ij}^0$  on the  $\Delta_{i0}$  so the overall  $J_{ij} \propto \Delta^2$ . This vanishes as  $U/t \rightarrow 0$ . At large  $U$ ,  $J_{ij}^0 \sim \frac{1}{\Delta^3}$  so  $J_{ij} \sim \frac{1}{\Delta} \sim 1/U$  capturing the large  $U$  asymptote. The model interpolates between the small  $U$  and large  $U$  limits.

Now disorder. We use the approach above to compute  $J_{ij}$ . In presence of disorder effective  $J_{ij}$  become inhomogeneous. Fig 6.14 compares the results of the full MC with that of  $H_{XY}$  for two speckle sizes. There is a discrepancy at small disorder, traceable to the clean results at intermediate  $U$ , Fig 6.13 (we are working at  $U = 4t$ ), but the match improves at large disorder.

To understand the effect of disorder on the  $J_{ij}$  we plot the distribution of nearest neighbour bond  $J_{nn}$  for speckle sizes  $\sigma = 1, 4$  in Fig 6.15. At both  $V = 1.5t$  and  $2.5t$  the  $P(J)$  has a strong peak at low  $J$  when  $\sigma$  is small. By contrast most of the weight at large  $\sigma$  is concentrated at intermediate  $J$ . The  $P(J)$  forms an interesting counterpoint to the  $P(|\Delta|)$  that we have seen before. The large  $\sigma$  system has relatively smaller number of large  $\Delta_i$  sites coupled strongly and

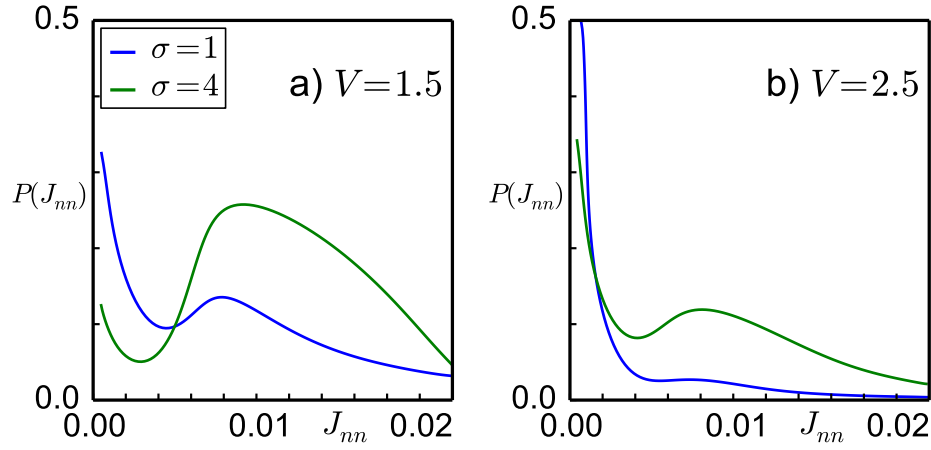


Figure 6.15: Distribution of nearest neighbour bonds, averaged over the system and disorder configurations (a)  $\sigma = 1$  and (b)  $\sigma = 4$ . With increase in disorder strength distribution becomes broad and peak of the distribution shifts to small values of  $J_{nn}$ . At the same disorder the peak is  $P(J_{nn})$  is at a larger  $J_{nn}$  at larger  $\sigma$ . This is the origin of the larger  $T_c$ .

- referring to the spatial maps - in a percolative pattern.

### 6.5.3 Cold atom experiments

To the extent we know, superfluidity of fermions in an *optical lattice* has not been observed yet, although superfluidity in the ‘continuum’, *i.e.*, in a trap has been achieved. This is related to the lower  $T_c$  (and entropy level) needed to achieve lattice superfluidity. Given this, there are no experiments yet that test out the effect of disorder, speckle or otherwise, on lattice Fermi superfluids. However, most of the qualitative features that we observe on increasing speckle size, *e.g.*, the increase in  $T_c$ , the increase in low energy spectral weight, and the weakening localisation, are not lattice specific features. These effects should be visible in the continuum case as well.

Specifically, (i) The change in  $T_c$  on increasing speckle size can be studied by tracking the condensate fraction via time of flight measurements. Such measurements are standard in clean superfluids and can be adapted to the disordered case [193–196]. (ii) The suppression of the gap in the global DOS on increasing speckle size can be probed via radio frequency (RF) spectroscopy, already used in several cold atom experiments [197–199]. In fact there is now a proposal to measure the *local* DOS via an “energy-resolved atomic scanning probe” [200]. If such a method is implemented it would directly visualise the order parameter variation across the speckle disordered sample. (iii) Localisation effects in the disordered potential, and their

weakening with increasing speckle size, can be probed via ‘expansion’ of the disordered gas on removing the trapping potential[116, 117]. (iv) We did not consider transport effects since our degrees of freedom were supposed to be neutral (atoms). However, mass transport measurements in such disordered superfluids are already possible [119], and the impact of increasing speckle size at fixed disorder would be fascinating to observe.

## 6.6 Conclusion

We studied the speckle disorder driven superfluid-insulator transition for intermediate coupling fermions in a two dimensional lattice. The speckle disorder has an exponential on site distribution, and a correlation length  $\sigma$ . We observe the increase of the superfluid window at  $T = 0$ , as well as increase in  $T_c$ , with increasing speckle size. In contrast to the disorder driven superfluid to insulator transition, which is well studied, we mapped out a speckle size driven *insulator to superfluid* transition. While some of the effects of increasing speckle size are crudely like a decrease in disorder, the underlying physics is more complex and contradicts this naive expectation.

Growing speckle size at strong disorder leads to an energy landscape with large scale undulations. In such a background the pairing amplitude is large only in a small fraction of sites. The small amplitude on the rest of the sites leads to suppression of the overall spectral gap, unlike what one would expect from an effective decrease in disorder. The smooth background leads to greater delocalisation of single particle states which generate an effective intersite coupling that grows with speckle size. This compensates for having fewer sites having a large  $\Delta_i$  and leads to a higher  $T_c$ . The variation in the superfluid window with speckle size, the increase in  $T_c$ , and the unusual low energy spectral feature, are testable predictions from our work.



## Appendix A

### A.1 Approximate SPA functional at $T = 0$

The full partition function is given by

$$\begin{aligned}
 Z_{SPA} &= \int D[\psi, \psi^*] D[b, \bar{b}] e^{-S} \\
 &= S_0 + S_{pert} \\
 S_0 &= \int_0^\beta d\tau \left[ \sum_i \bar{b}_i (\partial_\tau - \mu) b_i + \psi_i^* \psi_i + \frac{U}{2} \bar{b}_i b_i (\bar{b}_i b_i - 1) \right] \\
 S_{pert} &= \int_0^\beta d\tau \sum_{ij} -C_{ij} (\bar{b}_i(\tau) \psi_j + h.c)
 \end{aligned}$$

At zero temperature the minimum energy solution is where  $\psi$  is uniform. So we take  $\psi_j = \psi$ .

Now

$$S_{pert} = \int_0^\beta d\tau \sum_i (-2\sqrt{t} \bar{b}_i(\tau) \psi_j + h.c)$$

since  $\sum_j C_{ij} = 2\sqrt{t}$

$$Z_{SPA} = \int D[\psi, \psi^*] D[b, \bar{b}] e^{-S_0} (1 - S_{pert} + \frac{S_{pert}^2}{2!} + \dots)$$

odd power in  $S_{pert}$  is zero due to number conservation The cumulant expansion till fourth order and dropping higher order terms and exponentiating one gets

$$Z_{SPA}(T=0) \approx \int (d\psi d\psi^*)^N e^{-\beta E(\psi)}$$

$$\frac{E(\psi)}{N} = a_0 + a_2 |\psi|^2 + a_4 |\psi|^4$$

The ground state phase boundary is obtained by minimizing  $E(\psi)$ , where  $a_0$ ,  $a_2$  and  $a_4$  is defined in terms of atomic green function.  $N$  is the number of sites.

$$a_0 = [U/2n(n-1) - \mu n]$$

$$a_2 = (1 + 4t G_{ii}(0))$$

$$a_4 = -4t^2 G_{ii}^{2c}$$

$G_{ii}(0)$  and  $G_{ii}^{2c}$  is defined as below

$$G_{ii}(0) = \int_0^\beta d\tau - \langle T_\tau a(\tau) a^\dagger(0) \rangle$$

$$G_{ii}^{2c} = \int_0^\beta d\tau_1 d\tau_2 d\tau_3 \langle T_\tau a(\tau_1) a(\tau_2) a^\dagger(0) a^\dagger(\tau_3) \rangle - 2\beta G_{ii}(0)^2$$

At zero the temperature SPA functional is same as the mean field functional

## A.2 Approximate PSPA functional at $T = 0$

The full partition function is given by

$$Z = \int \prod_i D[\psi, \psi^*] D[b, \bar{b}] e^{-(S_b + S_{pert} + S_b)}$$

At zero temperature the minimum energy solution is where  $\psi$  is uniform.

$$Z(T=0) = \int (d\psi d\psi^*)^N D[b, \bar{b}] e^{-S_0} (1 - (S_b + S_{pert} + \frac{(S_b + S_{pert})^2}{2!} + \dots))$$

After integrating out bosons order by order one gets

$$= \int (d\psi d\psi^*)^N \langle e^{-S_0} \rangle \left( 1 + \frac{\langle S_{pert}^2 \rangle}{2!} + \frac{\langle S_{pert}^4 \rangle}{4!} \right. \\ \left. + \frac{\langle S_b^2 \rangle}{2!} + \frac{\langle S_{pert}^2 S_b^2 \rangle}{4} + \text{higher order terms} \right)$$

One can do cumulant expansion and drop higher terms. Above series can be approximated by

$$Z_{PSPA}(T=0) \approx \int (d\psi d\psi^*)^N e^{-\beta E_{corr}(\psi)}$$

$$E_{corr}(\psi) = E(\psi) + \delta E(\psi)$$

$$E(\psi) = -\frac{1}{\beta} (\log(e^{-\langle S_0 \rangle}) + \frac{\langle S_{pert}^2 \rangle}{2!} + \frac{\langle S_{pert}^4 \rangle}{4!})$$

$$\delta E(\psi) = -\frac{1}{\beta} \left( \frac{\langle S_b^2 \rangle}{2!} + \frac{\langle S_{pert}^2 S_b^2 \rangle}{4} \right)$$

This is the approximated PSPA functional whose terms are explained as below

$$\frac{E_{corr}(\psi)}{N} = (a_0 + \delta a_0) + (a_2 + \delta a_2)|\psi|^2 + a_4|\psi|^4$$

$$\frac{E(\psi)}{N} = (a_0) + (a_2)|\psi|^2 + a_4|\psi|^4$$

where  $a_0, a_2, a_4$  are described as in previous section.

$$\frac{\delta E(\psi)}{N} = \delta a_0 + \delta a_2|\psi|^2$$

$\delta a_0$  and  $\delta a_2$  are obtained from atomic green function

$$\delta a_0 = -\frac{2}{\beta} \int d\tau_1 d\tau_2 t^2 G_{ii}(\tau_1, \tau_2) G_{jj}(\tau_2, \tau_1)$$

$$\delta a_2 = -\frac{8}{\beta} \left( \int_0^\beta d\tau_1 d\tau_2 d\tau_3 d\tau_4 G^2(\tau_1, \tau_2; \tau_3, \tau_4) G(\tau_2, \tau_3) \right. \\ \left. + G^2(i\omega_1 = 0, i\omega_2 = 0; i\omega_3 = 0, i\omega_4 = 0) \right)$$

$$\times G(i\omega_5 = 0, i\omega_6 = 0)) \frac{1}{\beta^2}$$

where  $G^2$  is two particle green function given as below and  $G$  is single particle green function

$$G^2(\tau_1, \tau_2; \tau_3, \tau_4) = \langle T_\tau a(\tau_1) a(\tau_2) a^\dagger(\tau_3) a^\dagger(\tau_4) \rangle$$

$$G(\tau_1, \tau_2) = - \langle T_\tau a(\tau_1) a^\dagger(\tau_2) \rangle$$

The bosonic SPA is a ‘single site’ theory, albeit with a spatially correlated hybridisation field. The PSPA incorporates effects due to tunneling of particles to other sites. To lowest order PSPA corrects the  $|\psi|^2$  term and leads to shifting of the phase boundary.

### A.3 Internal energy

We are interested in computing energy, given by sum of kinetic energy and potential energy

$$E = \frac{\text{Tr}[e^{-\beta H} \sum_{\langle ij \rangle} -t_{ij} a_i^\dagger a_j - \mu \sum_i \hat{n}_i]}{\text{Tr}[e^{-\beta H}]} + \frac{U \text{Tr}[e^{-\beta H} \sum_i \hat{n}_i(\hat{n}_i - 1)]}{2 \text{Tr}[e^{-\beta H}]}$$

#### A.3.1 Approximation I: SPA

$Z_{SPA}$  is the adiabatic partition function

$$\begin{aligned} Z_{SPA} &= \int \prod_i d[\psi_i, \psi_i^*] \mathcal{D}[b, \bar{b}] e^{-S} \\ &= \int \prod_i d[\psi_i, \psi_i^*] \text{Tr}[\exp(-\beta H')] \end{aligned}$$

$$H' = - \sum_{ij} C_{ij} (a_i^\dagger \psi_j + h.c.) + \sum_i \frac{U}{2} \hat{n}_i(\hat{n}_i - 1) - \mu \hat{n}_i + \psi_i^* \psi_i$$

Under SPA approximation energy is given by,

$$E_{SPA} = \frac{\int \prod_i d[\psi_i, \psi_i^*] \text{Tr}[e^{-\beta H_{eff}} \sum_{\langle ij \rangle} -t_{ij} a_i^\dagger a_j - \mu \sum_i \hat{n}_i]}{\int \prod_i d[\psi_i, \psi_i^*] \text{Tr}[e^{-\beta H'}]} + \frac{U}{2} \frac{\int \prod_i d[\psi_i, \psi_i^*] \text{Tr}[e^{-\beta H_{eff}} \sum_i \hat{n}_i(\hat{n}_i - 1)]}{\int \prod_i d[\psi_i, \psi_i^*] \text{Tr}[e^{-\beta H'}]}$$

which gives

$$E_{SPA} = \langle (T(\psi, \psi^*) + U(\psi, \psi^*)) \rangle_{SPA}$$

where  $T(\psi, \psi^*)$  is the expectation value of kinetic energy operator including chemical potential term and  $U(\psi, \psi^*)$  is the expectation value of interaction energy operator in a auxiliary field configuration and angular brackets stand for thermal average over stored MC configurations.

Since within SPA approximation, Hamiltonian is site decoupled,

$$T(\psi, \psi^*) = - \sum_{\langle ij \rangle} t_{ij} \langle a_i^\dagger \rangle \langle a_j \rangle$$

$$\langle a_i^\dagger \rangle = \frac{\sum_{n_i} \exp -\beta E^{n_i} \langle n_i | a_i^\dagger | n_i \rangle}{\sum_{n_i} \exp -\beta E^{n_i}}$$

where  $E^{n_i}$  and  $|n_i\rangle$  are the eigenvalues and eigenstates of  $H'_i$  Hamiltonian at site  $i$ . Similarly one can compute the expectation value of  $b_j$ .

Similarly

$$U(\psi, \psi^*) = \frac{U}{2} \sum_i \frac{\sum_{n_i} \exp -\beta E^{n_i} \langle n_i | \hat{n}_i(\hat{n}_i - 1) | n_i \rangle}{\sum_{n_i} \exp -\beta E^{n_i}} - \mu \sum_i \frac{\sum_{n_i} \exp -\beta E^{n_i} \langle n_i | \hat{n}_i | n_i \rangle}{\sum_{n_i} \exp -\beta E^{n_i}}$$

### A.3.2 Approximation II: PSPA

Under PSPA approximation,

$$\begin{aligned}
K.E. &= \frac{Tr[e^{-\beta H} \sum_{\langle ij \rangle} -t_{ij} a_i^\dagger a_j]_{PSPA}}{Tr[e^{-\beta H}]_{PSPA}} \\
&= \frac{\int D[\psi, \psi^*] e^{-F_{PSPA}(\psi\psi^*)} T(\psi, \psi^*)}{\int D[\psi, \psi^*] e^{-F_{PSPA}(\psi\psi^*)}}
\end{aligned}$$

$$\begin{aligned}
T(\psi, \psi^*) &= - \sum_j t_{ij} \frac{Tr[e^{-\beta H_{eff,i}} a_i^\dagger]}{Tr[e^{-\beta H'_i}]} \frac{Tr[e^{-\beta H'_j} a_j]}{Tr[e^{-\beta H'_j}]} \\
&- \sum_{i,j} t^2 (F1_{i,j;i,j+1} + F1_{i,j;i+1,j} + F2_{i,j;i+1,j} + F2_{i,j;i,j+1})
\end{aligned}$$

For potential energy

$$P.E. = \frac{U}{2} \frac{Tr[e^{-\beta H} \sum_i \hat{n}_i (\hat{n}_i - 1)]_{PSPA}}{Tr[e^{-\beta H}]_{PSPA}}$$

$$= \frac{\int D[\psi, \psi^*] e^{-F_{PSPA}(\psi\psi^*)} U(\psi, \psi^*)}{\int D[\psi, \psi^*] e^{-F_{PSPA}(\psi\psi^*)}}$$

$$U(\psi, \psi^*) = \frac{Tr[e^{-\beta H'} U/2 \sum_i \hat{n}_i (\hat{n}_i - 1) - \mu \hat{n}_i]}{Tr[e^{-\beta H'}]}$$

The total energy is sum of kinetic(K.E.) and potential energy(P.E.) contributions.

$F1_{i,j;k,l}$  and  $F2_{i,j;k,l}$  are defined in Chapter 2(see equations 2.16 and 2.17).

## A.4 Momentum distribution

Within PSPA  $n(\vec{k})$  is given by

$$n(\vec{k})_{PSPA} = n(\vec{k})_{th} + n_{qc}(\vec{k})$$

$$n(\vec{k})_{th} = \frac{1}{N} \sum_{\vec{r}, \vec{r}'} e^{-i\mathbf{k} \cdot (\vec{r} - \vec{r}')} < \frac{Tr[e^{-\beta H'} a_{\vec{r}}^\dagger a_{\vec{r}'}]}{Tr[e^{-\beta H'}]} >$$

$n(\vec{k})_{th}$  depend on the thermal fluctuations of auxiliary field.

$$n_{qc}(\vec{k}) = \frac{1}{N} \sum_{\vec{r}, \vec{r}'} e^{-i\mathbf{k} \cdot (\vec{r} - \vec{r}')} t_{\vec{r}, \vec{r}'} (F1_{ij;kl} + F2_{ij;kl})$$

where  $\vec{r} = i a \hat{x} + j a \hat{y}$  and  $\vec{r}' = k a \hat{x} + l a \hat{y}$ , where  $a$  is the lattice spacing.

$n_{qc}(\vec{k})$  takes into account the effect of quantum tunneling of bosons to nearest neighbour sites to the leading order in hopping.

Within the Mott Phase, at  $T = 0$ , effective hybridisation,  $\Phi = 0$ .

$n(\vec{k})_{th} = 1$  and  $n(\vec{k})_{qc} = \frac{4t_{\vec{k}}}{U}$ , at  $T = 0$  in the Mott phase.

The temperature leads to thermally generated auxiliary field whose magnitude is small at low temperatures. The effect of temperature is more prominent on  $n(\vec{k})_{th}$  than  $n(\vec{k})_{qc}$ . So we just focus on the effect of temperature on  $n(\vec{k})_{th}$ . Now,

$$\begin{aligned} n(\vec{k})_{th} &= \frac{1}{N} \sum_{\vec{r}, \vec{r}'} e^{-i\mathbf{k} \cdot (\vec{r} - \vec{r}')} \frac{Tr[e^{-\beta H'} a_{\vec{r}}^\dagger a_{\vec{r}'}]}{Tr[e^{\beta H'}]} \\ &= \frac{1}{N} \sum_{\vec{r}} \frac{Tr[e^{-\beta H'_r} a_{\vec{r}}^\dagger a_{\vec{r}}]}{Tr[e^{\beta H'_r}]} \\ &\quad + \frac{1}{N} \sum_{\vec{r} \neq \vec{r}'} e^{-i\mathbf{k} \cdot (\vec{r} - \vec{r}')} \frac{Tr[e^{-\beta H'} a_{\vec{r}}^\dagger a_{\vec{r}'}]}{Tr[e^{\beta H'}]} \end{aligned}$$

. First part of the summation is  $\vec{k}$  independent and second part has  $\vec{k}$  dependence.

Let's focus on the  $\vec{k}$  dependent part of the summation when  $\vec{r} \neq \vec{r}'$

$$\frac{Tr[e^{-\beta H'} a_{\vec{r}}^\dagger a_{\vec{r}'}]}{Tr[e^{\beta H'}]} = \frac{Tr[e^{-\beta H'_r} a_{\vec{r}}^\dagger]}{Tr[e^{\beta H'_r}]} \frac{Tr[e^{-\beta H'_{r'}} a_{\vec{r}'}]}{Tr[e^{\beta H'_{r'}}]}$$

Now

$$\frac{Tr[e^{-\beta H'_r} a_{\vec{r}}^\dagger]}{Tr[e^{\beta H'_r}]} = \frac{\sum_{n_{\vec{r}}} \exp -\beta E_{n_{\vec{r}}} < n_{\vec{r}} | a_i^\dagger | n_{\vec{r}} >}{\sum_{n_{\vec{r}}} \exp -\beta E_{n_{\vec{r}}}}$$

where  $|n_{\vec{r}} >$  and  $E_{n_{\vec{r}}}$  are eigenstates and eigenvalues at site  $\vec{r}$ .

So within the Mott phase, we can truncate the Hilbert space at each site to three states with

0, 1, and 2 occupancy.

In presence of small non-zero hybridisation,

$$H'_i = H_i^0 + H_i^p$$

$$H_i^0 = \frac{U}{2}n_i(n_i - 1) - \mu n_i$$

$$H_i^p = \Phi_i b_i^\dagger + h.c.$$

$|0\rangle, |1\rangle, |2\rangle$  are eigenstates of  $H^0$  problems with  $0, -\mu, U - 2\mu$  eigenvalues respectively.

So for  $\mu = 0.4U$ ,  $|1\rangle$  would be the ground state of  $H_0$  problem and  $|0\rangle, |2\rangle$  are the excited states of the problem.

we include corrections in energy eigenstates to second order in hybridisation and correct states to first order in hybridisation, we get.

$$E_0 = |\Phi_i|^2/\mu, E_1 = -\mu + |\Phi_i|^2(\frac{2}{U-\mu} - \frac{1}{\mu}), \text{ and } E_2 = U - 2\mu + 2|\Phi_i|^2/(U - \mu)$$

$$|0'\rangle = |0\rangle + \frac{\Phi_i}{\mu}|1\rangle$$

$$|1'\rangle = |1\rangle - \frac{\Phi_i^*}{\mu}|0\rangle - \frac{\sqrt{2}\Phi_i}{(U - \mu)}|2\rangle$$

$$|2'\rangle = |2\rangle + \frac{\sqrt{2}\Phi_i^*}{(U - \mu)}|1\rangle$$

The gap from the ground state to the excited state would be  $E_0 - E_1 = \mu + |O(\Phi)|^2$  and  $E_2 - E_1 = U - \mu + |O(\Phi)|^2$ .

The gap from the ground state to the excited state is of the order of  $0.4U$  or  $0.6U$ .

So for temperatures less than  $0.2U$  contribution to  $Tr[e^{-\beta H'_r} a_r^\dagger]$  from the excited states can be neglected.

$$Tr[e^{-\beta H'_r} a_r^\dagger] \approx \langle 1_r | a_r^\dagger | 1_r \rangle = \left( \frac{-\Phi_r^*}{\mu} + 2 \frac{\Phi_r}{\mu - U} \right)$$



Substituting above expressions for  $a_r^\dagger$  and  $a_r$  in the  $n(\vec{k})_{th}$  and simplifying we get when  $\Phi$  is small,

$$n(\vec{k})_{th}^{Mott} \approx 1 + \alpha(U, \mu) \langle \Phi_k \Phi_k \rangle + \beta(U, \mu) \langle \Phi_k^* \Phi_k^* \rangle \\ + \gamma(U, \mu) \langle |\Phi_k|^2 \rangle$$

Since within the mott phase  $\langle \Phi_k \Phi_k \rangle$  is zero, can be seen from the gaussian theory, we get

$$n(\vec{k})_{th}^{Mott} \approx 1 + \gamma(U, \mu) \langle |\Phi_k|^2 \rangle \\ \gamma(U, \mu) = 4/(U - \mu)^2 + 1/\mu^2$$



# Appendix B

## Appendix B

### B.1 Random phase approximation (RPA)

At  $T = 0$  the field  $\phi_i$  is uniform,  $\phi_0$  say, so the Green's function is:

$$G(\vec{k}, \omega) = \frac{1}{G_{at}^{-1}(\omega, \phi_0) - \epsilon(\vec{k})}$$

where  $G_{at}(\omega, \phi_0)$  is the atomic Green's function in the presence of a 'hybridisation'  $\phi_0$ .  $G_{at}(\omega, \phi_0)$  is a sum of simple poles at  $T = 0$ . RPA Green's function also has a set of undamped excitations for each  $\vec{k}$ . Very close to superfluid-Mott transition phase boundary order parameter  $|\Phi|^2$  is small.

$G_{at}(\omega, \phi_0)$  to leading orders in  $\phi_0^2$  can be approximated by

$$G_{at}(\omega, \phi_0) \approx G_{at}(\omega, 0) + \hat{B}$$

where

$$G_{at}(\omega, 0) = \begin{bmatrix} \frac{1}{\omega+\mu} - \frac{2}{\omega-U+\mu} & 0 \\ 0 & \frac{1}{-\omega+\mu} - \frac{2}{-\omega-U+\mu} \end{bmatrix}$$

$$\hat{B} = \begin{bmatrix} g\phi^2 & g\phi^2/2 \\ g\phi^2/2 & g\phi^2 \end{bmatrix}$$

where  $g$  is the four point function.

$$g = -\frac{4(n+1)(n+2)}{(2\mu - (2n+1)U)(Un - \mu)^2} - \frac{4n(n-1)}{(\mu - U(n-1))^2(U(2n-3) - 2\mu)} \\ + \frac{4n(n+1)}{(\mu - Un)(-\mu + U(n-1))^2} + \frac{4n(n+1)}{(\mu - Un)^2(-\mu + U(n-1))} \\ + \frac{4n^2}{(-\mu + U(n-1))^3} + \frac{4(n+1)^2}{(\mu - Un)^3}$$

For small  $|\Phi|^2$  one can approximate,

$$G_{at}(\omega, \phi)^{-1} \approx G_{at}(\omega, 0)^{-1} - \Sigma$$

$$\Sigma = G_{at}(\omega, 0)^{-1} \hat{B} G_{at}(\omega, 0)^{-1}$$

where  $\Sigma$  is the self energy due to presence of non-zero value of hybridisation. We neglect the frequency dependence of self energy. When value of hybridisation is zero, occupation number basis forms the good eigen states. The presence of non-zero hybridisation creates mixing in number basis states. It leads to generating a non-zero self energy.

$$\Sigma(\omega = 0) = \begin{bmatrix} g\phi^2/f & g\phi^2/2f \\ g\phi^2/2f & g\phi^2/f \end{bmatrix}$$

where  $f = (\frac{1}{\mu} - \frac{2}{-U+\mu})^2$  and we have included only zero frequency part in the self energy.  $g$  is the four point function.

So RPA green's function can be approximated by,

$$\bar{G}(\vec{k}, \omega) \approx \frac{1}{[\bar{G}_{at}(\omega, 0)]^{-1} - \Sigma(\omega = 0) - \epsilon(\vec{k})}$$

## Appendix C

### C.1 Effective action in the spin orbit problem

The full partition function is defined in Eq.2.51. Keeping  $S^{loc}$  intact we wish to decompose the  $S^{hop}$  by a Hubbard-Stratonovich (HS) transformation. In order to implement it we need to segregate the negative part of the bands, so that the bosonic Gaussian integral remains well defined. This leads to

$$S^{hop} = S^{neg} + S^{pos} \quad (\text{C.1})$$

with,

$$S^{neg} = \sum_{k\sigma n} \psi_{k\sigma n}^\dagger \tilde{E}_k^\sigma \psi_{k\sigma n} \quad (\text{C.1a})$$

$$S^{pos} = \sum_{k\sigma n} \psi_{k\sigma n}^\dagger \left( E_k^\sigma - \tilde{E}_k^\sigma \right) \psi_{k\sigma n} \quad (\text{C.1b})$$

where  $n$  is the Matsubara frequency label. In this work, we neglect the  $S^{pos}$  part and implement a HS transformation on the  $S^{neg}$ .

$$\begin{aligned} e^{-S^{neg}} &= e^{-\sum_{k\sigma n} \psi_{k\sigma n}^\dagger \tilde{E}_k^\sigma \psi_{k\sigma n}} \\ &= \prod_{k\sigma n} \left\{ \int \mathcal{D} [\phi_{k\sigma n}^*, \phi_{k\sigma n}] e^{\phi_{k\sigma n}^* \tilde{E}_k^{-1} \phi_{k\sigma n}} \right\} \end{aligned} \quad (\text{C.2a})$$

$$\times e^{-\left(\psi_{k\sigma n}^* \phi_{k\sigma n} + \phi_{k\sigma n}^* \psi_{k\sigma n}\right)} \} \quad (\text{C.2b})$$

$$\begin{aligned} & \stackrel{\phi \rightarrow \sqrt{-\tilde{E}}\phi}{=} \prod_{k\sigma n} \left\{ \int \mathcal{D}[\phi_{k\sigma n}^*, \phi_{k\sigma n}] e^{-\phi_{k\sigma n}^* \phi_{k\sigma n}} \right. \\ & \quad \left. \times e^{-\sqrt{-\tilde{E}_{k\sigma}} \left( \psi_{k\sigma n}^* \phi_{k\sigma n} + \phi_{k\sigma n}^* \psi_{k\sigma n} \right)} \right\} \quad (\text{C.2c}) \end{aligned}$$

where  $\{\phi_n^+\}$  and  $\{\phi_n^-\}$  are the auxiliary fields which couple with the respective chiral bosonic modes. This procedure therefore leads to Eq. 2.52 of the main text.

# Appendix D

## Appendix D

### D.1 Derivation of an effective XY model

We outline here the derivation of effective model. The partition function fermion auxillary field model is given by

$$Z = \int D[\Delta, \Delta^*] D[\phi] D[c, \bar{c}] e^{-S_{eff}} \quad (D.1)$$

$$S_{eff} = \int_0^\beta d\tau \sum_{i,\sigma} \bar{c}_{i,\sigma} (\partial_\tau - \mu) c_{i,\sigma} + H_{eff}(\bar{c}, c, \Delta, \Delta^*, \phi) \quad (D.2)$$

$$H_{eff} = H_0 + H_{coup} + \frac{1}{|U|} \sum_i (|\Delta_i|^2 + \phi_i^2) \quad (D.3)$$

$$H_0 = -t \sum_{\langle ij \rangle}^\sigma c_{i\sigma}^\dagger c_{j\sigma} + \sum_{i\sigma} (V_i - \mu) n_{i\sigma} \quad (D.4)$$

$$H_{coup} = \sum_i (\Delta_i c_{i\uparrow}^\dagger c_{i\downarrow}^\dagger + h.c) + \sum_i \phi_i n_i \quad (D.5)$$

Now we approximate  $\phi_i = \phi_{0,i}$  where  $\phi_{0,i}$  is the  $T = 0$  saddle point value of  $\phi$  field and similarly we approximate  $\Delta_i = \Delta_{0,i} + \delta\Delta_i$  where  $\Delta_{0,i}$  is the  $T=0$  saddle point value of  $\Delta$  field.

Now  $S_{eff}$  can be rewritten as

$$S_{eff} \approx S_1 + S_2 + S_3 + S_4 \quad (D.6)$$

$$S_1 = \int_0^\beta d\tau \sum_{i,\sigma} \bar{c}_{i,\sigma} (\partial_\tau - \mu) c_{i,\sigma} + \sum_i (\Delta_{0,i} c_{i\uparrow}^\dagger c_{i\downarrow}^\dagger + h.c) \quad (D.7)$$

$$+ \sum_i \phi_{0i} n_i + H_{0i} + \frac{1}{|U|} \sum_i (|\Delta_{0i}|^2 + \phi_{0i}^2) \quad (\text{D.8})$$

$$S_2 = \int_0^\beta \sum_i (\delta \Delta_i c_{i\uparrow}^\dagger c_{i\downarrow}^\dagger + h.c) \quad (\text{D.9})$$

$$S_3 = \frac{\beta}{|U|} \sum_i (\delta \Delta_i^* \Delta_{0i} + \delta \Delta_i \Delta_{0i}^*) \quad (\text{D.10})$$

$$S_4 = \frac{\beta}{|U|} \sum_i \delta \Delta_i^* \delta \Delta_i \quad (\text{D.11})$$

The original partition function is approximated by

$$Z \approx Z_{approx} = \int D[\delta \Delta, \delta \Delta^*] D[c, \bar{c}] e^{-S_1 - S_3 - S_4} \left( \sum_n \frac{(-S_2)^n}{n!} \right) \quad (\text{D.12})$$

$$= \int D[\delta \Delta, \delta \Delta^*] D[c, \bar{c}] e^{-S_1 - S_3 - S_4} \left( 1 - S_2 + \frac{(S_2)^2}{2!} + \dots \right) \quad (\text{D.13})$$

$$= \int D[\delta \Delta, \delta \Delta^*] Tr[e^{-\beta H_f}] e^{-S_3 - S_4} \left( 1 - \langle S_2 \rangle + \frac{\langle S_2^2 \rangle}{2!} + \dots \right) \quad (\text{D.14})$$

where

$$\int D[c, \bar{c}] e^{-S_1} = Tr[e^{-\beta H_f}]$$

$$H_f = H_0 + \sum_i ((\Delta_{0i} c_{i\uparrow}^\dagger c_{i\downarrow}^\dagger + h.c) + \phi_{0i} n_i) + \frac{1}{|U|} \sum_i (|\Delta_{0i}|^2 + \phi_{0i}^2)$$

$$\int D[c, \bar{c}] e^{-S_1} S_2 = \langle S_2 \rangle$$

due to saddle point solution ( $S_3 - \langle S_2 \rangle = 0$ ).

$$Z_{approx} = \int D[\delta \Delta, \delta \Delta^*] Tr[e^{-\beta H_f}] e^{-S_4} \left( 1 + \frac{\langle S_2^2 \rangle - \langle S_2 \rangle^2}{2!} + \dots \right) \quad (\text{D.15})$$

Now

$$\begin{aligned} & \frac{\langle S_2^2 \rangle - \langle S_2 \rangle^2}{2!} \\ &= \frac{1}{2!} \int_0^\beta d\tau_1 d\tau_2 \sum_{ij} (-\delta \Delta_i \delta \Delta_j F_{ij}(\tau_1 - \tau_2) F_{ji}(\tau_2 - \tau_1)) \end{aligned}$$



$$\begin{aligned}
& - \delta\Delta_i^* \delta\Delta_j^* F_{ji}(\tau_1 - \tau_2) F_{ij}(\tau_2 - \tau_1) \\
& + \delta\Delta_i^* \delta\Delta_j G_{ij\uparrow}(\tau_1 - \tau_2) G_{ij\downarrow}(\tau_1 - \tau_2) \\
& + \delta\Delta_i \delta\Delta_j^* G_{ji\downarrow}(\tau_2 - \tau_1) G_{ji\uparrow}(\tau_2 - \tau_1)
\end{aligned} \tag{D.16}$$

$$F_{ij}(\tau_2 - \tau_1) = Tr[e^{-\beta H_{eff}} T_\tau c_{i\uparrow}^\dagger(\tau_2) c_{j\downarrow}^\dagger(\tau_1)] / Tr[e^{-\beta H_{eff}}] \tag{D.17}$$

$$G_{ij\sigma}(\tau_2 - \tau_1) = Tr[e^{-\beta H_{eff}} T_\tau c_{i\sigma}(\tau_2) c_{j\sigma}^\dagger(\tau_1)] / Tr[e^{-\beta H_{eff}}] \tag{D.18}$$

Let's assume small angular fluctuations  $\delta\Delta_i = \iota\theta\Delta_{0i}$

$$\frac{\langle S_2^2 \rangle - \langle S_2 \rangle^2}{2!} = \beta \sum_{ij} \theta_i \theta_j \Delta_{0i} \Delta_{0j} J_{ij} \tag{D.19}$$

$$J_{ij}^0 = \frac{1}{\beta} \sum_n F_{ij}(\iota\omega_n) F_{ji}(\iota\omega_n) + G_{ij\uparrow}(\iota\omega_n) G_{ij\downarrow}(-\iota\omega_n) \tag{D.20}$$

$$J_{ij}^0 = \sum_{n1, n2} \frac{(u_{n1}^{i*} v_{n1}^j u_{n2}^{i*} v_{n2}^j + v_{n1}^i u_{n1}^{j*} v_{n2}^i u_{n2}^{j*} + \frac{u_{n1}^i u_{n1}^{j*} u_{n2}^i u_{n2}^{j*} + v_{n1}^{i*} v_{n1}^j v_{n2}^{i*} v_{n2}^j}{E_{n1} + E_{n2}})}{E_{n1} + E_{n2}} \tag{D.21}$$

where  $E_{n1}$  and  $E_{n2}$  are eigenvalues and  $u$  and  $v$  are eigenvectors of HBDG problem in presence of  $\Delta_{0i}$  and  $\phi_{0i}$ .

$$\frac{\langle S_2^2 \rangle - \langle S_2 \rangle^2}{2!} \approx -\beta \sum_{ij} \Delta_{0i} \Delta_{0j} J_{ij}^0 (1 - \cos(\theta_i - \theta_j))$$

$$Z_{approx} \approx Tr[e^{-\beta H_f}] e^{-\beta \sum_{ij} \Delta_{0i} \Delta_{0j} J_{ij}^0 (1 - \cos(\theta_i - \theta_j))} \tag{D.22}$$

The effective model that we derive for phase fluctuations over groundstate

$$H_\theta = \sum_{ij} \Delta_{0i} \Delta_{0j} J_{ij}^0 (1 - \cos(\theta_i - \theta_j)) \quad (\text{D.23})$$

# Bibliography

- [1] I. Bloch, J. Dalibard, W. Zwerger, *Rev. Mod. Phys.* **80**, 885 (2008).
- [2] I. Bloch, *Nature Physics* **1**, 23 (2005).
- [3] C. J. Pethick and H. E. Smith, *Bose Einstein Condensation in Dilute Gases* (2008).
- [4] H. J. Metcalf and P. van der Straten, *Laser Cooling and Trapping*, Springer-Verlag New York (1999).
- [5] J. Waruel and F. Liwag, *Cooling and trapping of  $^{87}\text{Rb}$  atoms in a magneto-optical trap using low-power diode lasers*, Thesis 621.39767 L767c (1999).
- [6] W. D. Phillips, *Rev. Mod. Phys.* **70**, 721 (1998).
- [7] C. Tannoudji, *Rev. Mod. Phys.* **70**, 707 (1998).
- [8] S. Chu, *Rev. Mod. Phys.* **70**, 685 (1998).
- [9] W. Ketterle and N. J. van Druten, *Advances in Atomic, Molecular, and Optical Physics* Volume **37**, 181 (1996).
- [10] M. H. Anderson, J. R. Ensher, M. R. Matthews, C. E. Wieman, E. A. Cornell, *Science* **269**, 198 (1995).
- [11] K. B. Davis, M.-O. Mewes, M. R. Andrews, N. J. van Druten, D. S. Durfee, D. M. Kurn, and W. Ketterle, *Phys. Rev. Lett.* **75**, 3969 (1995).
- [12] C. Chin, R. Grimm, P. Julienne, and E. Tiesinga, *Rev. Mod. Phys.* **82**, 1225 (2010).

- [13] F. Ferlaino and R. Grimm, *Physics* **3**, 9 (2010).
- [14] S. Inouye, M. R. Andrews, J. Stenger, H. J. Miesner, D. M. Stamper-Kurn, and W. Ketterle, *Nature* **392**, 151 (1998).
- [15] S. L. Cornish, N. R. Claussen, J. L. Roberts, E. A. Cornell, and C. E. Wieman, *Phys. Rev. Lett.* **85**, 1795 (2000).
- [16] P. O. Fedichev, Yu. Kagan, G. V. Shlyapnikov, and J. T. M. Walraveni, *Phys. Rev. Lett.* **77**, 2913 (1996).
- [17] M. Theis, G. Thalhammer, K. Winkler, M. Hellwig, G. Ruff, R. Grimm, and J. Hecker Denschlag, *Phys. Rev. Lett.* **93**, 123001 (2004).
- [18] Moerdijk, A. J., B. J. Verhaar, and A. Axelsson, *Phys. Rev. A* **51**, 4852 (1995).
- [19] M. P. A. Fisher, P. B. Weichman, G. Grinstein, and D. S. Fisher, *Phys. Rev. B* **40**, 546 (1989).
- [20] D. Jaksch, C. Bruder, J. I. Cirac, C. W. Gardiner, and P. Zoller, *Phys. Rev. Lett.* **81**, 3108 (1998).
- [21] Neil W. Ashcroft , N. Mermin *Solid State Physics* (1976).
- [22] Breaking up a superfluid, H. T. C. Stoof, *Nature* **415**, 25 ( 2002)
- [23] K. Sheshadri, H. R. Krishnamurthy, R. Pandit, T. V. Ramakrishnan, *Europhys. Lett.* **22**, 257 (1993).
- [24] F. Gerbier et al., *Phys. Rev. Lett.* **95**, 050404 (2005).
- [25] I. B. Spielman, W. D. Phillips, and J. V. Porto, *Phys. Rev. Lett.* **98**, 080404 (2007).
- [26] M. Greiner *et al.*, *Nature (London)* **415**, 39 (2002).
- [27] I. B. Spielman, W. D. Phillips, and J. V. Porto, *Phys. Rev. Lett.* **100**, 120402 (2008).
- [28] S. Trotzky, L. Pollet, F. Gerbier, U. Schnorrberger, I. Bloch, N.V. Prokof'ev, B. Svistunov, M. Troyer, *Nature Phys.* **6**, 998 (2010)

- [29] N. Gemelke, X. Zhang, C. L. Hung, C. Chin, *Nature* **460**, 995 (2009).
- [30] W. S. Bakr, A. Peng, M. Eric Tai, R. Ma, J. Simon, J. I. Gillen, S. Foelling, L. Pollet, M. Greiner, *Science* **329**, 547 (2010).
- [31] M. T. DePue, C. McCormick, S. L. Winoto, S. Oliver, D. S. Weiss, *Phys. Rev. Lett.* **82**, 2262 (1999).
- [32] P. Nozieres and D. Pines, *The theory of quantum liquids: superfluid Bose liquids*, Westview Press (1989).
- [33] N. N. Bogoliubov, *J. Phys. USSR* **11**, 23 (1947).
- [34] E. P. Gross, *Il Nuovo Cimento*. **20**, (3) 454 (1961), L. P. Pitaevskii, *Sov. Phys. JETP*. **13**, (2) 451 (1961).
- [35] F. Dalfovo, S. Giorgini, L. P. Pitaevskii and S. Stringari, *Rev. Mod. Phys.* **71**, 463 (1999).
- [36] J. K. Freericks, H. R. Krishnamurthy, Y. Kato, N. Kawashima, N. Trivedi, *Phys. Rev. A* **79**, 053631 (2009).
- [37] S. Sachdev, *Quantum Phase Transitions*, 2nd edn, Cambridge Univ. Press (2011).
- [38] E. Altman, A. Auerbach, *Phys. Rev. Lett.* **89**, 250404 (2002).
- [39] L. Pollet and N. Prokof'ev, *Phys. Rev. Lett.* **109**, 010401 (2012).
- [40] D. Podolsky, S. Sachdev, *Phys. Rev. B* **86**, 054508 (2012).
- [41] Endres, T. Fukuhara, D. Pekker, M. Cheneau, P. Schauupbeta, C. Gross, E. Demler, S. Kuhr, and I. Bloch, *Nature* **487**, 454 (2012).
- [42] T. L. Dao, A. Georges, J. Dalibard, C. Salomon, and I. Carusotto, *Phys. Rev. Lett.* **98**, 240402 (2007).
- [43] J. T. Stewart, J. P. Gaebler, and D. S. Jin, *Nature (London)* **454**, 744 (2008).
- [44] N. Fabbri, S. D. Huber, D. Clement, L. Fallani, C. Fort, M. Inguscio, and E. Altman, *Phys. Rev. Lett.* **109**, 055301 (2012).

- [45] T. Stofferle, H. Moritz, C. Schori, M. Kohl, T. Esslinger, Phys. Rev. Lett. **92**, 130403 (2004).
- [46] T. Stofferle, H. Moritz, C. Schori, M. Kohl, T. Esslinger, Phys. Rev. Lett. **93**, 240402 (2004).
- [47] L. Liu, Kun C., Youjin Deng, M. Endres, L. Pollet, and N. Prokofev, Phys. Rev. B **92**, 174521 (2015).
- [48] S. Huber, B. Theiler, E. Altman, G. Blatter, Phys. Rev. Lett. **100**, 050404 (2008).
- [49] C. Menotti, N. Trivedi, Phys. Rev. B **77**, 235120 (2008).
- [50] A. M. Rey, P. Blair Blakie, G. Pupillo, C. J. Williams, C. W. Clark, Phys. Rev. A **72**, 023407 (2005).
- [51] A. Brunello *et al.*, Phys. Rev. A **64**, 063614 (2001).
- [52] J. Stenger *et al.*, Phys. Rev. Lett. **82**, 4569 (1999).
- [53] D. Stamper-Kurn *et al.*, Phys. Rev. Lett. **83**, 2876 (1999).
- [54] S. B. Papp *et al.*, Phys. Rev. Lett. **101**, 135301 (2008).
- [55] D. Clément, N. Fabbri, L. Fallani, C. Fort, and M. Inguscio, Phys. Rev. Lett. **102**, 155301 (2009).
- [56] P. T. Ernst, S. Götze, J. S. Krauser, K. Pyka, D. Lühmann, D. Pfannkuche and K. Sengstock, Nature Physics **6**, 56 (2010).
- [57] N. Fabbri *et al.*, Phys. Rev. A **79**, 043623 (2009).
- [58] U. Bissbort, S. Götze, Y. Li, J. Heinze, J. S. Krauser, Malte Weinberg, C. Becker, K. Sengstock, W. Hofstetter, Phys. Rev. Lett. **106**, 205303 (2011).
- [59] D. Huber, E. Altman, H. P. Büchler, G. Blatter, Phys. Rev. B **75**, 085106 (2007).
- [60] N. Elstner, H. Monien, Phys Rev B **59**, 12184 (1999).
- [61] J. K. Freericks, H. Monien, Europhys. Lett, **26**, 545 (1994).
- [62] F. E. A. dos Santos, A. Pelster, Phys. Rev. A **79**, 013614 (2009).

- [63] A. Dutta, C. Trefzger, K. Sengupta, Phys. Rev. B **86**, 085140 (2012).
- [64] D. Lühmann, Phys. Rev. A **87**, 043619 (2013).
- [65] M. Knap, E. Arrigoni, W. von der Linden, Phys. Rev. B **83**, 134507 (2011).
- [66] S. Ejima, H. Fehske, F. Gebhard, K. zu Münster, M. Knap, E. Arrigoni, and W. von der Linden, Phys. Rev. A **85**, 053644 (2012).
- [67] M. Knap, E. Arrigoni, W. von der Linden, Phys. Rev. B **81**, 024301 (2010).
- [68] M. Knap, E. Arrigoni, W. von der Linden, Phys. Rev. B **81**, 235122 (2010).
- [69] D. B. M. Dickerscheid, D. van Oosten, P. J. H. Denteneer, H. T. C. Stoof, Phys. Rev. A **68**, 043623 (2003).
- [70] X. Lu, J. Li, Y. Yu, Phys. Rev. A **73**, 043607 (2006).
- [71] K. Byczuk, D. Vollhardt, Phys. Rev. B **77**, 235106 (2008).
- [72] W. Hu, N. Tong, Phys. Rev. B **80**, 245110 (2009).
- [73] P. Anders, E. Gull, L. Pollet, M. Troyer, P. Werner, Phys. Rev. Lett. **105**, 096402 (2010).
- [74] J Panas, A Kauch, J Kuneš, D Vollhardt, K Byczuk, Phys. Rev. B **92**, 045102 (2015)
- [75] P. Pippan, H. G. Evertz, M. Hohenadler, Phys. Rev. A **80**, 033612
- [76] D. van Oosten, D. B. M. Dickerscheid, B. Farid, P. vander Straten, H. T. C. Stoof, Phys. Rev. A **71**, 021601 (2005)
- [77] Y.-J. Lin, K. Jimenez-Garcia, I. B. Spielman, Nature, 471, **83** (2011).
- [78] M. C. Beeler, R. A. Williams, K. Jimenez-Garcia, L. J. Leblanc, A. R. Perry, I. B. Spielman, Nature, **498**, 201 (2013).
- [79] L J LeBlanc, M C Beeler, K Jimenez-Garcia, A R Perry, S Sugawa, R A Williams, I B Spielman, New Journal of Physics, **15(7)** 073011 (2013).
- [80] H. Zhai, International Journal of Modern Physics B, **26**, 30001 (2012).

- [81] S. C. Ji, J. Y. Zhang, L. Zhang, Z. D. Du, W. Zheng, Y. J. Deng, H. Zhai, S. Chen, J. W. Pan, *Nature Physics*, **10**, 314 (2014).
- [82] T L Ho, S Zhang, *Phys. Rev. Lett.* **107**, 150403 (2011).
- [83] Y. Li, L. P. Pitaevskii, S. Stringari, *Phys. Rev. Lett.* **108**, 225301 (2012).
- [84] D. L. Campbell, G. Juzeliunas and I. B. Spielman, *Phys. Rev. A* **84**, 025602 (2011).
- [85] J D Sau, R Sensarma, S Powell, I B Spielman, S Das Sarma, *Phys. Rev. B* **83**, 140510 (2011).
- [86] Xu Z F, You L, *Phys. Rev. A* **85** 043605 (2012).
- [87] Anderson B M, Spielman I B, Juzelinass G, *Phys. Rev. Lett.* **111**, 125301 (2013).
- [88] Xu Z F, You L , Ueda M, *Phys. Rev. A* **87** 063634 (2013).
- [89] D. Hugel, B. Paredes, *Phys. Rev. A* **89**, 023619 (2014).
- [90] J. Struck, J. Simonet, K. Sengstock, *Phys. Rev. A* **90**, 031601 (2014).
- [91] M. L. Wall, A. P. Koller, S. Li, X. Zhang, N. R. Cooper, J. Ye, A. M. Rey, *Phys. Rev. Lett.* **116**, 035301 (2016)
- [92] M. Atala, M. Aidelsburger, J. T. Lohse, M. Barreiro, B. Paredes, I. Bloch, *Nat. Phys.* **10**, 588 (2014).
- [93] L. F. Livi, G. Cappellini, M. Diem, L. Franchi, C. Clivati, M. Frittelli, F. Levi, D. Calonico, J. Catani, M. Inguscio, L. Fallani, *Phys. Rev. Lett.* **117**, 220401 (2016).
- [94] C. Hamner, Yongping Zhang, M.A. Kamehchi, M. J. Davis, P. Engels, *Phys. Rev. Lett.* **114**, 070401 (2015)
- [95] D Jaksch, P Zoller, *New Journal of Physics*, **5**, 56 (2003).
- [96] K. Osterloh, M. Baig, L. Santos, P. Zoller, M. Lewenstein, *Phys. Rev. Lett.* **95**, 010403 (2005).



- [97] N Goldman, F Gerbier, M Lewenstein, Journal of Physics B, **46(13)**,134010 (2013).
- [98] A. M. Dudarev, R. B. Diener, I. Carusotto, Q. Niu, Phys. Rev. Lett. **92**,153005 (2004).
- [99] T. Grass, K. Saha, K. Sengupta, M. Lewenstein, Phys. Rev. A **84**, 053632 (2011).
- [100] S. Mandal, K. Saha, K. Sengupta, Phys. Rev. B **86**, 155101 (2012).
- [101] L. He, A. Ji, W. Hofstetter, Phys. Rev. A **92**, 023630 (2015).
- [102] G. Baym, T. Ozawa, Journal of Physics, **529**, 012006 (2014).
- [103] C. Hickey, A. Paramekanti, Phys. Rev. Lett. **113**, 265302 (2014).
- [104] P. W. Anderson, Phys. Rev. **109**, 1492 (1958).
- [105] J Billy, V Josse, Z Zuo, A Bernard, B Hambrecht, P Lugan, D Clément, L S Palencia, P Bouyer, A Aspect, Nature, **453**, 891 (2008)
- [106] G Roati, C D’Errico, L Fallani, M Fattori, C Fort, M Zaccanti, G Modugno, M Modugno, M Inguscio Nature, **453**, 895 (2008)
- [107] A Aspect, M Inguscio, Physics Today **62**, 8, 30 (2009).
- [108] J W. Goodman, *Speckle Phenomena in Optics: Theory and Applications*, Roberts and Company Publishers (2007).
- [109] L. Sanchez-Palencia, D. Clement, P. Lugan, P. Bouyer, G. V. Shlyapnikov, A. Aspect Phys. Rev. Lett. **98**, 210401 (2007).
- [110] J Billy, V Josse, Z Zuo, A Bernard, B Hambrecht, P Lugan, D Clement, L S Palencia, P Bouyer, A Aspect, Nature, **453**, 891 (2008).
- [111] G Roati, C D Errico, L Fallani, M Fattori, C Fort, M Zaccanti, G Modugno, M Modugno, M Inguscio, Nature, **453**, 895 (2008).
- [112] F. Jendrzejewski, A. Bernard, K. Müller, P. Cheinet, V. Josse, M. Piraud, L. Pezze, L. Sanchez-Palencia, A. Aspect, P. Bouyer Nature Phys, **8**, 398 (2012).

- [113] L. Fallani, J. E. Lye, V. Guarrera, C. Fort, M. Inguscio, Phys. Rev. Lett. **98**, 130404 (2007).
- [114] M. White, M. Pasienski, D. McKay, S. Q. Zhou, D. Ceperley, B. DeMarco, Phys. Rev. Lett. **102**, 055301 (2009).
- [115] M. Pasienski, D. McKay, M. White, B. DeMarco, Nature Phys, **6**, 677 (2010)
- [116] S. S. Kondov, W. R. McGehee, J. J. Zirbel, B. DeMarco, Science **334**, 66 (2011)
- [117] W. R. McGehee, S. S. Kondov, W. Xu, J. J. Zirbel, B. DeMarco, Phys. Rev. Lett. **111**, 145303 (2013).
- [118] S. S. Kondov, W. R. McGehee, W. Xu, B. DeMarco, Phys. Rev. Lett. **114**, 083002 (2015).
- [119] S Krinner, D Stadler, J Meineke, J P Brantut, T Esslinger, Phys. Rev. Lett. **115**, 045302 (2015).
- [120] M. Robert-de-Saint-Vincent, J.-P. Brantut, B. Allard, T. Plisson, L. Pezzé, L. Sanchez-Palencia, A. Aspect, T. Bourdel, P. Bouyer, Phys. Rev. Lett. **104**, 220602 (2010).
- [121] R. C. Kuhn, O. Sigwarth, C. Miniatura, D. Delande, C. A. Muller, New Journal of Physics **9**, 161 (2007).
- [122] S Sucu, S Aktas, S. E Okan, Z Akdeniz, P Vignolo, Phys. Rev. A **84**, 065602 (2011).
- [123] M Piraud, L Pezze, L S Palencia, Europhys. Lett. **99**, 50003 (2012).
- [124] M Piraud, L Pezze, L S Palencia, New Journal of Physics **15**, 075007 (2013).
- [125] D Delande, G Orso, Phys. Rev. Lett. **113**, 060601 (2014).
- [126] E. Fratini, S. Pilati, Phys. Rev. A **92**, 063621 (2015).
- [127] W. Morong, B. DeMarco, Phys. Rev. A **92**, 023625 (2015).
- [128] M Pasek, G Orso, D Delande, Phys. Rev. Lett. **118**, 170403 (2017).
- [129] R. C. Kuhn, C. Miniatura, D. Delande, O. Sigwarth, C. A. Muller, Phys. Rev. Lett. **95**, 250403 (2005).

- [130] F. Kruger, J. Wu, P. Phillips, Phys. Rev. B **80**, 094526 (2009).
- [131] U. Bissbort, R. Thomale, W. Hofstetter, Phys. Rev. A **81**, 063643 (2010).
- [132] D. Semmler, J. Wernsdorfer, U. Bissbort, K. Byczuk, W. Hofstetter, Phys. Rev. B **82**, 235115 (2010).
- [133] V. W. Scarola, B. DeMarco, Phys. Rev. A **92**, 053628 (2015).
- [134] D. van Oosten, P. van der Straten, H. T. C. Stoof, Phys. Rev. A **63**, 053601 (2001).
- [135] T. McIntosh, P. Pisarski, R. J. Gooding, E. Zaremba, Phys. Rev. A **86**, 013623 (2012).
- [136] P. Pisarski, R. M. Jones, R. J. Gooding, Phys. Rev. A **83**, 053608 (2011).
- [137] P. Buonsante, V. Penna, A. Vezzani, Phys. Rev. A **70**, 061603 (2004).
- [138] P. Jain, C. W. Gardiner, J. Phys. B **37**, 3649 (2004).
- [139] K. Sengupta, N. Dupuis, Phys. Rev. A **71**, 033629 (2005).
- [140] B. Bradlyn, F. E. A. dos Santos, A. Pelster, Phys. Rev. A **79**, 013615 (2009).
- [141] M. Ohliger, A. Pelster, *World Journal of Condensed Matter Physics* **3**, 125-130 (2013).
- [142] D. Podolsky, A. Auerbach, and D. P. Arovas, Phys. Rev. B **84**, 174522 (2011).
- [143] S. Gazit, D. Podolsky, and A. Auerbach, Phys. Rev. Lett. **110**, 140401 (2013).
- [144] B. Capogrosso-Sansone, S. G. Söyler, N. Prokof'ev, B. Svistunov, Phys. Rev. A, **77**, 015602 (2008).
- [145] B. Capogrosso-Sansone, N. V. Prokof'ev, B. V. Svistunov, Phys. Rev. B **75**, 134302 (2007).
- [146] N V Prokof'ev., B V Svistunov, I Tupitsyn, Sov. Phys. JETP **87**, 310–321 (1998).
- [147] L Pollet, K V Houcke, S M A Rombouts, J. Comput. Phys. **225**, 2249 (2007).
- [148] K. Chen, L. Liu, Y. Deng, L. Pollet, N. Prokof'ev, Phys. Rev. Lett. **110**, 170403 (2013).
- [149] D. Hügel, L. Pollet, Phys. Rev. B **91**, 224510 (2015).

- [150] A. P. Kampf, G. T. Zimanyi, Phys. Rev. B **47**, 279 (1993).
- [151] J. Radic, A. Di Ciolo, K. Sun, V. Galitski, Phys. Rev. Lett. **109**, 085303 (2012).
- [152] Zi Cai, Xiangfa Zhou, Congjun Wu, Phys. Rev. A **85**, 061605 (2012).
- [153] S Sinha, R Nath, L Santos, Phys. Rev. Lett. **107**, 270401 (2011).
- [154] Hui Hu, B. Ramachandhran, Han Pu, Xia-Ji Liu, Phys. Rev. Lett. **108**, 010402 (2012).
- [155] X Zhou, Yi Li, Zi Cai, C Wu, Journal of Physics B **46(13)**, 134001 (2013).
- [156] M Gong, Y Qian, M Yan, V. W. Scarola, C Zhang, Scientific Reports volume **5**, 10050 (2015)
- [157] W S. Cole, S Zhang, A Paramekanti, N Trivedi, Phys. Rev. Lett. **109**, 085302 (2012).
- [158] A. T. Bolukbasi, M. Iskin, Phys. Rev. A **89**, 043603 (2014).
- [159] Mi Yan, Y Qian, H Y Hui, M Gong, C Zhang, V. W. Scarola, Phys. Rev. A **96**, 053619 (2017).
- [160] S. Tarat, P. Majumdar, Eur. Phys. J. B **88**, 68 (2015) .
- [161] S. Kumar, P. Majumdar, Eur. Phys. J. B, **50**, 571 (2006).
- [162] A. S. Sajna, T. P. Polak, R. Micnas, P. Rožek, Phy. Rev. A **92**, 013602 (2015).
- [163] S Wessel, F Alet, M Troyer, G. G Batrouni, Phys. Rev. A **70**, 053615 (2004).
- [164] D Malpetti and T Roscilde, Phys. Rev. Lett. **119**, 040602
- [165] T. A. Zaleski, Phys. Rev. A **85**, 043611 (2012).
- [166] S. Schmidt, G. Blatter, Phys. Rev. Lett. **103**, 086403 (2009).
- [167] J Li, W Huang, B Shteynas, S Burchesky, F C Top, E Su, J Lee, Alan O. Jamison, W Ketterle, Phys. Rev. Lett. **117**, 185301 (2016).
- [168] J.R. Li, J. Lee, W. Huang, S. Burchesky, B. Shteynas, F. A. Top, A. O. Jamison, W. Ketterle, Nature **543**, 91 (2017)

- [169] Y.J. Lin, K. Jimenez-Garcia, I. B. Spielman, *Nature* **471**, 83 (2011).
- [170] V. Galitski, I. B. Spielman, *Nature* **494**, 49 (2013).
- [171] R. A. Hart, P. M. Duarte, Tsung-Lin Yang, X. Liu, T. Paiva, E. Khatami, R. T. Scalettar, N. Trivedi, D. A. Huse, R. G. Hulet, *Nature* **519**, 211-214 (2015)
- [172] *Introduction to Many-Body Physics*, Piers Coleman, Cambridge University Press.
- [173] Eiji Kawasaki and Markus Holzmann, *Phys. Rev. A* **95**, 051601(R) (2017).
- [174] P. W. Anderson, *J. Phys. Chem. Solids* **11**, 26 195921.
- [175] A. A. Abrikosov, L. P. Gorkov, *Zh. Eksp. Teor. Fiz.* **36**, 319 (1959).
- [176] E. Abrahams, P. W. Anderson, D. C. Licciardello, T. V. Ramakrishnan, *Phys. Rev. Lett.* **42**, 673 (1979).
- [177] For reviews, see A. M. Goldman and N. Markovic, *Phys. Today* **51**, No 11, 39 (1998), D. Belitz, T. Kirkpatrick, *Rev. Mod. Phys.* **66**, 261 (1994), M. V. Sadovskii, *Phys. Rep.* 282, 225 (1997), V. F. Gantmakher, V. T. Dolgoplov, *Phys. Usp.* **53**, 3-53 (2010).
- [178] A. Ghosal, M. Randeria, N. Trivedi, *Phy. Rev. B* **65**, 014501 (2001)
- [179] N. Trivedi, R. T. Scalettar, M. Randeria, *Phys. Rev. B* **54**, 3756 (1996).
- [180] M. Mayr, G. Alvarez, C. Sen, E. Dagotto, *Phys. Rev. Lett.* **94**, 217001 (2005).
- [181] Y. Dubi, Y. Meir, Y. Avishai, *Nature*, **449**, 876 (2007).
- [182] K. Bouadim, Y. L. Loh, M. Randeria, N. Trivedi, *Nature Phys.* **7**, 884 (2011)
- [183] D. B. Haviland, Y. Liu, A. M. Goldman, *Phys. Rev. Lett.* **62**, 2180 (1989).
- [184] D. Shahar, Z. Ovadyahu, *Phys. Rev. B* **46**, 10917 (1992).
- [185] W. Escoffier, *et al.*, *Phys. Rev. Lett.* **93**, 217005 (2004).
- [186] T. I. Baturina, *et al.*, *Phys. Rev. Lett.* **99**, 257003 (2007).

- [187] T. Esslinger, Annu. Rev. Condens. Matter Phys. **1**, 129 (2010).
- [188] A. Erez, Y. Meir, Phys. Rev. Lett. **111**, 187002 (2013).
- [189] A. Erez, Y. Meir, Phys. Rev. B **88**, 184510 (2013).
- [190] S. Tarat, P. Majumdar, Europhys. Lett. **105** (2014) 67002.
- [191] There is strictly no superfluid-insulator transition at  $T = 0$  within the HFBdG scheme since quantum phase fluctuations are absent. However, at any small finite  $T$  thermal fluctuations can cause a SIT.
- [192] S. Tarat, P. Majumdar, arXiv:1406.5423v1, supplementary material.
- [193] C. A. Regal, M. Greiner, D. S. Jin, Phys. Rev. Lett. **92**, 040403 (2004)
- [194] M. W. Zwierlein, C. A. Stan, C. H. Schunck, J. S. M. F. Raupach, A. J. Kerman, W. Ketterle, Phys. Rev. Lett. **92**, 120403 (2004)
- [195] Q Chen, C. A. Regal, M. Greiner, D. S. Jin, K. Levin, Phys. Rev. A **73**, 041601(R) (2006).
- [196] Y Inada, M Horikoshi, S Nakajima, M K Gonokami, M Ueda, T Mukaiyama, Phys. Rev. Lett. **101**, 180406 (2008).
- [197] C. Chin, M. Bartenstein A. Altmeyer, S. Riedl, S. Jochim, J. Hecker Denschlag, R. Grimm, Science **305**, 1128 (2004).
- [198] A Schirotzek, Y Shin, C H. Schunck, W Ketterle, Phys. Rev. Lett. **101**, 140403 (2008).
- [199] Y. Shin, C. H. Schunck, A. Schirotzek, W. Ketterle, Phys. Rev. Lett. **99**, 090403 (2007).
- [200] D. Gruss, C. C. Chien, M. Di Ventura, M. Zwolak, New Journal of Physics **20**, 115005 (2018).

## Thesis Highlight

Name of the Student: Abhishek Joshi

Name of the CI/OCC: Harish-Chandra Research Institute, Prayagraj

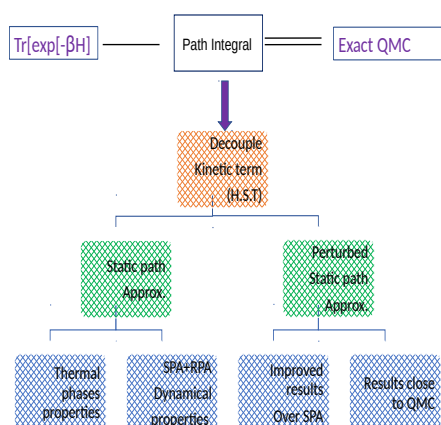
Enrolment No.: PHYS08201005001

Thesis Title: Thermal phase transitions in correlated Bose and Fermi superfluids

Discipline: eg. **Physical Sciences**

Sub-Area of Discipline: **condensed matter theory**

Date of viva voce: 7<sup>th</sup> August 2020



Ultracold atomic systems have emerged as a powerful tool to engineer model Hamiltonians, including correlated Bose and Fermi superfluids, in the laboratory. The fundamental degree of freedom in these systems is the atom. While atoms are composites of elementary particles, at the low energy relevant to cold atom experiments the internal structure of the atom is irrelevant. The center of mass coordinate and the effective 'spin' are the only dynamical variables. The spin also decides the fermionic or bosonic character of the atom.

In the optical lattice realisations of cold atoms one can explore model Hamiltonians over a wide parameter window, avoiding uncontrollable 'solid state' effects like phonons and disorder.

Important achievements, which highlight the connection to condensed matter physics, include the realization of a superfluid to Mott insulator transition in bosons and the BCS to BEC crossover in attractively interacting fermions. The results from these atomic studies provide insight on the role of interparticle interactions in condensed matter systems. Outstanding problems that still await optical lattice realisation include 'high temperature' superfluidity in the repulsive Fermi Hubbard model and the interplay of disorder and interactions in Fermi systems. On another front, cold atoms have already created insight into the out of equilibrium dynamics in interacting systems. The wide possibility in cold atom physics motivate us to test out methods and study models of superfluidity that do not have a straightforward condensed matter realisation. In the Bose case we focus on the Bose Hubbard model (BHM) at filling  $n = 1$ , where increasing interaction drives a superfluid to Mott insulator transition. The thesis devises a new approach to this much studied problem, first establishing thermodynamic results which can be compared to quantum Monte Carlo (QMC) and then moving on to spectral features which are hard to access with other methods. An extension of this approach allows us to study spin-orbit coupling in bosons with internal degrees of freedom. In the Fermi case the thesis studies an intermediate coupling superfluid in the presence of spatially correlated 'speckle' disorder and clarifies its impact on thermal scales and spectral properties.